Investigation of Secondary (Dean) Flows in Curved Microchannels and Application to Microparticle Manipulation in Various Fluids

Arsalan Nikdoost

A DISSERTATION SUBMITTED TO

THE FACULTY OF GRADUATE STUDIES

IN PARTIAL FULFILLMENT OF THE REQUIREMENTS

FOR THE DEGREE OF DOCTOR OF PHILOSOPHY

GRADUATE PROGRAM IN MECHANICAL ENGINEERING

YORK UNIVERSITY

TORONTO, ONTARIO

October 2022

Abstract

Separation, solution exchange, and detection of microparticles and microorganisms, such as DNA, bacteria, and cancer cells are essential steps in a wide range of biomedical applications. Conventional methods such as centrifugation and mechanical filtration rely on laborious processes and deal with the possibility of damaging particles and cells. Microfluidic methods such as inertial manipulation of particles in microchannels, on the other hand, offer low cost and fast sample processing down to the single cell manipulation and detection level. The Dean flow-coupled inertial and elasto-inertial systems, taking advantage of secondary vortices lateral to the direction of the flow in curved microchannels, have provided an improved level of precision over particle separation throughput compared to straight channels. However, the dynamics of fluid flow and particle focusing in fluids with various rheological characteristics like blood and milk still requires a thorough fundamental investigation.

In this thesis, we attempt to fully investigate the control parameters of both fluids and particles in a curvilinear microchannel, with an aim to provide fundamental understanding of the fluid dynamics and particle focusing in various aqueous microenvironments, with a focus on non-Newtonian fluids. In objective 1 of the thesis, we focused on understanding the physics of the secondary Dean flow of viscoelastic fluids and shear-thickening nanofluids in curved microchannels. Various parameters such as channel dimensions and fluid properties were investigated to obtain a comprehensive knowledge of the secondary vortices. Two empirical correlations were developed for the average Dean velocity (V_{De}) of viscoelastic PEO solutions and SiO_2 nanofluids, which significantly reduced the prediction error compared to the existing water-based V_{De} correlations in the literature. In objective 2, the particle dynamics in Dean-coupled elasto-inertial systems were experimentally investigated to understand the effects of different

channel geometries and fluid viscosity on particle focusing behavior in curved microchannels. In objective 3, we demonstrated a proof-of-concept duplex particle washing process in viscoelastic PEO solutions. The developed knowledge of particle and fluid interactions in Dean-coupled elasto-inertial systems could be vital in various biomedical applications that require a target particle washing process. In objective 4, for the first time, we presented the particle behavior analysis in SiO_2 nanofluids and investigated the effects of channel curvature, fluid axial velocity, and viscosity on particles focusing at the channel outlet. Our investigations could be utilized to enhance the throughput and efficiency of microdevices to address real life challenges in microparticle purification and detection in fluids with various rheological properties.

Acknowledgments

First and foremost, I would like to express my earnest gratitude to my supervisor Prof. Pouya Rezai for giving me the opportunity to study at York University and his guidance and patience throughout my PhD studies.

I would like to thank Prof. Sergey Krylov and Prof. Ronald Hanson for their support and advices during my comprehensive exam and annual committee meetings. I am also grateful to Prof. Satinder Brar and Prof. Majid Warkiani for their consideration and patience during the thesis examination.

I express my sincere thanks to my colleagues at York University for their support and guidance during my PhD studies. Especially, Dr. Khaled Youssef, Dr. Arezoo Khalili, Dr. Alireza Zabihi, and Dr. Ali Doostmohammadi for their valuable advices and support over the past years. I am also grateful to my dear friends, Nazanin Roghani, Arash Kalatian, and Siavash Soltani for their friendship and encouragements, and always being there for me through thick and thin.

Finally, I would like to acknowledge my family, my parents and my lovely sister, for their unconditional help in every step of my life.

Table of Contents

List of Tables

List of Figures

Abbreviations

3D: Three-dimensional

Al_2O_3: Aluminum (III) oxide

CAD: Computer aided design

Cq: Quantification cycle

DI Water: Deionized water

FWHM: Full width at half maximum

FACS: Fluorescence activated cell sorting

MACS: magnetic activated cell sorting

NNP: Normalized number of particles

PAA: Poly[acrylamide]

PC: Peak centroid

PCR: Polymerase chain reaction

PDF: Probability distribution function

PDMS: Poly[dimethyl siloxane]

PEO: Poly[ethylene oxide]

PVP: Poly[vinyl pyrrolidone]

RoI: Region of interest

SiO_2: Silicon (iv) oxide

UV-VIS: Ultraviolet-Visible

Glossary of Terms

Acoustophoresis: Migration of particles under the effect of acoustic force exerted by ultrasound waves.

Analytes: A component or chemical substance that is the subject of an analytical procedure.

Biodetection: A universal term for general strategies for the detection of biological matters.

Blockage ratio: The ratio of particle diameter to the channel hydraulic diameter.

Dean flow: Secondary fluid movement in lateral direction due to the channel curvature.

Dielectrophoresis: The movement of neutral particles when subjected to a non-uniform electric field.

Duplex: Investigation of particle behavior in a solution containing two distinct particle types/sizes.

Lab-on-a-chip: A microdevice, which integrates different laboratory functions on a single integrated circuit with a size up to few square centimeters.

Magnetophoresis: This method utilizes the magnetic field gradients to apply a force to particles or cells with magnetic susceptibilities different from the carrying fluid.

Microfluidics: The technology to manipulate fluids in channels with tens of micrometer in size.

Nanofluid: A fluid containing nanoparticles (nanometer-sized particles).

Non-Newtonian fluid: A fluid, which do not follow the Newton's law of viscosity.

Particle washing: Particle focusing and transfer of target cells and particles from a source solution to a clean buffer.

Relaxation time: A characteristic time of a fluid in which it relaxes from a deformed state.

Shear-thinning fluid: A non-Newtonian behavior in which the fluid viscosity decreases at higher shear rates.

Shear-thickening fluid: A non-Newtonian behavior in which the fluid viscosity increases at higher shear rates.

Singleplex: Investigation of particle behavior in a solution containing one distinct particle types/size.

Spectrophotometry: A quantitative analysis to investigate the optical properties of materials over a wide range of wavelength.

Viscoelastic fluid: A type of non-Newtonian fluid, which exhibit both viscous and elastic behavior towards deformation.

Chapter 1

1 Introduction and Theory*

Separation and detection of harmful analytes in bodily fluids, food and water have proven to be vital steps in human health and safety applications[1]. Isolation and enrichment (meaning enhancing concentration without culturing) of target cells and particles, especially at the site of sample acquisition, have attracted widespread attention in the fields of medicine, tissue engineering, drug delivery, environmental monitoring and microparticles coating[2,3]. After isolation and enrichment, there is often a need for separation of various particles and cells from each other, as well as

* Contents of this chapter has been partially published in:

1. Nikdoost, A. & Rezai, P. Dean flow velocity of viscoelastic fluids in curved microchannels. *AIP Adv*. **10**, 085015 (2020).
2. Nikdoost, A. & Rezai, P. Dean Flow Velocity of Shear Thickening SiO_2 Nanofluids in Curved Microchannels. *Phys. Fluids* **34**, 062009 (2022).
3. Nikdoost, A., Doostmohammadi, A., Romanick, K., Thomas, M.,& Rezai, P. Integration of microfluidic sample preparation with PCR detection to investigate the effects of simultaneous DNA-Inhibitor separaton and DNA solution exchange, *Anal. Chim. Acta*, **1160**, 338449 (2021)

transferring them from the original suspension liquid to a target buffer that is more suitable for detection.

Two very common sample preparation operations that are needed in batch or single cell/particle analysis are **particle focusing** and transfer **of target cells and particles from a source solution to a clean buffe**r, a process which is called particle solution exchange or washing in this thesis. Solution exchange is necessary because the source samples usually possess a high level of fluid complexity, such as non-Newtonian properties as well as suspended particulate and molecular matter that are disruptive to detection. Various methods have been used for particle separation and washing, together called particle manipulation in this thesis. Brief reviews of conventional and microfluidic-based particle manipulation methods are presented in sections 1.1 and 1.2.

1.1 Conventional Methods for Particle Manipulation

Conventional technologies for particle separation and washing mainly rely on label-based isolation and transport of cells. Fluorescence and magnetic activated cell sorting (FACS and MACS) methods[4,5] provide cell separation based on specific antigens attached on the cell surface. FACS relies on measurement of optical parameters of a fluid flowing in a channel to isolate the target cells expressing specific fluorescent proteins[6]. In the MACS, target cells are tagged with magnetic nanoparticles, which allow the application of magnetic forces for high throughput sorting and isolation of target particles[7]. Label-based separation is usually irreversible, and needs specific molecular biomarkers[8]. On the other hand, label-free methods such as centrifugation and mechanical filtration offer a non-destructive separation based on the difference in physical properties such as size, density, and deformability of cells[3]. These techniques are often bulky and expensive and only enable the manipulation of batch samples, which contradicts with the need for

continuous processing of large-volume samples such as water and food at the point of sample acquisition (point-of-need).

1.2 Microfluidic Methods for Particle Manipulation

Microfluidic[†] and lab-on-a-chip devices enable the automation and integration of physical and biochemical processes such as sample handling[9,10], detection and analysis[11,12] on a chip at the point of need. Microscale methods offer a wide range of advantages such as reduced reagent volumes, lower cost, higher sensitivity, and faster processing[13]. Microfluidic platforms for particle manipulation are categorized as active or passive methods as discussed below.

1.2.1 Active Microfluidic Methods

Active methods require an external source of energy and this usually increases their design complexity. Common methods include dielectrophoresis, magnetophoresis, and acoustophoresis.

Dielectrophoresis[14–16] is the movement of neutral particles when subjected to a non-uniform electric field. For instance Tornay et al.[15] utilized the dielectric force to push the microparticles towards a buffer solution as shown in Figure 1-1. Their microfluidic device consisted of three different regions. In the pre-focusing region, particles were transferred towards the channel wall. Upon introduction of the buffer solution in the exchange zone, the dielectric force enabled the solution exchange by pushing the particles towards the buffer solution. Later on, different outlets were implemented to separate the fluid streams in the extraction region. They reported a maximum

[†] The technology to manipulate small volumes of fluids in channels with tens of micrometer in size[145].

flow rate of 0.24 µl/min for separation of microparticles between 0.5 – 2.0 µm. The complicated fabrication process and the low working flow rates limit the applications of this method.

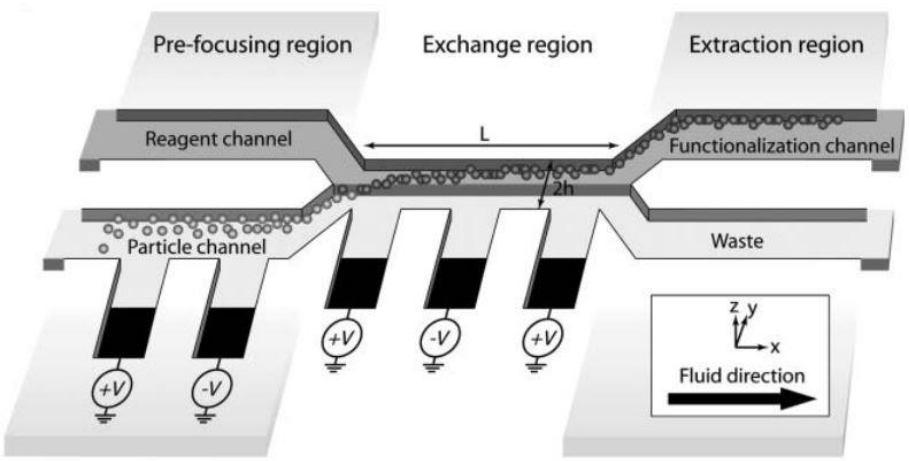

Figure 1-1: Particle solution exchange device using dielectrophoresis force. In pre-focusing region, particles are initially focused close to the channel wall, and later transferred to the buffer solution at the exchange region. Finally, the particles were collected in the extraction region (Reprinted with permission from Royal Society of Chemistry[15]).

Magnetophoresis[17–19] utilizes the magnetic field gradients to apply a force to particles or cells with magnetic susceptibilities different from the carrying fluid. In order to achieve magnetic manipulation of non-magnetic particles in this method, either magnetic particles should be used or the magnetic susceptibility of the carrier solution should be made different from that of neutral particles. Vojtisek et al.[18] reported a multi-step DNA hybridization using magnetic particles. As illustrated in Figure 1-2. Figure 1-2a and Figure 1-2b reagents and buffer solutions were co-flown into the microchannels, where the magnetic particles could be extracted from the buffer stream due to the effect of the permanent magnet on the chip. However, their maximum working flow rate of 0.25 µl/hr was not enough to process large volumes of samples, hence limiting the application of this method to low-volume diagnostics where the concentration of target analyte is relatively high in the sample. Moreover, magnetophoresis is limited to magnetic and magnetically

susceptible particles and cells[20], and the practical flow rates limit its throughput similar to the dielectrophoresis method.

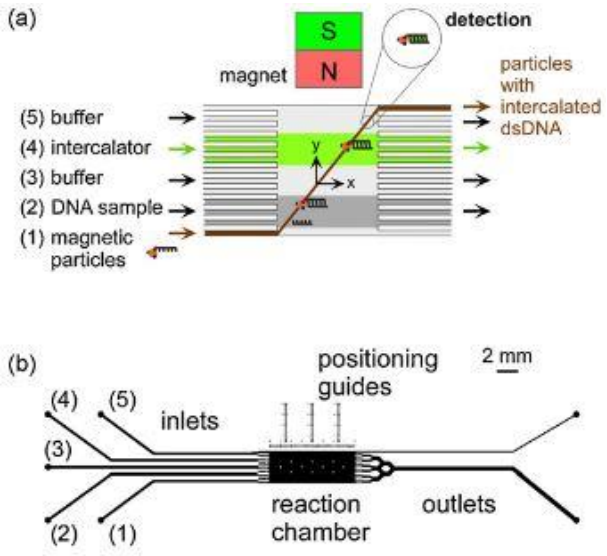

Figure 1-2: (a) The principle of DNA hybridisation using magnetic particles in a continuous flow platform, and (b) the CAD schematic of microdevice with five inlet, a long reaction chamber and two outlets to collect the washed samples (Reprinted with permission from Elsevier[18]).

In acoustophoresis[21–23], particles can be moved to the buffer solution under the effect of acoustic force exerted by ultrasound waves. Petersson et al.[22] used the ultrasound waves to transfer the particles to the pressure nodes in the buffer solution, as shown in Figure 1-3a, and Figure 1-3b. When the ultrasound was off, the target particles could be transferred to the side outlets; however, when the ultrasound was on, the particles were transferred to the clean buffer collected from the channel center. Their method was also limited to a moderate flow rate of 0.3 ml/min, and a low transfer efficiency of 80%. A detailed review of active systems for cell separation and sorting could be found elsewhere[24].

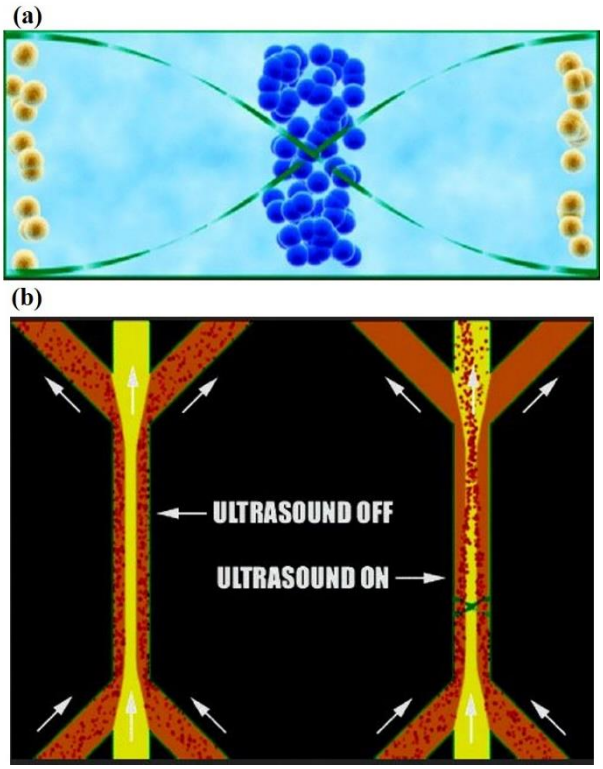

Figure 1-3: (a) Medium exchange principle schematic using acoustophoresis. A piezo-ceramic plate alongside the straight channel enabled the microparticle transfer under the effect of acoustic forces. (b) Under the effect of acoustic waves the particles will either travel towards the center (pressure nodes) or close to the walls (i.e., pressure antinodes). Reprinted with permission from American Chemical Society[22].

1.2.2 Passive Microfluidic Methods

Passive techniques provide a precise control over the microparticles position in microchannels using inertial, drag, and other flow-induced forces. These methods could be categorized based on the fluid's characteristics in various microchannel geometries. The majority of the particle manipulation methods are performed in Newtonian fluids such as water. However, in many of the real life applications, we deal with non-Newtonian fluids, which do not follow the Newton's law of viscosity[25]. Here, we initially review the underlying physics of inertial particle migration in Newtonian fluids in straight and curved microchannels. Later on, we move to the particle behavior investigations in non-Newtonian fluids.

1.2.2.1 Particle Manipulation in Newtonian Fluids

Segre and Silberberg[26] were first to investigate the radial migration of buoyant particles in a cylindrical Poiseuille[‡] flow due to inertial forces. The two dominant components of inertial force are the shear-induced and the wall-induced lift forces[27,28]. Figure 1-4 represents these forces acting on the particles in a pressure driven flow in straight microchannels. Shear-induced lift force is due to the parabolic velocity profile inside a straight microchannel. In order to reduce the velocity difference on either side of the particle, the particles tend to move away from the center of the channel. This is caused by the natural curvature in the velocity profile for particles with blockage ratio $\beta = a/D_h > 0.07$, where a is the particle diameter and D_h is the channel hydraulic diameter[29]. Eq. (1-1) gives an estimation of the shear-induced lift force (F_{LS})[30].

$$F_{LS} = \rho U_{max}^2 C_w \, a^3 / D_h \tag{1-1}$$

where ρ is the fluid density, U_{max} is the maximum fluid velocity, and C_w is the lift coefficient, which is a function of the particles' distance from the channel wall and the Reynolds number [Eq. (1-4)].

When a particle with a comparable size with the channel reaches close to the wall, its motion is hindered in both parallel and perpendicular directions. The existence of a wall retards the motion of the particle and changes the flow field around it, driving the immersed particle away from the wall[31]. This wall-induced lift force is an inverse function of the distance from the wall and could be estimated by Eq.(1-2). In Eq. (1-2), the lift coefficient (C_w) is dependant on the Reynolds number and the particle position[30,32].

[‡] Poiseuille flow profile is achieved when a constant pressure gradient is applied between the channel inlet and outlet in a long duct (i.e., pipe).

$$F_{LW} = \rho U_{max}^2 C_w \, a^6 \Big/ D_h^4 \tag{1-2}$$

As the particles move laterally across streamlines in a channel due to the above inertial forces, they experience a drag force (F_D) against their lateral direction of movement, that could be estimated using the Stokes drag force formula[33] when the particle's Reynolds number (for the flow in lateral direction) is less than unity:

$$F_D = 3\pi\mu a U_L \tag{1-3}$$

where μ shows the fluid dynamic viscosity and U_L represents the particle's lateral velocity as shown in Figure 1-4d.

Reynolds number presented in Eq. (1-4) is a commonly used non-dimensional number that indicates the ratio of inertial forces to viscous forces and is used to determine the fluid flow regime.

$$Re = \rho U D_h / \mu \tag{1-4}$$

In Eq.(1-4), U represents the fluid velocity either in the axial (e.g.,U_{ax}) or lateral (e.g.,U_L) directions. Particle's Reynolds number could be calculate using the relative particle size to the channel hydraulic diameter ($Re_p = \rho Ua/\mu$).

Fluid inertial (f_I) and viscous forces (f_V) per unit volume could be presented as equations (1-5) and (1-6), respectively.

$$f_I = \frac{\rho V_x^2}{D_h} \tag{1-5}$$

$$f_V = \frac{\mu V_x}{D_h^2} \tag{1-6}$$

Here, V_x is the average axial velocity of the fluid inside the microchannel.

The balance between the two dominant inertial forces determines the net inertial lift force acting on particles and specifies their equilibrium positions as shown in Figure 1-4, for different channel cross sections. As reported by Segre and Silberberg[26] in a circular cross section, particles migrate to the radial position of ~ 0.3×D with respect to the channel center, where D is the channel diameter. In square microchannels, particles occupy four equilibrium positions at the center of each side. Altering the channel aspect ratio (AR = height/width) would modify the balance between inertial lift forces. This would transfer the particles towards two equilibrium positions along the longer sides of the channel about 0.2×h, in low aspect ratio channels, where h is the channel height[31]. The minimum required channel length (L_{min}) for the particles to reach to their equilibrium position (X_{eq}) could be estimated using the Eq. (1-7)[13].

$$L_{min} \cong \frac{3\pi\mu H^3}{\rho U a^3} \tag{1-7}$$

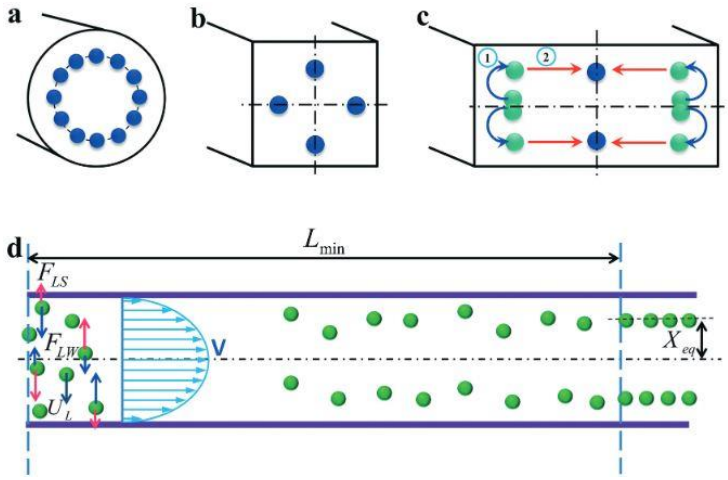

Figure 1-4: Demonstration of equilibrium positions in a straight microchannel with (a) circular, (b) square, and (c) rectangular cross section with AR=0.5. (d) The dominant forces acting on the particles in pressure driven flow in straight microchannel. The shear induced lift force, F_{LS}, pushes the particle towards the walls, while the wall induced lift forces, F_{LW}, resist the particle motion towards the walls. L_{min} is the minimum channel length for the particles to reach to the lateral equilibrium positions (X_{eq}). Reprinted with permission from Royal Society of Chemistry[31].

Mach and Di Carlo[8] investigated label-free and size-based blood filtration using inertial microfluidics. Figure 1-5 shows the microchannel design using gradual expansions to transfer the blood cells close to the channel walls. Depending on the particle size, the net inertial lift force pushed them to different equilibrium positions, so the red blood cells could be collected closer to the walls. By implementing 40 single microchannels in a radial array, they achieved an efficiency higher than 80% with at a high flow rate of 240 ml/hr.

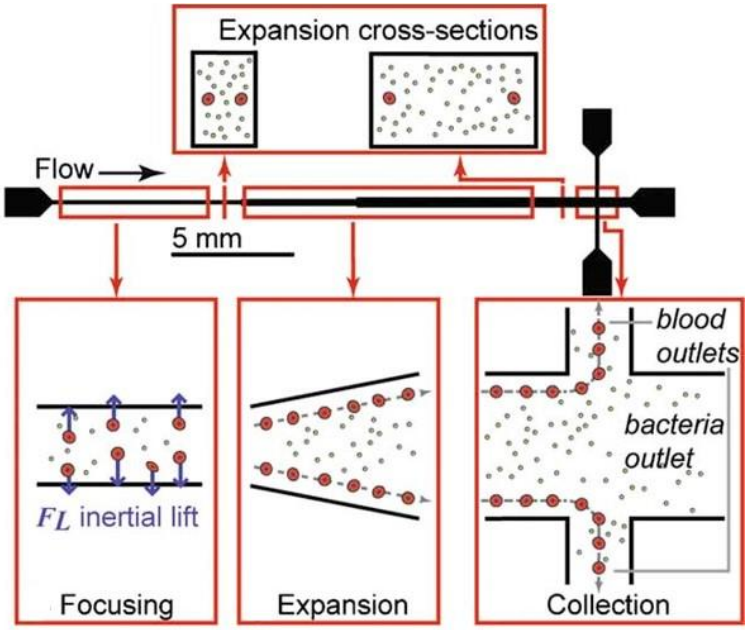

Figure 1-5: Inertial particle focusing with a gradual expansion microchannel. The design consisted of one inlet and three outlets. The inertial lift pushed the larger particles towards the channel side walls. At the outlet the red blood cells could be separated from the bacteria using the implemented side outlets. Reprinted with permission from John Wiley and Sons[8].

Gosset et al.[33] used a straight microchannel to manipulate the net inertial forces on particles toward a clean buffer. They controlled the particles or cells positions using the balance between the wall-induced and shear-induced inertial forces in the microchannel. The microchannel design shown in Figure 1-6 enabled the particle transfer to a clean solution across the laminar streams at a rate of 1000 particles per second. They investigated the size dependant inertial forces and

obtained the critical particle size, which could be transferred between the co-flows as shown in Figure 1-6. A maximum purity of 97% was reported for 19 µm particles for a specific flow condition and geometry.

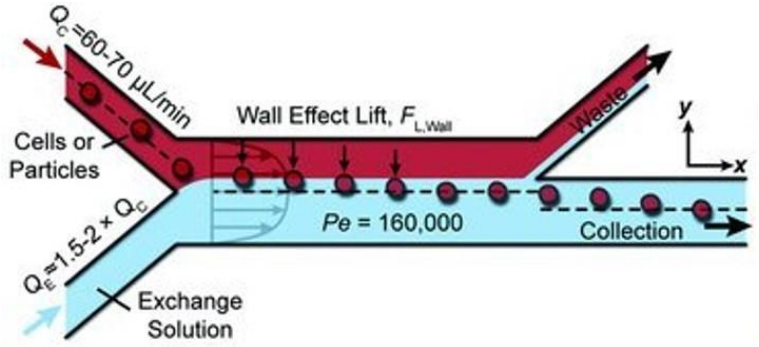

Figure 1-6: Microdevice for the rapid inertial solution exchange, where the net lift force towards the channel center transferred the particles to a clean solution. Reprinted with permission from John Wiley and Sons[33].

Manipulation of inertial forces in a straight microchannel provides a low-cost control on particle equilibrium positions compared to the active methods. Despite the advantages, particle separation and washing in straight microchannels is usually limited to low efficiencies and throughputs. Passive methods using curved microchannels (Figure 1-7) have been introduced to address these challenges.

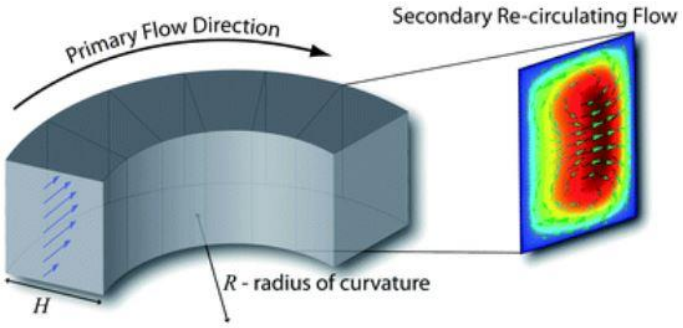

Figure 1-7: Dean flow in curvilinear microchannels. The fluid elements close to the channel center experience a higher centripetal force and travel to the outer side of the curve. The stagnant elements close

to the walls travel inwards and this result in two symmetric vortices. Reprinted with permission from Royal Society of Chemistry[29].

As shown in Figure 1-7, curvilinear microchannels add a pressure gradient to the fluid flow along the radial direction[30]. The velocity difference between the fluid elements near the centerline and the wall region creates a secondary Dean flow in curved microchannels. The larger inertia of the fluid elements near the channel centerline pushes them outward, which creates the radial pressure gradient. To satisfy the continuity equation, the relatively motionless fluid elements near the wall have to recirculate inward[29] as represented in Figure 1-7. These symmetric Dean vortices can be characterized by the dimensionless Dean number which scales with the ratio of inertial (f_I) and centrifugal (f_C) forces with respect to viscous forces (f_V) [31,34,35] as presented in Eq.(1-8). Dean number is often used to specify the strength of secondary flows.

$$De = \sqrt{\frac{\frac{1}{2} \times f_I \times f_C}{f_V}} = Re\sqrt{\frac{D_h}{2R}} \tag{1-8}$$

Here, f_C stands for centrifugal forces per unit volume as presented in Eq.(1-9), and R represents the radius of curvature of the microchannel.

$$f_C = \frac{\rho V_x^2}{R} \tag{1-9}$$

In curved and spiral microchannels the additional viscous drag due to the secondary vortices (called Dean drag) could modify the inertial equilibrium positions of particles. The ratio of the Dean drag and the inertial lift forces specifies the new equilibrium streams as a function of particle size. As shown in Eq.(1-10), R_f could specify the dominant force on particle movement in the presence of secondary vortices.

$$R_f = \frac{F_L}{F_D} \tag{1-10}$$

where F_L , and F_D are the net inertial lift force and the Dean drag acting on the particles in a curvilinear microchannel as shown in Eq. (1-11) and Eq. (1-12), respectively.

$$F_L = \rho \dot{\gamma}^2 C_L a^4 \tag{1-11}$$

$$F_D = 3\pi\mu a V_{De} \tag{1-12}$$

In Eq.(1-11), $\dot{\gamma}$ is the shear rate, and C_L is the average lift coefficient (~ 0.5 for Re < 100)[36,37]. The shear rate is defined as the ratio of maximum axial velocity (U_{max}), and the channel hydraulic diameter (D_h) as shown in Eq.(1-13) below.

$$\dot{\gamma} = \frac{U_{max}}{D_h} \tag{1-13}$$

Channel hydraulic diameter could be calculated using the Eq.(1-14).

$$D_h = \frac{4wh}{2(w+h)} \tag{1-14}$$

where w represents the channel width.

Therefore, the net inertial lift forces could be scaled as[38]:

$$F_L \sim \rho a^4 (\frac{V_x}{D_h})^2 \sim \rho a^4 V_x^2 (\frac{w+h}{wh})^2 \tag{1-15}$$

When the R_f >>1, the net inertial force has a dominant effect on particle focusing, while R_f <<1 results in the dominance of the Dean drag force[30,39]. This enables a complete size-based particle separation with a reduced channel footprint while decreasing the required power.

Manipulation of microparticle positions using the secondary vortices have been extensively investigated by Jiang's group[40,41], Papautsky's group[42,43], Han's group[44,45], and Ding's group[46,47]. For instance, Bhagat et al.[42] reported a continuous duplex particle separation, where complete separation of 7.3 μm, from 1.9 μm particles was achieved using a 5-loop spiral microchannel. Throughout the channel, larger particles tend to occupy a single equilibrium position close to the inner side of the curve. However, smaller particles were entrained with the Dean vortices and moved to the outer wall.

Since Dean flow exerts another drag force on the particles which could alter their equilibrium positions, it is necessary to fully understand the effect of secondary vortices in a microfluidic device. Martel and Toner[30] numerically simulated the Dean flow in the spiral channel to calculate the average Dean flow velocity (V_{De}), and obtained the velocity profile of these lateral secondary flows.

In order to understand the physics of Dean coupled inertial focusing, the effects of microchannel geometry (height, width, and radius of curvature), and fluid properties (density and viscosity) on the average Dean velocity, had to be thoroughly investigated[48,49]. Ookawara et al.[49] numerically studied Dean flows in rectangular curvilinear microchannel and reported a correlation for the average Dean flow velocity [Eq.(1-16)].

$$V_{De} = 1.8 \times 10^{-4} De^{1.63} \left[{}^{m}/_{S} \right] \tag{1-16}$$

Bara et al.[50] experimentally examined the square curved microchannels and validated the formation of symmetric vortices at *De* = 125 and *De* = 137. Ligrani and Niver[51] investigated Dean flow patterns in large aspect ratio microchannels for a wide range of *De* numbers between 40 and 220.

Considering the common range of *De* in microfluidic applications ($0 < De < 30$), experimental and numerical studies were carried out in our group to fully investigate the effects of channel aspect ratio, radius of curvature, and hydraulic diameter. Bayat and Rezai[52] reported a semi-empirical correlation which could provide a better estimation of the average Dean flow velocity of water in a curved microchannel [Eq.(1-17)].

$$V_{De} = 0.031 \times {\vartheta}/{s}\, De^{1.63}\ [{m}/{s}] \tag{1-17}$$

where ϑ is the kinematic viscosity of the fluid, and s is the largest channel cross-sectional dimension.

Kinematic viscosity of the fluid could be calculated as the ratio of dynamic viscosity (μ), and the fluid density (ρ) as shown in Eq.(1-18).

$$\vartheta = {\mu}/{\rho} \tag{1-18}$$

Utilizing this estimation, we designed high throughput particle washing devices, where the target microparticles were transferred from source water into a clean buffer with high efficiencies (> 90%)[53,54]. For instance, we applied a curved-channel microfluidic device to separate DNA from PCR-inhibitor-containing water and simultaneously wash them into clean water for detection using a portable PCR thermocycler. Our device consisted of a half-circle microchannel with a DNA-inhibitor sample inlet, a clean buffer inlet, and multiple outlets. By using the flow-induced inertial forces, 10 μm DNA-conjugated microparticles were focused at the inner-wall of the curved microchannel while separation from 1 μm inhibitor-conjugated microparticles and DNA washing were achieved simultaneously with the Dean flow. We achieved singleplex focusing, isolation and washing of 10 μm particles at an efficiency of 94.5±2.0%. In duplex experiments with 1 μm and 10 μm particles, larger particles were washed with an efficiency of 92.1±1.6% and a purity of

79±2%. By surface-functionalizing the microparticles with affinity groups against Atlantic salmon DNA and humic acid (HA), and processing samples of various concentrations in our device, we achieved an effective purification and detection of DNA molecules using the portable PCR thermocycler. Our method significantly decreased PCR quantitation cycles from Cq >38 to Cq = 30.35±0.5, which confirmed enhancement of PCR amplification[53]. More details on this project is available in Appendix A.

The correlations offered above in Equations (1-16) and (1-17) only predict the average Dean flow velocity of Newtonian fluids (mainly water); however, real life applications usually deal with non-Newtonian fluids like viscoelastic blood. In non-Newtonian fluids the rheological characteristics highly depend on the applied force or stress. Under deformation, the viscoelastic fluids possess both viscous and elastic behavior, as opposed to Newtonian fluids, where their behavior linearly depends on the applied stress[55]. Hence, it is of utmost importance to focus on the physics of non-Newtonian fluids to fully investigate the Dean flow principles, for instance in viscoelastic liquids. This gap was addressed in chapter 3 of this thesis.

1.2.2.2 Particle Manipulation in Non-Newtonian Flows

In non-Newtonian flows, the viscosity does not follow the linear relationship between the shear stress and the shear rate. Non-Newtonian fluids could be prepared by dissolving long polymeric chains or metallic nanoparticles in a Newtonian base solvent[25]. Most of the polymeric solutions and biological fluids exhibit a shear-thinning behavior in which the viscosity decreases with the increasing shear rate. However, a small group of non-Newtonian fluids such as metallic oxides in water possess a shear-thickening behavior and their viscosity increases at higher shear rates[56].

1.2.2.2.1 Shear-thinning Fluids

In non-Newtonian fluids, the non-uniform normal stress differences (N_1 and N_2) cause the lateral migration of particles. These normal stress differences are represented in Eq.(1-19) and Eq.(1-20) based on the normal stresses (τ_{xx}, τ_{yy}, and τ_{zz}) acting on an infinitesimal fluid element shown in Figure 1-8.

$$N_1 = \tau_{zz} - \tau_{xx} \tag{1-19}$$

$$N_2 = \tau_{xx} - \tau_{yy} \tag{1-20}$$

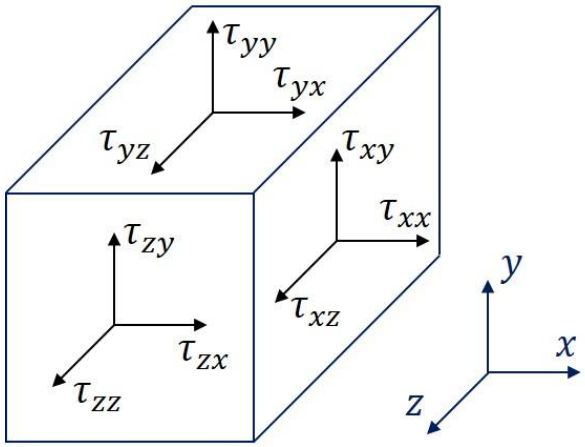

Figure 1-8: The stress tensor acting on an infinitesimal element, where three components exist on each plane. The first subscript represents the perpendicular axis to the plane and second one shows the parallel axis. Here, the flow direction is along the z-axis, while the velocity gradient is in x direction. The vorticity direction is indicated by τ_{yy}.

As illustrated in Figure 1-8, and Eq. (1-19), N_1 represents the difference between the normal stresses in the flow direction (τ_{zz}) and the velocity gradient direction (τ_{xx}). The second normal stress difference (N_2), on the other hand, is the difference between the normal stress in the velocity and the vorticity direction (τ_{yy}).

As mentioned earlier, the viscoelastic effect of non-Newtonian fluids creates a non-uniform distribution of normal stresses (N_1 and N_2). These normal stresses differences generate transverse forces and manipulate the lateral position of particles[57]. Leshansky et al.[58] were first to report on the effect of solution rheology on particle focusing in diluted poly[acrylamide] (PAA) solution in straight channels. Lim et al.[59] investigated the effect of second normal stress difference on the lateral migration of particles. They showed that the non-zero magnitude of N_2 in an aqueous solution of PAA, creates a secondary flow and alters the lateral position of microparticles. However, in general cases, the magnitude of N_2 is around 10% of N_1. Hence, the effect of the second normal stress difference could be neglected. For the fluids with negligible N_2, such as poly[ethylene oxide] (abbreviated as PEO in this report), the non-dimensionalized first normal stress difference could be predicted using the Oldroyd-B model[60–62] in Eq.(1-21).

$$N_1 = \tau_{zz} - \tau_{xx} = 2\eta_p \lambda \dot{\gamma}^2 \tag{1-21}$$

where η_p is the contribution of polymer to the viscosity of the solution, and λ is the fluid relaxation time.

For cylindrical and square microchannels, the normalized $\dot{\gamma}^2$ could be plotted in the channel cross section as shown in Figure 1-9 [63–65]. As illustrated in Figure 1-9a, for a cylindrical channel, the first normal stress tensor has its minimum value at the channel center. Therefore, the particles tend to occupy the channel centerline, as first demonstrated by Karnis et al.[66] for microparticles in circular pipes with millimeter diameters. The effects of fluid rheology, flow rate, particle size and channel length on viscoelastic focusing in circular microchannels have been also reported by Seo et al.[65] and D'avino et al.[67] in PVP (Poly[vinyl pyrrolidone]) and PEO solutions. Meanwhile, in a square cross section (only the upper quarter of the cross section Figure 1-9c), N_1 becomes smaller at the channel center and corners.

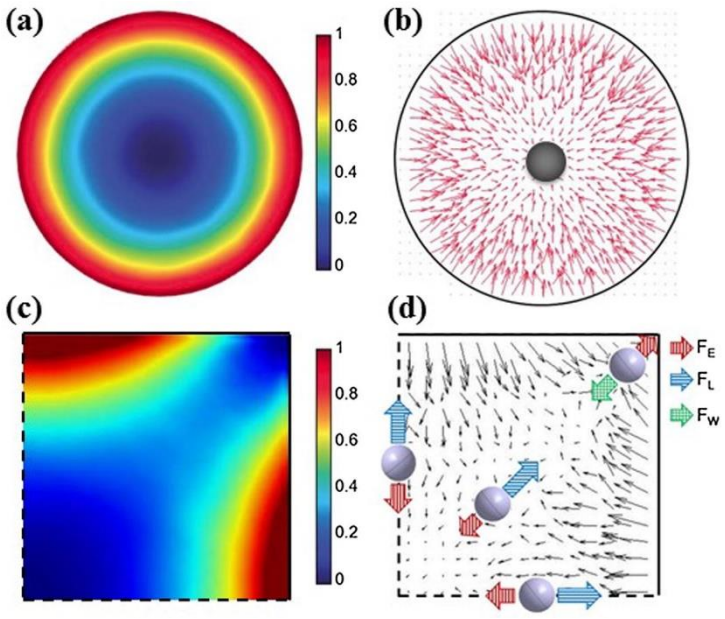

Figure 1-9: The contours of normalized shear rate ($\dot{\gamma}^2$) in the cross section of cylindrical (a), and the upper right quarter of a square microchannel (c). The elastic force (F_E) points to the channel center for cylindrical cross section (b). For a square channel (d), F_E pushes the particles to the channel center and four corners. F_L and F_W represent the shear-induced and wall-induced lift forces. Reprinted with permission from AIP Publishing[64,65] and Elsevier[63].

The viscoelastic lift force acting on the microparticles within a non-Newtonian flow could be calculated based on the N_1 gradient in Eq.(1-22).

$$F_E = C_{el} a^3 \nabla N_1 = -2 C_{el} a^3 \eta_p \lambda \nabla \dot{\gamma}^2 \quad (1\text{-}22)$$

Here, C_{el} is the elastic lift coefficient (~0.05 from Ref. [68]), and a represents the particle diameter. The direction of elastic force is towards the regions with minimum shear rate[69]. Under the sole effect of F_E, the particles are pushed towards the channel center in cylindrical cross section (Figure 1-9b). As shown for the upper right quarter of a square microchannel in Figure 1-9d, the elastic force tends to move the particles towards the channel center and corners.

The non-dimensional Weissenberg number (*Wi*) is a measure to characterize the fluid viscoelasticity. As shown in Eq.(1-23), *Wi* is a product of the shear rate ($\dot{\gamma}$) and the fluid relaxation time (λ).

$$Wi = \dot{\gamma}\lambda \tag{1-23}$$

In a rectangular microchannel, the expression for *Wi* number could be simplified based on the channel characteristics and the flow rate as shown in Eq.(1-24).

$$Wi = \frac{2U_{avg}}{h}\lambda = \frac{2\lambda Q}{wh^2} \tag{1-24}$$

where U_{avg} is the average fluid axial velocity, and $Q = U_{avg}wh$ is the flow rate.

The balance between the elastic and inertial forces could be characterized using the non-dimensional elasticity number, as shown in Eq.(1-25).

$$El = \frac{Wi}{Re} = \frac{\lambda\mu(h+w)}{\rho wh^2} = \frac{Elastic\ Force}{Inertial\ Force} \tag{1-25}$$

The balance between elastic and inertial effects indicates the dominant effect in a non-Newtonian fluid flow. Since both *Wi* and *Re* are linearly dependent on the flow rate, the elasticity number would become independent of the flow rate when the fluid viscosity remains constant. Figure 1-10 demonstrates the effect of adding the viscoelasticity effect in particle equilibrium positions[61]. When the inertial forces are dominant (Figure 1-10a), the elasticity number is close to zero and the particles occupy the center of each wall as the equilibrium positions. In a viscoelastic dominant regime where $El >> 1$ (Figure 1-10b), particles tend to migrate to four corners of the microchannel as well as the center. Finally, the combined effect of inertial and elastic forces in an elasto-inertial flow with $El \approx \mathcal{O}(1)$ (order of 1, Figure 1-10c) transfers the particles towards the channel center.

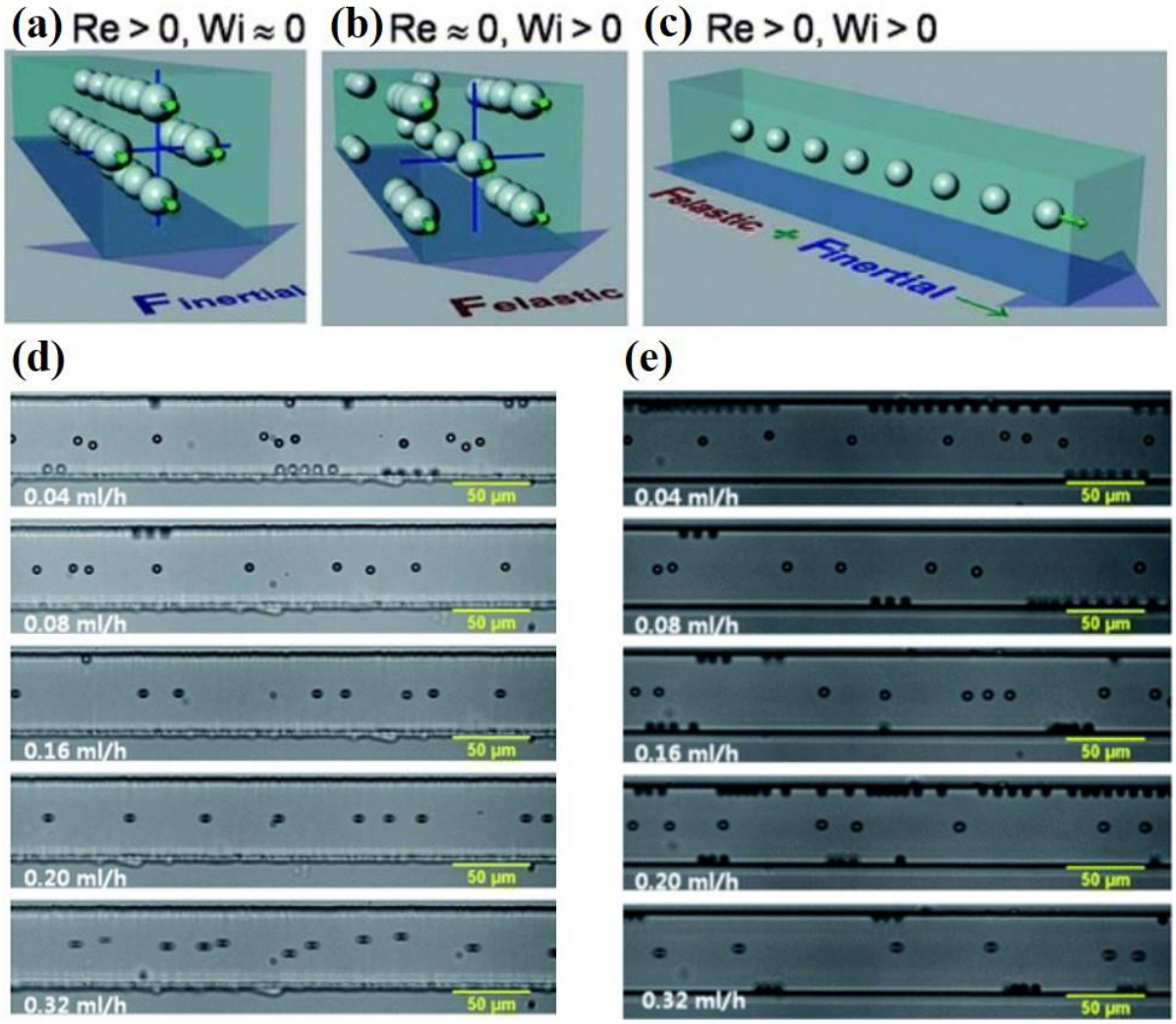

Figure 1-10: Particle alignment in a square microchannel where (a) inertial and (b) elastic forces are dominant. (c) Particle focusing in an elasto-inertial flow where El ≈ O(1). (d-e) Focusing behavior of 5.9 µm particles in (d) 500 ppm PEO solution and (e) 8% v/v PVP solution inside a 50 µm wide square microchannel. Reprinted with permission from Royal Society of Chemistry (Great Britain)[61].

Yang et al.[61] demonstrated the focusing behavior of 5.9 µm polystyrene particles in 500 ppm PEO solution (Figure 1-10d), and 8% v/v PVP solution (Figure 1-10e) inside a square microchannel with a width of 50 µm. As illustrated in Figure 1-10d particles in mild elastic flows (*El* = 21.51) at a flow rate of 20 ml/hr, tend to occupy the channel centerline. Moreover, a higher flow rate results in the dominance of inertial forces and spreads the particles alongside the channel

width. Particle focusing at the channel center was also reported by Del Giudice et al.[70] for 10 µm particles in a PVP solution inside a 50 µm wide square channel with *El* = 49. However, in the case of strong elastic[64] and strong shear-thinning fluids[71], the particle focusing would not work as effectively. As shown in Figure 1-10e, the 5.9 µm particles in a strong elastic PVP solution (8% v/v, *El* = 258) occupied multiple focusing lines at a wide range of flow rates[61]. Additionally, Del Giudice et al.[71] and Seo et. al.[64] showed that in a strong shear-thinning flow (1% PEO solution) the particles shift from the channel centerline towards the four corners as the flow rate increases.

For a Poiseuille flow in dilute PEO solutions with a shear thinning behavior, particles tend to migrate to the channel center with minimized shear rate. When dissolved in water, the entangled polymer strings, could initially withstand the fluid movement. However, the increasing force (~shear rate) would finally break down this resistance, which results in a descent in viscosity at higher shear rates. As the viscosity drops at increasing shear rates, the required pressure to induce the flow decreases and it reduces the shear stresses acting on the particles. This could enable applying higher flow rates and achieving higher throughputs in a distinct channel geometry[72].As reported by Song et al.[73] polymeric solutions with lower molecular weights and shorter length would result in a narrower particle focusing bandwidth.

The coupling effect of the inertial and elastic forces have been reported for low inertia regimes, where the small wall-induced lift forces result in single line particle focusing at the channel center[59,74–80]. For instance, Lim et al.[59] reported focusing of 10 µm particles suspended in PEO solution at a total flow rate of 4.5 µl/min in square microchannel. Kim et al.[74] also investigated the particle movement in 500 ppm PEO solutions inside a 50 × 50 μm^2 square microchannel and achieved a single line focusing for 10 µm particles at flow rates lower than 3.5 µl/min. A comprehensive study on the relationship between particle focusing behavior and dimensionless

numbers (*Re*, *Wi*, and *El*) is reported by Song et al.[73], where they evaluated the particle focusing in various PEO solutions (0.01 to 1.0 wt%) at different flow rates (40 – 320 µl/hr).

Different channel aspect ratios would affect the particle focusing as the net inertial lift [Eq. (1-11)] and elastic forces [Eq. (1-22)] are a strong function of fluid shear rate, and hence the channel geometry. For instance, Xiang et al.[81] investigated the particle focusing behavior when the inertia effects are comparable to the elastic effects and achieved higher throughputs with a rectangular microchannel. The focusing behavior of 10 µm particles was investigated in PEO solution through a low aspect ratio (height/width = 1/3), over a range of flow rates (Q = 1 to 180 µl/min). As shown in Figure 1-11a, the lateral movement of particles go through four stages. At low flow rates, the strong effect of elastic force aligns the particles along the channel height (stage I). As the flow rate increases (stage II), the shear-induced lift force alters the equilibrium positions and pushes the particles towards two symmetrical focusing positions. A further increase in the flow rate, results in a faster increase of the elastic force ($F_E \sim Q^3$) compared to the inertial lift force ($F_L \sim Q^2$), where Q is the flow rate. Therefore, the particles would migrate towards the channel center and form three focusing line as illustrated in the Figure 1-11a (stage III). The particles start to defocus at higher flow rates due to the shear-thinning behavior of the PEO solution (stage IV). The reduced viscosity of the solution would decrease the dominance of the elastic effects and strengthen the inertial lift forces and causes the particle defocusing[67]. Compared to particle behavior in PEO solution (Figure 1-11b), in Newtonian flows (water) the particles occupy a single streak (as shown in Figure 1-11c), which is in fact the overlap of two streams in the channel center.

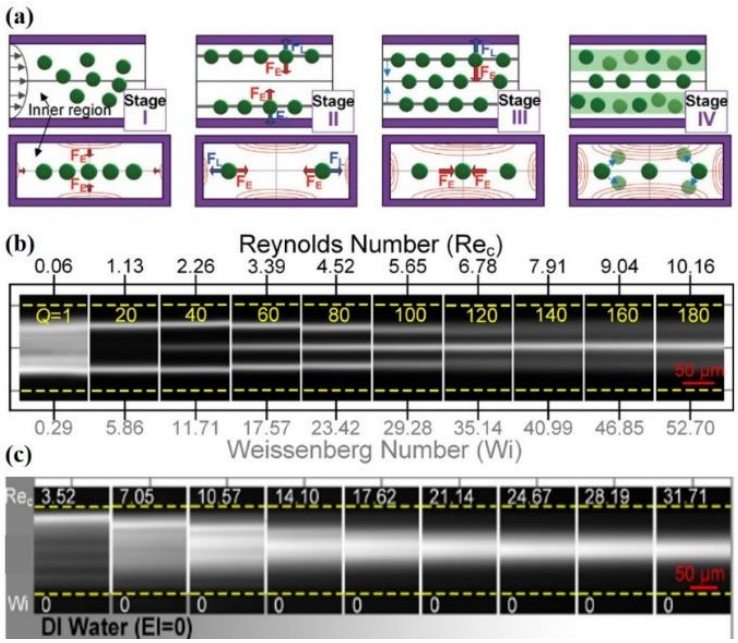

Figure 1-11: (a) Four stages of particle movement under the coupled effect of inertial and elastic forces with increasing flow rates. The top row shows the horizontal plane and the bottom row shows the channel cross section. (b) Particle focusing map of 10 μm particles suspended in PEO solution under a range of flow rates (Q = 1 to 180 μl/min) in a square microchannel with AR = 1/3. (c) Particle focusing behavior in Newtonian flows (DI water, El = 0) over a range of flow rates (Q = 20 to 180 μl/min). Reprinted with permission from AIP Publishing[81].

Similarly, Liu et al.[82] investigated the focusing behavior of 5 μm and 15 μm particles in 2000 ppm PEO solutions in a rectangular microchannel with *AR* = 1/2. At limited range of flow rates, the larger particles occupied two symmetric focusing lines around the channel center, while the smaller particles were focused at the channel center. They have also reported the particle spreading at higher flow rates.

As previously shown net inertial lift force [F_L in Eq. (1-11)], and the elastic force [F_E in Eq. (1-22)] are both strong functions of particle diameter ($F_L \propto a^3$, and $F_E \propto a^4$); therefore, a size-based separation is possible in viscoelastic fluids. Multiplex elasto-inertial particle sorting investigations were reported at relatively low flow rates in the range of ~ O(10) μl/min[61,75,83–86].

For instance, Li et al.[86] reported a parametric study on size-based particle separation in viscoelastic fluids inside low aspect ratio straight microchannels. They investigated the separation of 3 μm, 5 μm, and 10 μm particles in different concentrations of PEO solutions (500, 1000, and 2000 ppm) inside a straight microchannel with a length of 2 cm at wide range of flow rates (50 μl/hr to 500 μl/hr). Figure 1-12a illustrates the effect of PEO concentration on separation of 5 μm, and 10 μm particles in a rectangular microchannel (50 × 25 μm^2) at three different flow rates of 50, 250, and 500 μl/hr. As shown in Figure 1-12a, no separation was detected in water without the viscoelasticity effect of PEO solution. Increasing the PEO concentration results in an enhanced contribution of the elastic force (F_E), and an increase in the *El* number. As a result, particle focusing in 500 ppm PEO (*El* = 9.3) appeared to be weaker compared to 1000 ppm PEO (*El* = 18.8) for both 5 μm, and 10 μm particles, with two symmetric focusing lines for each respective particle. In 2000 ppm PEO solution (*El* = 52.1), microparticles are further pushed towards the channel center under the increased effect of elastic forces. They also reported a multiplex particle separation for three different particle sizes in 1000 ppm PEO solutions inside a rectangular microchannel (*AR* = 0.5). As shown in Figure 1-12b at a flow rate of 300 μl/hr, both 5 μm, and 10 μm particles occupy two symmetric focusing lines around the channel center. Meanwhile, the smaller 3 μm particles were mainly distribute around the centerline, with a slight overlap with 5 μm particles.

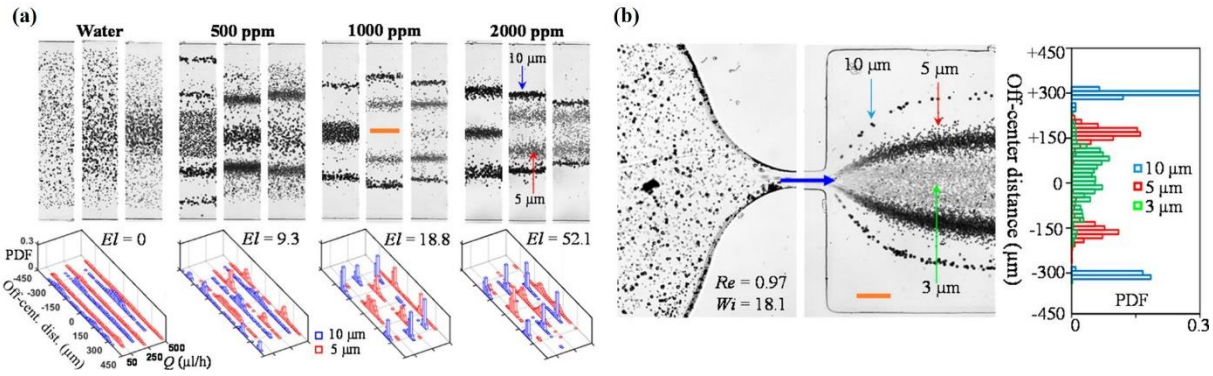

Figure 1-12: Viscoelastic separation of various microparticles in a rectangular straight microchannel (50 × 25 µm²). (a) Effect of PEO concentration on separation of 5 µm and 10 µm particles at three different flow rates of 50, 250, and 500 µl/hr. Bottom panels show the probability distribution function (PDF) along the channel outlet width. (b) Multiplex particle separation for 3 µm, 5 µm, and 10 µm in 1000 ppm PEO solution at a flow rate of 300 µl/hr. The left panel represents the channel entrance, and the middle panel shows the channel expanded outlet. The right panel shows the particles PDF along the outlet width. The scale bars represent 100 µm. Reprinted with permission from ACS Publishing[86].

In spite of reports on multiplex viscoelastic separation, the combination of elastic and inertial effects have been rarely reported for particle washing process due to complications of particle movement under elasto-inertial regimes[87]. Ha et al.[88] reported a high efficiency transfer of Microparticles from a non-Newtonian fluid to a Newtonian domain. As shown in Figure 1-13a, by manipulating the viscoelastic and inertial forces, they conveyed the larger 9.9 µm microparticles from a PEO-spiked solution to a Newtonian fluid in a rectangular microchannel with two inlets and two outlets. As illustrated in the Figure 1-13b, in a non-Newtonian domain, Microparticles are pushed to the channel center under the dominant effect of elastic force. On the other hand, in a Newtonian medium, particles occupy two equilibrium positions close to the center of the wider channel faces. As a result, in a co-flow of Newtonian and non-Newtonian fluids, larger particles suspended in the non-Newtonian fluid could be transferred to the Newtonian stream. Their method enabled the separation 9.9 µm particles from smaller 2.0 µm particles with a throughput of 40

µl/min. After transferring to the Newtonian flow, the larger particles tend to go towards the channel walls, which results in a high purity of 97%.

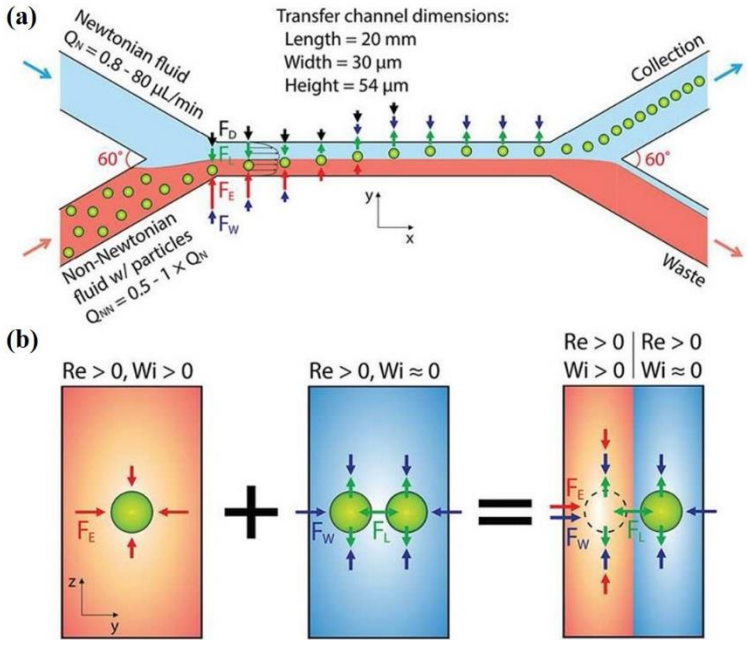

Figure 1-13: Microparticle washing from a non-Newtonian to a Newtonian fluid. (a) Microchannel Schematic representing the particle transfer across the laminar flow (b) Co-flow of non-Newtonian and Newtonian fluid resulting in a single equilibrium position in microchannel cross section. Reprinted with permission from American Chemical Society[88].

The coupled effect of Dean flow and elastic force could accelerate the particle focusing. The new particle equilibrium positions would highly depend on the viscoelastic properties and microchannel geometry. Xiang et al.[89] proposed a hypothesis that could describe the microparticle movement under various flow rates in a spiral microchannel. They tested 10 µm particles suspended in 500 ppm PEO solution (with 22%wt glycerin) through a spiral microchannel with a rectangular cross section. As shown in Figure 1-14a, for the lowest flow rate regime (Q = 1.0 µl/min, Wi = 0.27), when both the Reynolds and Dean number are close to zero, the particle movement in the horizontal plane would be under the sole effect of fluid elasticity (stage I). At this stage, the elastic force would dominate the particle lateral migration, but due to the weak

elastic effect, no significant focusing stream is observed. As the flow rates increase to Q = 20 µl/min (Wi = 5.39) in stage II, the contribution of fluid inertia would alter the equilibrium positions and pushes the particles towards the center of the long faces. This effect is further strengthened when the flow rates increase up to Q = 60 µl/min (Wi = 16.18) at stage III, where the balance of elastic and inertial forces results in three different focusing streams (channel center and the two centers of long faces). Up to this stage particle movement is only affected by the elastic and inertial forces since the Dean number is still close to zero. Moving to the moderate flow rates at stage IV, the Dean drag force starts to change the equilibrium positions. Since the elastic force is still dominant, the particles are pushed towards the outer half under the added effect of Dean drag. As the elastic force direction changes in the outer half, there would be a point where a single focusing line is achieved due to the balance of Dean drag, inertial and elastic forces (stage V). As the particle stream in the outer half approaches the channel walls, the increasing effect of wall-induced lift force pushes the particles towards the channel center. Therefore, the particles start to move back and this creates a secondary focusing stream (stage VI) at high flow rates. Finally, at some point, Dean mixing would entrain the particles as the dominant force and defocus the particle streams as shown in Figure 1-14a at stage VI.

As shown in Figure 1-14b, in the absence of the Dean drag (straight microchannel), the elastic force would be dominant in low to moderate flow rates (Q = 1 to 20 µl/min). Therefore, the particles would occupy three equilibrium streams at the channel center and the corners of the low aspect ratio rectangular channel. It could be concluded that the added effect of Dean drag, could potentially lead to single line particle focusing in curvilinear microchannels.

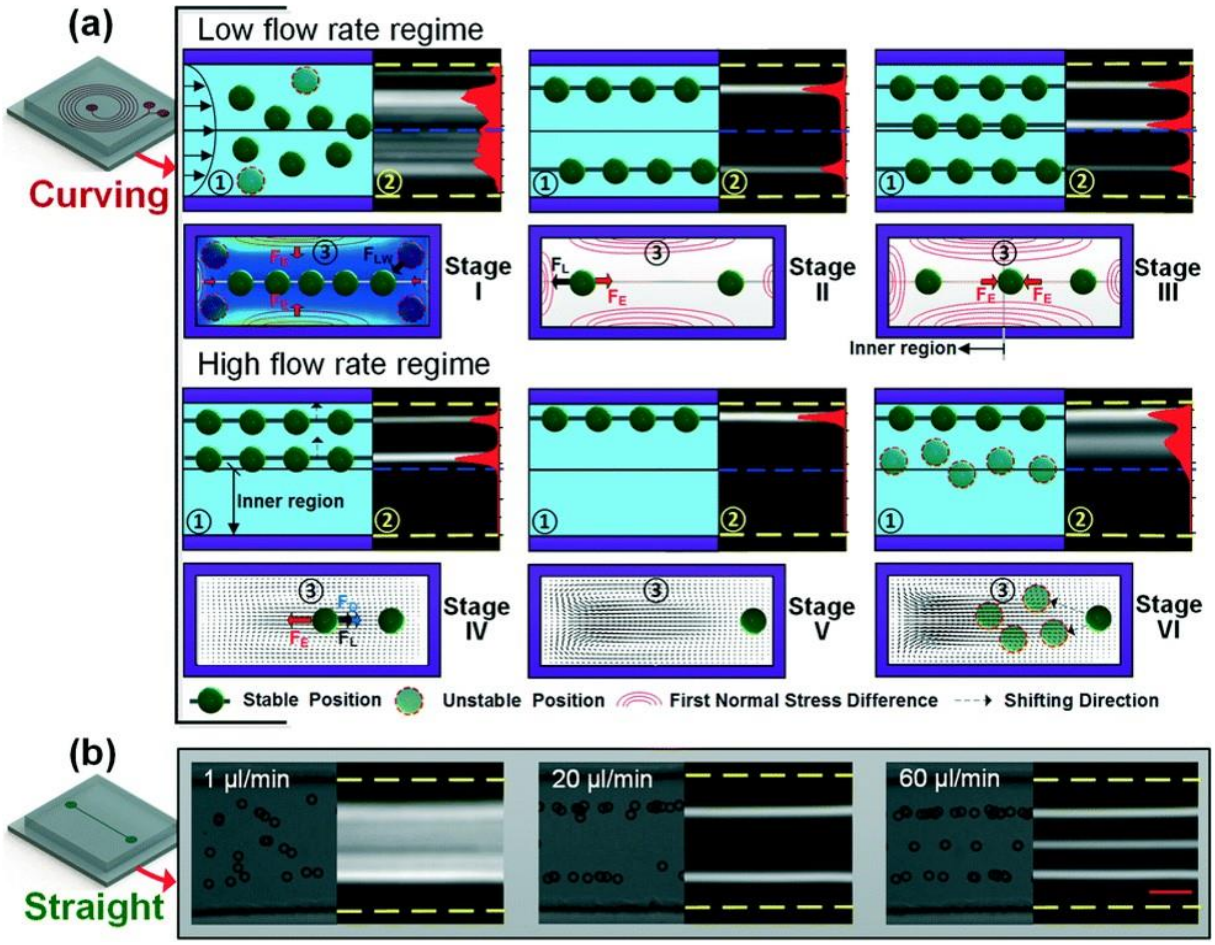

Figure 1-14: (a) Different steps of the particle focusing process in a viscoelastic flow in spiral microchannel. This six-stage process, start with a random particle distribution at low flow rates (stage I). As the flow rate increases, the balance of elastic and inertia effects pushes the particles towards two focusing streams (stage II), which would be further increased to three streams at the channel center and the centers of channel width (stage III). Dean drag effect would alter the equilibrium positions at moderate flow rates and push the particles to the outer half of the channel (stage IV and V). The particle streams would finally defocus at high flow rates as the particles are entrained with the dominant Dean vortices (stage VI). (b) Different steps of the particle focusing process in a viscoelastic flow in a straight microchannel. Under the dominant effect of elastic force, the particles are pushed to three focusing streams at the channel center and centers of wider faces. Reprinted with permission from Royal Society of Chemistry[89].

Xiang et al.[90] also reported a controlled Dean-coupled elasto-inertial particle focusing via manipulating the polymer concentrations in viscoelastic fluids. They tested different

concentrations (up to 8 wt%) of Poly[vinyl pyrrolidone] (PVP), and investigated the particle focusing behaviour at various flow rates between 10 to 60 µl/min, using a 5-loop spiral microchannel. As shown in Figure 1-15a, the dominant effect of elastic force at higher concentration of PVP (8 wt%), pushes the 10 µm particles towards a single focusing line at the center. Particle migration towards the centerline was observed at 40 µl/min, and a perfect and narrow single-line particle trace was achieved at the highest flow rate of 60 µl/min (*Re* = 0.076, *Wi* = 4.4) as shown in Figure 1-15b. The single line particle focusing at 60 µl/min indicated the dominant effect of elastic forces compared to the inertial forces. It also illustrated the fact that the small Dean drag (*De* = 0.014) in the spiral microchannel could not overcome the effect of the elastic force for the 10 µm particles.

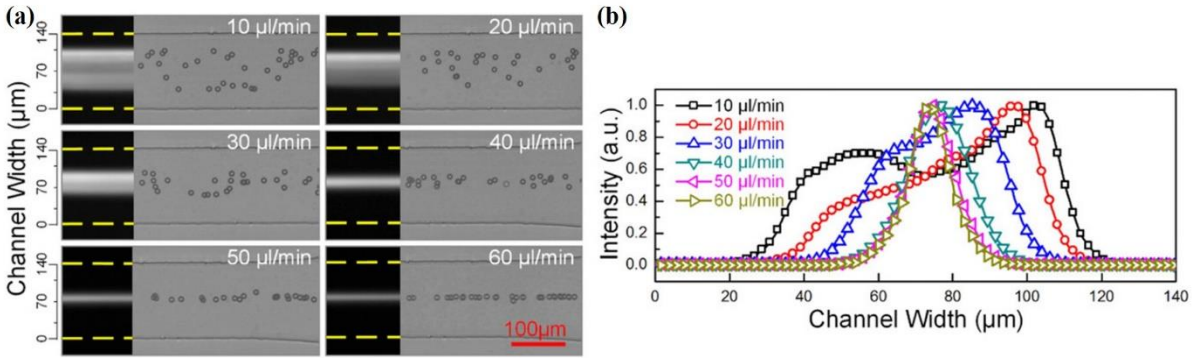

Figure 1-15: Particle focusing in 8 wt% PVP solution using a spiral microchannel. (a) Overlaid images of particle positions at different flow rates of 10 µl/min to 60 µl/min. (b) The normalized intensity profile showing the possible particle distribution inside the channel at different flow rates. Reprinted with permission from John Wiley and Sons[90].

The coupling effect of Dean drag and elasto-inertial forces was also investigated by Yuan et al.[91], where they utilized a zigzag serpentine microchannel with a rectangular cross section to analyze the particle focusing process as shown in Figure 1-16. Particle focusing behavior was studied using 1000 ppm PEO solution and 13 µm particles at different flow rates (5 to 30 µl/min).

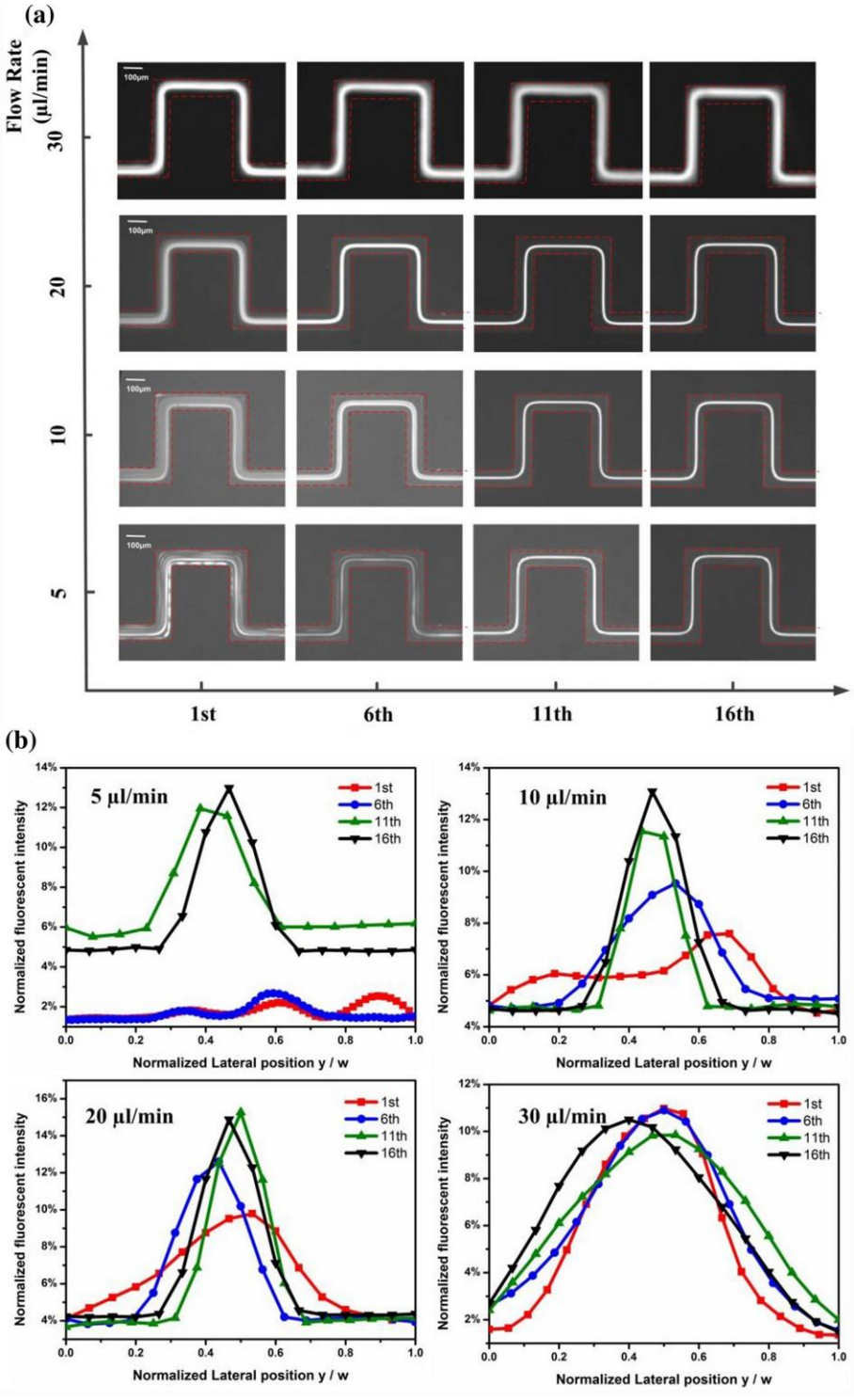

Figure 1-16: Particle focusing behavior in a zigzag serpentine microchannel. (a) Fluorescent images of particles at different channel intervals and different flow rates. (b) Intensity profiles at the middle of zigzag turns at different flow rates. Reprinted with permission from Springer Nature[91].

As shown in fluorescent images in Figure 1-16a, a single focusing line was observed at flow rates up to 20 µl/min. However, with increasing effect of inertial forces and the Dean drag, particles become dispersed at higher flow rates, which could be observed as the wider particle distribution in Figure 1-16b. Here, compared to a similar straight microchannel, Dean flow has enhanced the particle focusing at low flow rates and shorter channel length.

As illustrated above, the particle lateral motion could be controlled by the balance between the Dean drag, inertial, and elastic forces. The magnitude of these forces directly depends on particle size and flow characteristics. Therefore, a multiplex particle separation could be achieved by manipulating the balance between the dominant forces. Lee et al.[55] successfully separated 10 µm and 1.5 µm particles using a ten-loop spiral microchannel via a viscoelastic medium (PEO solution). As shown in Figure 1-17a, larger particles tend to get closer to the outer wall under the dominant effect of elastic force at the optimum flow rate of 50 µl/hr. Meanwhile, smaller particles remain around the channel centerline, and could be separated at the bifurcated outlet. Figure 1-17b illustrates the initial and final particle positions along the channel cross section. The balance between the Dean drag and the elasto-inertial forces varies for different particle sizes. Therefore, larger particles occupy different equilibrium positions compared to the smaller microparticles. The direction of the dominant elastic force is towards the minimum values of first normal stress difference in the outer curve as shown in the contour.

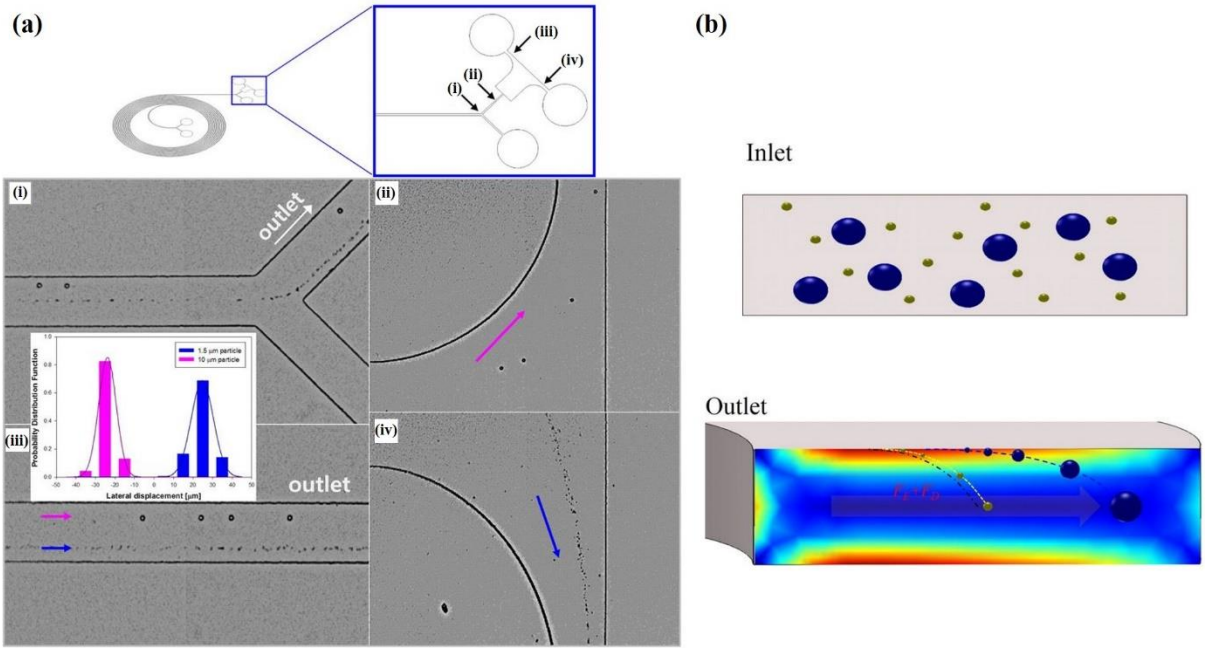

Figure 1-17: (a) Multiplex particle sorting in a ten-loop spiral microchannel with AR=0.25. Larger particles tend to get closer to the outer wall and could be collected via bifurcated outlet. (b) Random distribution of particles at the inlet and their respective lateral motion at the outlet of spiral channel. First normal stress difference contour show asymmetry, as the minimum values occur close to the outer half of the curve (indicating the direction of the elastic force). Reprinted with permission from Springer Nature[55].

Similarly, microparticle focusing has been reported based on manipulation of the Dean drag and the elasto-inertial forces, elsewhere[92–96]. For instance, Feng et al.[92] investigated the viscoelastic separation of microparticles in a 3-loop spiral microchannel with a rectangular cross section (200 × 50 μm^2). They reported on the focusing behavior of 3, 10, and 20 μm particles in a wide range of PEO concentrations (0.001 wt% to 0.4 wt%) at flow rates between 0.05 ml/min to 0.4 ml/min, and observed a transitional PEO concentration for each particle size, in which the focusing is governed by inertial lift or elastic forces. As presented in Figure 1-18 in low PEO concentrations (i.e., 0%), all particles occupy the inner side of the microchannel, while a narrower focusing bandwidth is achieved for larger particles at higher flow rates. As the PEO concentration increases to 0.005 wt%, the small 3 μm particles are pushed towards the outer wall, while the

larger particles tend to focus close to the channel center. The focusing positions tend to shift towards channel outer wall at higher flow rates. Moreover, the transitional PEO concentration for the largest 20 µm particles appears to occur at 0.1 wt% PEO, where they are focused close to the outer sidewall.

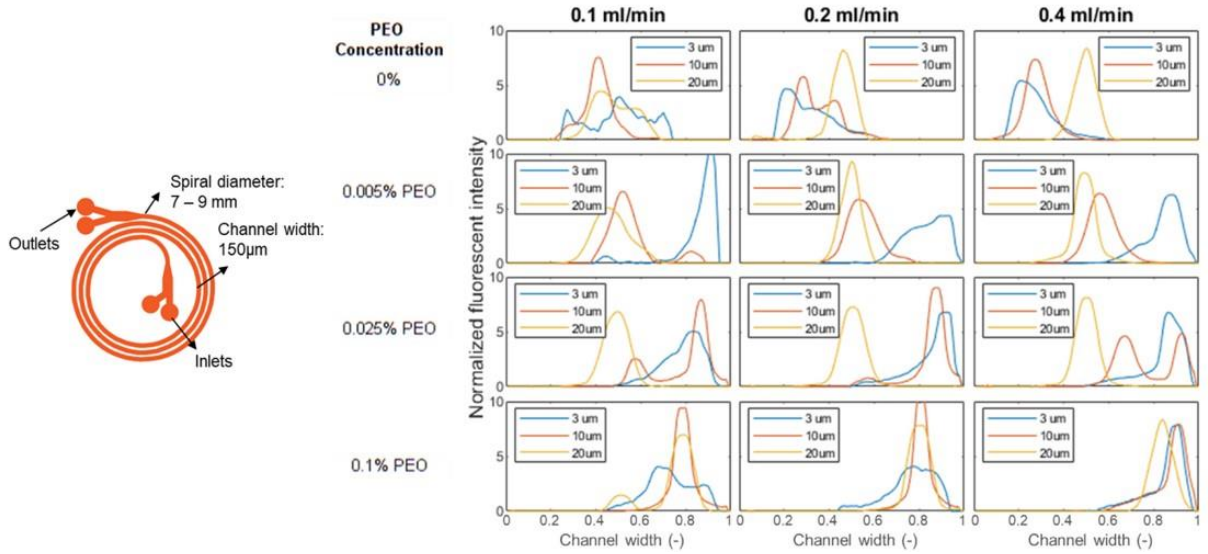

Figure 1-18: Schematic view of the spiral microchannel with a 200 × 50 µm^2 cross section and a radius between 7 to 9 mm, and the particles distributions at the channel outlet for 4 different PEO concentrations at various flow rates. The PEO concentration and the flow rates increase from top to bottom, and left to right, respectively. Reprinted with permission from MDPI [92].

In another study, Zhou et al. [93,97] reported a tunable particle focusing and sorting in viscoelastic PEO solutions inside a spiral microchannel. As shown in Figure 1-19a, their wavy microchannel included two inlets to supply the particles and a sheath flow, and a trifurcated outlet which was used to separate microparticles with a rectangular cross section of 125 × 40 µm^2. They examined seven different particle sizes (0.3 µm to 15 µm) in three concentrations of PEO solution (0.001, 0.01, and 0.1 wt%) at four different flow rates between 49.41 µl/min and 197.6 µl/min. As illustrated in Figure 1-19b, in the absence of PEO, no focusing line was observed for smaller

microparticles, while 3 µm and 5 µm particles occupied two symmetric focusing lines across the channel width. Here, the larger particles were transferred towards the channel outer sidewall.

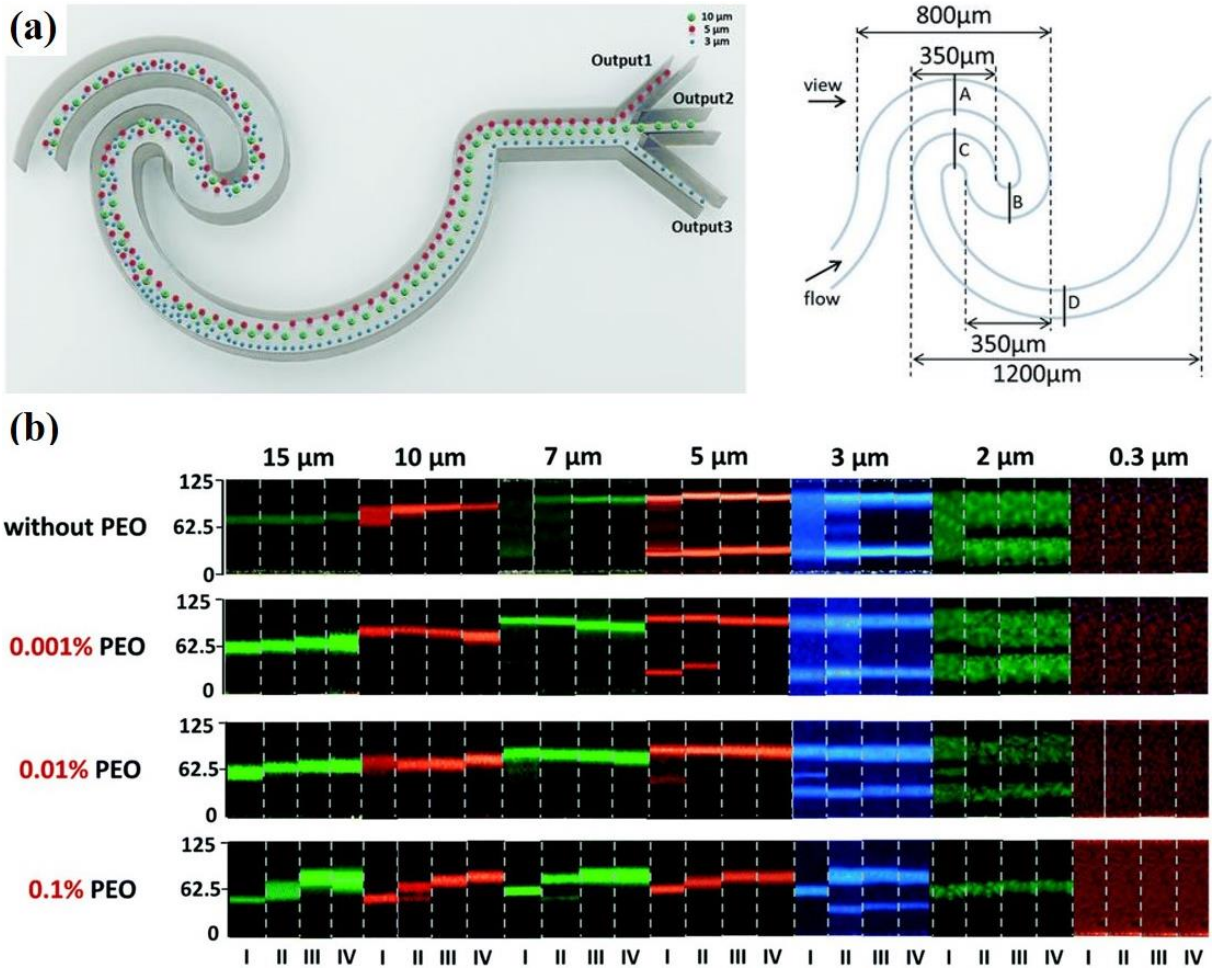

Figure 1-19: Dynamically tunable particle focusing and sorting in viscoelastic fluids inside a wavy microchannel. (a) Schematic of the wavy microchannel with a 125 × 40 µm^2 cross section alongside the detailed geometric parameters. (b) Fluorescence images of microparticle focusing in four different PEO concentrations (0 to 0.1 wt%), at four flow rates of (I) 49.41 µl/min, (II) 98.83 µl/min, (III) 148.25 µl/min, and (IV) 197.60 µl/min. Reprinted with permission from Royal Society of Chemistry[93].

Moreover, increasing the flow rate enhanced the observed intensity for larger particles as they were pushed into a narrower focusing bandwidth. As the PEO concentration increases to 0.001 wt% and 0.01 wt%, the medium and larger sized-particles are further pushed towards the channel centerline under the added effect of elastic forces. However, a further increase in PEO

concentration (up to 0.1 wt%) results into the dispersion of focusing lines, as shown in the bottom panel of Figure 1-19b. Building on their parametric study, they achieved a size-based separation between 3 μm, 5 μm, and 10 μm particles in 0.001 wt% PEO solutions at a flow rate of 160 μl/min.

Most recently, Iyengar et al.[98] and Kumar et al.[99] have reported high resolution and rapid elasto-inertial particle separation in spiral microchannels at a total throughput of 1 ml/min. Iyengar et al.[98] utilized a two-turn spiral microchannel with a rectangular cross section (500 × 50 μm^2) to separate particles in diluted blood samples with a resolution of 1 μm at a total flow rate of 1 ml/min alongside a sheath buffer (PEO solution). They demonstrated bacteria separation from larger blood cells with efficiencies of 82 % to 90%, depending on the blood dilution rate. However, despite the high processing throughput of 1 ml/min, the sheath flow constituted the main part of the flow rate (950 μl/min) and the sample flow rate was 50 μl/min. No solution exchange or washing was demonstrated as well.

Additionally, Kumar et al.[99] demonstrated a high throughput particle focusing and separation in a 10-turn spiral microchannel with a width of 500 μm. They investigated the effects of PEO concentration (250 ppm to 5000 ppm), and channel aspect ratio (AR = 0.25 and 0.1) on particle migration across the channel width. They observed that 10 μm and 15 μm particles occupy the outer sidewall in low PEO concentrations (up to 1000 ppm) and then travel towards the channel center in higher PEO concentrations due to the dominance of the elastic force. Finally, they demonstrated a sheath-free high throughput separation in an integrated spiral microchannel with 89% and 99% efficiencies for 10 μm and 15 μm particles, respectively. As shown in Figure 1-20, in the first spiral channel both particles are focused close to the channel outer wall. However, inside the second spiral the smaller 10 μm particles are pushed away from the channel inner wall and this enables a high efficiency separation at the channel bifurcated outlet.

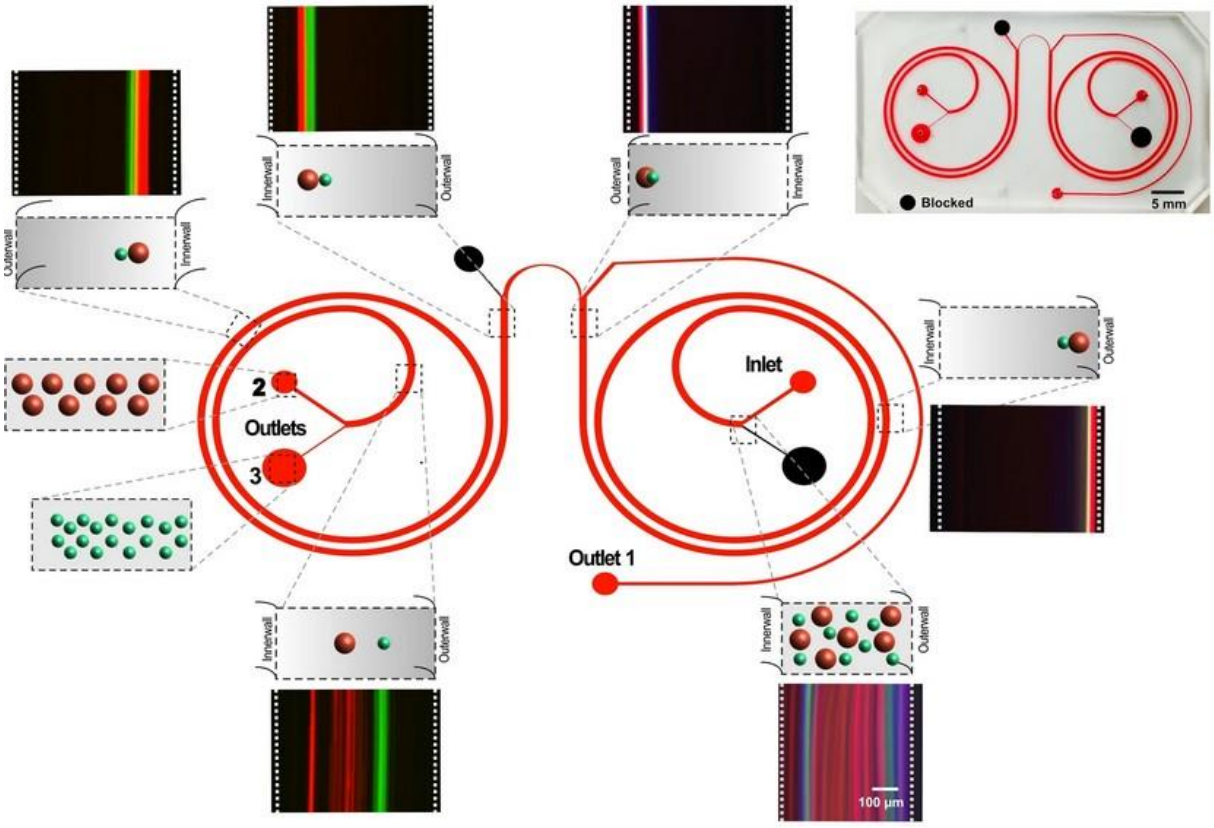

Figure 1-20: A sheath-less high throughput particle separation in 500 ppm PEO using an integrated spiral microchannel with a cross section of 500 × 100 µm^2 (R = 9.7 and 10.7 mm). Both 10µm and 15 µm particles are supplied through the inlet, and pre-focused in the first spiral section. In the second spiral, 15 µm particles remain at the channel inner wall, while 10 µm particles drift away towards the channel outer wall. Reprinted with permission from Springer Nature[99].

The literature of viscoelastic flow-based particle manipulation in curved channels is mostly application-driven, such as particle focusing in saliva and blood plasma[100], and bacteria separation from diluted blood[101]. There are still opportunities for thorough and fundamental studies in this area. For instance, recently, Raoufi et al.[102] reported the effects of PEO fluid rheology on particle focusing inside spiral microchannels (with variable radius of curvature along the channel) at flow rates below 200 µl/min. They utilized a seven-loop spiral microchannel with a cross section of 200 × 70 µm^2 to investigate the focusing behavior of 3 µm particles in PEO solutions with various concentrations (250, 500, and 1000 ppm) and molecular weights (1, 2, and 4 MDa). They reported

that a higher polymer molecular weight would result in stronger elastic forces and enables a tighter particle focusing closer to the channel outer wall, even at lower concentrations. Their results indicate that an accurate manipulation of elastic, inertial, and Dean forces could enable the tight focusing of particles at low (10 µl/min) and high (125 µl/min) flow rates.

Considering the reported studies, there are still gaps for examining the effects of particle size and polymer concentration at higher flow rates (e.g., up to 2 ml/min in single channels) on particle dynamics in curvilinear microchannels with constant radius along the channel. This will allow us to understand the effects of fluid rheology and speed, particle size, and channel width, height, and radius of curvature on particle focusing. Non-dimensional analysis of these effects can also add novelty and scientific value, while making the outcomes useful for others in the field. This gap has been pursued in chapter 5 of this thesis. Moreover, our investigation on the average Dean velocity of viscoelastic fluids will enable us to achieve a simultaneous particle sorting and washing, a process that is also demonstrated in chapter 5. Analytical solutions have also been reported for particle movement in non-Newtonian fluids[55,103–105]. For instance, Poole et al.[106] used the Oldroyd-B model to predict the polymeric extra-stress tensor in the evolution equation. However, their findings were only applicable for very low Weissenberg numbers. Recently, Yu et al.[107] reported a numerical model to predict the equilibrium positions of the particles migrating in a viscoelastic fluid in rectangular channel. Their method was also unable to deal with high Weissenberg numbers and could not model the actual rheological properties of the fluid. These extensive simplifications in the solutions usually limit the real life applications of numerical models. Numerical simulation of particle lateral migration in the elastic medium inside a curved microchannel would be an essential step towards an in-depth understanding of the underlying physics. Numerical models could also help in the investigation of various unexplored experimental cases that might be

physically unreachable, such as small channel dimensions and high flow rates. Therefore, comprehensive studies are still required to investigate the effect of different parameters, such as polymer concentration and particle size on the movement of particles in a co-flow of non-Newtonian fluids in curved microchannels specifically at higher flow rates.

1.2.2.2.2 Shear-thickening Fluids

To paint a complete picture of various non-Newtonian fluid types, and based on our interest in fundamental studies of particle dynamics inside curved microchannels, we also focus our attention towards shear-thickening fluids such as the mixtures of metallic nanoparticles with water[108]. The shear-thickening colloidal suspensions exhibit a drastic increase in viscosity as the shear rate increases[109–112]. Under deformation, the randomly dispersed particles in the medium shape into layered structures, which cause a shear-thinning behavior at lower shear rates. However, beyond a critical shear rate threshold, these layered structures form hydroclusters and cause the drastic viscosity increase[113] as shown in Figure 1-21. Rheological characteristics of these fluids depend on several factors such as the liquid medium, particles, particle interactions, temperature, etc.[114] For instance, Moldaveanu et al.[115] investigated the rheological characteristics of metallic Al_2O_3 and SiO_2 nanofluids and offered few correlations for a better estimation of their viscosity over a wide range of shear rates.

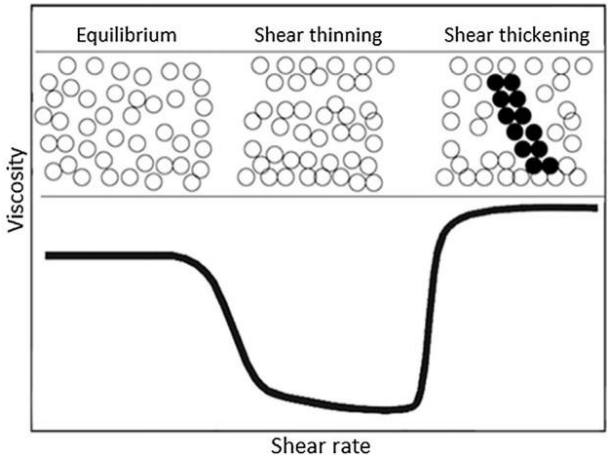

Figure 1-21: Schematic demonstration of shear-thinning and shear-thickening behavior of colloidal suspensions. Reprinted with permission from Springer Nature[113].

The colloidal dispersions of metallic oxides such as aluminium oxide (Al_2O_3) and silicon dioxide (SiO_2) with enhanced thermal properties already have a wide range of applications in chemical and petrochemical industries[116–119]. A near-future use of these shear-thickening fluids in curved microchannels is envisioned for the purposes of fundamental fluid mechanics investigations, microparticle manipulation, and sample processing. In this area, the average Dean velocity of such metallic nanofluids in curved microchannels is the first research question that was needed to be addressed. The application of the previous correlations for water would probably result in high errors for the prediction of Dean velocity in metallic nanofluids. Therefore, we hypothesized that a new correlation is required for the estimation of V_{De} of shear-thickening SiO_2 nanofluids in curved microchannels. Utilizing the reported rheological measurements[115], we carried out an in-depth investigation of effecting parameters on the average Dean velocity of SiO_2 nanofluids (chapter 4 of this thesis). Then, we studied the microparticle focusing behavior in these nanofluids for the first time as reported in chapter 6.

1.3 Scientific and Technological Gaps

The coupled effect of Dean drag with the inertial and elastic forces enhances the throughput in curved channels, compared to particle focusing in elasto-inertial regimes in straight microchannels[70,120,121]. The particle lateral motion could be controlled by the balance between the Dean drag, inertial, and elastic forces. The magnitude of these forces directly depends on particle size, polymer concentrations, and flow characteristics[88–91]. Hence, it is of utmost importance to study the non-Newtonian flows in non-straight channels, and to investigate the axial and Dean flow velocities as a first step, for instance in viscoelastic and shear-thickening liquids.

Despite multiple reports on particle sorting and multiplex separation in Dean-coupled elasto-inertial systems, no significant effort has been made towards enhancement of the particle washing process. Transferring the target particles to a clean buffer could play a vital role in sample preparation and detection in various biomedical applications. Therefore, by utilizing the advantages of the aforementioned systems, different industrial applications such as particle separation and isolation could be significantly improved. Therefore, there is a knowledge gap for a thorough and fundamental study in this area such as examining the effects of particle size at various polymer concentrations and flow rates on the particle dynamics in curved microchannels with various designs to capture the effects of channel width, height, and radius of curvature. This fundamental study would provide an in-depth understanding of the underlying physics of particle and fluids behavior and enable potential designs for duplex and/or triplex particle sorting and washing applications in the future.

We also envision a near-future application of shear-thickening metallic fluids such as Al_2O_3 and SiO_2 nanofluids in curved microchannels for the purposes of fundamental fluid mechanics

investigations, microparticle manipulation, and sample processing in areas such as heat exchangers, solar energy collectors, nanoplastics detection and so on. Thus, as the initial step, the average Dean velocity of these metallic nanofluids in curved microchannels should be investigated. Despite the various reports on the rheological characteristics of such metallic nanofluids, microparticle focusing behavior has not been studied as of yet. Therefore, to complete the fundamental analysis it is important to investigate the microparticles' focusing behavior in these metallic nanofluids inside straight and curved microchannels.

1.4 Thesis Statement and Objectives

While most of the previous studies on non-Newtonian fluids were focused on the understanding of particle transfer between two fluids in straight microchannels, few investigations have been reported on particle movement in curvilinear microchannels. The Dean-coupled elasto-inertial systems enable multiplex particle separation at higher throughputs compared to elasto-inertial microsystems. Therefore, in order to utilize these advantages, an in depth understating of the underlying physics of particle and fluid movement is of utmost importance. In this thesis, we attempt to fully investigate the control parameters of both fluids and particles in a curvilinear microchannel, with an aim to enhance the processing flow rate and efficiency of particle washing. A co-flow of non-Newtonian fluids (PEO-spiked solutions and SiO_2 nanofluids, separately) with spiked non-biological particles will be studied to characterize the secondary flows and microparticle movements based on the channel geometry, particle characteristics and fluid properties. The lateral motion of particles will be studied in order to gain a full understanding of particle motion under the coupled effect of Dean drag and elasto-inertial effects. The final goal will be to develop a particle washing microfluidic device for point-of-need applications utilizing

the duplex particle sorting in non-Newtonian fluids. To achieve our goal, the work will be organized into four objectives discussed below.

Objective 1: *Understanding the Dean flow and average Dean velocity of viscoelastic shear-thinning and SiO_2 shear-thickening nanofluids in curvilinear microchannels.*

Developing the knowledge of the Dean flow of viscoelastic fluids requires the investigation of all the contributing factors, such as different channel geometries and fluid properties. PEO will be used to enhance the viscoelasticity of aqueous solutions. Altering the concentration of PEO in solutions would enable a thorough investigation on fluid viscoelasticity. Different channel aspect ratios and radii of curvature would provide a full understanding of channel geometry. Finally, different flow rates will be examined to develop a valid empirical correlation for the average Dean flow velocity of viscoelastic fluids in curved microchannels. Similarly, an in-depth parametric study will be carried away to investigate the average Dean velocity of shear-thickening fluids. Here, different concentrations of silicon dioxide (SiO_2) nanofluids will be tested in various channel configurations at a wide range of flow rates. The results would lead to a separate empirical correlation predicting the average Dean velocity of Silicon dioxide nanofluids.

Objective 2: *Experimental investigation of particle dynamics in viscoelastic shear-thinning flows inside curvilinear microchannels.*

An accurate correlation developed for the viscoelastic fluids could enable a better control on particle manipulation and solution exchange in curvilinear microchannels. Particle movement in viscoelastic fluids in curved channels will be investigated from a fundamental point of view in order to understand the underlying physics of multiplex particle sorting at a wide range of flow rates. This step includes particle movement investigation for different particle sizes, fluid properties, and channel dimensions at a range of flow rates inside a curved microchannel.

Objective 3: *Proof of concept demonstration of duplex particle separation and washing in viscoelastic shear thinning flows in curvilinear microchannels.*

The developed knowledge in objectives 1 and 2 could be the basis of the design for a new microdevice that would enable a controlled fluid exchange and particle migration based on the fluid properties in point-of-care diagnostic and food safety applications. At this stage, the precise control over the microparticle manipulation would be used to demonstrate a duplex particle sorting and washing in viscoelastic PEO solutions as a proof of concept. As the future work, the developed designs may be used to implement a particle washing process in biological fluids such as diluted blood.

Objective 4: *Experimental investigation of particle dynamics in SiO_2 shear-thickening fluids in curvilinear microchannels.*

Based on the developed correlation for the average Dean velocity of SiO_2 nanofluids, particle dynamics in shear-thickening fluids would be investigated to explore the particle focusing behavior in curved microchannels with different fluid properties at a wide range of flow rates.

1.5 Thesis Outline

This thesis consists of 7 chapters, starting with an introduction to microfluidic particle focusing and washing methods, followed by an overview of the underlying physics of the particle and fluid behavior in the theory section. In the second chapter, experimental methods and materials utilized in this thesis are reviewed, including the microdevice fabrication, solution preparation and Dean flow and particle analysis methods. Third chapter reports on the Dean flow characterization of the viscoelastic PEO solutions in the curved microchannels, followed by the proposed empirical

correlation for the prediction of the average Dean velocity (Obj. 1). In chapter 4, the average Dean velocity of the shear-thickening SiO_2 nanofluids in curvilinear microchannels is investigated to complete the first thesis objective. Chapter 5 presents a fundamental investigation on the particle focusing behavior in the co-flow of PEO solutions under various flow conditions and microchannel designs (Obj. 2). Utilizing the developed knowledge of the particle and fluid interactions in viscoelastic fluids, we also demonstrate a proof of concept of duplex particle washing in PEO solutions (Obj. 3). In the sixth chapter, microparticle behavior is studied in different SiO_2 nanofluids concentrations inside curved microchannels to investigate the particle behaviour in these shear-thickening nanofluids (Obj. 4). Finally, in chapter seven, we provide a summary of the thesis achievements alongside its limitations and possible future directions in this field of research. This thesis also includes 6 appendices. The published paper on DNA-inhibitor separation is amended in Appendix A. Appendix B represents the details on experimental methods and rheological characteristics. Appendix C, and Appendix D include all the experimental results on V_{De} investigation in PEO solutions and SiO_2 nanofluids, respectively. Finally, particle distribution graphs in co-flows of PEO solutions and SiO_2 nanofluids are presented in Appendix E, and Appendix F.

1.6 Contributions

This thesis has been constructed based on the papers co-authored by the PhD candidate (completed list is available in the thesis publication section). Chapters three and four are based on two published manuscripts[122,123], which were co-authored by me and my supervisor, Prof. Pouya Rezai. The initial results of the investigations in these two chapters were also presented in MicroTAS 2018, and μFIP 2022 conferences. The content of chapter 5 is submitted to the *Soft*

Matter journal and is currently under-review. These three papers are originally drafted by me and revised by Prof. Pouya Rezai. For these papers, I have performed the formal analysis, and lead the investigations and methodologies under supervision of Prof. Pouya Rezai. Moreover, the final results of particle behavior investigation in SiO_2 nanofluids (chapter 6) will be converted to a manuscript in near future. I have also co-authored a manuscript on microfluidic sample preparation to investigate the effects of simultaneous DNA-Inhibitor separation[53] (Appendix A). In this project, I lead the investigation and formal analysis, and wrote the original draft alongside Dr. Ali Doostmohammadi. Mr. Kevin Romanick also contributed in data curation and analysis. Dr. Mario Thomas and my supervisor, Prof. Pouya Rezai, revised the manuscript.

Chapter 2

2 Materials and Methods*

This chapter reviews the material preparation and experimental methods used throughout this thesis. Initially, the design and fabrication techniques for microfluidic devices are covered in sections 2.1 and 2.2. Afterwards, solutions preparation methods are presented in section 2.3, followed by their rheological measurement and characterization in 2.4. Later on, the experimental setup is illustrated (section 2.5) followed by the data analysis for Dean flow (2.6), and solution exchange (2.7) characterization. Finally, the particle behavior analysis is presented in section 2.8.

* Contents of this chapter has been partially published in:

1. Nikdoost, A. & Rezai, P. Dean flow velocity of viscoelastic fluids in curved microchannels. *AIP Adv*. **10**, 085015 (2020).
2. Nikdoost, A. & Rezai, P. Dean Flow Velocity of Shear Thickening SiO_2 Nanofluids in Curved Microchannels. *Phys. Fluids* **34**, 062009 (2022).

2.1 Microfluidic Device Fabrication

Photolithography and soft lithography were used to fabricate the replication molds and the microfluidic devices, respectively. The master molds were prepared using SU-8 2075 photoresist (MicroChem Corp., USA) patterned on a silicon wafer (Wafer World Inc., USA). For instance, for a channel height of h = 150 μm, the negative photoresist was initially spin coated on a cleaned 4-inch diameter wafer at 1600 rpm for 30 seconds as shown in steps (1) and (2) in Figure 2-1. Pre-exposure bake step was performed at 65°C for 5 minutes, and at 95°C for 30 minutes, followed by UV light exposure with a dose of 260 mJ/cm^2 using a photomask (printed by ArtnetPro Inc., USA), and an ultraviolet (UV) light exposure system (UV-KUB 2, KLOE, France), as illustrated in step (3). The master mold was then developed in SU8 developer after post exposure bake at 65°C for 5 minutes, and at 95°C for 12 minutes [step (4)]. Finally, the silicon master mold was hard-baked at 200°C for 20 minutes. As shown in steps (5) and (6), microfluidic devices were fabricated from casting 10:1 ratio base-to-reagent Polydimethylsiloxane (PDMS) prepolymer (Sylgard 184 kit, Dow Corning, USA) on the molds using the standard soft lithography technique[124] and bonding the layers onto glass slides using pre-exposure to oxygen plasma (Harrick Plasma Inc., USA). Here, the spin speed, exposure dose and the baking times depend on the desired channel height, as illustrated in Table 2-1. Microchannel dimensions were measured at different cross sections to ensure the accuracy.

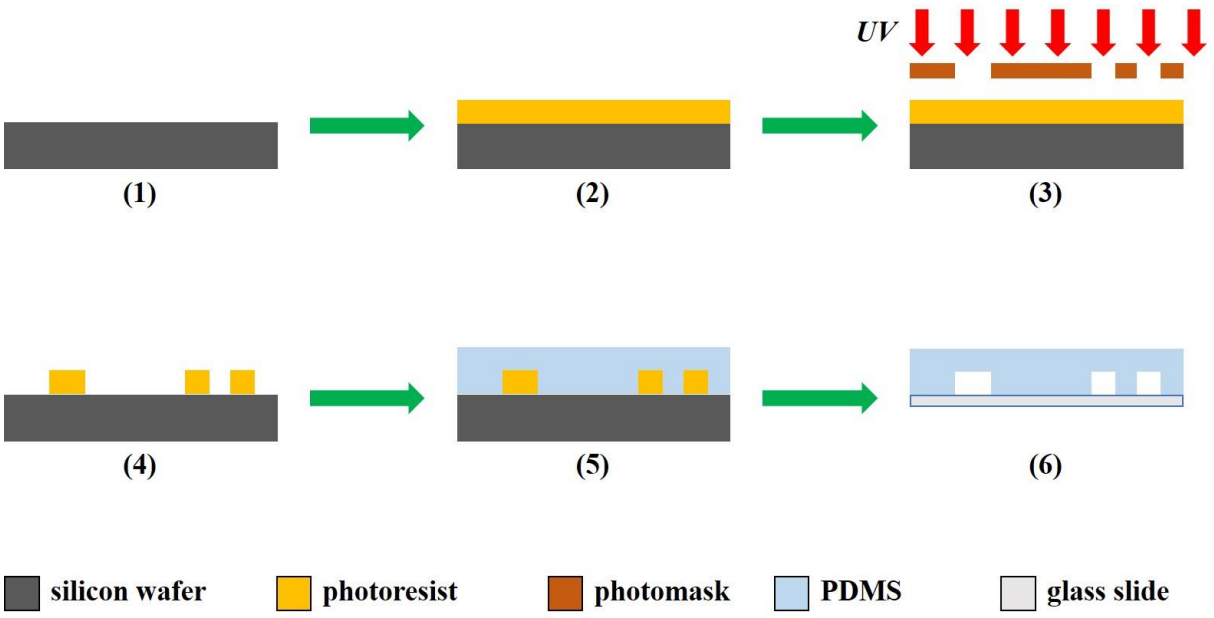

Figure 2-1: Photolithography and soft lithography steps for microfluidic device fabrication. Silicon substrates are initially cleaned (1), and then a layer of photoresist is spin coated (2), followed by a pre-exposure bake step. Then, the substrate is exposed to UV using a photomask to create the desired patterns (3). After a post exposure bake step, the photoresist is developed to prepare the final mold (4). Finally, a layer of PDMS is used to create the microchannels (5), which is bonded to a glass slide using the oxygen plasma (6).

Table 2-1: Microfabrication processing guideline with SU-8 2075 photoresist.

Channel Height (µm)	**Spin Speed** (rpm)	**Pre-bake time** (min)		**Exposure Dose** (mJ/cm^2)	**Post exposure bake time (min)**		**Development Time** (min)
		at **65°C**	at **95°C**		at **65°C**	at **95°C**	
75	2700	3	9	210	2	7	7
150	1600	5	30	260	5	12	15
225	1100	7	45	350	5	15	17

2.2 Design of Microfluidic Device

Various channel geometries were utilized to facilitate our parametric studies in this thesis. To investigate the average Dean velocity of PEO solutions in curved microchannels in chapter 3, the design included 330° curved microchannels with a width of w = 150 µm as shown in Figure 2-2a. Three aspect ratios (AR = 0.5, 1.0, and 1.5), and four radii of curvature (R = 0.5, 1.0, 1.5, and 2.0 cm) were tested. Devices included two inlets to co-introduce various pairs of viscoelastic PEO solutions into the channel (one stream dyed with trypan blue from Sigma Aldrich, USA), and two outlets. In chapter 4, SiO_2 nanofluids behavior were examined using 300° curved PDMS microchannels with a constant radius of curvature as shown in Figure 2-2b. The expanded straight outlet was implemented for visualization of particles in the device in particle behavior analysis in chapter 5, and chapter 6. Microchannels were designed with three different channel widths of w = 150, 225, and 300 µm, and three different radii of curvature of R = 1.0, 1.5, and 2.0 cm. Microdevices were fabricated with two different channel heights of h = 150 and 225 µm to capture the effect of channel aspect ratio (AR = 0.5, 0.67, 1.0, and 1.5) at a constant curvature radius of R = 1.0 cm.

In order to capture the effect of channel curvature in chapter 5, and chapter 6, microchannels with three different radii of curvature of R = 1.0, 1.5, and 2.0 cm were fabricated with a square cross section of 150×150 µm^2, and a constant curved channel length (300°, 225°, and 150° curvatures, respectively). As illustrate in Figure 2-2c straight microchannels with similar length (~5.23 cm), and three different cross sections (150×75 µm^2, 150×150 µm^2, and 150×225 µm^2) were also tested for a comprehensive channel curvature analysis. A complete list of all channel geometries used throughout this thesis could be found in Appendix B.

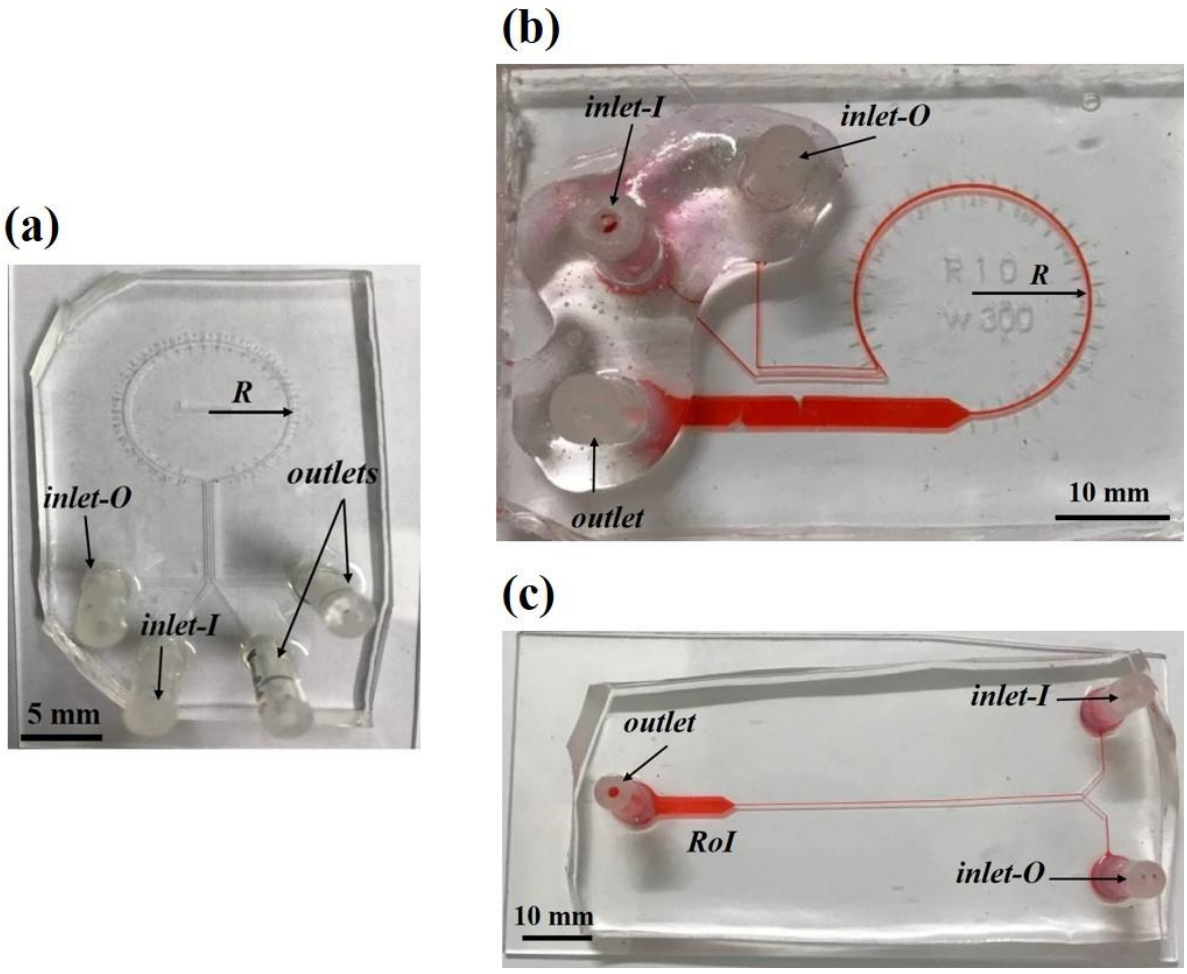

Figure 2-2: Example of curved microchannels tested in this thesis. (a) Microfluidic device consisting of a 330° curved microchannel with a radius of curvature of R = 1.0 cm and cross section area of 150 × 150 μm^2, which was utilized in chapter 3. (b) A 300° Curvilinear channel with a constant radius of curvature (R = 1.0 cm), and cross section area of 300 × 150 μm^2(used in chapters 4,and 5). (c) Straight microchannel with a channel length of ~ 5.23 cm, and a square cross section (150 × 150 μm^2), utilized in chapters 4, 5 and 6. Reprinted with permission from AIP Publishing[122].

The duplex particle washing process in chapter 5 is demonstrated using a curved microchannel with tri-furcate outlets as illustrated in Figure 2-3. The microchannel in Figure 2-3 consists of two inlets to supply the particles (inlet-I) and a clean buffer (inlet-O) with a 150 × 75 μm^2 cross section and R = 1.0 cm. The expanded outlet is also divided into three branches (outlet-I, outlet-M, and outlet-O) enabling the particle separation based on their lateral position at the outlet.

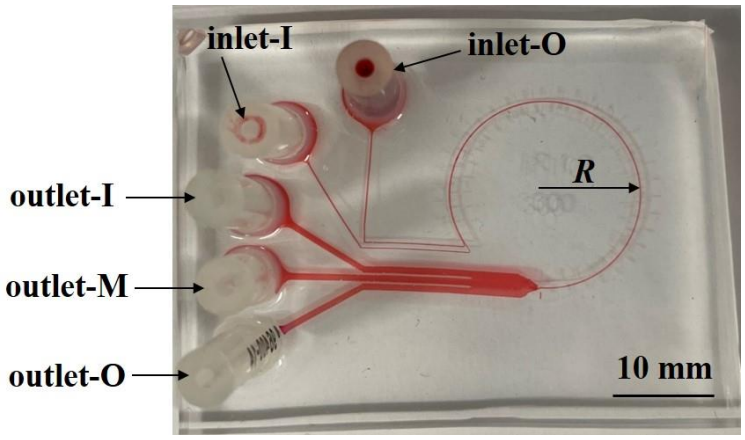

Figure 2-3: Curved microchannel with a 150 × 75 μm² cross section and R = 1.0 cm. Tri-furcate outlets are implemented for particle separation in the duplex washing process.

2.3 Sample Preparation

Fluid behavior analysis in chapter 3 was conducted using three concentrations (125, 500, and 1000 ppm) of polyethylene oxide (PEO) powder with a molecular weight of 2×10^6 Da (Sigma-Aldrich, USA) in water. In chapter 4, three different concentrations (φ= 1%, 2%, and 3% v/v) of colloidal dispersion of SiO_2 (40% in water, Alfa Aesar, USA) with previously reported viscosities[115] were tested inside our curved microchannels. As given by the manufacturer, the solutions were prepared using SiO_2 particles with an average size of 20 nm. Trypan blue (Sigma Aldrich, USA) with 10% v/v concentration was used to color dye one of the two streams that were infused into the microfluidic device for better visualization and imaging in the microchannels.

For particle behavior investigation in chapter 5, viscoelastic PEO solutions were prepared by dissolving the PEO powder (M_w = 2×10^6 Da, Sigma-Aldrich-USA) in water at three different concentrations of 500 ppm, 1000 ppm, and 2000 ppm, and stirred for 12 hours at room temperature. Four different particle sizes of 5.37 μm (~5 μm, CM-50-10, 2.5% w/v), 10.6 μm (~10 μm, CM-

100-10, 1% w/v), 14.5 μm (~15 μm, CM-150-10, 1% w/v), and 22 μm (CM-200-10, 1% w/v) with a density of 1.05 kg/m^3 were obtained from Spherotech Inc., USA. Different solutions were prepared using an approximate particle concentration of ~ 2×10^5 particles/ml with 0.5% v/v of Tween 20 (Sigma-Aldrich, USA) to avoid particle aggregation. In chapter 6, microparticle solutions were prepared using three different concentrations (φ= 1%, 2%, and 3% v/v) of colloidal dispersion of SiO_2 (40% in water, Alfa Aesar, USA), with similar particle concentrations. Here, only the average microparticle sizes are reported and used in calculations. However, as per reported by the manufacturer, the size variation in each product could cause some uncertainties and reduced the accuracy.

2.4 Rheological Characterization

Considering the shear thinning behavior of PEO-spiked solutions at high shear rates[125], the viscosity of our PEO solutions were measured with a roughened 40 mm parallel plate geometry using a DHR-2 TA rheometer. The measured viscosities* are shown in Figure 2-4, where the shear thinning behavior is apparent specifically in the shear rate range of $100<\dot{\gamma}<5000$ 1/s. The shear rate at any given experimental flow rate could be calculated using Eq. (1-13).

* Measured viscosities could be found in Appendix B.

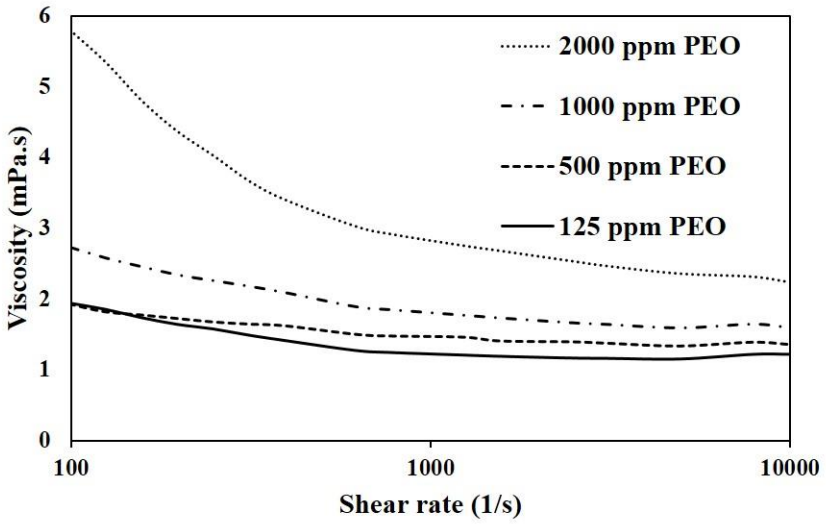

Figure 2-4: Viscosity measurement for PEO-spiked solutions at different shear rates using a roughened parallel plate rheometer. Four different concentrations of PEO solutions were tested up to $\dot{\gamma}$ = 10000 1/s. The shear thinning behavior is apparent till $\dot{\gamma}$ ~5000 1/s, after which the viscosities could be considered constant for PEO concentrations up to 1000 ppm.

The relaxation times for these PEO concentrations were obtained from previous reports (according to the Zimm theory[126,127]), i.e. λ=1.75, 4.3, 6.8, and 10.6 ms for PEO concentrations of 125, 500, 1000, and 2000 ppm, respectively[128–130].

For the shear-thickening SiO_2 nanofluids, the viscosities were previously reported[115,119]. In this thesis, the viscosities for each SiO_2 concentration were characterized as a power function of the shear rate ($\dot{\gamma}$ >100 [1/s]) based on the reported measurements by Moldoveanu et al.[115] (Figure 2-5) as presented in Equations (2-1), (2-2), and (2-3):

$$\varphi = 1\%\ v/v : \mu = (8.77 \times 10^{-5}) \times \dot{\gamma}^{0.80}\ [Pa.s] \quad (2\text{-}1)$$

$$\varphi = 2\%\ v/v : \mu = (1.06 \times 10^{-4}) \times \dot{\gamma}^{0.79}\ [Pa.s] \quad (2\text{-}2)$$

$$\varphi = 3\%\ v/v : \mu = (1.24 \times 10^{-4}) \times \dot{\gamma}^{0.77}\ [Pa.s] \quad (2\text{-}3)$$

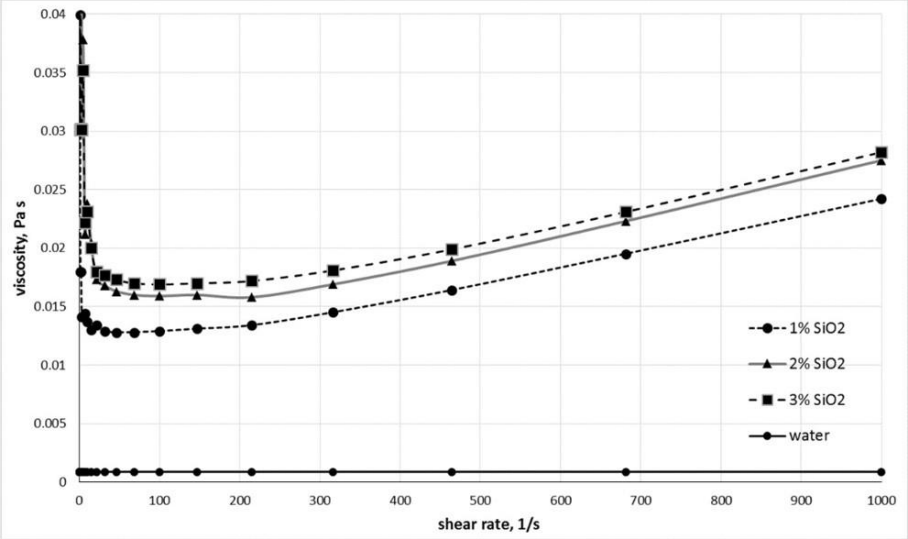

Figure 2-5: Viscosity variation of water and SiO_2 nanofluids reported by Moldoveanu et al.[115] Reprinted with permission from Elsevier.

All fluidic samples were prepared and used at room temperature. Variation in viscosity was therefore possible due to potential variations in the temperature that was not very carefully monitored through this thesis, hence contributing to potential uncertainties. For example, assuming that the temperature changed by ±3 degrees, the change in the viscosity of water could be around 5% as reported by Harris et al.[131]. The viscosity variation for PEO solutions[132] and SiO_2 nanofluids[133,134] vary based on the polymer molecular weight, nanoparticle size, concentration, and the shear rate. The exact viscosity variation is not available in the literature for the specific solutions used in this thesis. Therefore, future investigations are required to decrease this source of uncertainty.

2.5 Experimental Procedure

Our experimental setup consisted of an inverted microscope (Bioimager BIM-500FL, Canada) equipped with a high speed camera (FASTEC IL5, Canada), and a dual syringe infusion pump (LEGATO 210, KD Scientifics, USA) to supply the co-flow through the microchannels, as shown in Figure 2-6. For the fluid behavior analysis in chapter 3, the co-flows of PEO solutions (one dyed with 10% v/v trypan blue) were introduced inside the microchannel at total flow rates of $0.2 < Q_t < 2.0$ ml/min (i.e., 0.1-1.0 ml/min in each inlet), corresponding to average axial velocities of $0.148 < V_x < 1.48$ m/s. The average axial velocity was approximated by dividing the volumetric flow rate by the square cross-cross sectional area of the microchannel (150×150 μm^2). Similarly, the V_{De} investigation of SiO_2 nanofluids in chapter 4 was carried out by introducing the co-flows of these nanofluids at total flow rates of $0.1 < Q_t < 1.5$ ml/min, translating to axial velocities of $0.074 < V_x < 1.11$ m/s in the square microchannel.

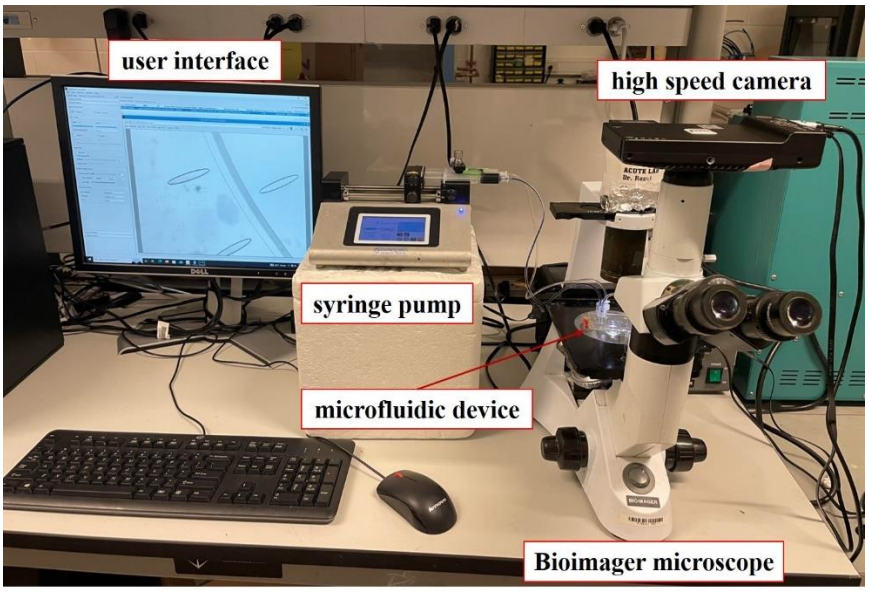

Figure 2-6: Experimental setup consisting of a Bioimager microscope, a high-speed camera, and a double infuse syringe pump.

The flow was video recorded at a rate of 50 frames per second under 5x magnification using the inverted microscope. Each experiment was repeated three times and the captured videos were analyzed frame by frame using the open source software ImageJ[135,136]. Dean flow characterization is described in detail in section 2.6.

In the particle behavior analysis in chapter 5, different concentrations of PEO solutions (one with particles at inlet-I and one clean buffer at inlet-O in Figure 2-2b and Figure 2-2c) were co-flown inside the curved microchannel at combined flow rates of $0.05 < Q_t < 2.0$ ml/min (i.e., 0.025 to 1.0 ml/min in each inlet). These flow rates correspond to average axial velocities of $0.037 < V_x < 1.48$ m/s (i.e., 0.00185 to 0.74 m/s in each inlet) in the square microchannel with a 150 × 150 μm^2 cross section. Particle behavior analysis in SiO_2 nanofluids in chapter 6, was conducted using the co-flows of different concentrations of SiO_2 nanofluid at total flow rates up to $Q_t = 1.5$ ml/min. Microparticles trajectories at the expanded outlet (Figure 2-2b and Figure 2-2c) were video recorded at different frame rates (up to 1400 fps with respect to the average axial velocity) using the high-speed camera on the inverted microscope at 2.5x magnification. Each experiment was repeated two times and video recordings were transferred to the open source ImageJ software[135,136] for analysis. Section 2.82.8 elaborates on the characterization of particle migrations inside curved microchannels.

2.6 Dean Flow Characterization

We examined the V_{De} of viscoelastic and shear-thickening fluids in curved microchannels fabricated in PDMS. Devices included two inlets to co-introduce various pairs of viscoelastic solutions into the channel, and two outlets, as shown in Figure 2-2. PEO solutions (one dyed with

10% v/v trypan blue) with the same concentration were co-flown in the curved channel. Videos were processed into image frames and analyzed by the open software ImageJ[135].

The schematic demonstration of Dean-based fluid switching is shown in Figure 2-7a, where a co-flow of PEO solutions is supplied inside the microchannel. Figure 2-7b illustrates the channel sections close to the entrance, middle and switching point (half fluid recirculation), when 500 ppm PEO solutions were co-flown in a square cross-section curved channel at V_x = 0.59 m/s. The color intensities, c_i, across the channel width (lines AB) were measured at 10-degree intervals along the channel (Figure 2-7c). The normalized standard deviation of intensities was defined as the Switching Index [*SI* in Eq.(2-4)], and plotted along the channel length in Figure 2-7d, where σ is the standard deviation of intensities at line AB at measurement intervals along the channel [Eq. (2-5)], and σ_{max} represents the maximum standard deviation observed at the channel entrance. N is the number of points (pixels) on line AB, and $\bar{c}$ is the average intensity value at each line.

$$SI = \sigma/\sigma_{max} \tag{2-4}$$

$$\sigma = \sqrt{(1/N)\sum_{i=1}^{N}(c_i - \bar{c})^2} \tag{2-5}$$

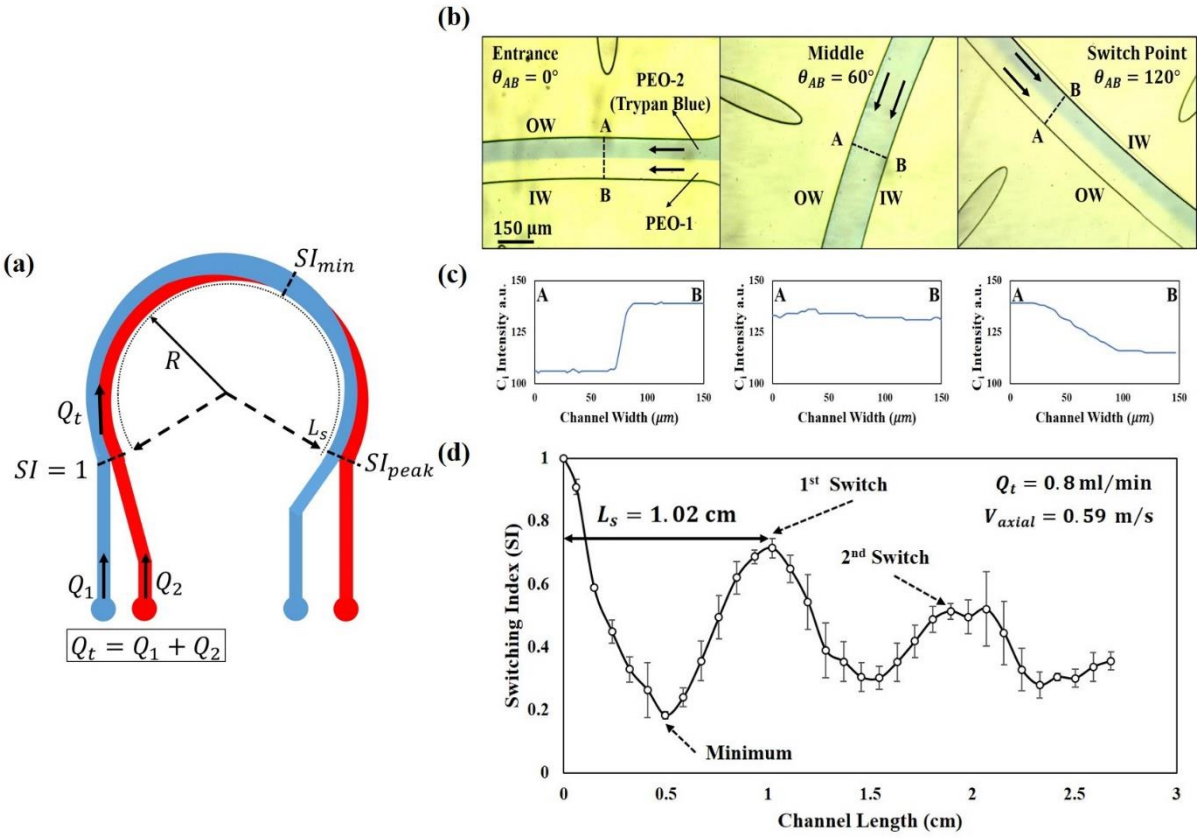

Figure 2-7: Dean flow characterization method. (a) Schematic demonstration of Dean flow-based fluid switching inside the microchannel, showing the SI and the fluids' lateral exchange length (L_s). (b) Co-flow images of trypan blue and undyed PEO solutions with 500 ppm concentration at an axial velocity of 0.59 m/s along the length of the microchannel (R = 0.5 cm, AR = 1.0) at the entrance, middle and the switch point. (c) Color intensity values measured along the lines AB in (b). (d) Switching index, SI, values of 1, 0.18, and 0.71 were obtained at the entrance, minimum and first switch points, respectively. L_s demonstrates the channel length at which the first switch occurred. Reprinted from Ref [123](AIP Adv.,2020).

As shown in Figure 2-7c, *SI*-value is equal to 1 at the channel entrance ($\sigma = \sigma_{max}$). As the fluids start the lateral Dean recirculation, *SI* decreases gradually alongside the channel up to a point that the minimum *SI*-value represents where the undyed PEO solution is sandwiched by the trypan blue dyed PEO. Then *SI* increases to a peak-value, which shows a 0.5 recirculation and lateral position switching of the fluids at a certain length of the channel called the switching length, L_s. The average V_{De} could be calculated based on L_s, axial fluid velocity V_x, and the average lateral migration length

of fluid particles L_R in our square channel[52,137,138], as shown in Eq.(2-6), where t is the time. The average lateral migrations for other channel aspect ratios were calculated based on the literature[52,137,138], and could be found in Appendix BAppendix B.

$$V_{De} = \frac{L_R}{t} = \frac{L_R V_x}{L_s} \tag{2-6}$$

In each experimental condition, the switching length, L_s, was measured three times and used to calculate the average Dean velocity, while standard deviation was reported as the error bars in the graphs.

2.7 Solution Exchange Characterization

The purity of the solution exchange in the particle washing process demonstration in chapter 5, associated with the dissolved trypan blue concentration in PEO solutions, was examined using optical spectrophotometry[139]. For this purpose, we measured the absorbance of different trypan blue concentrations (0% to 10 % v/v) in 500 ppm PEO solution using a spectrometer (Shimadzu, UV2600, Japan), as shown in Figure 2-8. As illustrated in Figure 2-8, the absorbance peaks rise, as the trypan blue concentrations increase in 500 ppm PEO solution.

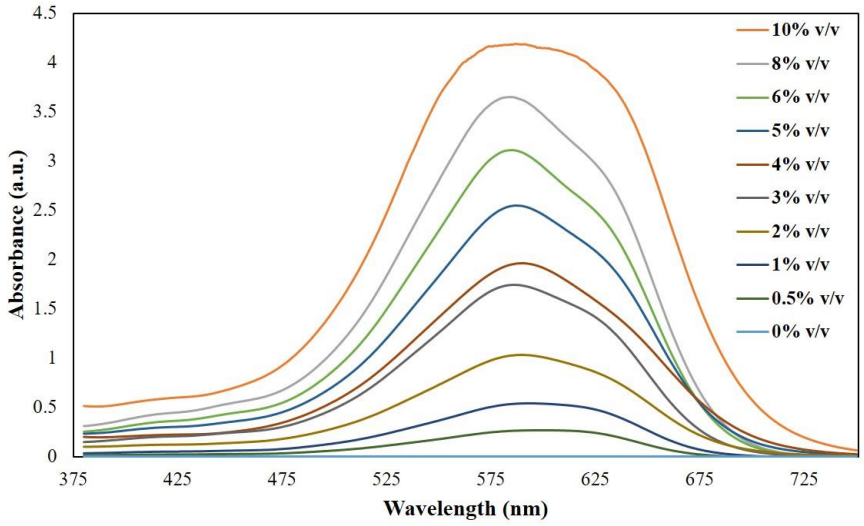

Figure 2-8: Absorbance of various trypan blue concentrations in 500 ppm PEO solution in the visible spectrum. Here, the 0% v/v concentration represents the undyed 500 ppm PEO solution, and a concentration of 10% v/v trypan blue indicates the dyed inlet solution.

The absorbance peaks at a wavelength of ~ 590 nm were used to develop a calibration curve with respect to the concentration of the dyed inlet solution (10% v/v trypan blue). As shown in Figure 2-9, a linear function [Eq. (2-7)] was fitted over 0-40% data points with R^2 = 0.99.

$$y = 0.052\,x + 0.02 \tag{2-7}$$

Here, *y* represents the absorbance of the solution and *x* stands for the concentration of collected solution with respect to the dyed inlet solution (i.e., 10% v/v trypan blue in 500 ppm PEO) The linear correlation in Eq. (2-7) could be used to characterize the solution exchange purity of the collected samples in section 5.2.8.

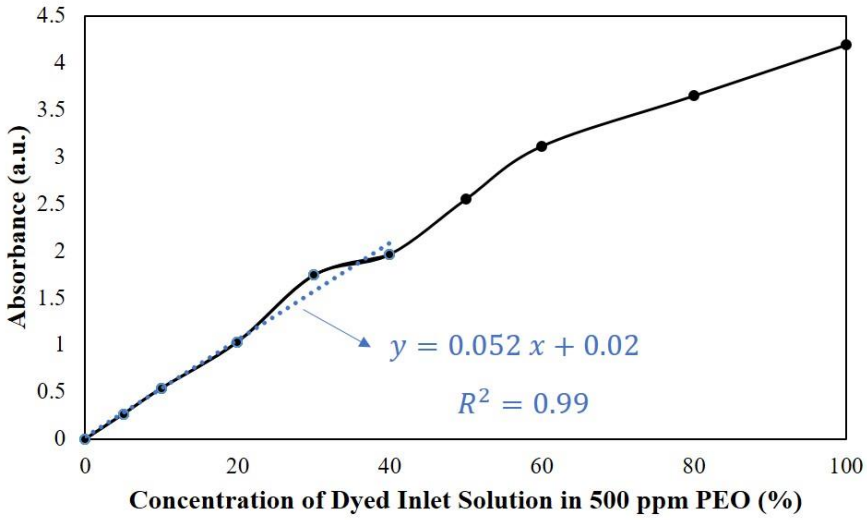

Figure 2-9: Absorbance vs. concentration of the dyed inlet solution (i.e., 10% v/v trypan blue in 500 ppm PEO solutions). A linear function could be fitted over the 0-40% concentration range with R^2 = 0.99.

2.8 Particle Behavior Analysis

Our curved channel microdevices consisted of two inlets to supply the co-flow of PEO or SiO_2 solutions, i.e., one with particles (inlet-I) and one clean buffer (inlet-O), into a 300° curvilinear channel with a constant radius of curvature as shown in Figure 2-10a. An expanded outlet (~2.55 mm in width) was implemented for particle visualization at a lower speed.

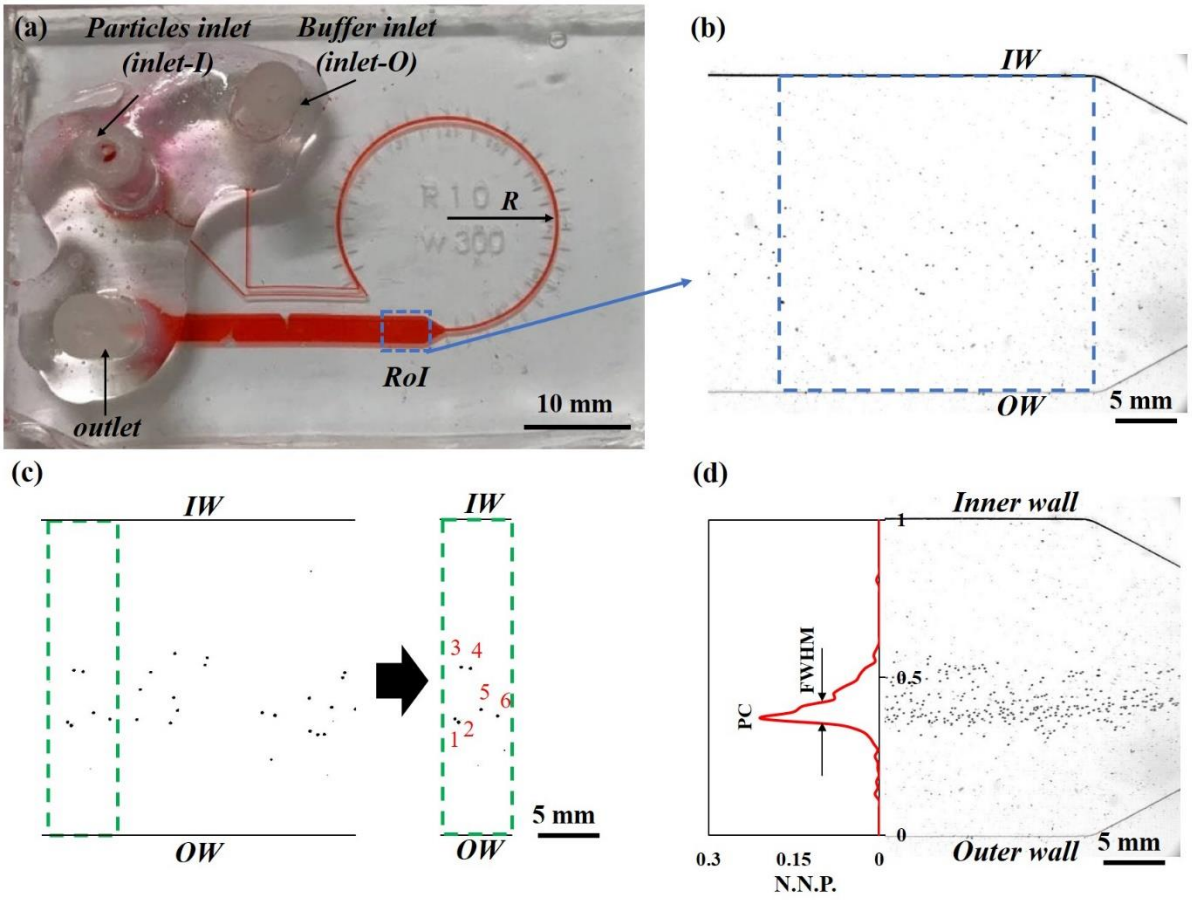

Figure 2-10: Microfluidic device for particle focusing investigation. Microchannel design with two inlets for the particles (inlet-I), and the buffer solution (inlet-O), and one expanded outlet with a width of 2.55 mm. (a) curvilinear channel with a constant radius of curvature (R). The representative microchannel shown consists of a 300° curvature with a cross section of w×h= 300 × 150 μm² and R = 1.0 cm. (b) Example of the captured frame at RoI. (c) The background is subtracted from the image stacks, and the particles are traced using the WrMTrck plugin. (d) Image overlaps of particle trajectory at the region of interest [RoI in (b)] for a = 15 μm particles in 2000 ppm PEO solution at a total axial velocity of V_x = 0.148 m/s. Normalized number of particles (NNP) are drawn alongside the non-dimensional channel width. FWMH indicates the full width at half maximum, representing particles' distribution, and PC indicates the peak centroid.

The recorded videos at the channel outlet were analyzed frame by frame using the WrMTrck plugin[140] in ImageJ. As illustrate in Figure 2-10b, the region of interest is cropped in each video and the background is subtracted from the frame stacks. Later on, the color intensities were

adjusted in ImageJ to get a black and white image stack similar to Figure 2-10c. A specific portion of the frame (~ 5 mm in width) is used to trace the particles in WrMTrck plugin, as specified in Figure 2-10c. As shown in the image overlap of particle trajectories in Figure 2-10d, microparticles lateral positions were normalized with respect to the outlet width (here 0 indicates the channel outer wall and 1.0 shows the channel wall close to the center of curvature). To obtain the particle distribution graphs, the outlet channel width was divided into 50 equal sections. Normalized number of particles (NNP) with respect to the total detected particles were plotted along the normalized channel width as illustrated in Figure 2-10d. At each stage, particle distributions were analyzed using OriginPro (Origin 2021b, OriginLab Corp., USA) to obtain the number of peaks, peak values, and peak locations (i.e., peak centroids, PC), as well as the full width at half maximum (FWHM) representing particles distribution in the channel.

The fraction of normalized number of particles in a normalized bandwidth of ±0.1 around each PC was used to characterize the focusing behavior of particles. A full focusing was defined for NNP fractions higher than 90%, while NNP fractions between 70% to 90% were considered a partial focusing. Any NNP fraction less than 70% within the above bandwidth was deemed as a no focusing condition. Particle distributions with more than one peak in NNP graphs were categorized separately as “two peaks”.

Fluid recirculation could be predicted using our reported correlations in chapter 3 and chapter 4 for the average Dean velocity of PEO solutions, and SiO_2 nanofluids, respectively. The required channel length for the first fluid switch (i.e., switching length, L_s) could be obtained using the predicted V_{De}, where $L_s = L_R V_x / V_{De}$.[139] Here L_R is the average lateral migration of fluid elements, which could be estimated based on the reported values in Appendix B. Considering the total channel length of L_{curve} = 5.23 cm (for all radii of curvatures), the number of fluid switches could

be roughly estimated as L_{curve}/L_s. This value could predict the lateral location of the particles (if only affected by drag force) and the buffer solutions at the channel outlet.

In case of duplex particle investigation in chapter 5, a hemocytometer (Marienfeld, Germany) was used to count the number of captured particles in different channel outlets in Figure 2-3. Particle separation efficiencies at each outlet could be calculated using the number of collected particles at each outlet divided by the total number of particles as shown in Eq. (2-8).

$$Efficiency = \frac{Number\ of\ Target\ Particles\ in\ Selected\ Outlet}{Total\ Number\ of\ Target\ Particles\ in\ All\ Outlets} \times 100 \quad (2\text{-}8)$$

During the duplex particle separation, the purity of the collected samples could be calculated by dividing the number of collected target particles (in this case 15 μm) by the total number of collected particles (5 μm, and 15 μm) in each outlet, as shown in Eq. (2-9).

$$Purity = \frac{Number\ of\ Target\ Particles\ in\ Selected\ Outlet}{Total\ Number\ of\ All\ Particles\ in\ Selected\ Outlet} \times 100 \quad (2\text{-}9)$$

In section 5.2.8, each experiment was repeated two times and particle were counted three times for each sample. Results are presented as the average efficiencies and purities ± the standard deviations.

Chapter 3

3 Dean Flow Velocity of Shear-Thinning Viscoelastic PEO Solutions in Curved Microchannels*

In this chapter, the effects of curved channel height, radius of curvature and kinematic viscosity were investigated to derive an empirical correlation for V_{De} of viscoelastic water (Obj. 1). The developed knowledge of viscoelastic Dean flow velocity will be vital in design of elasto-inertial microfluidic devices, for determination of fluids lateral displacement in fluid exchange and Dean drag force in particle focusing and separation applications, as pursued in chapter 5 of this thesis.

* Contents of this chapter have been published in:
Nikdoost, A. & Rezai, P. Dean flow velocity of viscoelastic fluids in curved microchannels. *AIP Adv*. **10**, 085015 (2020).

3.1 Introduction

In curved and spiral microchannels, the secondary Dean vortices modify the inertial equilibrium positions of the particles. The balance between inertial and Dean drag forces enables a complete size-based particle separation with a reduced channel footprint, high separation efficiency and throughout, and low power requirement[43,54].

Previous studies in curved microchannels have focused on Dean flow characteristics of Newtonian fluids [Equations (1-16) and (1-17)] and lack in-depth understanding of the effect of fluid viscosity, especially in second order fluids. In non-Newtonian fluids such as blood and raw milk, the rheological characteristics highly depend on the applied shear stress. Under deformation, viscoelastic fluids possess both viscous and elastic behaviors, as opposed to Newtonian fluids, where their viscosity remains constant under the applied stress[55].

A non-Newtonian fluid flowing in a curved channel would impose changes in the lateral migration and equilibrium of particles. The coupled effect of Dean drag with the inertial and elastic forces enhances the throughput compared to the particle focusing in elasto-inertial regimes in straight microchannels[59,70,75,77,120,121]. The particle lateral motion could be controlled by the balance between the Dean drag, inertial, and elastic forces. The magnitude of these forces directly depends on particle size, polymer concentrations, and flow characteristics[88–91]. Hence, it is of utmost importance to study the non-Newtonian flows in non-straight channels, and to investigate the axial and Dean flow velocities as a first step, for instance in viscoelastic liquids.

In this chapter, we investigated the effect of channel geometries and polymer concentration (e.g., relaxation time) to obtain an empirical correlation for the average velocity of the secondary vortices in a co-flow of viscoelastic fluids in curvilinear microchannels. Our correlation can be

used for more accurate design of particle and cell sorting microdevices involving curved channels and viscoelastic solutions.

For this purpose, three concentrations of polyethylene oxide (PEO) powder with a molecular weight of 2×10^6 Da in water (125, 500, and 1000 ppm) were tested at flow rates of $0.2 < Q_t < 2.0$ ml/min (0.1-1.0 ml/min at each inlet). PEO solutions (one dyed with 10% v/v trypan blue) with the same concentration were co-flown in the curved channel (Figure 2-2) and video-recorded along the channel length at 5x magnification under an inverted microscope. Videos were processed into image frames and analyzed by the open source software ImageJ[135] as previously explained in section 2.5 and section 2.6.

3.2 Results and Discussion

3.2.1 Effect of Axial Velocity (V_x) on V_{De}

In a representative experiment, we investigated the effect of axial flow velocity on *SI* for co-flows of 500 ppm PEO solutions in a square cross section channel (150 µm × 150 µm) with R = 0.5 cm. As shown in Figure 3-1, by increasing the axial velocity by ~5 folds, the switching length decreased by more than 3.5 folds. A higher axial velocity results in a higher *De* number and a stronger Dean flow, and therefore a decrease in L_s and observation of multiple switches at higher velocities. Moreover, the three switching lengths of L_s = 2.07, 0.85, and 0.58 cm correspond to Dean velocities of V_{De} = 1.33, 8.14, and 23.56 mm/s in Figure 3-1, respectively. The expected increase in V_{De} is also a result of the enhanced *De* number at higher flow rates. This clearly shows the direct dependency of V_{De} on axial velocity and hence the flow rate, which is also illustrated in Figure 3-2 for all the tested PEO concentrations. For instance, a 10-fold increase in the average

axial velocity in 125 ppm PEO solutions resulted in ~ 63-fold increase in the average Dean velocity (from 0.5 mm/s to 31.5 mm/s).

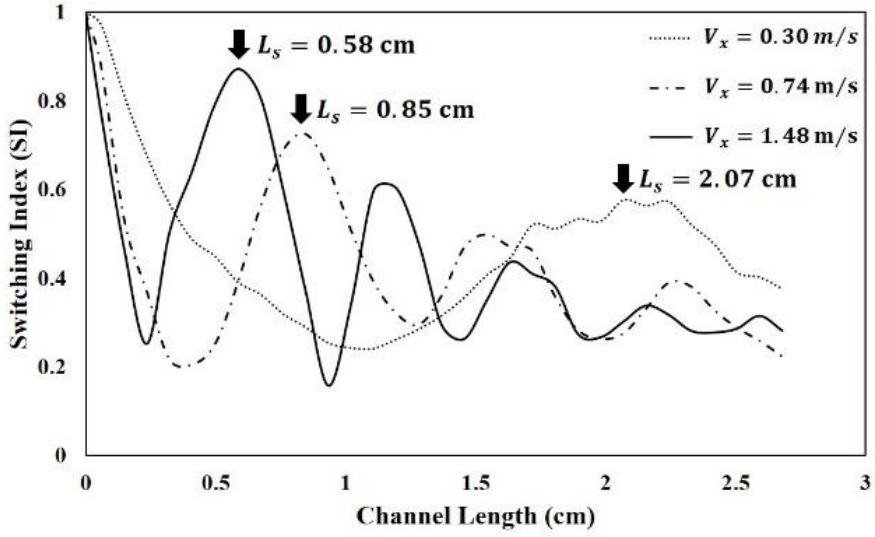

Figure 3-1: The switching index (SI) of PEO solutions with 500 ppm concentration flowing at three axial velocities along the curved microchannel (AR = 1.0, R = 0.5 cm) shown in Figure 2-2a. The first SI peak, L_s, demonstrates the channel length from the entrance at which the first switch occurred.

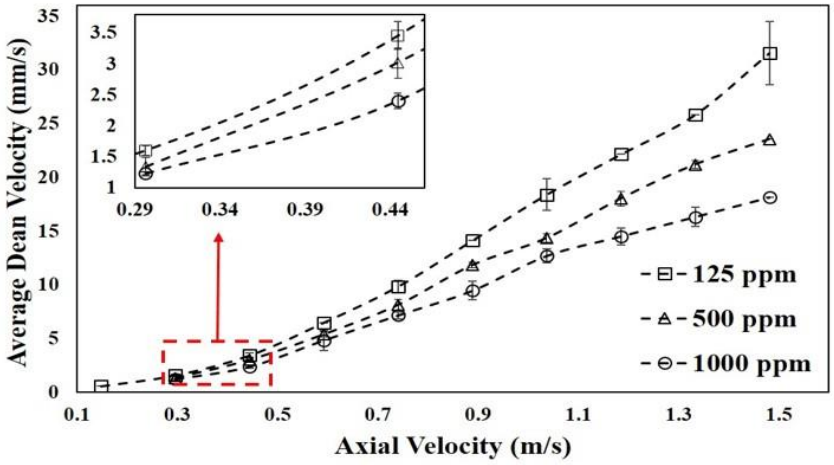

Figure 3-2: Representative experiments showing the effects of axial flow velocity on V_{De} for co-flows of PEO solutions in curved microchannels with a 150 µm×150 µm cross section and R = 0.5 cm. Error bars are included for all data points but not visible in cases where they are very small.

3.2.2 Effect of Channel Radius of Curvature (R) on V_{De}

The effect of channel radius of curvature on V_{De} was studied in a square microchannel (150 µm × 150 µm). Figure 3-3 shows the average V_{De} for a co-flow of 500 ppm PEO solutions in channels with R = 0.5, 1.0, 1.5, and 2.0 cm. Here, at an axial velocity of V_x = 1.48 m/s (Wi = 63.7), the four different radii of curvature corresponded to De = 19.44, 13.75, 11.22, and 9.72, respectively. As the De number decreased at higher radii of curvatures, the average V_{De} dropped from an initial value of 23.56 mm/s for R = 0.5 cm to 7.87 mm/s when R = 2.0 cm. Therefore, we concluded that increasing the radius of curvature has an inverse effect on the average V_{De} as it leads to weaker Dean vortices at a constant axial velocity.

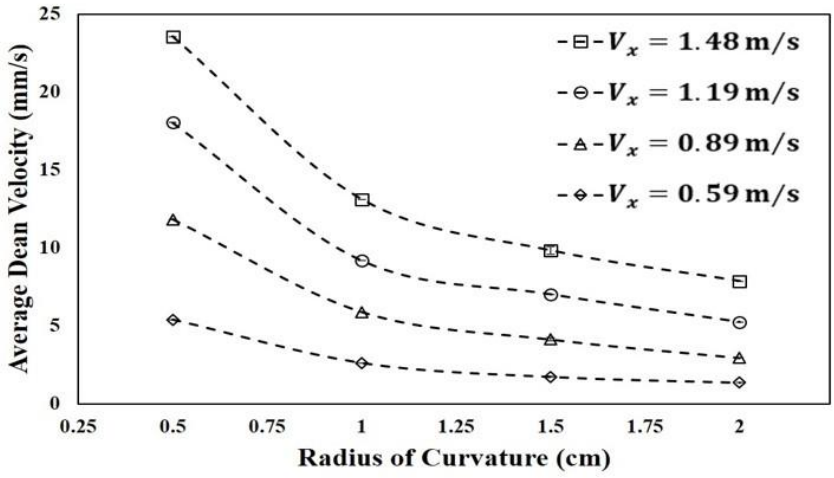

Figure 3-3: Representative experiments showing the effects of channel radius of curvature on V_{De} for co-flows of 500 ppm PEO solutions in curved microchannels with a 150 µm×150 µm cross section. Error bars are included for all data points but not visible in cases where they are very small.

3.2.3 Effect of PEO Concentration on V_{De}

The effect of PEO concentration, and hence fluid viscosity and relaxation time, was investigated using co-flows of 125, 500, and 1000 ppm PEO solutions (λ = 1.75, 4.3, and 6.8 ms, respectively[128,130]) in the square microchannel with R=0.5 cm. As shown in Figure 3-4, at the axial

velocity of V_x = 1.48 m/s, V_{De} dropped from an initial value of 31.58 mm/s for a co-flow of 125 ppm PEO (*De* = 22.68, and *Wi* = 25.9), down to 18.14 mm/s for a co-flow of 1000 ppm PEO (*De* = 16.3, and *Wi* = 100.7). Increasing the concentration of PEO solution increases its viscosity, which resulted in lowering the *De* number at a constant axial velocity. Since a decrease in *De* number weakens the secondary vortices, the concentration of PEO solutions has an inverse effect on the average V_{De} as shown for selected axial velocities in Figure 3-4.

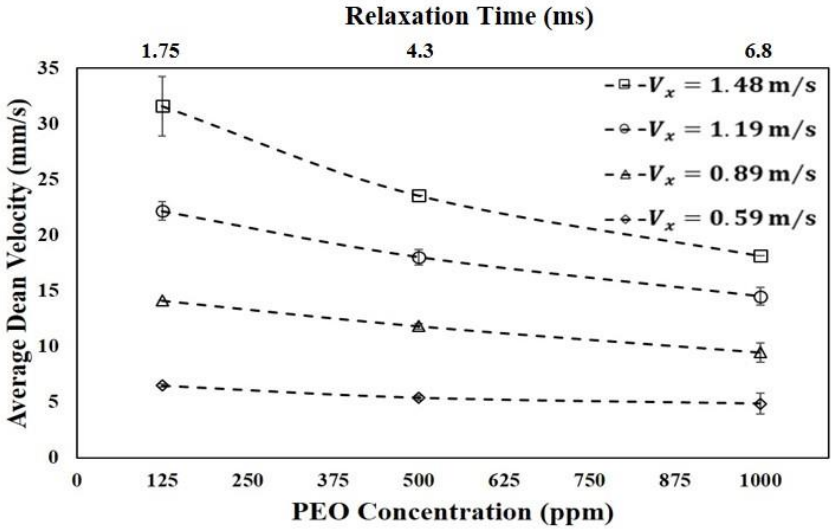

Figure 3-4: Representative experiments showing the effects PEO concentration (and relaxation time), on V_{De} for co-flows of PEO solutions in curved microchannels with a 150 µm×150 µm cross section and R = 0.5 cm. Error bars are included for all data points but not visible in cases where they are very small.

3.2.4 Effect of Channel Height (*h*) on V_{De}

Different channel heights were used to investigate the effect of channel aspect ratio on V_{De}. At a constant axial velocity, increasing the channel height (*h* = 75, 150, and 225 µm) resulted in an increase in the *De* number. For instance in Figure 3-5, a co-flow of 125 ppm PEO solutions at V_x = 0.89 m/s, at three different aspect ratios, resulted in three *De* numbers of 4.91, 8.25, and 12.65 (*Wi* = 21.0, 15.6, and 12.8), and the average Dean velocities of V_{De} = 2.29, 5.9, and 7.02 mm/s,

respectively. Therefore, increasing the channel height led to an increase in V_{De}, as the higher *De* numbers translate into stronger Dean vortices.

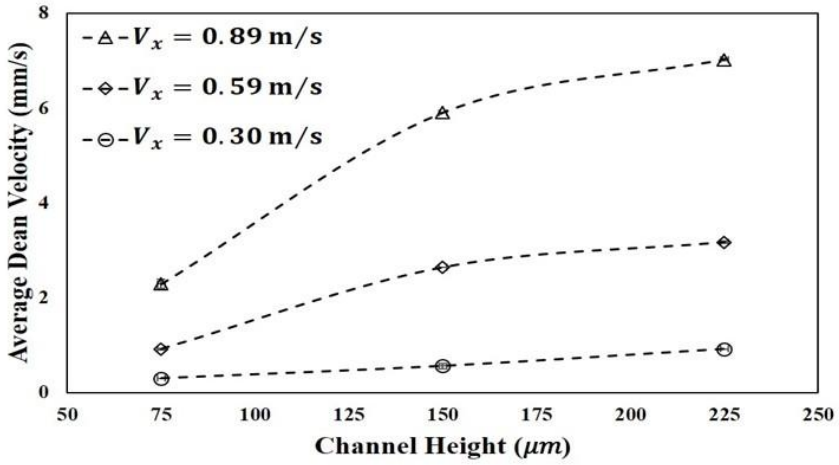

Figure 3-5: Representative experiments showing the effects of channel height on V_{De} for co-flows of PEO solutions in curved microchannels with a width of w =150 µm and R = 1.0 cm. Error bars are included for all data points but not visible in cases where they are very small.

3.2.5 Non-dimensional Analysis

In order to further depict the effects of the tested parameters in a non-dimensional manner, we plotted the Dean velocity-based Reynolds number ($Re_{V_{De}} = V_{De}D_h/\vartheta$) as a function *Wi* and *De*, for different PEO concentrations and flow conditions (Figure 3-6). In Figure 3-6, we attempted to group data points with close or identical *De* and *Wi* numbers together so the effects of these non-dimensional groups on $Re_{V_{De}}$ could be better visualized. Accordingly, the experimental conditions between data points may be different in Figure 3-6. For plots of $Re_{V_{De}}$ at constant channel radii of curvature and aspect ratios, please refer to the Appendix C. We observed that the *De* number had a more significant effect on $Re_{V_{De}}$ compared to the *Wi* number. As illustrated in Figure 3-6a, at a constant *Wi* number, $Re_{V_{De}}$ drastically changed by increasing the *De* number. For instance, at *Wi* = 50.96, only a 2-fold increase in *De* (7.8 to 15.6) was enough to result in ~3.5 fold increase in

$Re_{V_{De}}$ (0.56 to 1.93), corresponding in an increase in V_{De} from 5.24 mm/s to 18.04 mm/s. On the other hand, for all the data points with a *De* number between 9-10 in Figure 3-6b, increasing the *Wi* number by ~ 10 folds (10.4 to 100.7) resulted in a fluctuation in $Re_{V_{De}}$ between 0.69 and 0.87, corresponding a range of V_{De} from 5.48 to 9.47 mm/s. Even this change may be attributed to the slight variation in the *De* number between 9 to 10 rather than the *Wi* number.

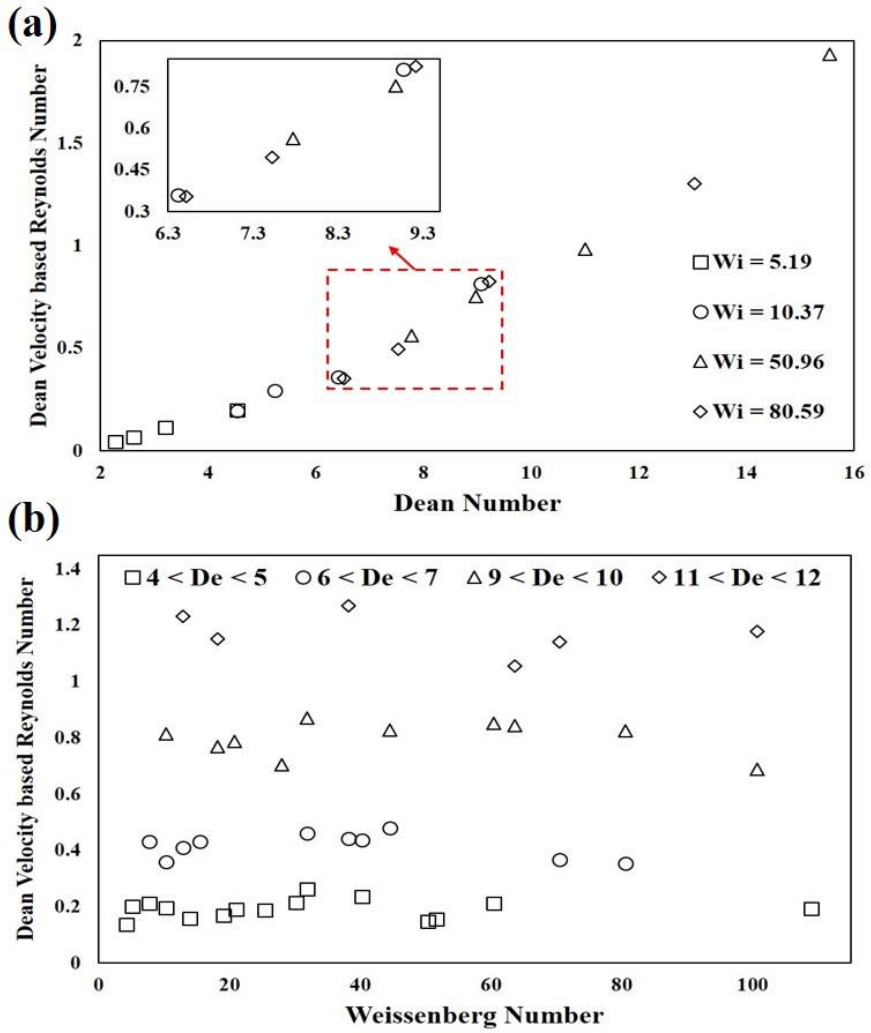

Figure 3-6: Dean velocity-based Reynolds number ($Re_{V_{De}} = V_{De}D_h/\upsilon$) plotted against (a) Dean and (b) Weissenberg numbers for co-flows of PEO solutions in curved microchannels.

From the experimental results obtained in this study with examples shown in Figure 3-2 to Figure 3-6, and in order to capture the effects of channel dimension (D_h), fluid kinematic viscosity (v) and relaxation time (λ) in non-dimensional formats, we assumed that the Dean velocity-based Reynolds number of viscoelastic fluids in curved microchannels is dependent on the *De* and *Wi* numbers via a power function as $Re_{V_{De}} = aWi^b De^c$. All experimental $Re_{V_{De}}$values were plotted and different correlation constants *a, b and c* were investigated. The best fit was obtained by *a* = 0.01, *b* = 0.01 and *c* = 1.89 as shown in Figure 3-7 with R^2=0.98. Figure 3-7 represents the Dean velocity-based Reynolds number, $Re_{V_{De}}$, for all the experiment data points plotted against $Wi^{0.01}De^{1.89}$. The fitted line in Figure 3-7 indicate our empirical correlation.

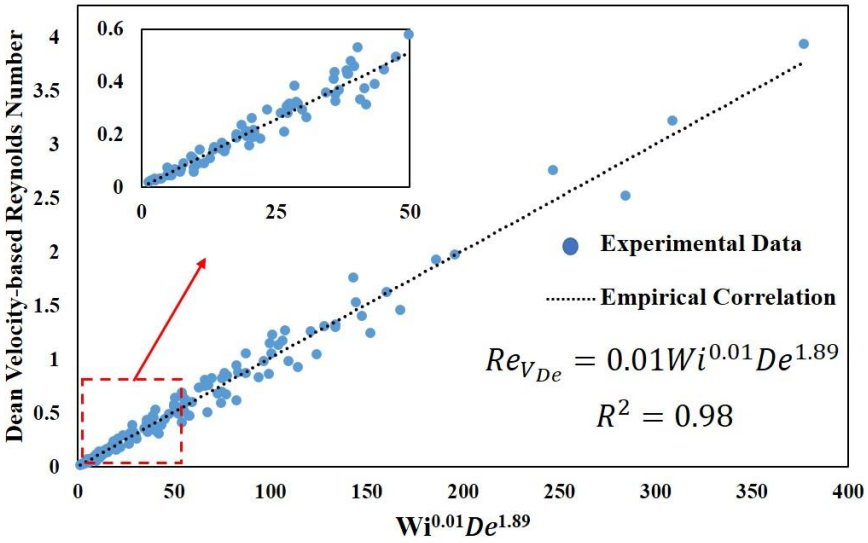

Figure 3-7: Dean velocity-based Reynolds number,$Re_{V_{De}}$, plotted against $Wi^{0.01}De^{1.89}$ for all the experimental data obtained in this study.

As discussed before, our experimental data confirmed that the *De* number had a more significant effect on the Dean velocity of viscoelastic liquids in curved microchannels. Considering the weak effect of *Wi* on $Re_{V_{De}}$ (and V_{De}), simplified versions of the empirical correlation can be obtained as shown in Eq. (3-1), and Eq. (3-2).

$$Re_{V_{De}} = 0.01\, De^{1.89} \tag{3-1}$$

$$V_{De} = 0.01\, {\vartheta}/{D_h}\, De^{1.89} \tag{3-2}$$

Our empirical correlation in Eq. (3-2) enables a more precise prediction of the average Dean velocity of viscoelastic flows in curved channels with an average error of 12.7%. The previous empirical correlations by Ookawara [Eq. (1-16)][49] and us [Eq. (1-17)][52] were developed for Newtonian fluids. Applying these equations to viscoelastic liquids, which is commonly done in the field, is not recommended as they will result in V_{De} estimations with average errors in the range of 25-40% with respect to the experimental values.

As mentioned earlier in section 2.4, temperature fluctuation could affect the viscosities of PEO solutions, depending on the concentration and shear rate. Thus, this will cause reduced accuracy and applicability of the proposed correlation as the viscosity variations due to the temperature were not considered in our calculations. Other sources of uncertainty are the measurement methods for the fluid average lateral displacement and the switching length, which could be further enhanced as discussed in chapter 7.

Conclusion

In summary, different concentrations of PEO-spiked viscoelastic water solutions were tested in a curved microchannel with different radii of curvature and aspect ratios, and an empirical correlation for the average V_{De} of viscoelastic fluids was proposed. The new correlation captures the effect of fluid kinematic viscosity and the channel hydraulic diameter, and significantly reduces the prediction error for V_{De} of viscoelastic liquids down to 12.7%. This correlation provides a better understanding of non-Newtonian fluid behavior in curved microchannels, which can be used

widely in the design of microfluidic devices for microparticle separation and washing applications. In the future, we aim to further improve the correlation using analytical and numerical methods and test its suitability for a wider range of non-Newtonian fluids.

Chapter 4

4 Dean Flow Velocity of Shear-Thickening SiO_2 Nanofluids in Curved Microchannels*

In this chapter, we report the effects of a curvilinear microchannel width, height, and radius of curvature, as well as the kinematic viscosity and axial velocity of shear-thickening nanofluids, on the average Dean velocity (V_{De}) of the secondary flow in curved microchannels, and an empirical correlation is reported (Obj. 1).

* Contents of this chapter have been published in:
Nikdoost, A. & Rezai, P. Dean Flow Velocity of Shear Thickening SiO_2 Nanofluids in Curved Microchannels. *Phys. Fluids* **34**, 062009 (2022).

4.1 Introduction

In a non-Newtonian fluid, the lateral migration of microparticles inside the curved microchannels is further modified under the combined effects of inertial, elastic, and Dean drag forces[59,70,75,77,120,121]. Detailed reviews on particle migration in viscoelastic fluids can be found elsewhere[63,141]. As illustrated in chapter 3, we carried out an experimental investigation on the effect of channel dimensions and fluid viscosity on V_{De} of viscoelastic fluids and reported a modified correlation [Eq. (3-2)] for the prediction of V_{De} of PEO in water solutions[123]. The new correlation provided a more precise prediction of V_{De} in PEO solutions with an average error of 12.7%, compared to a 25-40% error with the application of previous water-based correlations by Ookawara[49] and Bayat[52].

To perform a comprehensive study in this thesis on various fluid types, we shifted our attention towards shear-thickening fluids such as the mixtures of metallic nanoparticles with water in this chapter[108]. The colloidal dispersions of metallic oxides such as Aluminium oxide (Al_2O_3) and silicon dioxide (SiO_2) nanoparticles with enhanced thermal properties have found a wide range of applications in chemical and petrochemical industries[116–119]. We envision that such shear-thickening fluids are on the verge of entering the field of inertial microfluidics for particle and cell sorting. In this area, the average Dean velocity of such metallic nanofluids in curved microchannels is the first research question that needs to be answered. The application of the previous correlations for water [Eq. (1-17)], and PEO [Eq. (3-2)] solutions would probably result in high errors for the prediction of Dean velocity in metallic nanofluids. Therefore, a new correlation is required for the estimation of V_{De} of shear-thickening SiO_2 nanofluids in curved microchannels.

Here, we present an experimental investigation to study, for the first time, the effects of channel geometry (h, w, D_h, and R) and fluid viscosity (i.e., nanoparticle concentration) on the average Dean velocity of SiO_2 nanofluids in curved microchannels. Three different concentrations (φ= 1%, 2%, and 3% v/v) of colloidal dispersion of SiO_2 (40% in water, Alfa Aesar, USA) with previously reported viscosities[115] were tested inside our curved microchannels. The experimental procedure and data analysis were previously elaborated in sections 2.5 and 2.6.

An empirical correlation for estimating the V_{De} of SiO_2 nanofluids will be offered, which can enable not only fundamental studies on particle dynamics in such fluids (chapter 6 in this thesis), but also the design of future cell and particle sorting devices that use shear-thickening fluids as their carrier solution.

4.2 Results and Discussion

4.2.1 Dean Flow of Shear-thickening SiO_2 Nanofluids in Curved Microchannels

In a representative experiment, we studied the effect of axial velocity, V_x, on the switching index, *SI* in Eq. (2-4), in a co-flow of 1% v/v SiO_2 in a rectangular microchannel (w = 300 μm, h = 150 μm) with R= 1.0 cm. As shown in Figure 4-1, at any V_x, *SI* has a maximum value of one at the channel entrance. *SI* decreases gradually until the middle section of the channel where the dyed SiO_2 stream sandwiches the undyed nanofluid, resulting in a minimum value for *SI*. Then, *SI* rises and reaches a peak value indicating a point along the channel at which half fluid recirculation happens due to Dean vortexing (called the switching length, L_s). As illustrated in Figure 4-1, at V_x = 0.15 m/s, the co-flow of 1% SiO_2 nanofluids did not reach to a half recirculation point and the fluid switch did not occur in the 300° curved channel. However, increasing the axial velocity to V_x

= 0.3 and 0.60 m/s resulted in the switching lengths of L_s = 4.19 and 1.80 cm, respectively. Therefore, a two-fold increase in the axial velocity resulted in ~2.3x reduction in the switching length, and according to Eq. (2-6), almost 4.7x increase in the average V_{De} (from 1.42 to 6.62 mm/s). This increase in the average V_{De} could be explained because of the enhanced *De* number at higher axial velocities and the added strength to the Dean flow.

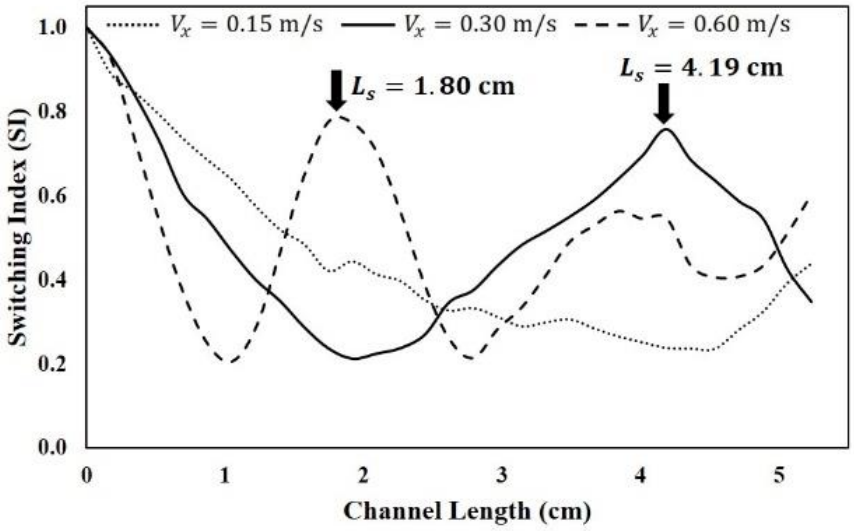

Figure 4-1: Switching index (SI) of 1% SiO_2 nanofluids co-flown at three different axial velocities in a curved channel with w = 300 µm, h =150 µm (AR = 0.5), and R = 1.0 cm. The first peaks in SI graphs, shown by L_s, indicate the required channel length to reach the first fluid switch due to Dean vortexing. Reprinted with permission from AIP Publishing[122].

4.2.2 Effect of Axial Velocity (V_x) on V_{De}

To investigate the effect of axial velocity on the average V_{De}, we tested co-flows of SiO_2 nanofluids in curved channels at inlet axial velocities of $0.15 < V_x < 1.11$ m/s. In a representative case for the co-flow of 1% SiO_2[*] in a square microchannel (150 × 150 µm^2) with R = 1.0 cm, the average V_{De} is plotted for different axial velocities in Figure 4-2. Here, a 4-fold increase in the

[*] Results for 2% and 3% SiO_2 are presented in Appendix D.

axial velocity from 0.15 to 0.6 m/s (*De* = 0.064 to 0.084), resulted in a ~14x increase in V_{De} (from 0.28 to 3.93 mm/s). A higher axial velocity results in a more dominant increase in the inertial [$f_I \propto V_x^2$ in Eq.(1-5)], and centrifugal [$f_C \propto V_x^2$ in Eq. (1-9)] forces, compared to the increase in the viscous forces [$f_V \propto \mu V_x$ in Eq. (1-6)]. Therefore, an increase in the axial velocity translates into a larger Dean number and stronger Dean vortices, hence leading to a direct effect of V_x on the average V_{De} in SiO_2 nanofluids.

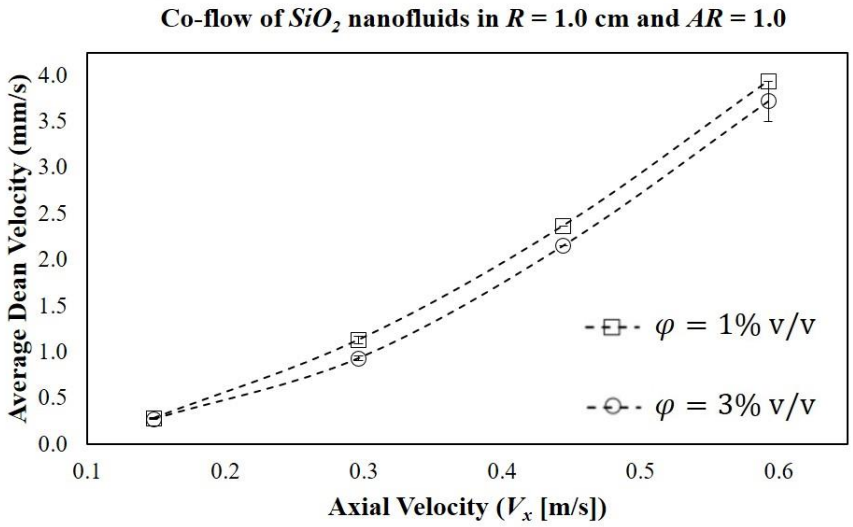

Figure 4-2: Representative experiments illustrating the effect of axial velocity (V_x) on V_{De} for the co-flows of SiO_2 nanofluids in curvilinear microchannels with a 150 × 150 μm² cross section. Error bars are included for all data points but are not visible in cases of small errors. Reprinted with permission from AIP Publishing[122].

4.2.3 Effect of Channel Radius of Curvature (*R*) on V_{De}

The effect of channel curvature was studied in a square microchannel (150 × 150 μm²) with three different radii of curvature (*R* = 1.0, 1.5, and 2.0 cm). For a co-flow of 1% SiO_2 at an axial velocity of V_x = 0.6 m/s, these radii of curvature corresponded to *De* = 0.084, 0.069, and 0.059, respectively. As shown in Figure 4-3, increasing the channel radius of curvature from 1.0 cm to

2.0 cm resulted in a ~2.2x decrease in the average V_{De} (from 3.94 to 1.76 mm/s). Here, increasing the channel radius of curvature leads to lower centrifugal forces [$f_C \propto \frac{1}{R}$ in Eq. (1-9)], and weaker vortices at a constant axial velocity; therefore, it has an inverse effect on the average Dean velocity.

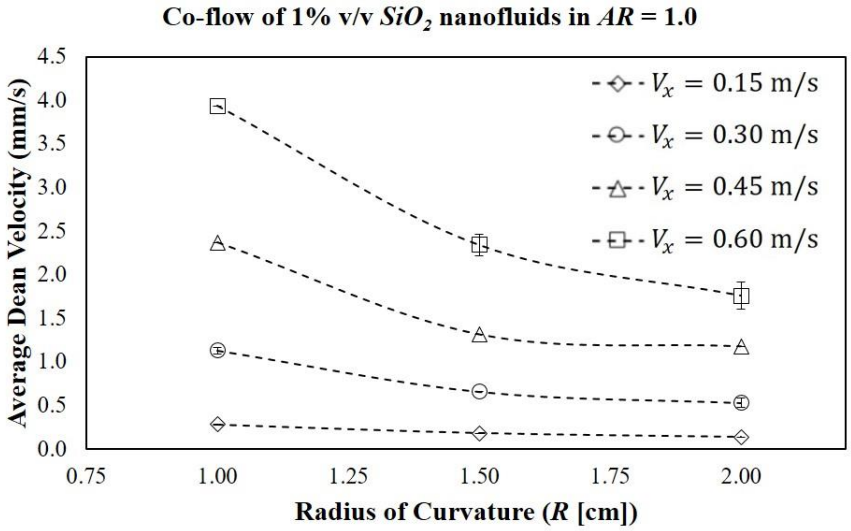

Figure 4-3: Representative experiments illustrating the effect of radius of curvature (R) on V_{De} for the co-flows of 1% v/v SiO_2 nanofluids in curvilinear microchannels with a 150 × 150 μm^2 cross section. Error bars are included for all data points but are not visible in cases of small errors. Reprinted with permission from AIP Publishing[122].

4.2.4 Effect of SiO_2 Concentration (φ) on V_{De}

Next, to investigate the effect of SiO_2 concentration, and hence the fluid viscosity we tested co-flows of three different concentrations of SiO_2 nanofluids (φ = 1%, 2%, and 3% v/v) in water in the curved microchannel. As a representative experiment, the averaged Dean velocities for the co-flows of SiO_2 in a rectangular microchannel (w = 150 μm, h = 225 μm) with R = 1.0 cm were plotted for different axial velocities in Figure 4-4. Here, the co-flows of 1%, 2%, and 3% v/v SiO_2 at V_x = 0.75 m/s corresponded to De = 0.133, 0.124, and 0.120, respectively. As shown in Figure 4-4, by increasing the nanofluid concentration, the average V_{De} dropped from an initial value of

7.37 mm/s for a co-flow of 1% SiO_2 to 6.61 mm/s for the co-flows of 3% SiO_2 nanofluids. An increase in the nanofluid concentration (i.e., fluid viscosity) increases the viscous forces [$f_V \propto \mu$ in Eq. (1-6)]; hence, it decreases the Dean number and weakens the secondary vortices. Therefore, we concluded that the concentration of SiO_2 nanofluids has an inverse effect on the average V_{De}.

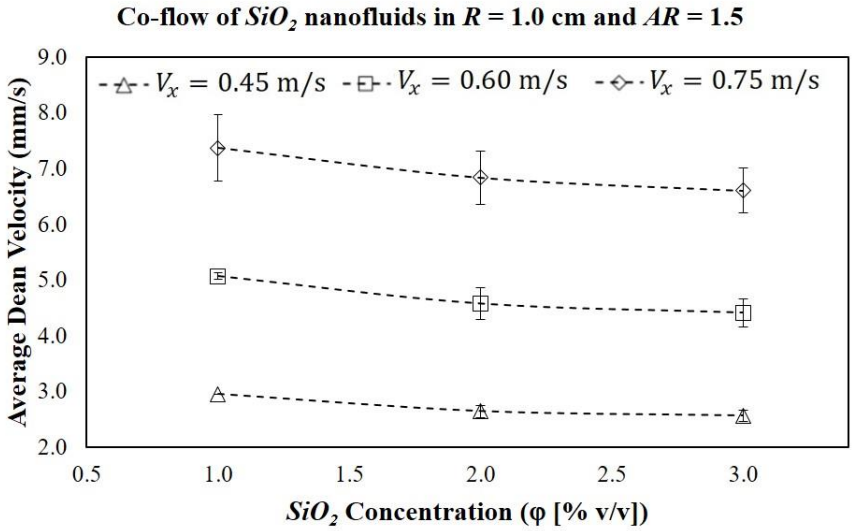

Figure 4-4: Representative experiments illustrating the effect of SiO_2 concentration (φ) on V_{De} for the co-flows of SiO_2 nanofluids in curvilinear microchannels with a 150 × 225 μm^2 cross section. Error bars are included for all data points but are not visible in cases of small errors. Reprinted with permission from AIP Publishing[122].

4.2.5 Effect of Channel Width (w) on V_{De}

Finally, different channel widths were used to investigate the effect of channel aspect ratio on V_{De}. At a constant channel height of h = 150 μm, co-flows of 1% SiO_2 nanofluids were tested in three different channel widths of w = 150, 225, and 300 μm (AR = 1.0, 0.67, and 0.5, respectively). As shown in Figure 4-5, at a constant axial velocity of V_x = 0.45 m/s, the co-flows of SiO_2 nanofluids in microchannels with the three widths above resulted in V_{De} = 2.36 mm/s (De = 0.079), V_{De} = 3.46 mm/s (De = 0.121), and V_{De} = 3.54 mm/s (De = 0.153), respectively. Here, increasing the channel width at a constant axial velocity resulted in an increase in the De number since a

higher channel hydraulic diameter (D_h = 150 µm, 180 µm, 200 µm) was obtained and translated to lower shear rates ($\dot{\gamma}$=1.5V_x/D_h)[141], which resulted in a lower fluid viscosity and lower viscous forces [$f_V \propto \mu/D_h$ in Eq. (1-6)] in the shear-thickening fluid.

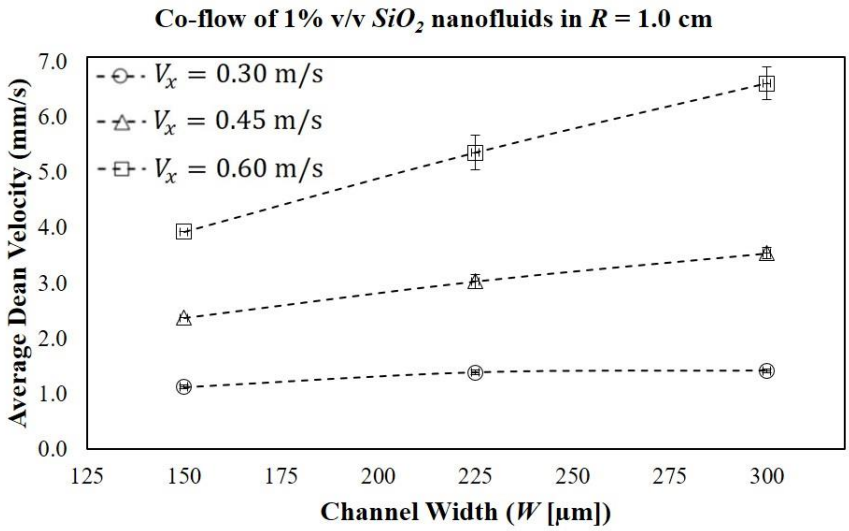

Figure 4-5: Representative experiments illustrating the effect of channel width (w), on V_{De} for the co-flows of SiO_2 nanofluids in curvilinear microchannels with channel height of h = 150 µm. Error bars are included for all data points but are not visible in cases of small errors. Reprinted with permission from AIP Publishing[122].

4.2.6 Non-dimensional Analysis towards an Empirical Correlation for V_{De}

To further illustrate the effects of the tested parameters in a non-dimensional form, the Dean velocity-based Reynolds number ($Re_{V_{De}} = V_{De}D_h/\vartheta$) for some of the experimental conditions presented in Figure 4-2 to Figure 4-5 was plotted as a function of Dean number (*De*), and the relative kinematic viscosity of the SiO_2 nanofluids ($\vartheta/\vartheta_{water}$). As shown in Figure 4-6a, increasing the Dean number at constant relative viscosities had a direct effect on $Re_{V_{De}}$. For instance, when the relative kinematic viscosity is equal to 9.56, increasing the Dean number from

0.059 to 0.084 (~1.4x) resulted in a ~2.2x increase in $Re_{V_{De}}$ from 2.87×10^{-3} to 6.43×10^{-3}. Therefore, we concluded that the Dean number has a direct effect on $Re_{V_{De}}$.

As illustrated in Figure 4-6b at constant Dean numbers, increasing the relative kinematic viscosity of SiO_2 nanofluids increased the Dean velocity-based Reynolds number. Here, when *De* = 0.087, a ~5.7x increase in the relative kinematic viscosity ($\vartheta/\vartheta_{water}$ =3.05 to 17.45) increased the $Re_{V_{De}}$ from 2.28×10^{-3} to 10.64×10^{-3} (~4.67x). Therefore, we concluded that the relative kinematic viscosity of SiO_2 solutions has a direct effect on $Re_{V_{De}}$.

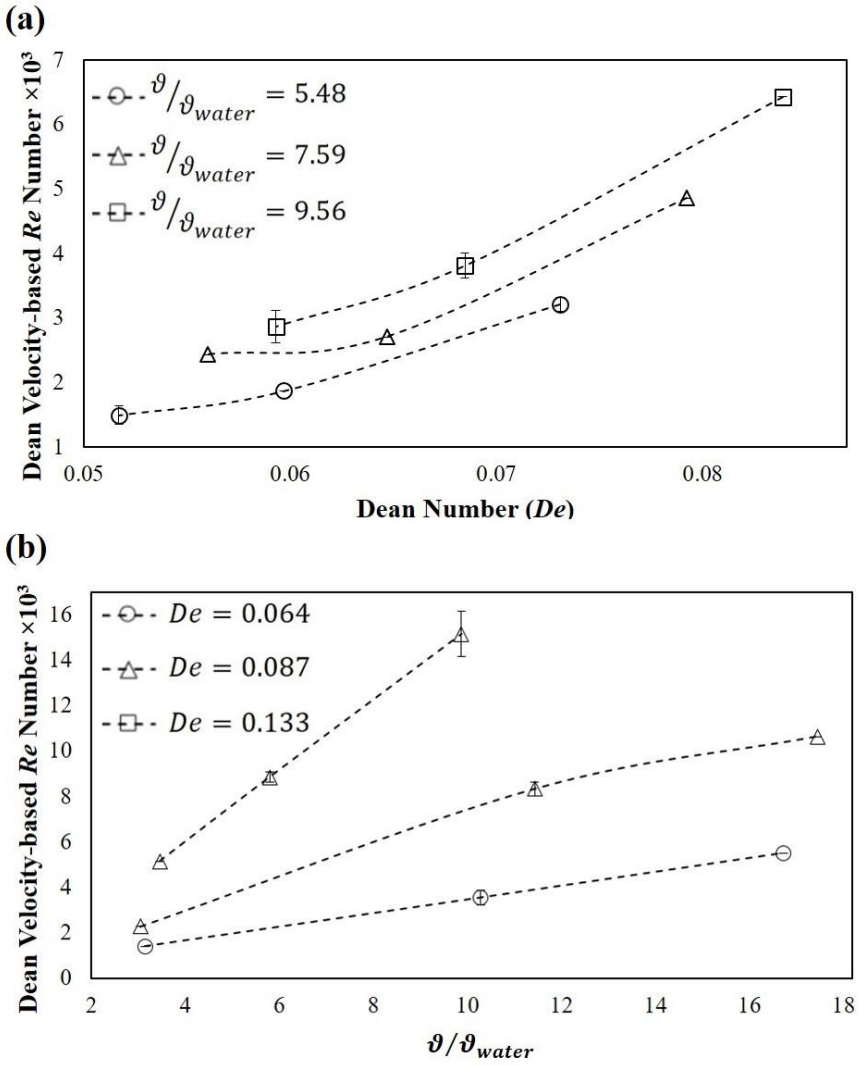

Figure 4-6: Dean velocity-based Reynolds number, $Re_{V_{De}}$, plotted against (a) Dean number and (b) relative kinematic viscosity ($\frac{\vartheta}{\vartheta_{water}}$) for SiO_2 nanofluid flows in curved microchannels. Error bars are included for all data points but are not visible in cases of small errors. Reprinted with permission from AIP Publishing[122].

Based on the experimental results of our investigation with representative cases shown in Figure 4-2 to Figure 4-6, and in order to illustrate the effect of channel dimensions (D_h, w, h, and R) and fluid characteristics (V_x and ϑ), we predicted that the Dean velocity based Reynolds number of shear-thickening SiO_2 nanofluids is a power function of the introduced non-dimensional groups

(in Figure 4-6) as $Re_{V_{De}} = aDe^{b}(\frac{\vartheta}{\vartheta_{water}})^{c}$. The above variables were changed in a wide range as already explained in the experimental procedure in chapter 2. In order to obtain the best fit, all experimental $Re_{V_{De}}$ values were plotted and different correlation constants *a*, *b*, and *c* were sought using MATLAB. As shown in Figure 4-7, the best fit was obtained with *a* = 0.08, *b* = 1.88, *c* = 0.90, with R^2 = 0.99 resulting in empirical correlations shown in Eq. (4-1) and Eq. (4-2).

$$Re_{V_{De}} = 0.08De^{1.88}(\frac{\vartheta}{\vartheta_{water}})^{0.90} \tag{4-1}$$

$$V_{De} = 0.08\,{}^{\vartheta}/_{D_h}\,De^{1.88}(\frac{\vartheta}{\vartheta_{water}})^{0.90} \tag{4-2}$$

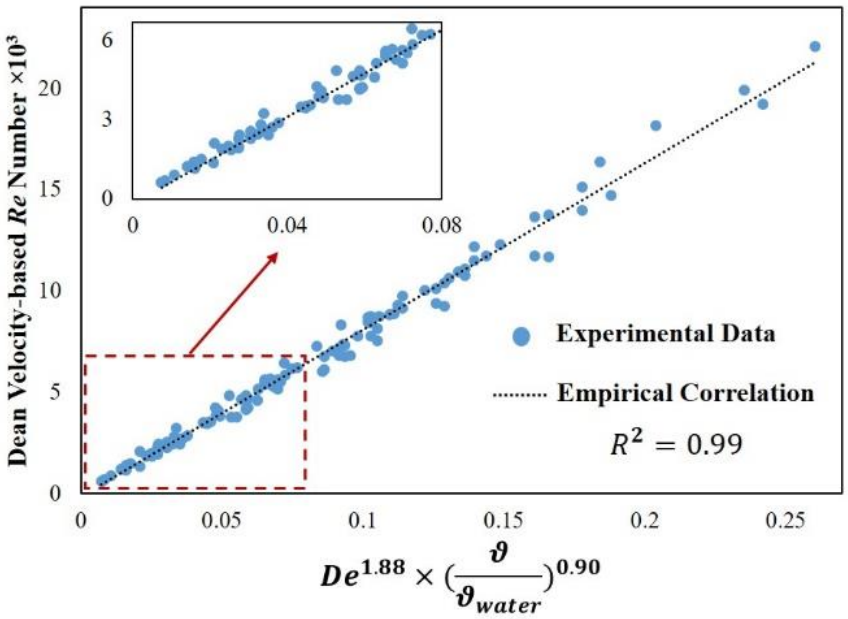

Figure 4-7: Dean velocity-based Reynolds number,$Re_{V_{De}}$, plotted against $(De)^{1.88} \times (\frac{\vartheta}{\vartheta_{water}})^{0.90}$ for all the experimental results from SiO_2 nanofluid flows in curved microchannels. Reprinted with permission from AIP Publishing[122].

Our empirical correlation in Eq. (4-2) could provide a precise prediction of the average Dean velocity of shear-thickening SiO_2 nanofluids in curved channels with an average error of 5.9% with respect to the experimental results. This correlation takes the effects of channel dimensions, fluid viscosity and density, and flow velocity into consideration and may be applicable to other shear-thickening fluids within curved microchannels. Here, applying the previous empirical correlations for Newtonian fluids [Eq. (1-17) in chapter 1 from Ref.[52]] and for viscoelastic liquids [(Eq. (3-2) in chapter 3 from Ref.[123]] will result in estimation of V_{De} with errors in the range of 85%-90%. This clearly supports our hypothesis that a new correlation for shear-thickening nanofluids is needed for future particle focusing and sorting studies in these fluids. Similar to chapter 3, the sources of uncertainty could be addressed in the future investigations.

4.3 Conclusion

In summary, we tested different concentrations of SiO_2 nanofluids in curved microchannels with different aspect ratios and radii of curvatures, and obtained an empirical correlation for the average V_{De} of shear-thickening SiO_2 solutions. Our new correlation successfully captures the effects of channel dimensions and fluid kinematic viscosity and axial velocity, providing a precise prediction of average V_{De} with an average error of 5.9%. Our developed correlation could enable a better control on particle manipulation and solution exchange in shear-thickening liquids in future applications. Others can expand our study in the future to improve our correlation with numerical methods and investigate its application for a wider range of shear-thickening fluids.

Chapter 5

5 Investigation of Microparticle Focusing in Shear-Thinning Viscoelastic PEO Flows in Curved Microchannels*

In this chapter, we investigated the particle migration and their focusing behavior in a co-flow of viscoelastic fluids in curvilinear microchannels with different widths, heights, and radii of curvature. The effects of flow axial velocity, fluid viscoelasticity, and particle size were also studied using various concentrations of PEO in water (Obj. 2). Particle lateral migration alongside the channel width was also quantified under the effects of inertial lift, elastic, and Dean drag forces. A non-dimensional analysis was used to categorize the particle focusing behavior according to the

* Contents of this chapter have been submitted to the *Soft Matter* journal and is currently under review.

strength of secondary vortices and the fluid viscoelasticity. Finally, a proof-of-concept demonstration of a duplex particle separation and washing process is presented based on the developed knowledge in this chapter (Obj. 3).

5.1 Introduction

The coupled effect of Dean flow and elastic force could accelerate the particle focusing in curved channel viscoelastic flows. The new particle equilibrium positions would highly depend on the viscoelastic properties and microchannel geometry. As previously reviewed in chapter 1, there are still gaps for examining the effects of particle size and polymer concentration at higher flow rates (e.g., up to 2 ml/min) on particle dynamics in curvilinear microchannels with constant radius along the channel. This will allow us to understand the effects of fluid rheology and speed, particle size, and channel width, height, and radius of curvature on particle focusing. Non-dimensional analysis of these effects can also add novelty and scientific value, while making the outcomes useful for others in the field. Here, we report the effects of channel width, height and radius of curvature, fluid viscosity, and particle size on microparticle migration in a co-flow of viscoelastic PEO solutions inside curvilinear microchannels.

As presented in chapter 3, we experimentally studied the effects of channel geometry and fluid properties on the Dean velocity of shear-thinning PEO in water solutions[123]. A modified empirical correlation was reported with a precise estimation of V_{De} in the viscoelastic PEO solutions [Eq. (3-2)]. The V_{De} correlations can be used to design microfluidic devices for particle manipulation and solution exchange in Newtonian and viscoelastic fluids inside curvilinear microchannels.

As mentioned before, particles in microchannels are under the effects of inertial lift, drag and elastic forces. We showed earlier that the net inertial lift forces could be scaled as[38]:

$$F_L \sim \rho a^4 \left(\frac{V_x}{D_h}\right)^2 \sim \rho a^4 V_x^2 \left(\frac{w+h}{wh}\right)^2 \quad (5\text{-}1)$$

Moreover, the Dean drag [F_D in Eq. (1-12)] acting on the particles in a curvilinear microchannel is a direct function of V_{De}. Here, V_{De} could be estimated using our reported empirical correlation for viscoelastic fluids in Eq. (3-2). Thus, the Dean drag could be scaled as:

$$F_D \sim a\mu^{0.1}\rho^{0.9}\frac{V_x^{1.9}D_h^{1.9}}{R^{0.95}} \sim a\mu^{0.1}\rho^{0.9}\frac{V_x^{1.9}}{R^{0.95}}\left(\frac{w+h}{wh}\right)^{1.9} \quad (5\text{-}2)$$

In non-Newtonian fluids, the elastic lift force [F_E in Eq. (1-22)] acting on the particles in rectangular microchannels scales as[38]:

$$F_E \sim a^3 Wi\dot{\gamma}^2 \sim a^3\lambda\left(\frac{V_x}{D_h}\right)^3 \sim a^3\lambda V_x^3\left(\frac{w+h}{wh}\right)^3 \quad (5\text{-}3)$$

The equations above have been used in this chapter to investigate the particle migration in curved microchannels under the coupled effect of Dean drag and elasto-inertial forces.

Our curved channel microdevices consisted of two inlets to supply the co-flow of PEO solutions, i.e., one with particles (inlet-I) and one clean buffer (inlet-O), into a 300° curvilinear channel with a constant radius of curvature as shown in Figure 5-1b. As illustrate in Figure 5-1a straight microchannels with similar length (~5.23 cm), and three different cross sections (150×75 μm^2, 150×150 μm^2, and 150×225 μm^2) were also tested for a comprehensive comparison between curved and straight channels. Experimental procedure and data analysis were carried out as previously explained in sections 2.5 and 2.8.

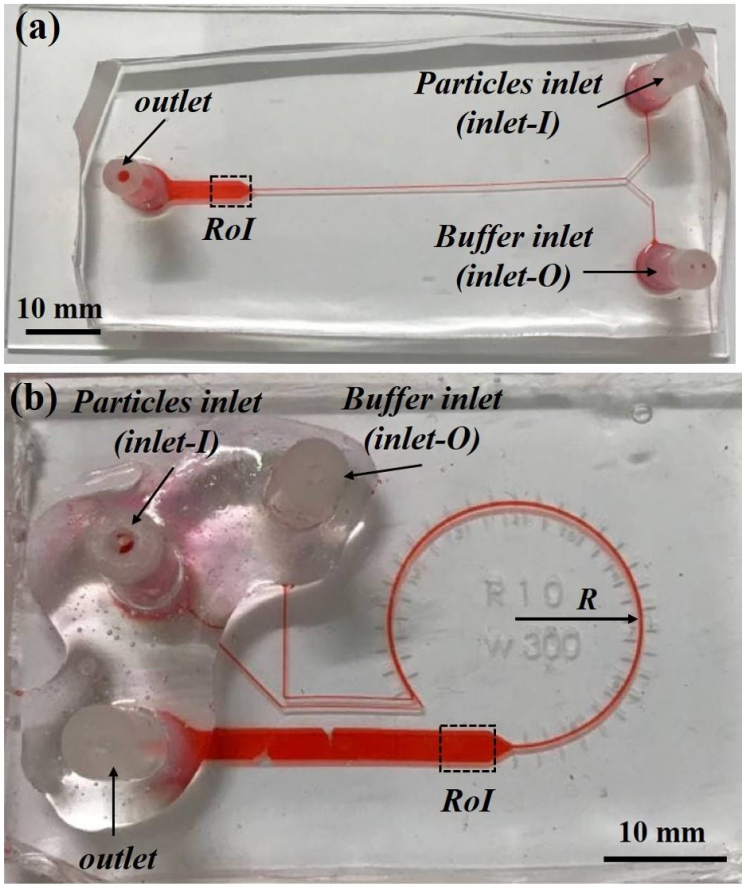

Figure 5-1: Microfluidic device for particle focusing investigation in PEO solution. Microchannel design with two inlets for the particles (inlet-I), and the buffer solution (inlet-O), and one expanded outlet with a width of 2.55 mm. (a) Straight microchannel with a channel length of ~ 5.23 cm, and (b) curvilinear channel with a constant radius of curvature (R). The representative microchannel shown in (b) consists of a 300° curvature with a cross section of w×h = 300 × 150 μm² and R = 1.0 cm.

5.2 Results and Discussion

Particle migration under the combined effects of Dean drag, inertial, and elastic forces in curvilinear channels was investigated for three different particle sizes (~10, 15, and 22 μm) inside co-flows of various concentrations of PEO solutions (0, 500, 1000, and 2000 ppm). Straight (Figure 5-1a) and curvilinear (Figure 5-1b) microchannels with different cross sections and radii

of curvature were used to study the effects of channel curvature and aspect ratio. As mentioned in the section 2.82.8, particle trajectories at the outlet were used to draw the normalized number of particles alongside their normalized lateral position, to identify the number of focusing peaks, peak centroids (PCs) and the FWHMs, representing particles distribution bands, for each experiment.

We started our investigations with a straight microchannel with two inlets to obtain an understanding about the effect of PEO in our devices. As shown in Figure 5-2a, inside a square (150 ×150 μm^2) straight microchannel at an axial velocity of V_x = 0.222 m/s, the 15 µm particles in DI water ended up close to the inner side of the outlet (i.e., where they were initially supplied) with the peak centroid located at PC_a = 0.81 and FWMH = 0.06. Upon introduction of the elastic force with a 1000 ppm PEO carrier solution (*El* = 0.76), the peak centroid moved closer to the channel center (PC_b = 0.65) without any significant change in the FWHM=0.07, as shown in Figure 5-2b. Here the particles in DI water were partially focused (~86% within the ±0.1 peak bandwidth) and fully focused inside the 1000 ppm PEO with ~90% of the particles within the ±0.1 bandwidth around the PCs.

The addition of Dean drag with a curvilinear microchannel scattered the particle trajectories inside the DI water. As illustrated in Figure 5-2c for the 15 µm particles in a square (150 ×150 μm^2) channel with *R* = 1.0 cm, fluid recirculation (~ 3.1 fluid switches with *De* = 3.21) dispersed the particles at the outlet with PC_c = 0.75, FWHM=0.09, and only ~54% of particles within the ±0.1 peak bandwidth (no focusing). However, as shown in Figure 5-2d, the Dean drag (~0.8 fluid switches with *De* = 1.72) transferred the particles inside the 1000 ppm PEO (*El* = 0.76) towards the outer wall (PC_d = 0.13, FWHM=0.05), while elasto-inertial effects helped with more than 99% of particles focusing within the ±0.1 bandwidth around the peak centroid (full focusing).

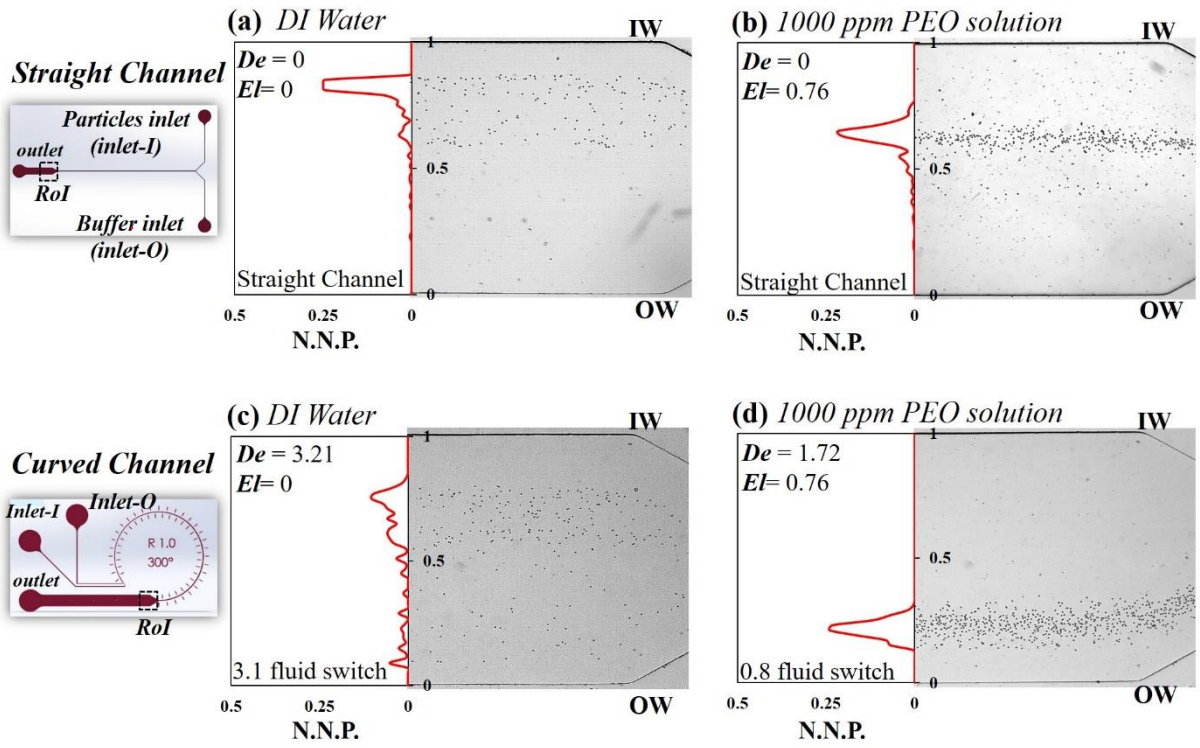

Figure 5-2. Particle trajectories and normalized number of particles (NNP) across the RoI of the channels for 15 µm particles at an axial velocity of V_x = 0.222 m/s inside square microchannels (150 × 150 µm^2). Particles were co-flown alongside a clean buffer inside a straight channel in (a) DI water and (b) 1000 ppm PEO solution, and inside a curved channel with R = 1.0 cm in (c) DI water, and (d) 1000 ppm PEO solution.

Representative experiments* in the following sections are used to illustrate the effects of fluid axial velocity, PEO concentration, channel radius of curvature, width, and height, and the particle size on the focusing behavior of microparticles.

5.2.1 Effect of Fluid Axial Velocity (V_x)

Microparticle trajectories were examined over a wide range of axial velocities between 0.037 < V_x < 0.74 m/s. In a representative case for 10 µm particles in 1000 ppm PEO solution inside a

* Full set of experimental results are presented in Appendix E.

square microchannel (150 ×150 μm^2) with R = 1.0 cm, particle lateral distributions alongside the channel width at the outlet are presented in Figure 5-3. At the lowest axial velocity of V_x = 0.037 m/s (*De* = 0.23, *El* = 0.95), microparticles were fully focused close to the channel center (PC = 0.58) with FWHM = 0.14. As the axial velocity increased, the peak centroids moved towards the outer wall (PC = 0.45, 0.25, 0.13, and 0.07 for V_x = 0.074, 0.148, 0.222, and 0.37 m/s, respectively). Here, with a slight change in the Elasticity number (from 0.95 to 0.74), the increase in the *De* number (from 0.23 to 2.97), and the fluid recirculation (from 0.1 switch to 1.3 switches) dominated the particle migration towards the outer wall. Meanwhile, the quality of focusing was enhanced within flow streams (FWHM was decreased) due to the enhanced elasto-inertial effects at higher axial velocities. Upon further increase in the *De* number, i.e., *De* = 2.97 and 5.87 at V_x = 0.37 and 0.74 m/s, respectively, Dean drag contribution became a lot more significant and disturbing to focusing similar to previous reports[88–91]. Here, microparticles were partially focused at V_x = 0.37 m/s (~79% within the ±0.1 bandwidth), and not focused at V_x = 0.74 m/s with two weak peaks at PC = 0.08 and 0.78. It appears that at the two highest axial velocities, the elasto-inertial effects still pushed the particles to stay focused close to the outer wall while the enlarged Dean drag force pushed them to continue recirculating in the channel, hence resulting in focusing disturbance at the maximum axial velocity. Overall, in these cases, the Dean drag remained the dominant force for all axial velocities ($F_D > F_L$ and $F_D > F_E$); therefore, the particles were entrained with the secondary vortices. As the fluids and particles surpassed the first switch at V_x = 0.74 m/s, microparticles were dispersed alongside the channel width due to opposition between the drag and elasto-inertial forces.

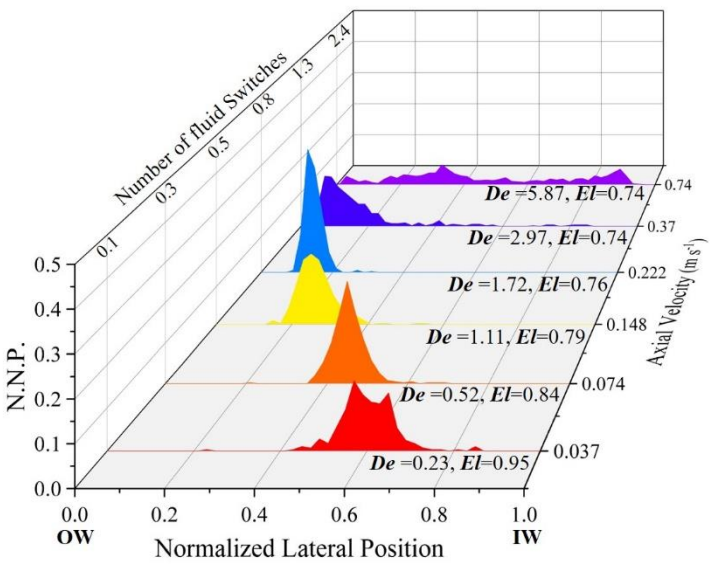

Figure 5-3. Normalized number of particles alongside their normalized lateral position for 10 µm particles in 1000 ppm PEO inside a square microchannel (150 ×150 µm^2) with R = 1.0 cm at various axial velocities.

5.2.2 Effect of Fluid Viscoelasticity (PEO Concentration)

To investigate the effect of fluid viscoelasticity, microparticle trajectories were examined in different concentrations of PEO solutions in water (0, 500, 1000, and 2000 ppm). As an example, for a co-flow of 15 µm particles at V_x = 0.37 m/s inside the square microchannel (150 × 150 µm^2), with the radius of curvature R = 1.0 cm, the normalized number of particles alongside their normalized lateral position are presented in Figure 5-4. In DI water (De = 5.34, El = 0), microparticles were dispersed close to the channel inner wall (PC = 0.75, FWHM = 0.04), with only ~58% of the particles within the ±0.1 peak bandwidth. Here, lift forces and the Dean drag are comparable (F_L ~ 1.7 F_D), and microparticles are scattered after the second fluid switch inside the channel. Upon addition of fluid viscoelasticity at 500 ppm PEO (De = 3.48, El = 0.4), microparticles were transferred towards the outer wall (PC = 0.09, FWHM = 0.05). However, since the elastic force was smaller compared to the lift force and the Dean drag, particle migration was

dominated by the fluid recirculation (~ 1.5 fluid switches), and particles were not focused (~48% within the ±0.1 peak bandwidth). As the PEO concentration increased to 1000 ppm (*De* = 2.97, *El* = 0.74), the elastic force became comparable to the Dean drag and ~87% of particles were focused around the peak centroid at PC = 0.07 with FWHM = 0.04 after ~ 1.3 fluid switches inside the channel. A further increase in the PEO concentration to 2000 ppm (*De* = 2.0, *El* =1.72), kept the particles close to the outer wall with ~90% of particles focused around the PC = 0.09 under the dominant effect of the elastic force. Therefore, we concluded that the addition of the elastic force at higher PEO concentrations could control the particle migration while reducing the fluid recirculation and the effect of the Dean drag.

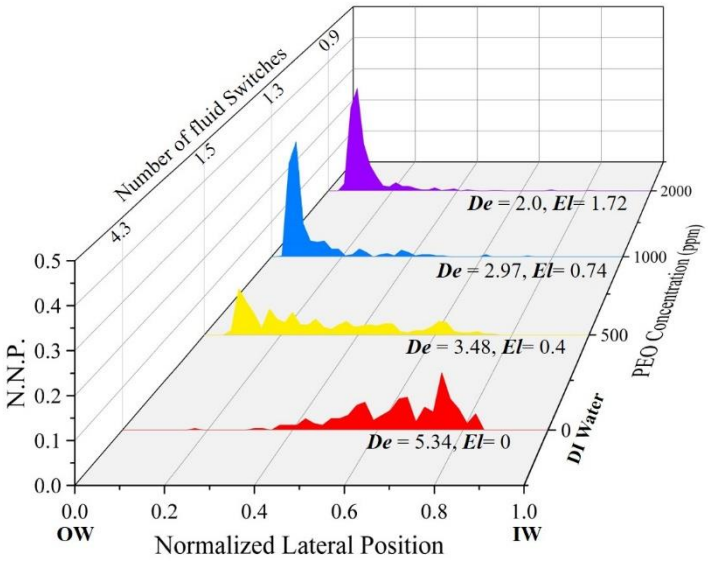

Figure 5-4. Normalized number of particles alongside their normalized lateral position for 15 µm particles in a square microchannel (150 ×150 µm^2) with R = 1.0 cm in DI water, and 500, 1000, and 2000 ppm PEO at V_x = 0.37 m/s.

5.2.3 Effect of Channel Radius of Curvature (*R*)

In order to study the effect of channel curvature, microparticles migration was examined in square microchannels (150 × 150 µm^2) with different radii of curvatures of *R* = 1.0, 1.5, and 2.0

cm. In a representative experiment, 15 µm particles were co-flown in 500 ppm PEO solution alongside a clean buffer inside a straight (R→∞) and the above curvilinear microchannels (*El* = 0.4). As shown in Figure 5-5, at an axial velocity of V_x = 0.37 m/s inside the straight microchannel (*De* = 0), particles were partially focused (~81%) around the peak center of PC = 0.63 with a FWHM = 0.10 under the dominant effect of the lift force ($F_L > F_E$). The introduction of channel curvature with *R* = 2.0 cm (*De* = 4.9), resulted in ~ 1.4 fluid recirculation and fully focused the particles close to the outer wall with more than 99% of particles around the peak centroid PC = 0.11 with FWHM = 0.04. At a lower radius of curvature of *R* = 1.5 cm (*De* = 5.7), particles remained focused close to the outer wall (PC = 0.15, FWHM = 0.07) under the dominance of lift forces despite the fluid recirculation (~ 1.9 fluid switches). A further increase in the Dean drag at a lower *R* = 1.0 cm (*De* = 7.0) dispersed the particles alongside the channel width after ~ 2.7 fluid switches, with only ~ 41% of particles within the ±0.1 bandwidth around the peak centroid (PC = 0.09, FWHM =0.05). Here, the Dean drag facilitated the particle focusing at higher radii of curvatures, and disrupted the particle distribution at smaller curvatures (i.e., higher *De* numbers).

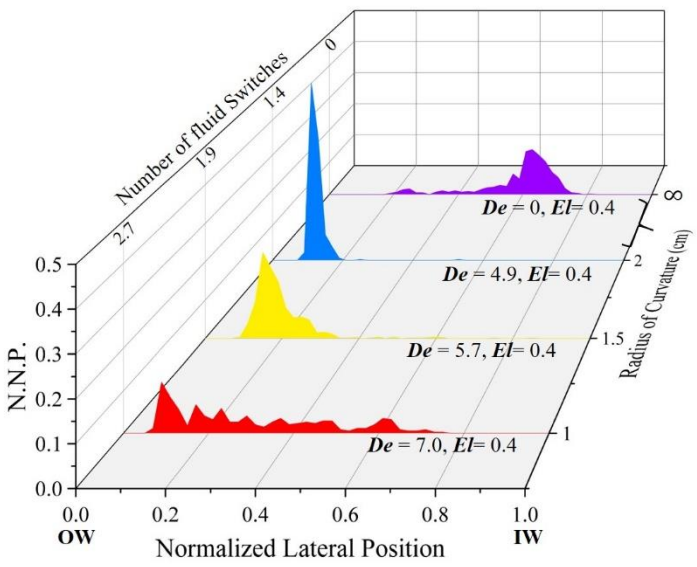

Figure 5-5: Effect of radius of curvature on normalized number of particles alongside the channel outlet. Representative experiments are shown for 15 µm particles at an axial velocity of V_x = 0.37 m/s in co-flow of 500 ppm PEO solution inside the straight and curved microchannels with R = 1.0, 1.5, and 2.0 cm with a square cross section (150×150 µm^2).

5.2.4 Effect of Channel Width (*w*)

To investigate the effect of channel width on the particle migration, microparticles were co-flown alongside a clean buffer in curved channels with various channel widths of w = 150, 225, and 300 µm, at a constant height of h = 150 µm, and a constant radius of curvature of R = 1.0 cm. In a representative experiment, the outlet distributions for the 15 µm particles inside 500 ppm PEO solutions at an axial velocity of V_x = 0.222 m/s are shown in Figure 5-6. In the square microchannel (150 × 150 µm^2), particles were dispersed close to the channel outer wall (PC = 0.27, FWHM = 0.14) under the dominant effect of the lift forces ($F_L > F_D$, De = 2.08, El =0.4) with only ~ 57% of particles within the ±0.1 bandwidth around the peak centroid (no focusing). As the channel width increased, the elastic forces [$F_E \sim (\frac{w+h}{w\times h})^3$ in Eq. (5-3)] declined at a faster pace compared to the lift [$F_L \sim (\frac{w+h}{w\times h})^2$ in Eq. (5-1)] and the Dean drag [$F_D \sim (\frac{w+h}{w\times h})^{1.9}$ in Eq. (5-2)] forces. Here, with a

channel width of w = 225 µm (De = 2.73, El =0.28), the Dean drag dominated the particle migration with ~ 72% of the particles in the ±0.1 bandwidth around the peak centroid at PC = 0.13, and FWHM = 0.04. When the channel width increased to w = 300 µm (De = 3.17, El =0.23), the stronger Dean drag focused the particles close to the outer wall with ~ 91% of particles within the bandwidth around the PC = 0.27, and FWHM = 0.08. We concluded that when El < 1, increasing the channel width resulted in the dominance of the Dean drag and entrained the particles with the secondary vortices towards the channel outer wall (fluid switches ≤ 1).

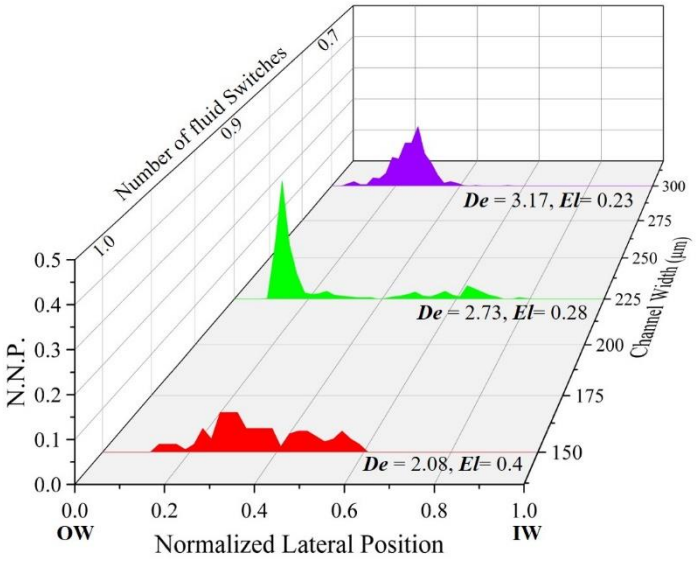

Figure 5-6: Effect of channel width on normalized number of particles alongside the channel outlet. Representative experiments are shown for 15 µm particles at an axial velocity of V_x = 0.37 m/s in co-flow of 500 ppm PEO solution inside a curved microchannel with h = 150 µm, R = 1.0 cm, and various channel widths of w = 150, 225, and 300 µm.

5.2.5 Effect of Channel Height (*h*)

The effect of channel height was investigated using three different channel heights of h = 75, 150, and 225 µm at a constant width of w = 150 µm with a channel curvature of R = 1.0 cm. As shown in Figure 5-7, particle distributions alongside their lateral position are presented for 15 µm

particles in 1000 ppm PEO solutions at an axial velocity of V_x = 0.37 m/s. For h = 75 µm (De = 1.64, El =1.63), the particle migration is dominated by the coupled effect of the lift and elastic forces ($F_L \approx 1.2 \times F_E \approx 7.7 \times F_D$). At h = 75 µm, particles are fully focused (more than 99%) around the peak centroid of PC = 0.19 with FWHM = 0.03. As the channel height increased to h = 150 µm (De = 2.97, El =0.74), the lift and elastic forces experienced a faster decline compared to the Dean drag ($F_L \approx 1.8 \times F_E \approx 1.6 \times F_D$). Here, around 87% of the particles could be found within the ±0.1 bandwidth around the peak centroid at PC = 0.07 with a FWHM = 0.04 (i.e., partially focused). At the largest channel height of h = 225 µm (De = 3.86, El =0.52), the Dean drag became the dominant force governing the particle migration ($F_L \approx 6.7 \times F_E \approx 0.8 \times F_D$) after the faster decline in the lift and elastic forces. As illustrated in Figure 5-7, the particles were entrained with the secondary vortices (~ 1.6 fluid switches) and scattered alongside the outlet width with ~ 63% of them within the ±0.1 bandwidth around the peak center at PC =0.27 with FWHM = 0.07. Therefore, increasing the channel height resulted in the faster decrease in the lift and elastic forces (i.e., decrease in El number), and the particle migration was governed by the fluid recirculation inside the channel under the effect of the Dean drag.

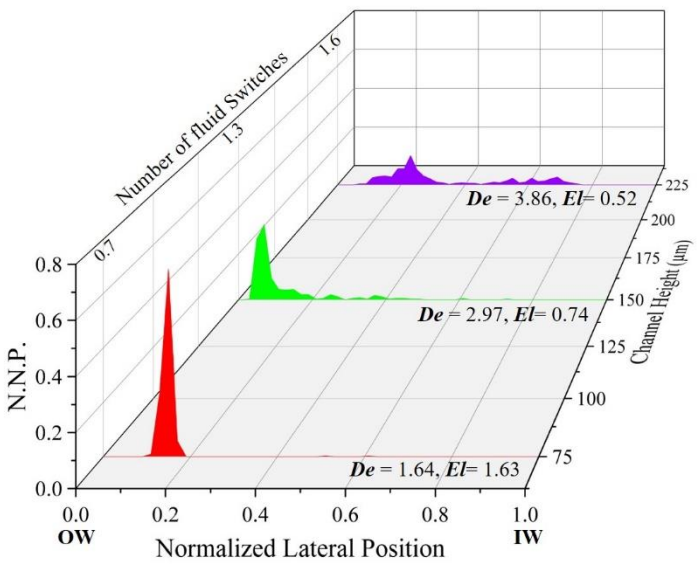

Figure 5-7: Effect of channel height on normalized number of particles alongside the channel outlet. Representative experiments are shown for 15 µm particles at an axial velocity of V_x = 0.37 m/s in co-flow of 1000 ppm PEO solutions inside a curved microchannel (w = 150 µm) with R = 1.0 cm, with various channel heights of h = 75, 150, and 225 µm.

5.2.6 Effect of Microparticle Size (*a*)

Finally, the effect of particle size was investigated using three different particle sizes of a = 10, 15, and 22 µm. As a representative experiment, particle distributions alongside the channel width in 500 ppm PEO solution at an axial velocity of V_x = 0.222 m/s in a curved channel with a 225 × 150 µm^2 cross section with R = 1.0 cm, are presented in Figure 5-8. Here, the co-flow of 500 ppm PEO solutions resulted in ~ 0.9 fluid recirculation with a *De* = 2.73, and *El* = 0.28, which indicated the stronger lift forces compared to the elastic forces. The smaller 10 µm particles (β = 0.06), were pushed towards the outer wall (PC = 0.15, FWHM = 0.12) under the dominant effect of the lift force and the Dean drag. Here, only ~ 70% of the smaller particles were within the ±0.1 bandwidth around the PC = 0.15 and the particles were partially focused. As the particle size increased to a = 15 µm (β = 0.08), the lift ($F_L \sim a^4$) and elastic ($F_E \sim a^3$) forces increased faster compared to the

Dean drag ($F_D \sim a$) and dominated the particle migration. As shown in Figure 5-8, approximately ~ 72% of the 15 µm particles were within the ±0.1 bandwidth around the peak centroid of PC = 0.13, with a narrower distribution (FWHM = 0.04) compared to smaller particles. Upon further increase in the particle size up to 22 µm (β = 0.12), the lift and elastic forces governed the particle focusing around the PC = 0.15 (FWHM = 0.05), with ~ 96% of the particles within the defined bandwidth. Therefore, we concluded that increasing the particle size amplifies the dominance of the lift and elastic forces compared to the Dean drag and results in a more focused particle distribution alongside the channel width.

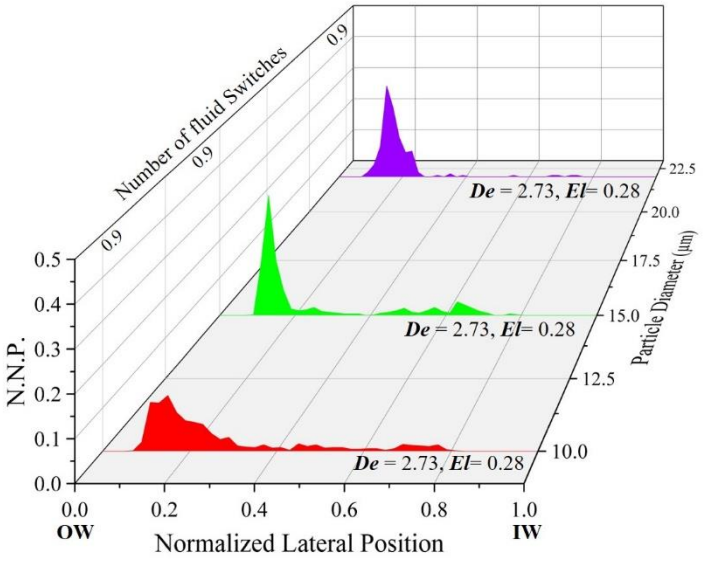

Figure 5-8. Effect of particle size on normalized number of particles alongside the channel outlet. Representative experiments are shown for three different particle sizes of 10, 15, 22 µm microparticles in co-flow of 500 ppm PEO solutions at V_x = 0.222 m/s inside a microchannel with a 225 × 150 µm^2 cross section and R = 1.0 cm.

5.2.7 Non-dimensional Analysis

Overall, more than 400 different experiments in co-flows of PEO solution were carried out to investigate the effects of flow axial velocity, channel width, height and radius of curvature, fluid viscoelasticity, and particle size on the particle migration in curved channels with only 25 representative cases shown in the results sections above. The results for all different experiments could be found in Appendix E. To comprehensively depict the effects of tested parameters on the particle migration, our experimental results were categorized into four groups of fully focused particles (single peak), partially focused particles, no focusing, and two peak focusing alongside the channel width as described in the methods section. As shown in Figure 5-9 for all of our experiments, the blockage ratio (β) could be plotted against the Dean (De) and Weissenberg (Wi) numbers, which represent the strength of secondary vortices, and the fluid viscoelasticity, respectively. As illustrated in Figure 5-9a, for a confined range of blockage ratios ($0.08 < \beta < 0.12$) and Dean numbers ($De \leq 2$), a full focusing behavior was observed. Moreover, for stronger Dean vortices ($3.5 < De < 20$), our experiments mainly resulted in particle dispersion alongside the channel width (i.e., no focusing with one or two peaks), which indicated the disruptive effect of the strong Dean drag forces on particle focusing.

As shown in Figure 5-9b, for a limited range of blockage ratio ($0.08 < \beta < 0.12$) and Weissenberg ($0.5 < Wi < 13$), a fully focused particle distribution was spotted in our experiments. Furthermore, we observed that stronger elastic forces ($63 < Wi < 240$) largely resulted into a no focusing particle behavior (either with one or two peaks) for the investigated size range of particles. Therefore, this classification of our experimental data could specify practical conditions to achieve a full particle focusing in the elasto-inertial particle sorting and washing devices.

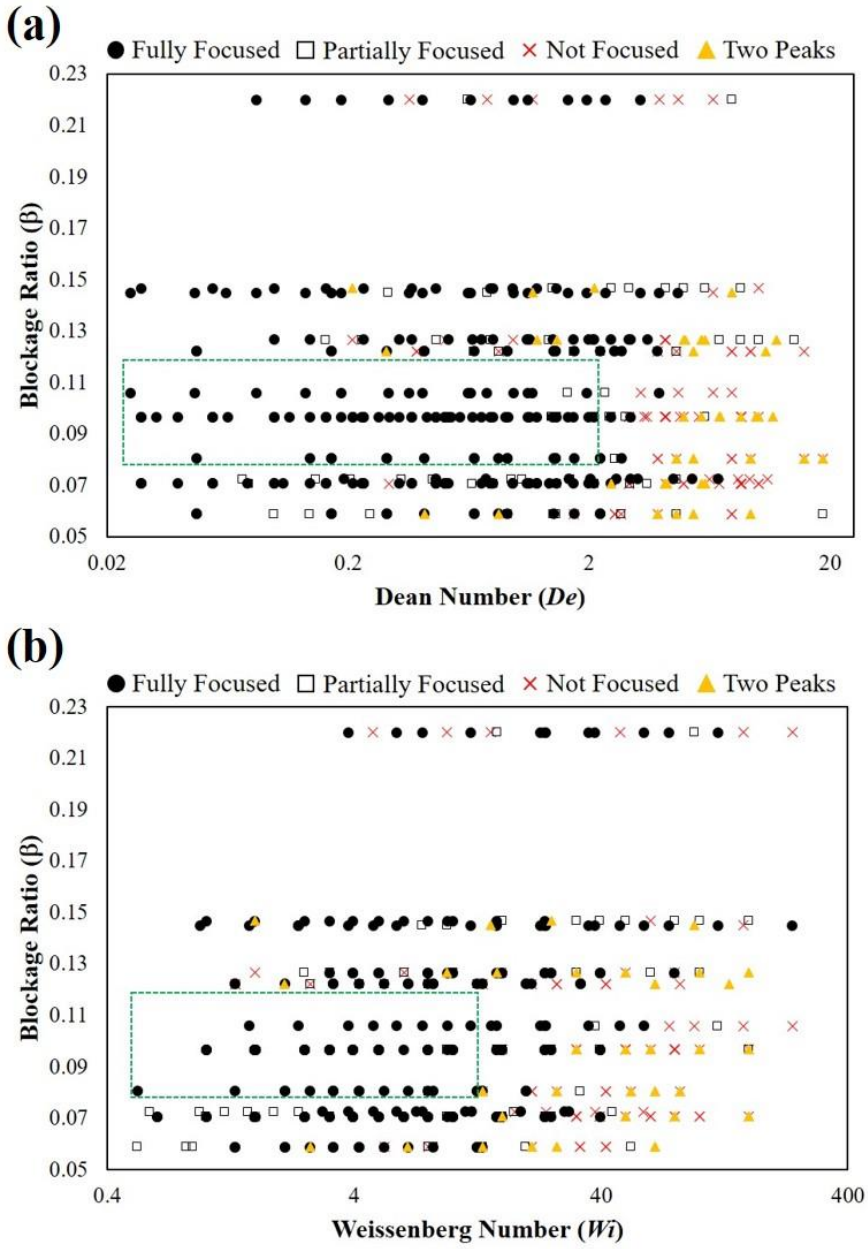

Figure 5-9. Channel blockage ratio, β, plotted against (a) Dean number and (b) Weissenberg number for different particle focusing behaviors tested using PEO solutions in our curved channel devices.

5.2.8 Demonstration of Duplex Particle Washing Process

Utilizing the developed knowledge on the particle focusing behavior in PEO solution, here we present a demonstration of a duplex particle separation and simultaneous washing process. As

previously explained in chapter 1, diluted concentrations of PEO solutions could be used to simulate rheological characteristics of bodily fluids such as blood plasma and saliva[100,142,143]. Moreover, various particle sizes have been reported as surrogates for the biological samples. For instance, 5 μm and 15 μm microparticles have been used to imitate the presence of red and white blood cells, respectively[100].

In this section two different particle sizes of 5 μm and 15 μm were used to demonstrate the particle separation and washing process in 500 ppm PEO solutions inside a curved microchannel. Initially, we investigated the singleplex particle behavior analysis in a curved microchannel with a 150 × 75 μm^2 cross section and R = 1.0 cm. Representative experiments for 5 μm and 15 μm particles are shown in Figure 5-10 at three different axial velocities of V_x = 0.3, 0.74, and 1.2 m/s. These axial velocities correspond to an approximate 1, 2, and 3 fluid switches inside the microchannel, respectively.

As illustrated in Figure 5-10a, at an axial velocity of V_x = 0.3 m/s (De = 1.56, El = 0.86) the smaller 5 μm (β = 0.05) were initially entrained with the Dean vortices towards the outer channel wall under the dominant effect of Dean drag ($F_D \approx 2.5 \times F_L \approx 3 \times F_E$). Here, approximately ~ 60% of particles could be found within the defined bandwidth around the peak center of PC = 0.09. As the axial velocity increases to V_x = 0.74 m/s (De = 3.91, ~ 2 fluid switches), and V_x = 1.2 m/s (De = 6.25, ~ 3 fluid switches), the increased strength of the Dean vortices results in the dispersion of 5 μm particles across the channel width with no apparent peaks (no focusing). Therefore, we concluded that for the smaller 5 μm particles, the Dean drag dominates the particle focusing behavior inside our curved microchannel.

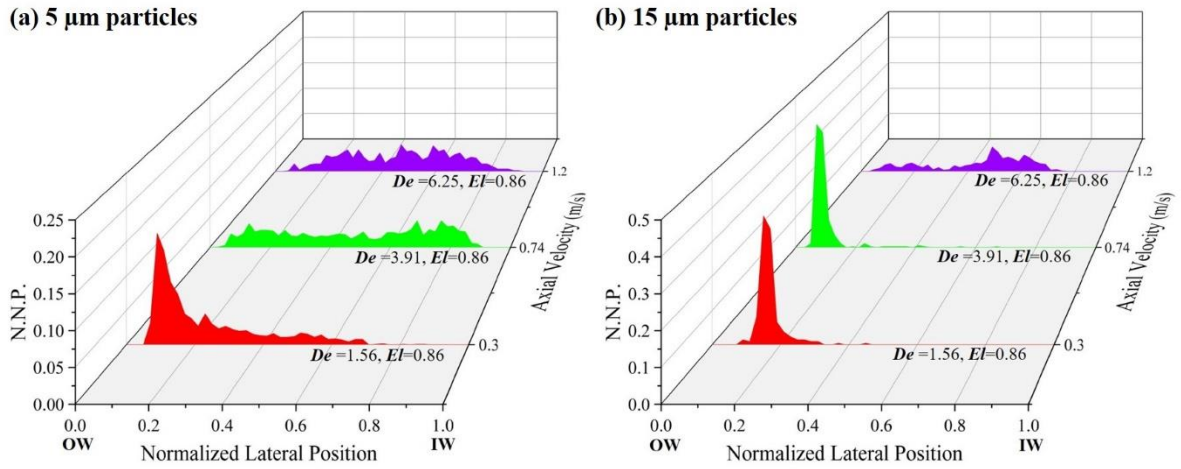

Figure 5-10: Effect of axial velocity on normalized number of particles alongside the channel outlet. Representative experiments are shown for (a) 5 µm, and (b) 15 µm particles inside a co-flow of 500 ppm PEO solutions in a curved microchannel with a 150 × 75 µm^2 cross section and R = 1.0 cm.

For the larger 15 µm particles (β = 0.15), the net inertial lift forces control the particle migration across the channel width at low and moderate axial velocities ($F_L \approx 4\times F_E \approx 8\times F_D$). As shown in Figure 5-10b, at V_x = 0.3 m/s (*De* = 1.56, ~ 1 fluid switch), 15 µm particles are pushed towards the outer wall with ~ 96% of the particle within the ±0.1 bandwidth around PC = 0.15 (full focusing). As the axial velocity increases to V_x = 0.74 m/s (*De* = 3.91, ~ 2 fluid switches), particles remained fully focused around the PC = 0.07. However, further increase in the axial velocity to V_x = 1.2 m/s (*De* = 6.25, ~ 3 fluid switches) resulted in the microparticle dispersion alongside the channel width, where only ~ 50% of particles were found around PC = 0.49. Hence, the dominant F_L could be used to focus 15 µm particles close to the channel outer wall before the Dean drag scatters them at V_x = 1.2 m/s.

Based on the singleplex experiments above, a particle separation and simultaneous washing process could be implemented for a co-flow of 500 ppm PEO solutions at an axial velocity of V_x = 0.74 m/s (*De* = 3.91, *Wi* = 47.8), where larger 15 µm particles are transferred towards the channel

outer wall, and the approximate 2 fluid switches would enable the solution exchange at the outlet. For the duplex particle investigation, a new microchannel was designed with tri-furcate outlets as illustrated in Figure 2-3. Here, 5 µm and 15 µm particles were supplied inside the microchannel with a total concentration of 2×10^5 particles/ml through inlet-I, alongside a clean buffer in inlet-O at a total flow rate of Q_t = 0.5 ml/min (V_x = 0.74 m/s),. Approximately, 1 ml of solutions were collected from three different channel outlets (outlet-I, outlet-M, and outlet-O in Figure 2-3). Microparticle collection efficiencies [Eq. (2-8)] were calculated as previously explained in section 2.8.

As presented in Figure 5-11 at an axial velocity of V_x = 0.74 m/s, under the dominant effect of inertial and elastic forces ($F_L \approx 3.7 \times F_E \approx 8.5 \times F_D$), 97.0 ± 1% of 15µm particles could be collected close to the outer wall from outlet-O, and only 3.0 ± 1% of the larger 15µm ended up in outlet-M. However, the smaller 5 µm particles were scattered alongside the channel width under the dominant effect of Dean drag ($F_L \approx 1.4 \times F_E \approx 0.5 \times F_D$). Here, 32.7 ± 3.5 % of smaller particles were collected at outlet-O, while 36.9 ± 2%, and 30.4 ± 1.5% were found in outlet-M and outlet-I, respectively. Therefore, the collected sample from outlet-O yields an average separation purity of 74.8% according to Eq. (2-9).

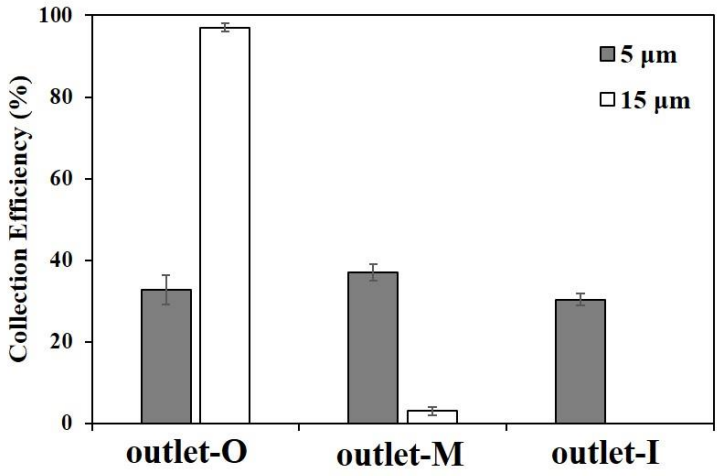

Figure 5-11: Collection efficiencies at different outlets for 5 µm and 15 µm particles in a co-flow of 500 ppm PEO solutions at a total axial velocity of V_x = 0.74 m/s inside a curved microchannel with a 150 × 75 µm^2 cross section with R = 1.0 cm. Error bars indicate the standard deviation of two experiments, with three separate measurements, respectively.

The quality of the solution exchange at the channel outlet was also investigated according to sections 2.6 and 2.7. Figure 5-12 demonstrates the co-flow of 500 ppm PEO solutions at an axial velocity of V_x = 0.74 m/s inside our curved microchannel with tri-furcate outlets (Figure 5-12a). Here, the dyed solution (with 10% v/v trypan blue) was supplied through the inlet-I, alongside a clean buffer in inlet-O. Co-flow images at the channel entrance [A-A´ in panel (a)], middle section [B-B´ in panel (a)], and channel outlet [C-C´ in panel (a)] are presented in Figure 5-12b. Color intensity measurements in Figure 5-12c demonstrate two fluid switches inside our curved microchannels, where the dyed stream has completed a full fluid recirculation back to the channel inner wall.

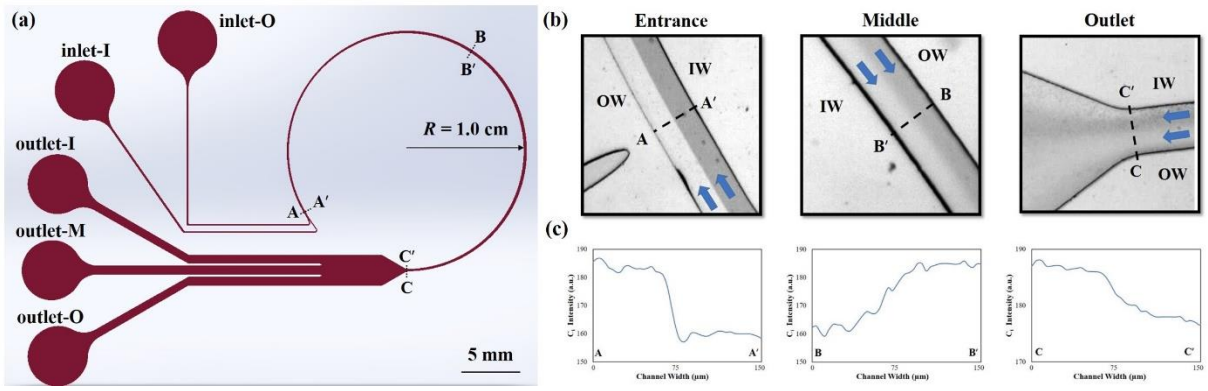

Figure 5-12: (a) Schematic of curved microchannel with AR = 0.5 (150 × 75 μm^2) and R = 1.0 cm with tri-furcate outlets. (b) Co-flow images of 500 ppm PEO solutions at a total axial velocity of V_x = 0.74 m/s at the channel entrance (A-A´), middle section (B-B´), and outlet (C-C´). (c) Color intensity measurements at the channel entrance, middle section and outlet.

To quantitatively characterize the solution exchange efficiency, collected samples from outlet-O containing the target 15 μm particles were examined using the UV-VIS spectrometer. Figure 5-13 represent the absorbance of the solutions in inlet-I (10% v/v trypan blue), inlet-O (undyed), and outlet-O (target sample). As shown in Figure 5-13, the absorbance of the collected sample (0.736 a.u.) was used to calculate the concentration of trypan blue based on the represented method in section 2.7. According to Eq. (2-7), an absorbance of 0.736 indicates the presence of an approximate 1.37% v/v trypan blue in outlet-O, which indicates a 86.3% efficiency for the solution exchange of 15 μm particles using our tri-furcate outlet microdevice.

It is true that duplex particle separation in curved microchannel has been reported already[98,99]; however, considering the previous reports in straight channels[88], the proof-of-concept experiments performed in this sub-section are novel from the perspective of particle washing which is performed simultaneously with separation in viscoelastic fluids at higher flow rates using curved microchannels. We acknowledge that our methods has room for improvement in terms of particle

separation efficiency and purity as well as solution exchange. We will provide some insight on the ways to improve this method in section 7.2.

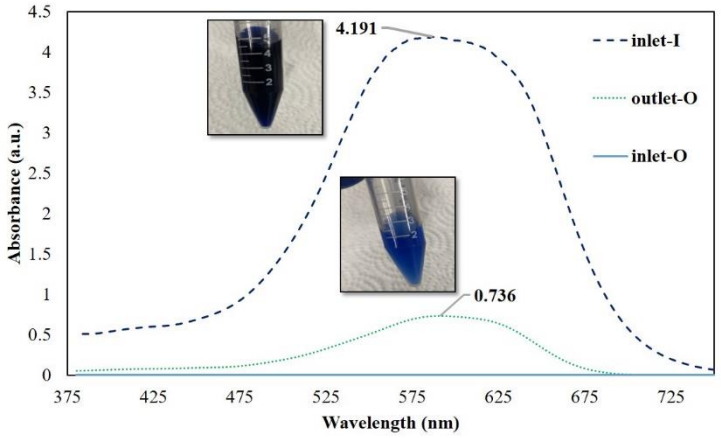

Figure 5-13: Absorbance of solutions in inlet-I (10% v/v trypan blue), inlet-O (undyed), and outlet-O of our microdevice for the co-flow of 500 ppm PEO solutions at V_x = 0.74 m/s.

5.3 Conclusion

In summary, we thoroughly investigated the particle focusing behaviour for different particle sizes in a co-flow of various concentrations of PEO solutions in curvilinear microchannels with different radii of curvature and aspect ratios. The effect of each parameter was studied on the particle focusing behavior at the channel outlet. We found out that the fluid viscoelasticity in curved microchannels with larger radii of curvatures could enhance the focusing behavior. Additionally, at higher flow rates particles were dispersed alongside the channel width under the dominant effect of Dean vortices. Our non-dimensional analysis could potentially provide a guideline to design elasto-inertial particle focusing, washing, and separation devices. For a confined range of blockage ratio ($0.08 < \beta < 0.12$) with small Dean numbers ($De \leq 2$), and limited range of Weissenberg ($0.5 < Wi < 13$), a fully focused particle distribution was observed. We also

showed a proof of concept demonstration of duplex particle separation and washing for 5 μm and 15 μm particles in co-flows of 500 ppm PEO solutions with an average collection efficiency of 97 ± 1%, and an average purity of 74.8% for the target 15 μm particles. Based on the optical spectrophotometry of the collected samples, we have also achieved an efficiency of 86.3% in the simultaneous solution exchange process for 15 μm particles. We would further expand our investigation in the future to enhance the efficiencies of multiplex particle sorting devices based on the fundamental studies above, and to cover wider ranges of Dean and Weissenberg numbers with numerical methods to compliment the experimental results.

Chapter 6

6 Investigation of Microparticle Focusing in Shear-Thickening SiO_2 Nanofluids in Curved Microchannels

In this chapter, we demonstrate the particle behavior in co-flows of SiO_2 nanofluids inside curvilinear microchannels. The effects of fluid axial velocity (i.e., flow rate), nanofluid concentration, channel radius of curvature, and particle size were investigated in square cross sections (Obj. 4). To the best of our knowledge, this is the first demonstration of particle focusing and dynamics in shear-thickening fluids inside microchannels. Theoretically speaking, the effects of inertial and Dean drag forces on the particles can be discussed; however, as opposed to the shear-thinning fluids with understood elastic forces exerted on the particles, the force effect of nanofluids on the particles in microchannels is not well understood. Since this investigation was one of the last objectives of the thesis, we were only able to pursue it experimentally, with the

hope that others can shed light on the particle dynamics using the theory behind forces exerted by nanofluids.

6.1 Introduction

The colloidal suspensions of metallic oxides exhibit a drastic increase in viscosity as the shear rate increases[109–112] as previously illustrated in Figure 2-5. We envision a near future application for these nanofluids, such as the suspensions of SiO_2 nanoparticle in water, for microparticle manipulation in microfluidic devices. Utilizing the developed correlation [Eq. (4-2)] for the average Dean velocity of SiO_2 nanofluids in chapter 34, here we aimed to propose a fundamental study on the particle behavior in these shear-thickening fluids. It is worth noting that as opposed to shear-thinning fluids, there is a lack of knowledge on the governing non-dimensional numbers (i.e., *Wi*, and *El*) to characterize the shear-thickening effects and the hydrodynamic forces acting on the particles. We are actively pursuing additional information to improve understanding of the particle migration in our experiments. In this chapter, particle migration is described using the available non-dimensional numbers (*Re* and *De*), and the balance between net inertial lift force and the Dean drag.

Early investigations on particle behavior in SiO_2 nanofluids in our group[144] indicated that inside a straight microchannel, particles tend to occupy two focusing lines on the channel sides at lower axial velocities where the effect of inertial focusing is not significant. Moreover, at higher axial velocities (i.e., larger Reynolds numbers), the particles migration in SiO_2 nanofluids were

comparable to inertial focusing in water*, where three focusing lines were observed in a square microchannel.

Here, for the first time we present the particle migration behavior inside co-flows of SiO_2 nanofluids inside curved microchannels. The normalized lateral positions of microparticles are used to describe the effects of fluid axial velocity, nanofluids concentration, channel radius of curvature, and particle size as previously explained in sections 2.5 and 2.8.

6.2 Results and Discussion

Particle migration in curvilinear channels was investigated for three different particle sizes (~10, 15, and 22 μm) inside co-flows of various SiO_2 nanofluids concentrations (φ = 1%, 2%, and 3% v/v). Straight (Figure 6-1a) and curvilinear (Figure 6-1b) microchannels with different radii of curvature were used to study the effects of channel curvature. As mentioned in section 2.8, particle trajectories at the outlet were used to draw the normalized number of particles alongside their normalized lateral position, to identify the number of focusing peaks, peak centroids (PCs) and the FWHMs, representing particles distribution bands, for each experiment.

Initially, we investigated the straight microchannel with two inlets to obtain an understanding about the effect of SiO_2 presence in a simple device in which the effect of Dean flow was eliminated. As shown in Figure 6-1a, inside a square (150 ×150 μm^2) straight microchannel at an axial velocity of V_x = 0.222 m/s, the 15 μm particles in DI water ended up close to the inner side of the outlet (i.e., where they were initially supplied) with the peak centroid located at PC_a = 0.81 and $FWMH_a$ = 0.06. However, inside the shear-thickening 2% v/v SiO_2 nanofluids, microparticles

* Representative experiments on particle migration in straight microchannels could be found in Appendix F.

were dispersed alongside the channel width with two apparent peak centroids of PC_{b1} = 0.57 ($FWHM_{b1}$ =0.06), and PC_{b2} = 0.87 ($FWHM_{b2}$ =0.18) as shown in Figure 6-1b. Here, the particles in DI water were partially focused (~86% within the ±0.1 peak bandwidth), while ~ 42% of particles were accumulated within ±0.1 peak bandwidth around each peak inside the 2% v/v SiO_2 nanofluids. Obviously, the SiO_2 nanofluid exerted a distracting effect on particle focusing in the straight microchannel.

We then conducted the same set of experiments as above in a curved microchannel with two inlets. As illustrated in Figure 6-1c for the 15 µm particles in a square (150 ×150 μm^2) channel with R = 1.0 cm, fluid recirculation (~ 3.1 fluid switches with De = 3.21) dispersed the particles at the outlet with PC_c = 0.75, $FWHM_c$=0.09, and only ~54% of particles within the ±0.1 peak bandwidth (no focusing). However, as shown in Figure 6-1d, the Dean drag (~1.4 fluid switches with De = 0.06) transferred the particles inside the 2% SiO_2 towards the outer wall with two weak peaks (PC_{d1} = 0.13, $FWHM_{d1}$=0.11, and PC_{d2} = 0.77, $FWHM_{d1}$=0.14). Here, ~ 32%, and 27% of particles were found within the ±0.1 peak bandwidth for the first and second peak, respectively. We concluded again that 1) the addition of Dean drag with a curvilinear microchannel scattered the particle trajectories inside DI water, and 2) the addition of SiO_2 nanoparticles changed the behaviour of particles inside the curved microchannel.

The outcomes of the above investigations encouraged us to conduct a parametric study on particle focusing inside SiO_2 nanofluids in curved microchannels. The results are presented in the following sections.

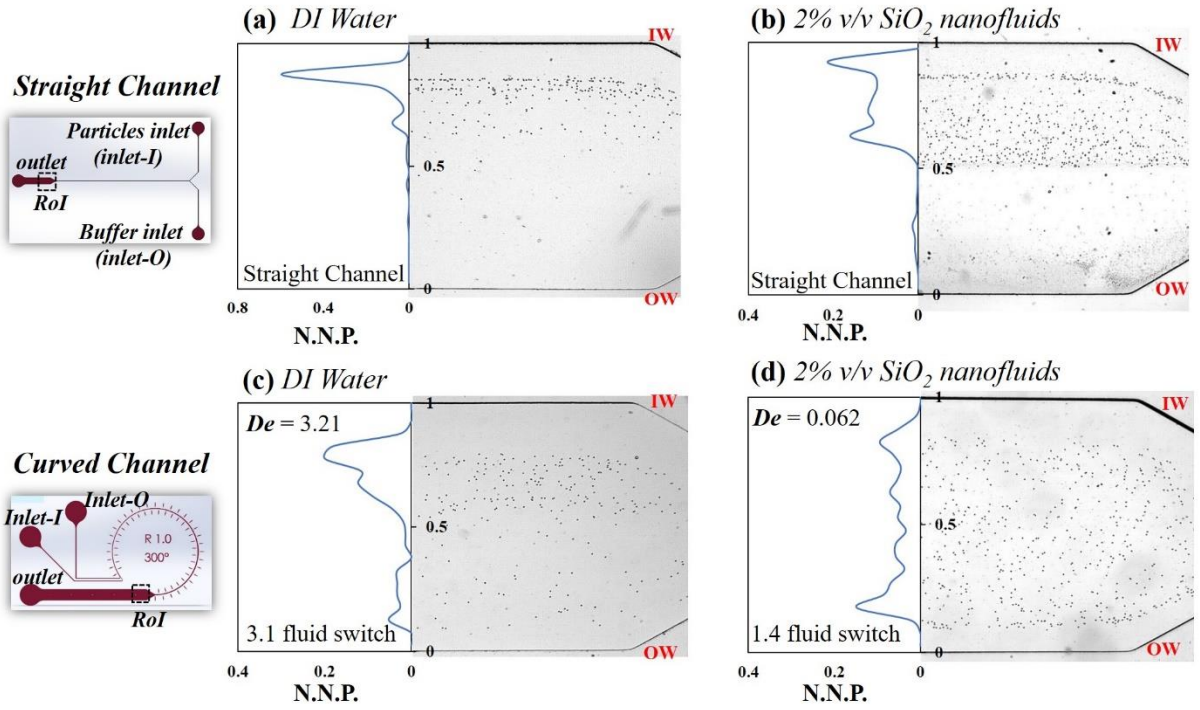

Figure 6-1: Particle trajectories and normalized number of particles (NNP) across the RoI of the channels for 15 µm particles at an axial velocity of V_x = 0.222 m/s inside square microchannels (150 × 150 µm^2). Particles were co-flown alongside a clean buffer inside a straight channel in (a) DI water and (b) 2% v/v SiO_2 nanofluids, and inside a curved channel with R = 1.0 cm in (c) DI water, and (d) 2% v/v SiO_2 nanofluids.

6.2.1 Effect of Fluids Axial Velocity (V_x)

Particle migration behavior was studied at a wide range of axial velocities between 0.037 < V_x < 0.74 m/s inside curved microchannels with square cross sections (150 × 150 µm^2). In a representative experiment* for 22 µm particles in co-flows of 3% v/v SiO_2 nanofluids inside a curved channel with square cross section (150 × 150 µm^2), and R = 1.0 cm, particles focusing behavior are presented in Figure 6-2 . Here, at an axial velocity of V_x = 0.037 m/s (*De* = 0.034, ~ 0.3 fluid switch), particles were fully focused close to the channel inner wall, with ~ 90% of

* Complete set of experimental results for all particle sizes and SiO_2 concentrations could be found in Appendix F.

particles within the ±0.1 bandwidth of peak centroid (PC = 0.81). As the axial velocity increased to V_x = 0.074 m/s (~ 0.5 fluid switch), and V_x = 0.148 m/s (~ 1 fluid switch), the peak centroids shifted slightly towards the channel center (PC = 0.79, and PC = 0.75, respectively), due to the higher fluid recirculation. Here, approximately ~ 85% of particles were found within the ±0.1 bandwidth around the peaks (i.e., partially focused) for both axial velocities. Upon further increase in axial velocity, the Dean drag dominated the particle migration. For instance, at V_x = 0.222 m/s, only ~ 48% of particles were found within the ±0.1 bandwidth around PC = 0.81 (no focusing). At higher axial velocities of V_x = 0.37 m/s to V_x = 0.74 m/s, two weak peaks appeared in particle distribution close to channel walls (PC = 0.17, and PC = 0.77). Similar to chapter 5, stronger Dean vortices at higher axial velocities resulted in particle dispersion along the channel width.

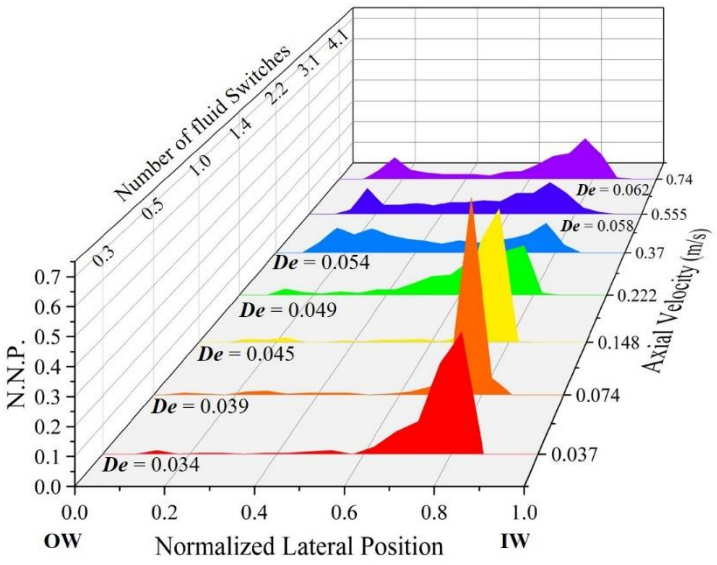

Figure 6-2: Normalized number of particles alongside their normalized lateral position for 22 µm particles in 3% SiO_2 nanofluid inside a square microchannel (150 ×150 µm^2) with R = 1.0 cm at various axial velocities.

6.2.2 Effect of Nanofluids Concentration (φ)

Different concentrations of SiO_2 nanofluids (φ = 1%, 2%, and 3% v/v) were examined to investigate the shear-thickening effect on particle migration. Representative experiments for 22 µm particles in curved microchannel with a square cross section of 150 × 150 µm^2, and R = 1.0 cm at two different axial velocities are presented in Figure 6-3.

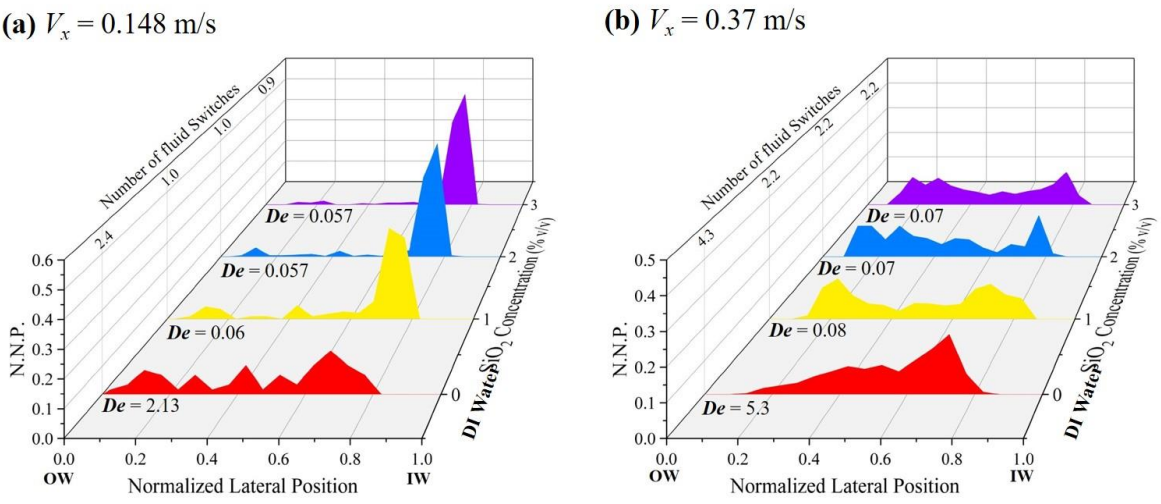

Figure 6-3: Normalized number of particles alongside their normalized lateral position for 22 µm particles in a square microchannel (150 ×150 µm^2) with R = 1.0 cm in DI water, and 1%, 2%, and 3% v/v SiO_2 nanofluids at (a) V_x = 0.148 m/s , and (b) V_x = 0.37 m/s.

As shown in Figure 6-3a, at an axial velocity of V_x = 0.148 m/s, particles in DI water (*De* = 2.13) were dispersed across the channel width after the second fluid switch. As the SiO_2 nanofluids were introduced, the fluid switches reduced to ~ 1 and microparticles remained close to the channel inner wall. Here, the added effect of shear-thickening fluid and the increased dominance of the Dean drag ($F_D > F_L$) at higher fluid viscosities, resulted in particle focusing at a peak centroid of PC = 0.75 for all three concentrations. For the co-flow of φ = 1%, and 2 % v/v SiO_2 (*De* = 0.06 and 0.057, respectively), particles were partially focused with ~ 73%, and ~ 83% of them within

the ±0.1 bandwidth of the peak centroid, respectively. Moreover, at a higher concentration of φ = 3% v/v, particles were fully focused around the PC = 0.75 (~90% within the defined bandwidth).

Particle distributions are also shown at a higher axial velocity of V_x = 0.37 m/s in Figure 6-3b. Here, inside DI water (*De* = 5.3, and ~ 4.3 fluid switches) particles were scattered across the channel width with only ~ 40% of them found within the ±0.1 bandwidth of PC = 0.73. For particles in 1% v/v SiO_2 (*De* = 0.08, and ~ 2.2 fluid switches), two peaks were observed at PC_1 = 0.23, and PC_2=0.81, with ~ 37%, and 26% of particles within their respective bandwidths. For higher SiO_2 concentrations (φ = 2%, and 3% v/v), particles were pushed towards the channel walls with PC_1 = 0.15, and PC_2 = 0.77, and only ~ 30% of particles within each peak's defined bandwidth. Here, we concluded that shear-thickening effect of SiO_2 nanofluids would enhance the particle focusing at lower axial velocities (Figure 6-3a). However, at higher axial velocities the dominant Dean drag leads to particle scattering and creation of two main peaks close to the channel walls (Figure 6-3b).

6.2.3 Effect of Channel Radius of Curvature (*R*)

To investigate the effect of channel curvature, 22 μm particles were co-flown in various SiO_2 concentrations inside curved microchannels with a square cross section and R = 1.0, 1.5, and 2.0 cm as previously explained in section 2.5. Experiments for straight channels ($R \rightarrow \infty$) were also conducted for comparison purposes. As an example*, the normalized particle distributions alongside the channel width in co-flows of 3% v/v SiO_2 nanofluids at two different axial velocities of V_x = 0.37 m/s and V_x = 0.74 m/s are presented in Figure 6-4.

* Complete set of experiments for 22 μm particles in different channel radii of curvatures are presented in Appendix F.

As shown in Figure 6-4a, inside a straight microchannel at an axial velocity of V_x = 0.37 m/s, microparticles occupied two peaks close to the channel inner wall and channel center line (PC_1 = 0.53, and PC_2 = 0.87), where ~ 40% and 56% of particles were within the ±0.1 bandwidth of each respective peak centroid. As a reminder, this behavior was due to the supply of the particles only from one of the two inlets into the straight microchannel. Upon introduction of channel curvature (and Dean drag) inside a curved channel with R = 2.0 cm (~ 1.1 fluid switch), particles were partially focused (~86% within the defined bandwidth) close to the inner wall with PC = 0.85. As the channel radius of curvature decreased to R = 1.5 cm (~ 1.5 fluid switches), particles were pushed towards the channel center, where they were partially focused (~ 85% within the defined bandwidth) with a peak centroid of PC = 0.75. A further decrease in channel radius of curvature to R = 1.0 cm, resulted in ~ 2.2 fluid switches and dispersed the particles across the channel width with two peaks close to the side channels (PC_1 = 0.15, and PC_2 = 0.77).

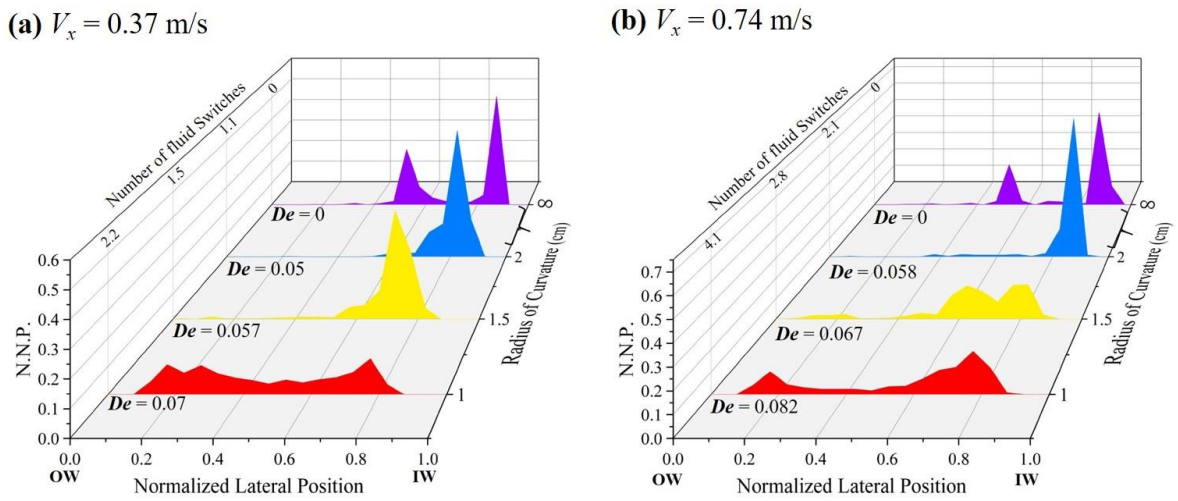

Figure 6-4: Effect of radius of curvature on normalized number of particles alongside the channel outlet. Representative experiments are shown for 22 µm particles in co-flow of 3% v/v SiO_2 nanofluids inside the straight ($R \rightarrow \infty$) and curved microchannels with R = 1.0, 1.5, and 2.0 cm with a square cross section (150×150 μm^2) at an axial velocity of (a) V_x = 0.37 m/s, and (b) V_x = 0.74 m/s.

The normalized lateral migration of particles at a higher axial velocity of V_x = 0.74 m/s is also presented in Figure 6-4b. Here, inside a straight microchannel ($R \rightarrow \infty$), two peaks were observed at PC_1 = 0.51, and PC_2 = 0.89, with ~ 28% and ~66% of particles within their respective ±0,1 bandwidths. As shown in Figure 6-4b, particles inside a curved channel with R = 2.0 cm were fully focused close to the channel inner wall, where ~ 92% of them were within the defined bandwidth around PC = 0.87. Further decrease in channel radius of curvature to R = 1.5 cm, resulted in the creation of two peaks (PC_1 = 0.67, and PC_2 = 0.87) with an approximate 3 fluid switches at the channel outlet. Here, ~ 45% of particles were found within the ±0.1 bandwidth of each peak. A further decrease in channel radius of curvature to R = 1.0 cm (~ 4 fluid switches) amplified the effect of Dean drag and pushed the particles towards side channels with two apparent peaks of PC_1 = 0.15, and PC_2 = 0.75, with ~ 19% and 50% of particles within their respective bandwidths.

According to the representative cases in Figure 6-4, we concluded that at lower channel curvatures (higher R values), the added effect of Dean drag could enhance the particle focusing, i.e., resulting transition from two peaks in straight channels into a single peak in a curved channel with SiO_2 nanofluid. However, stronger Dean vortices at lower channel radii would disperse the particles towards channel walls. At higher axial velocities, this phenomenon would occur faster at a higher channel radius of curvatures.

6.2.4 Effect of Microparticle Size (a)

Finally, the effect of particle size was investigated using three different particle sizes of 10, 15, and 22 μm in a curved microchannel with square cross section (150 × 150 μm^2) and R = 1.0 cm. Representative cases for microparticles in co-flows of 3% v/v SiO_2 nanofluids at two different axial velocities are presented in Figure 6-5, with the rest of the experiments demonstrated in Appendix F.

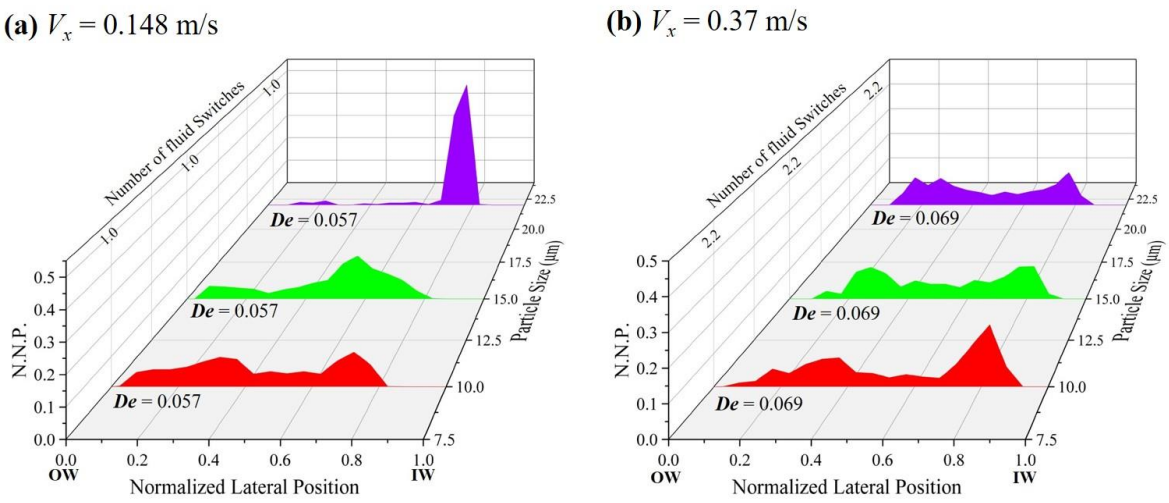

Figure 6-5: Effect of particle size on normalized number of particles alongside the channel outlet. Representative experiments are shown for three different particle sizes of 10, 15, and 22 μm microparticles in co-flow of 3% v/v SiO_2 nanofluids inside a microchannel with a 150 × 150 μm^2 cross section and R = 1.0 cm at (a) V_x = 0.148 m/s, and (b) V_x = 0.37 m/s.

As shown in Figure 6-5a, at an axial velocity of V_x = 0.148 m/s (~ 1 fluid switch) the smaller 10 μm particles (β = 0.07) were scattered across the channel width with two peaks of PC_1 = 0.33, and PC_2 = 0.71, with ~ 30% of particles within the ±0.1 bandwidth around each peak. As the particle size increased to 15 μm (β = 0.1), the net inertial lift forces [$F_L \sim a^4$ in Eq. (5-1)] increased faster compared to the Dean drag [$F_D \sim a$ in Eq. (5-2)]. Therefore, the particles were pushed towards the channel inner wall with PC = 0.59, with ~ 53% of them within the defined bandwidth (~ no focusing). However, the larger 22 μm particles (β = 0.15) were fully focused close to the channel inner wall with ~ 92% of the particles found within the defined bandwidth surrounding PC = 0.81. As shown in Figure 6-5b, at a higher axial velocity of V_x = 0.37 m/s (~ 2.2 fluid switches), microparticle migration was dominated by the Dean drag, and particles were scattered across the channel width with two weak peaks close to channel side walls for all particle sizes (PC_1 = 0.25, and PC_2 = 0.75).

Overall, we concluded that an increase in particle size could enhance the focusing behavior at lower axial velocities. However, as the Dean drag becomes dominant at higher axial velocities, all particles get dispersed in two main peaks close to the channel sidewalls.

6.3 Conclusion

In summary, we demonstrated the particle focusing behavior in SiO_2 nanofluids inside curved microchannels for the first time. The normalized lateral positions of particles were studied in co-flows of various SiO_2 nanofluid concentrations. The effects of fluid axial velocity, nanofluids concentration, channel radius of curvature, and particle size on the particle focusing at the channel outlet were investigated. We found out that the presence of shear-thickening nanofluids even at low concentrations, could enhance the particle focusing at lower flow rates. Moreover, the dominance of Dean drag at higher axial velocities (i.e., flow rates) would create two focusing peaks close to channel sidewalls. Our early results indicate a behavioral change and warrant a more comprehensive parametric study on this phenomenon in higher nanofluids concentrations, and different channel geometries at very low to very high flow rates.

Chapter 7

7 Thesis Summary and Future Work

7.1 Thesis Summary

Separation and detection of microparticles and harmful analytes in biological fluids and water have proven to be critical steps in human health and safety applications. Isolation and enrichment of target particles and transferring/washing them to a clean buffer is an essential step, especially at the point of need. Particle focusing and washing processes are required to prepare the target particles for detection in batch or single cell/particle analysis. Microfluidic methods could enable the automation and a faster analysis, and enhance the sample handling. Moreover, the secondary Dean vortices in curvilinear microchannels could be utilized to enhance the efficiency and

throughput of the particle focusing, simultaneously with fluid handling, compared to straight microchannels.

Most real life applications deal with non-Newtonian fluids such as blood and saliva, where the rheological characteristics vary depending on the applied shear rate. Therefore, it is important to focus on understanding the underlying physics of Dean-coupled elasto-inertial systems to gain control over the affecting parameters. Despite the previous reports on particle focusing in viscoelastic fluids, no significant attention has been paid to the concept of particle washing (i.e., particle focusing and transfer into a clean buffer) in non-Newtonian fluids. Transferring the target particles to a clean buffer could play a vital role in sample preparation and detection in various biomedical applications. Thus, various industrial and biomedical applications such as particles and cell separation and isolation could be enhanced using the advantages of these systems.

In this thesis, we attempted to address the need for an in-depth and thorough fundamental study of the fluids and particle dynamics in non-Newtonian fluids inside curved microchannels. We aimed to investigate the affecting parameters on the fluid and particle behavior, such as channel dimensions, polymer concentration, fluid viscosity, and axial velocity as well as the particle size. We also foresee a near-future application of shear-thickening metallic fluids such as SiO_2 nanofluids in curved microchannels for the purpose of fundamental fluids mechanics investigations, and sample processing. Hence, we expanded our investigations to study the shear-thickening SiO_2 nanofluids behavior in curved microchannels. Chapters 1 and 2 of the thesis were dedicated to the literature review and the methodologies related to this thesis, respectively.

In chapter 3, we tested various concentrations of viscoelastic PEO solutions in curved microchannels with different channel aspect ratio and radii of curvatures at various flow rates (Obj. 1). We developed an empirical correlation for the average V_{De} of viscoelastic fluids. Our

correlation captures the effects of channel hydraulic diameter and fluid kinematic viscosity, and considerably reduces the prediction error for V_{De} of viscoelastic fluids down to 12.7%. This correlation could be utilized in the design of microfluidic devices for microparticle separation and washing applications.

In chapter 4, we applied our Dean flow characterization method to investigate different concentrations of SiO_2 nanofluids in curved microchannels (Obj. 1). We studied the effects of channel dimensions and curvature as well as nanofluids concentration and offered an empirical correlation for the average V_{De} of shear-thickening SiO_2 nanofluids. Our correlation apprehends the effects of channel geometry and fluid kinematic viscosity and offers a precise prediction of the average V_{De} with an average error of 5.9%. Similarly, this correlation could be utilized to enhance the control on particle manipulation and washing in shear-thickening fluids in future applications.

In chapter 5, we carried out a thorough investigation on particle focusing behavior in a co-flow of various shear-thinning PEO-water fluids in curved microchannels (Obj. 2). We studied the effects of channel dimensions and curvature on particle focusing at various flow rates. We found out that the fluid viscoelasticity (i.e., polymer concentration) could enhance the focusing behavior in curved channels with larger radii of curvatures. In addition, we observed that particles tend to disperse alongside the channel width at higher flow rates under the dominant effect of secondary Dean vortices. Moreover, we provided a non-dimensional analysis that could potentially provide a comprehensive guideline to design Dean-coupled elasto-inertial particle focusing, washing and separation devices. For a confined range of blockage ratio ($0.08 < \beta < 0.12$) with small Dean numbers ($De \leq 2$), and limited range of Weissenberg ($0.5 < Wi < 13$), a fully focused particle distribution was observed. As a proof of concept, we also demonstrated a duplex particle separation and washing process (Obj. 3) for 5 µm and 15 µm particles in co-flow of 500 ppm PEO

solutions with an average collection efficiency of 97 ± 1%, and an average purity of 74.8% for the target 15 µm particles. We also achieved an efficiency of 86.3% in the solution exchange process according to the spectrophotometry examination of the collected target sample.

Finally, in chapter 6, we investigated the particle focusing behavior in SiO_2 shear-thickening nanofluids inside curvilinear microchannels (Obj. 4). We examined the normalized lateral position of particles for different particle sizes in various SiO_2 concentrations and different channel curvatures. We observed that the presence of shear-thickening nanofluids even at low concentrations could enhance the particle focusing at lower flow rates in curved channels with larger radius of curvature. Moreover, the dominance of Dean drag at higher axial velocities (i.e., flow rates) would create two focusing peaks close to channel sidewalls.

7.2 Thesis Limitations and Proposed Future Work

Despite considerable enhancements and advantages offered by the fundamental studies in this thesis, we acknowledge that there is still room for further improvement of the experimental results, and non-dimensional analysis. In this section, we explain the limitations of our experimental work and propose possible future work to enhance the applicability of our results in future particle focusing and washing processes. It is worth noting that our experimental results are specific to PDMS microchannels. Considering the channel deformability, specifically at higher flow rates, the effect of channel distortion on fluid and particle behavior should be investigated in the future. Both fluid and particle behavior could also be investigated in microchannels fabricated in stiff materials such as thermoplastics, glass, or silicon wafers.

We also acknowledge other sources of uncertainty, such as the fabrication process, pumping, viscosity measurement, and data analysis resolution. The replication molds were prepared with a maximum of ±5 μm height deviation, which translates into an average deviation of 4 % for the three different channel heights. This could cause an average error of 2% in the V_{De} correlations for PEO solutions and SiO_2 nanofluids. According to our control measurements, the syringe pumps would also cause an average 1% error compared to the nominal flow rate. Moreover, an average 5% viscosity deviation in the solution will also convert into ~4% variation in the prediction of the average Dean velocity. Lastly, the data analysis method for the switching length at 10-degree intervals alongside the channel curvature could translate into a maximum of 1.7% deviation. This error will linearly affect calculation of experimental V_{De} values in chapters 3 and 4.

In chapter 3, our Dean flow characterization and empirical correlation could be improved using analytical and numerical methods. The average prediction error could be further decreased by improving the data analysis resolution and implementing numerical solutions. As explained in chapter 2, Dean flow characterization was performed using color intensity measurements at 10-degree intervals alongside the channel curvature. To obtain a more precise switching length (L_s), we could increase the number of measurements (e.g., 5-degree intervals on the curved channel). The suitability of this correlation could be also enhanced for a wider range of non-Newtonian fluids by examining higher PEO concentrations and various polymer alternatives inside different channel geometries.

The proposed empirical correlation for the average V_{De} of SiO_2 nanofluids, could be also improved by testing higher nanofluids concentrations and acquiring a more precise rheological characterization of these shear-thickening metallic nanofluids. Moreover, according to the experimental results, SiO_2 concentrations between 0-1% v/v could be the most influential domain

on the fluid behavior and should be tested in the future. Concentrations higher than 3% SiO2 are also worth testing for the sake of experimental completion, if possible to be pumped in the channel at high flow rates. Similarly, the data analysis resolution could be increased to reduce the prediction error. Depending on possible future applications, different shear-thickening fluids could be examined to extend the suitability of the proposed correlation.

The fundamental investigations in chapter 5 on particle focusing in shear-thinning fluids could be further extended to examine more concentrations of viscoelastic PEO solutions to enhance its applicability to biological processes. While our non-dimensional analysis could provide a guideline to design the elasto-inertial particle washing devices, it is unable to accurately predict the particle's focusing location across the channel width. A more comprehensive study is required to provide a precise prediction of particle's lateral position under various fluid and microchannel dimensions. Our proposed duplex particle washing process could also be enhanced using different outlet designs in order to reduce the impurity of the final sample. Higher particle washing throughputs could be also possible using different channel geometries or stacking multiple PDMS microdevices depending on the specific application. We aim to further enhance the efficiency of our duplex particle washing process and utilize it for real life applications using diluted blood or plasma.

Finally, particle behavior analysis in SiO_2 nanofluids should be expanded to investigate the particle focusing behavior in lower and higher SiO_2 concentrations inside various channel cross sections. We aim to test different channel aspect ratios to paint a complete picture of particle behavior in both straight and curved microchannels. While our observations indicate a noticeable behavioral change in SiO_2 nanofluids, we still require a comprehensive parametric study to analyze the phenomenon. We are currently pursuing additional information to better understand and

describe the shear-thickening effects and the possible additional hydrodynamic forces that might be involved in particle manipulation. The parametric study should also include a non-dimensional analysis to extend its usefulness for future applications of these non-Newtonian fluids in heat exchangers, solar energy collectors, and nanoplastic detection in the food, energy, electronics, and environmental monitoring industries.

References

1. Zulkifli, S. N., Rahim, H. A. & Lau, W. J. Detection of contaminants in water supply: A review on state-of-the-art monitoring technologies and their applications. *Sensors Actuators, B Chem.* **255**, 2657–2689 (2018).

2. Tsai, S. S. H., Wexler, J. S., Wan, J. & Stone, H. A. Conformal coating of particles in microchannels by magnetic forcing. *Appl. Phys. Lett.* **99**, 1–4 (2011).

3. Hur, S. C., Brinckerhoff, T. Z., Walthers, C. M., Dunn, J. C. Y. & Di Carlo, D. Label-Free Enrichment of Adrenal Cortical Progenitor Cells Using Inertial Microfluidics. *PLoS One* **7**, (2012).

4. Geens, M. *et al.* The efficiency of magnetic-activated cell sorting and fluorescence-activated cell sorting in the decontamination of testicular cell suspensions in cancer patients. *Hum. Reprod.* **22**, 733–742 (2007).

5. Fong, C. Y., Peh, G. S. L., Gauthaman, K. & Bongso, A. Separation of SSEA-4 and TRA-1-60 labelled undifferentiated human embryonic stem cells from a heterogeneous cell population using magnetic-activated cell sorting (MACS) and fluorescence-activated cell sorting (FACS). *Stem Cell Rev. Reports* **5**, 72–80 (2009).

6. Bonner, W. A., Hulett, H. R., Sweet, R. G. & Herzenberg, L. A. Fluorescence Activated Cell Sorting Fluorescence Activated Cell Sorting. *Rev. Sci. Instrum.* **43**, (2012).

7. Adams, J. D., Kim, U. & Soh, H. T. Multitarget magnetic activated cell sorter. *Proc. Natl. Acad. Sci.* **105**, 18165–70 (2008).

8. Mach, A. J. & di Carlo, D. Continuous scalable blood filtration device using inertial microfluidics. *Biotechnol. Bioeng.* **107**, 302–311 (2010).

9. Lazar, I. M. & Karger, B. L. Multiple open-channel electroosmotic pumping system for microfluidic sample handling. *Anal. Chem.* **74**, 6259–6268 (2002).

10. Fu, L. M., Yang, R. J., Lee, G. B. & Liu, H. H. Electrokinetic injection techniques in microfluidic chips. *Anal. Chem.* **74**, 5084–5091 (2002).

11. Jiang, Y., Zou, S. & Cao, X. Rapid and ultra-sensitive detection of foodborne pathogens by using miniaturized microfluidic devices: A review. *Anal. Methods* **8**, 6668–6681 (2016).

12. Lee, W. *et al.* 3D-Printed micro fluidic device for the detection of pathogenic bacteria using size-based separation in helical channel with trapezoid cross-section. *Sci. Rep.* **5**, 1–7 (2015).

13. Zhang, J. *et al.* Fundamentals and applications of inertial microfluidics: A review. *Lab Chip* **16**, 10–34 (2016).

14. Kirby, B. *Micro-and Nanoscale Fluid Mechanics*. *Cambridge University Press* (2010). doi:10.1017/CBO9780511760723

15. Tornay, R. *et al.* Dielectrophoresis-based particle exchanger for the manipulation and

surface functionalization of particles. *Lab Chip* **8**, 267–273 (2008).

16. Li, M., Li, W. H., Zhang, J., Alici, G. & Wen, W. A review of microfabrication techniques and dielectrophoretic microdevices for particle manipulation and separation. *J. Phys. D. Appl. Phys.* **47**, 29 (2014).

17. Peyman, S. A., Iles, A. & Pamme, N. Mobile magnetic particles as solid-supports for rapid surface-based bioanalysis in continuous flow. *Lab Chip* **9**, 3110–3117 (2009).

18. Vojtíšek, M., Iles, A. & Pamme, N. Rapid, multistep on-chip DNA hybridisation in continuous flow on magnetic particles. *Biosens. Bioelectron.* **25**, 2172–2176 (2010).

19. Hejazian, M., Li, W. & Nguyen, N. Lab on a chip for continuous-flow magnetic cell separation. *Lab Chip* **15**, 959–970 (2015).

20. Fuh, C. B., Lin, L. Y. & Lai, M. H. Analytical magnetapheresis of magnetically susceptible particles. *J. Chromatogr. A* **874**, 131–142 (2000).

21. Hawkes, J. J., Barber, R. W., Emerson, D. R. & Coakley, W. T. Continuous cell washing and mixing drvien by an ultrasound standing wave within a microfluidic channel. *Lab Chip* **4**, 446–452 (2004).

22. Petersson, F., Nilsson, A., Jönsson, H. & Laurell, T. Carrier medium exchange through ultrasonic particle switching in microfluidic channels. *Anal. Chem.* **77**, 1216–1221 (2005).

23. Laurell, T., Petersson, F., Nilsson, A. & Petersson, F. Chip integrated strategies for acoustic separation and manipulation of cells and particles resulted in several national. (2007). doi:10.1039/b601326k

24. Sivaramakrishnan, M., Kothandan, R., Govindarajan, D. K., Meganathan, Y. & Kandaswamy, K. Active microfluidic systems for cell sorting and separation. *Curr. Opin. Biomed. Eng.* **13**, 60–68 (2020).

25. Yuan, D. *et al.* Recent progress of particle migration in viscoelastic fluids. *Lab Chip* **18**, 551–567 (2018).

26. Segré, G. & Silberberg, A. Radial particle displacements in poiseuille flow of suspensions. *Nature* **189**, 209–210 (1961).

27. Asmolov, E. S. The inertial lift on a spherical particle in a plane poiseuille flow at large channel Reynolds number. *J. Fluid Mech.* **381**, 63–87 (1999).

28. ho, B. P. & Leal, L. G. Inertial migration of rigid spheres in two-dimensional unidirectional flows. *J. Fluid Mech.* **65**, 365–400 (1974).

29. Di Carlo, D. Inertial microfluidics. *Lab Chip* **9**, 3038–3046 (2009).

30. Martel, J. M. & Toner, M. Inertial Focusing in Microfluidics. *Annu. Rev. Biomed. Eng.* **16**, 371–396 (2014).

31. Zhang, J. *et al.* Fundamentals and applications of inertial microfluidics: A review. *Lab Chip* **16**, 10–34 (2016).

32. Zhou, J. & Papautsky, I. Fundamentals of inertial focusing in microchannels. *Lab Chip* **13**,

1121–1132 (2013).

33. Gossett, D. R. *et al.* Inertial manipulation and transfer of microparticles across laminar fluid streams. *Small* **8**, 2757–2764 (2012).

34. Berger, S. A., Talbot, L. & Yao, L. S. Flow in Curved Pipes. *Annu. Rev. Fluid Mech.* **15**, 461–512 (1983).

35. Munson, B.R. and Young, D.F. and Okiishi, T.H. and Huebsch, W. W. Fundamentals of Fluid Mechanics. *Wiley* (2009).

36. Di Carlo, D., Irimia, D., Tompkins, R. G. & Toner, M. Continuous inertial focusing, ordering, and separation of particles in microchannels. *Proc. Natl. Acad. Sci. U. S. A.* **104**, 18892–18897 (2007).

37. Matas, J. P., Morris, J. F. & Guazzelli, É. Inertial migration of rigid spherical particles in Poiseuille flow. *J. Fluid Mech.* **515**, 171–195 (2004).

38. Xiang, N. *et al.* Fundamentals of elasto-inertial particle focusing in curved microfluidic channels. *Lab Chip* **16**, 2626–2635 (2016).

39. Martel, J. M. & Toner, M. Inertial focusing dynamics in spiral microchannels. *Phys. Fluids* **24**, 032001 (2012).

40. Sun, J. *et al.* Double spiral microchannel for label-free tumor cell separation and enrichment. *Lab Chip* **12**, 3952–3960 (2012).

41. Sun, J. *et al.* Size-based hydrodynamic rare tumor cell separation in curved microfluidic channels. *Biomicrofluidics* **7**, (2013).

42. Bhagat, A. A. S., Kuntaegowdanahalli, S. S. & Papautsky, I. Continuous particle separation in spiral microchannels using dean flows and differential migration. *Lab Chip* **8**, 1906–1914 (2008).

43. Kuntaegowdanahalli, S. S., Bhagat, A. A. S., Kumar, G. & Papautsky, I. Inertial microfluidics for continuous particle separation in spiral microchannels. *Lab Chip* **9**, 2973–2980 (2009).

44. Wu, L., Guan, G., Hou, H. W., Bhagat, A. A. S. & Han, J. Separation of leukocytes from blood using spiral channel with trapezoid cross-section. *Anal. Chem.* **84**, 9324–9331 (2012).

45. Warkiani, M. E. *et al.* Slanted spiral microfluidics for the ultra-fast, label-free isolation of circulating tumor cells. *Lab Chip* **14**, 128–137 (2014).

46. Abdulla, A., Liu, W., Gholamipour-Shirazi, A., Sun, J. & Ding, X. High-Throughput Isolation of Circulating Tumor Cells Using Cascaded Inertial Focusing Microfluidic Channel. *Anal. Chem.* **90**, 4397–4405 (2018).

47. Abdulla, A. *et al.* Label-free Separation of Circulating Tumor Cells Using a Self-Amplified Inertial Focusing (SAIF) Microfluidic Chip. *Anal. Chem.* **92**, 16170–16179 (2020).

48. Martel, J. M. & Toner, M. Particle focusing in curved microfluidic channels. *Sci. Rep.* **3**, 1–8 (2013).

49. Ookawara, S., Higashi, R., Street, D. & Ogawa, K. Feasibility study on concentration of slurry and classification of contained particles by microchannel. *Chem. Eng. J.* **101**, 171–178 (2004).

50. Bara, B. & Masliyah, J. H. An experimental and numerical study of the Dean problem: Flow development towards two-dimensional multiple solutions. *J. Fluid Mech.* **244**, 339–376 (1992).

51. Ligrani, P. M. & Niver, R. D. Flow visualization of Dean vortices in a curved channel with 40 to 1 aspect ratio. *Phys. Fluids* **31**, 3605–3617 (1988).

52. Bayat, P. & Rezai, P. Semi-Empirical Estimation of Dean Flow Velocity in Curved Microchannels. *Sci. Rep.* **7**, 1–13 (2017).

53. Nikdoost, A., Doostmohammadi, A., Romanick, K., Thomas, M. & Rezai, P. Integration of microfluidic sample preparation with PCR detection to investigate the effects of simultaneous DNA-Inhibitor separation and DNA solution exchange. *Anal. Chim. Acta* **1160**, 338449 (2021).

54. Bayat, P. & Rezai, P. Microfluidic curved-channel centrifuge for solution exchange of target microparticles and their simultaneous separation from bacteria. *Soft Matter* **14**, 5356–5363 (2018).

55. Lee, D. J., Brenner, H., Youn, J. R. & Song, Y. S. Multiplex particle focusing via hydrodynamic force in Viscoelastic Fluids. *Sci. Rep.* **3**, 3–10 (2013).

56. Irgens, F. *Rheology and non-newtonian fluids*. *New York: Springer International Publishing* **1**, (Springer, 2013).

57. Villone, M. M., D'Avino, G., Hulsen, M. A., Greco, F. & Maffettone, P. L. Particle motion in square channel flow of a viscoelastic liquid: Migration vs. secondary flows. *J. Nonnewton. Fluid Mech.* **195**, 1–8 (2013).

58. Leshansky, A. M., Bransky, A., Korin, N. & Dinnar, U. Tunable nonlinear viscoelastic 'focusing' in a microfluidic device. *Phys. Rev. Lett.* **98**, 1–4 (2007).

59. Lim, H., Nam, J. & Shin, S. Lateral migration of particles suspended in viscoelastic fluids in a microchannel flow. *Microfluid. Nanofluidics* **17**, 683–692 (2014).

60. James, D. F. Boger Fluids. *Annu. Rev. Fluid Mech.* **41**, 129–142 (2009).

61. Yang, S., Kim, J. Y., Lee, S. J., Lee, S. S. & Kim, J. M. Sheathless elasto-inertial particle focusing and continuous separation in a straight rectangular microchannel. *Lab Chip* **11**, 266–273 (2011).

62. Byron Bird, R. & M., W. J. CONSTITUTIVE EQUATIONS FOR POLYMERIC LIQUIDS. *Annu. Rev. Fluid Mech.* **27**, 169–193 (1995).

63. Lu, X., Liu, C., Hu, G. & Xuan, X. Particle manipulations in non-Newtonian microfluidics: A review. *J. Colloid Interface Sci.* **500**, 182–201 (2017).

64. Seo, K. W., Kang, Y. J. & Lee, S. J. Lateral migration and focusing of microspheres in a microchannel flow of viscoelastic fluids. *Phys. Fluids* **26**, (2014).

65. Seo, K. W., Byeon, H. J., Huh, H. K. & Lee, S. J. Particle migration and single-line particle focusing in microscale pipe flow of viscoelastic fluids. *RSC Adv.* **4**, 3512–3520 (2014).

66. Karnis, A. & Mason, S. G. Particle motions in sheared suspensions. XIX. Viscoelastic media. *Trans. Soc. Rheol.* **10**, 571–592 (1996).

67. D'Avino, G. *et al.* Single line particle focusing induced by viscoelasticity of the suspending liquid: Theory, experiments and simulations to design a micropipe flow-focuser. *Lab Chip* **12**, 1638–1645 (2012).

68. Tian, F. *et al.* Microfluidic co-flow of Newtonian and viscoelastic fluids for high-resolution separation of microparticles. *Lab Chip* **17**, 3078–3085 (2017).

69. Huang, P. Y., Feng, J., Hu, H. H. & Joseph, D. D. Direct simulation of the motion of solid particles in Couette and Poiseuille flows of viscoelastic fluids. *J. Fluid Mech.* **343**, 73–94 (1997).

70. Del Giudice, F. *et al.* Particle alignment in a viscoelastic liquid flowing in a square-shaped microchannel. *Lab Chip* **13**, 4263–4271 (2013).

71. Del, F., Gaetano, G., Greco, F., Netti, P. A. & Luca, P. Effect of fluid rheology on particle migration in a square - shaped microchannel. *Microfluid. Nanofluidics* **19**, 95–104 (2015).

72. Stoecklein, D. & Di Carlo, D. Nonlinear Microfluidics. *Anal. Chem.* **91**, 296–314 (2019).

73. Song, H. Y., Lee, S. H., Salehiyan, R. & Hyun, K. Relationship between particle focusing and dimensionless numbers in elasto-inertial focusing. *Rheol. Acta* **55**, 889–900 (2016).

74. Kim, B. & Kim, J. M. Elasto-inertial particle focusing under the viscoelastic flow of DNA solution in a square channel. *Biomicrofluidics* **10**, (2016).

75. Faridi, M. A. *et al.* Elasto-inertial microfluidics for bacteria separation from whole blood for sepsis diagnostics. *J. Nanobiotechnology* **15**, 1–9 (2017).

76. Nam, J. *et al.* Microfluidic device for sheathless particle focusing and separation using a viscoelastic fluid. *J. Chromatogr. A* **1406**, 244–250 (2015).

77. Yang, S. H., Lee, D. J., Youn, J. R. & Song, Y. S. Double-line particle focusing induced by negative normal stress difference in a microfluidic channel. *Microfluid. Nanofluidics* **23**, 1–10 (2019).

78. Nam, J., Lim, H., Kim, D., Jung, H. & Shin, S. Continuous separation of microparticles in a microfluidic channel via the elasto-inertial effect of non-Newtonian fluid. *Lab Chip* **12**, 1347–1354 (2012).

79. Holzner, G., Stavrakis, S. & DeMello, A. Elasto-Inertial Focusing of Mammalian Cells and Bacteria Using Low Molecular, Low Viscosity PEO Solutions. *Anal. Chem.* **89**, 11653–11663 (2017).

80. Ahn, S. W., Lee, S. S., Lee, S. J. & Kim, J. M. Microfluidic particle separator utilizing sheathless elasto-inertial focusing. *Chem. Eng. Sci.* **126**, 237–243 (2015).

81. Xiang, N., Dai, Q. & Ni, Z. Multi-train elasto-inertial particle focusing in straight

microfluidic channels. *Appl. Phys. Lett.* **109**, (2016).

82. Liu, C. *et al.* Size-Based Separation of Particles and Cells Utilizing Viscoelastic Effects in Straight Microchannels. *Anal. Chem.* **87**, 6041–6048 (2015).

83. Liu, C., Xue, C. & Hu, G. *Sheathless Separation of Particles and Cells by Viscoelastic Effects in Straight Rectangular Microchannels*. *Procedia Engineering* **126**, (Elsevier B.V., 2015).

84. Lu, X., DuBose, J., Joo, S. W., Qian, S. & Xuan, X. Viscoelastic effects on electrokinetic particle focusing in a constricted microchannel. *Biomicrofluidics* **9**, (2015).

85. Fan, L. L. *et al.* Enhanced viscoelastic focusing of particle in microchannel. *Electrophoresis* **41**, 973–982 (2020).

86. Li, D., Lu, X. & Xuan, X. Viscoelastic separation of particles by size in straight rectangular microchannels: A parametric study for a refined understanding. *Anal. Chem.* **88**, 12303–12309 (2016).

87. Villone, M. M. Lateral migration of deformable particles in microfluidic channel flow of Newtonian and viscoelastic media: a computational study. *Microfluid. Nanofluidics* **23**, 1–13 (2019).

88. Ha, B., Park, J., Destgeer, G., Jung, J. H. & Sung, H. J. Transfer of Microparticles across Laminar Streams from Non-Newtonian to Newtonian Fluid. *Anal. Chem.* **88**, 4205–4210 (2016).

89. Xiang, N. *et al.* Fundamentals of elasto-inertial particle focusing in curved microfluidic channels. *Lab Chip* **16**, 2626–2635 (2016).

90. Xiang, N., Ni, Z. & Yi, H. Concentration-controlled particle focusing in spiral elasto-inertial microfluidic devices. *Electrophoresis* **39**, 417–424 (2018).

91. Yuan, D. *et al.* Dean-flow-coupled elasto-inertial particle and cell focusing in symmetric serpentine microchannels. *Microfluid. Nanofluidics* **23**, 1–9 (2019).

92. Feng, H. *et al.* Viscoelastic Particle Focusing and Separation in a Spiral Channel. *Micromachines* **13**, 361 (2022).

93. Zhou, Y., Ma, Z. & Ai, Y. Dynamically tunable elasto-inertial particle focusing and sorting in microfluidics. *Lab Chip* **20**, 568–581 (2020).

94. Tang, W. *et al.* Elasto-inertial particle focusing in 3D-printed microchannels with unconventional cross sections. *Microfluid. Nanofluidics* **23**, 1–10 (2019).

95. Raoufi, M. A. *et al.* Fabrication of unconventional inertial microfluidic channels using wax 3D printing. *Soft Matter* **16**, 2448–2459 (2020).

96. Tang, D., Chen, M., Han, Y., Xiang, N. & Ni, Z. Asymmetric serpentine microchannel based impedance cytometer enabling consistent transit and accurate characterization of tumor cells and blood cells. *Sensors Actuators B. Chem.* **336**, 129719 (2021).

97. Zhou, Y., Ma, Z. & Ai, Y. Sheathless inertial cell focusing and sorting with serial reverse

wavy channel structures. *Microsystems Nanoeng.* **4**, 5 (2018).

98. Narayana Iyengar, S., Kumar, T., Mårtensson, G. & Russom, A. High resolution and rapid separation of bacteria from blood using elasto-inertial microfluidics. *Electrophoresis* **42**, 2538–2551 (2021).

99. Kumar, T., Ramachandraiah, H. & Iyengar, S. N. High throughput viscoelastic particle focusing and separation in spiral microchannels. *Sci. Rep.* **11**, 1–13 (2021).

100. Kim, B., Lee, S. S., Yoo, T. H. & Kim, J. M. Viscoelastic particle focusing in human biofluids. *Electrophoresis* **42**, 2238–2245 (2021).

101. Lu, X. *et al.* Sheathless and high-throughput elasto-inertial bacterial sorting for enhancing molecular diagnosis of bloodstream infection. *Lab Chip* **21**, 2163–2177 (2021).

102. Raoufi, M. A. *et al.* Effects of sample rheology on the equilibrium position of particles and cells within a spiral microfluidic channel. *Microfluid. Nanofluidics* **25**, 1–13 (2021).

103. Vamerzani, B. Z., Norouzi, M. & Firoozabadi, B. Analytical solution for creeping motion of a viscoelastic drop falling through a Newtonian fluid. *Korea Aust. Rheol. J.* **26**, 91–104 (2014).

104. Norouzi, M., Kayhani, M. H., Shu, C. & Nobari, M. R. H. Flow of second-order fluid in a curved duct with square cross-section. *J. Nonnewton. Fluid Mech.* **165**, 323–339 (2010).

105. Sprenger, L., Dutz, S., Schneider, T., Odenbach, S. & Hafeli, U. O. Simulation and experimental determination of the online separation of blood components with the help of microfluidic cascading spirals. *Biomicrofluidics* **9**, 044110 (2015).

106. Ducloué, L. *et al.* Secondary flows of viscoelastic fluids in serpentine microchannels. *Microfluid. Nanofluidics* **23**, 1–10 (2019).

107. Yu, Z., Wang, P., Lin, J. & Hu, H. H. Equilibrium positions of the elasto-inertial particle migration in rectangular channel flow of Oldroyd-B viscoelastic fluids. *J. Fluid Mech.* **868**, 316–340 (2019).

108. Nakanishi, H., Nagahiro, S. I. & Mitarai, N. Fluid dynamics of dilatant fluids. *Phys. Rev. E - Stat. Nonlinear, Soft Matter Phys.* **85**, (2012).

109. Boersma, W. H. & Stein, H. N. Shear Thickening (Dilatancy) in Concentrated Dispersions. **36**, (1990).

110. Lee, Y. S. & Wagner, N. J. Rheological Properties and Small-Angle Neutron Scattering of a Shear Thickening, Nanoparticle Dispersion at High Shear Rates. *Ind. Eng. Chem. Res.* **45**, 7015–7024 (2006).

111. Wagner, N. J., Brady, J. F., Wagner, N. J. & Brady, J. F. Shear thickening in colloidal dispersions. *Phys. Today.* **69**, 27–32 (2009).

112. Lee, Y. S. & Wagner, N. J. Dynamic properties of shear thickening colloidal suspensions. *Rheol. Acta* **42**, 199–208 (2003).

113. Hasanzadeh, M., Mottaghitalab, V., Hasanzadeh, M. & Mottaghitalab, V. The Role of

Shear-Thickening Fluids (STFs) in Ballistic and Stab-Resistance Improvement of Flexible Armor. **23**, 1182–1196 (2014).

114. Gürgen, S., Kuşhan, M. C. & Li, W. Shear thickening fluids in protective applications: A review. *Prog. Polym. Sci.* **75**, 48–72 (2017).

115. Moldoveanu, G. M., Ibanescu, C., Danu, M. & Minea, A. A. Viscosity estimation of Al2O3, SiO2 nanofluids and their hybrid: An experimental study. *J. Mol. Liq.* **253**, 188–196 (2018).

116. Fall, A., Bertrand, F., Ovarlez, G. & Bonn, D. Shear thickening of cornstarch suspensions. *J. Rheol. (N. Y. N. Y).* **56**, 575–591 (2012).

117. Mahmoodi, M. *et al.* Secondary flow structures in developing viscoelastic fluid flow through curved ducts with square cross section. *Meccanica* **56**, 2979–2999 (2021).

118. Namburu, P. K., Electric, L., Kulkarni, D. & Das, D. K. Experimental investigation of viscosity and specific heat of silicon dioxide nanofluids. *Micro Nano Lett.* **3**, 67–71 (2007).

119. Bahari, N. M., Nurliyana, S., Mohamed, C. & Hidayati, N. Synthesis of Al 2 O 3 – SiO 2 / water hybrid nanofluids and effects of surfactant toward dispersion and stability. *Part. Sci. Technol.* **39**, 844–58 (2020).

120. Yang, S. H., Lee, D. J., Youn, J. R. & Song, Y. S. Multiple-Line Particle Focusing under Viscoelastic Flow in a Microfluidic Device. *Anal. Chem.* **89**, 3639–3647 (2017).

121. Lim, E. J. *et al.* Inertio-elastic focusing of bioparticles in microchannels at high throughput. *Nat. Commun.* **5**, 1–9 (2014).

122. Nikdoost, A. & Rezai, P. Dean Flow Velocity of Shear Thickening SiO 2 Nanofluids in Curved Microchannels. *Phys. Fluids* **34**, 062009 (2022).

123. Nikdoost, A. & Rezai, P. Dean flow velocity of viscoelastic fluids in curved microchannels. *AIP Adv.* **10**, 085015 (2020).

124. Xia, Y. N. & Whitesides, G. M. Soft lithography. *Annu. Rev. Mater. Sci.* **37**, 551–575 (1998).

125. Ebagninin, K. W., Benchabane, A. & Bekkour, K. Rheological characterization of poly(ethylene oxide) solutions of different molecular weights. *J. Colloid Interface Sci.* **336**, 360–367 (2009).

126. Rodd, L. E., Scott, T. P., Boger, D. V., Cooper-White, J. J. & McKinley, G. H. The inertio-elastic planar entry flow of low-viscosity elastic fluids in micro-fabricated geometries. *J. Nonnewton. Fluid Mech.* **129**, 1–22 (2005).

127. Rodd, L. E., Cooper-white, J. J., Boger, D. V & Mckinley, G. H. Role of the elasticity number in the entry flow of dilute polymer solutions in micro-fabricated contraction geometries. *J. non* **143**, 170–191 (2007).

128. Lu, X. & Xuan, X. Continuous Microfluidic Particle Separation via Elasto-Inertial Pinched Flow Fractionation. *Anal. Chem.* **87**, 6389–6396 (2015).

129. Zilz, J. *et al.* Serpentine channels: Micro-rheometers for fluid relaxation times. *Lab Chip*

14, 351–358 (2014).

130. Tirtaatmadja, V., McKinley, H. G. & Cooper-White, J. J. Drop formation and breakup of low viscosity elastic fluids: Effects of molecular weight and concentration. *Phys. Fluids* **18**, 1–18 (2006).

131. Harris, K. R. & Woolf, L. A. Temperature and volume dependence of the viscosity of water and heavy water at low temperatures. *J. Chem. Eng. Data* **49**, 1851 (2004).

132. Bahlouli, M. I., Bekkour, K., Benchabane, A., Hemar, Y. & Nemdili, A. The effect of temperature on the rheological behavior of polyethylene oxide (PEO) solutions. *Appl. Rheol.* **23**, 1–15 (2013).

133. Meybodi, M. K. *et al.* A novel correlation approach for viscosity prediction of water based nanofluids of Al2O3, TiO2, SiO2 and CuO. *J. Taiwan Inst. Chem. Eng.* **58**, 19–27 (2016).

134. Meybodi, M. K., Naseri, S., Shokrollahi, A. & Daryasafar, A. Prediction of viscosity of water-based Al2O3, TiO2, SiO2, and CuO nanofluids using a reliable approach. *Chemom. Intell. Lab. Syst.* **149**, 60–69 (2015).

135. Schneider, C. A., Rasband, W. S. & Eliceiri, K. W. NIH Image to ImageJ: 25 years of image analysis. *Nat. Methods* **9**, 671–675 (2012).

136. Abràmoff, M. D., Magalhães, P. J. & Ram, S. J. Image processing with imageJ. *Biophotonics Int.* **11**, 36–41 (2004).

137. Helin, L., Thais, L. & Mompean, G. Numerical simulation of viscoelastic Dean vortices in a curved duct. *J. Nonnewton. Fluid Mech.* **156**, 84–94 (2009).

138. Poole, R. J., Lindner, A. & Alves, M. A. Viscoelastic secondary flows in serpentine channels. *J. Nonnewton. Fluid Mech.* **201**, 10–16 (2013).

139. Nikdoost, A. & Rezai, P. Dean flow velocity of viscoelastic fluids in curved microchannels. *AIP Adv.* **10**, (2020).

140. Nussbaum-Krammer, C. I., Neto, M. F., Brielmann, R. M., Pedersen, J. S. & Morimoto, R. I. Investigating the spreading and toxicity of prion-like proteins using the metazoan model organism C. Elegans. *J. Vis. Exp.* **95**, 1–15 (2015).

141. D'Avino, G. & Maffettone, P. L. Particle dynamics in viscoelastic liquids. *J. Nonnewton. Fluid Mech.* **215**, 80–104 (2015).

142. Tian, F. *et al.* Label-free isolation of rare tumor cells from untreated whole blood by interfacial viscoelastic. *Lab Chip* **18**, 3436–3445 (2018).

143. Zhang, J. *et al.* A novel viscoelastic-based ferrofluid for continuous sheathless microfluidic separation of nonmagnetic microparticles. *Lab Chip* **16**, 3947–3956 (2016).

144. Charjouei Moghadam, M. Investigation of microparticles behavior in Newtonian , viscoelastic , and shear-thickening flows in straight microfluidic channels. *York Univ.* (2021).

145. Ortseifen, V., Viefhues, M., Wobbe, L. & Grünberger, A. Microfluidics for Biotechnology:

Bridging Gaps to Foster Microfluidic Applications. *Front. Bioeng. Biotechnol.* **8**, 1–12 (2020).

Authors Contribution during PhD

Journal Papers:

1. **Arsalan Nikdoost** and Pouya Rezai, "Experimental Investigation of Microparticle Focusing in Shear-thickening SiO_2 Nanofluids inside Curvilinear Microchannels" (under preparation)
2. **Arsalan Nikdoost** and Pouya Rezai, "Microparticle Manipulation in Viscoelastic Flows inside Curvilinear Microchannels: A Thorough Fundamental Study with Application to Simultaneous Particle Sorting and Washing", *Soft Matter* (under review)
3. **Arsalan Nikdoost** and Pouya Rezai, "Dean Flow Velocity of Shear-thickening SiO_2 Nanofluids in Curved Microchannels", *Physics of Fluids* **34**, 062009 (2022)
   DOI: https://doi.org/10.1063/5.0094688
4. **Arsalan Nikdoost**, Ali Doostmohammadi, Kevin Romanick, Mario Thomas, and Pouya Rezai, "Integration of Microfluidic Sample Preparation with PCR Detection to Investigate the Effects of Simultaneous DNA-Inhibitor Separation and DNA Solution Exchange", *Analytica Chimica Acta* **1160** (2021):338449
   DOI: https://doi.org/10.1016/j.aca.2021.338449
5. **Arsalan Nikdoost** and Pouya Rezai, "Dean Flow Velocity of Viscoelastic Fluids in Curved Microchannels", *AIP Advances* **10:8** (2020):08515
   DOI: https://doi.org/10.1063/5.0019021

Conference Papers:

1. **Arsalan Nikdoost** and Pouya Rezai, “Dean Flow of Shear-thickening Nanofluids in Curved Microchannels”, Micro Flow and Interfacial Phenomena μFIP 2022 Conference, Irvine, USA, June 2022
2. **Arsalan Nikdoost** and Pouya Rezai, “Empirical Correlation for Dean Flow Velocity of Viscoelastic Fluids in Curved Microchannels”, 22nd International Conference on Miniaturized Systems for Chemistry and Life Sciences (MicroTAS 2018), Kaohsiung, Taiwan, November 2018
3. **Arsalan Nikdoost** and Pouya Rezai, “Towards Development of an Empirical Correlation for Dean Flow Velocity of viscoelastic Fluids in Curved Microchhanels“, 2018 Joint Ontario-on-a-Chip and TOeP Symposium, University of Toronto, Toronto, Canada, May 2018

Other Publications outside the Scope of the Thesis:

1. Nima Norouzy, **Arsalan Nikdoost** and Pouya Rezai, “Ultra high Throughput Inertial Microfluidic Device for Microparticle Enrichment and Solution Exchange”, Annual Conference and Exposition (ACE23), American Water Works Association, June 2023, under review

Appendices

Appendix A.

Published paper on integration of microfluidic sample preparation with PCR detection to investigate the effects of simultaneous DNA-Inhibitor separation and DNA solution exchange (Reprinted with permission from Elsevier).

Analytica Chimica Acta 1160 (2021) 338449

Contents lists available at ScienceDirect

Analytica Chimica Acta

journal homepage: www.elsevier.com/locate/aca

Integration of microfluidic sample preparation with PCR detection to investigate the effects of simultaneous DNA-Inhibitor separation and DNA solution exchange

Arsalan Nikdoost [a], Ali Doostmohammadi [a], Kevin Romanick [b], Mario Thomas [b], Pouya Rezai [a, *]

[a] Department of Mechanical Engineering, York University, Toronto, ON, Canada
[b] Precision Biomonitoring Inc., Guelph, ON, Canada

HIGHLIGHTS

- Integrated application of a microfluidic sample preparation chip with portable qPCR.
- Dean flow microfluidic DNA separation from inhibitor molecules using microparticles.
- Simultaneous DNA solution exchange to PCR buffer at continuous high flow rate.
- Device performance characterized in various DNA and inhibitor configurations.
- The microfluidic sample preparation significantly enhanced the performance of qPCR.

GRAPHICAL ABSTRACT

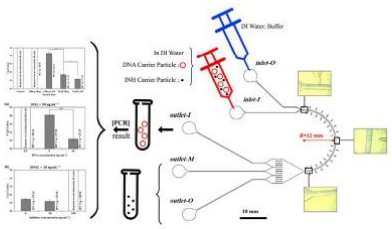

ARTICLE INFO

Article history:
Received 13 November 2020
Received in revised form
23 February 2021
Accepted 21 March 2021
Available online 26 March 2021

Keywords:
Microfluidic
Dean flow focusing
Dean flow solution exchange
DNA-Inhibitor separation
DNA Washing
PCR Detection

ABSTRACT

In this paper, we applied a curved-channel microfluidic device to separate DNA from PCR-inhibitor-containing water and simultaneously wash them into clean water for detection using a portable PCR thermocycler. Environmental DNA (eDNA) sampling has become an effective surveying approach for detecting rare organisms. However, low concentration eDNA molecules may be masked by PCR inhibitors during amplification and detection, increasing the risk of false negatives. Therefore, technologies for on-site DNA separation and washing are urgently needed. Our device consisted of a half-circle microchannel with a DNA-inhibitor sample inlet, a clean buffer inlet, and multiple outlets. By using the flow-induced inertial forces, 10 μm DNA-conjugated microparticles were focused at the inner-wall of the curved microchannel while separation from 1 μm inhibitor-conjugated microparticles and DNA washing were achieved simultaneously with the Dean flow. We achieved singleplex focusing, isolation and washing of 10 μm particles at an efficiency of 94.5 ± 2.0%. In duplex experiments with 1 μm and 10 μm particles, larger particles were washed with an efficiency of 92.1 ± 1.6% and a purity of 79 ± 2%. By surface-functionalizing the microparticles with affinity groups against Atlantic salmon DNA and humic acid (HA), and processing samples of various concentrations in our device, we achieved an effective purification and detection of DNA molecules using the portable PCR thermocycler. Our method significantly decreased PCR quantitation cycles from $Cq > 38$ to $Cq = 30.35 \pm 0.5$, which confirmed enhancement of PCR amplification. The proposed device takes a promising step forward in sample preparation towards an

* Corresponding author. BRG 433B, 4700 Keele St, Toronto, ON, M3J 1P3, Canada.
E-mail address: prezai@yorku.ca (P. Rezai).

https://doi.org/10.1016/j.aca.2021.338449

integrated device that can be used for simultaneous purification and solution exchange of DNA in point-of-need environmental monitoring applications.

1. Introduction

Comprehension of population dispersion and density of organisms is crucial to conserve rare or endangered biological species [1]. However, because of the large variety and diversity, gathering such data is often challenging, time-consuming, and sometimes unreliable [2]. Environmental DNA (eDNA) is DNA extracted from bulk environmental samples (e.g. soil, water, air) without isolating target organisms or their parts from the sample [3]. Detection of eDNA is a relatively new approach that can increase the accuracy of rare species detection and also reduce the expenses associated with data collection [2,3]. Therefore, eDNA detection, using the polymerase chain reaction (PCR), has become a powerful tool for the detection of rare or cryptic biological species, especially in aquatic systems [4]. The analysis of water for eDNA will have applications for aquatic organism surveys and conservation projects. Previous researches suggest that although eDNA surveillance methods may be substantially more sensitive and cost-effective than traditional sampling of species, there has been large variation in reported sensitivities. Moreover, eDNA production rates are still unknown for most species [5,6].

Environmental DNA produced by aquatic organisms is distributed in the environment and lost over time as a function of degradation, dilution, deposition, and re-suspension [5–7]. Therefore, it is important to perform sample preparation and eDNA detection on-site, as early as possible to prevent sample degradation. This need has led to the development of portable and rapid DNA extraction and detection methods that are commercially available. One of the examples used in this paper is the M1 Sample Prep Cartridge Kit (Biomeme Inc, USA) which is a compact mobile solution for rapid extraction of purified nucleic acids from a variety of targets [5]. Samples prepared with this kit can be detected using portable thermocyclers (e.g., Franklin™ Real-Time PCR Thermocycler, Biomeme Inc.). Surveys based on these portable technologies may eventually give more definitive answers with regard to species identification and community composition and have the potential to be faster and less costly than conventional methods. They also do not suffer from the limitations and risks of shipping samples to a central laboratory [5]. However, current portable eDNA detection tools still suffer from important limitations such as transferring of PCR-inhibitory molecules to the PCR reaction which reduces their sensitivity to detect rare eDNA molecules.

PCR inhibitors reduce detectability [5–7]. Theoretically, PCR enables the detection of a single DNA molecule. However, the presence of PCR inhibitors in the sample affects the amplification efficiency of PCR, thus lowering the detection performance, as well as the precision of sequence-specific nucleic acid quantification in real-time quantitative PCR (qPCR). For example, one of the most common problems when extracting DNA from environmental sediments is the co-extraction of humic substances (mainly humic acid) and other compounds like tannic and gallic acids, which inhibit DNA detection and quantification in PCR [8]. Humic substances are also ubiquitous in soil and water and can contaminate any exposed material, which may lead to false-negative results [9–11]. Therefore, there is a pressing need to develop simple-to-operate and field-deployable methods to separate DNA from inhibitor molecules automatically, continuously and with high efficiency, reasonable throughput and low cost. Conventional methods of DNA enrichment based on using microbeads and manual pipetting [12,13], centrifugation [14], or electrophoretic [15] separation have various drawbacks, including long experimental times and low throughput and/or enrichment quality. Additionally, these methods are difficult to deploy in the field. In recent years, many microfluidic devices for DNA analysis have been proposed encompassing new approaches for sample preparation and DNA extraction, separation, purification and detection [16–21]. Microfluidic approaches for DNA purification operate based on DNA absorbance on the surface of functionalized silica such as packing microchannels with magnetic silica beads [21–25] or fabricating micropillars in silicon microfluidic channels [26].

Bienvenue et al. [22] reported a microdevice capable of integrating DNA purification and multiplexed short tandem repeat amplifications using standard laboratory equipment. DNA extraction was performed using a microchannel packed with a silica solid phase and a syringe pump driving the extraction process at a flow rate 4.17 μL min^{-1}. Han et al. [25] introduced an automated microdevice for DNA extraction using monolithically integrated high-pressure microvalves, where DNA was passed through the extraction microchannel packed with silica beads at a flow rate of 180 μL h^{-1}. In spite of the sufficient quality of extracted DNA from the bare silica beads, the working throughput was relatively low. Low working flow rates and throughput are common issues in most developed DNA extraction microfluidic devices, which can limit their use in field applications that feature large volumes and complex samples. Additionally, another drawback of these methods is simultaneous transferring of PCR inhibitors that may reduce PCR performance in complex samples.

In this paper, we demonstrate the utility of an extraction device that addresses the challenges above, in which DNA molecules are separated from PCR-inhibitory molecules and simultaneously washed into a clean buffer via inertial focusing of microparticles and Dean flow recirculation of fluids in a curved microchannel. We have previously investigated the co-flows of water in curved microchannels with different channel geometries and characterized the lateral displacement of fluids in an empirical correlation for the average Dean velocity [27]. We also introduced a microfluidic curved-channel centrifuge for solution exchange of target microparticles and their simultaneous separation from bacteria [28]. Here, we demonstrate the application of curved microfluidic channels in manipulating DNA and inhibitor molecules as a novel application for this technology. Built on specific design optimization and particle focusing investigation, we implemented our method to separate Atlantic salmon DNA from HA PCR-inhibitors using 10 μm and 1 μm functionalized microparticles with surface affinity to target DNA and HA, respectively. The effects of particles surface affinity and DNA, and HA concentrations on the amount of target DNA detection by qPCR were investigated and the performance of the microdevice in DNA concentration enrichment was confirmed. With future developments, our device can be applied as a rapid and low-cost method for on-site DNA and inhibitor molecules separation and washing, with subsequent enhancement of DNA detection using PCR.

2. Theory

In this paper, microparticles with surface affinity to DNA and HA were manipulated in a curved-microchannel device for sample preparation, including DNA-HA separation and DNA solution exchange. Passive microfluidic techniques provide a precise control over the microparticles position in microchannels using inertial, drag, and other flow-induced forces. In square microchannels, particles larger than a threshold size experience inertial forces and occupy four equilibrium positions at the center of each channel wall. Altering the channel aspect ratio ($AR = height/width$) modifies the balance between inertial lift forces. In low aspect ratio channels, particles are transferred towards two central equilibrium positions along the longer cross sectional side of the channel [29,30].

As the particles move laterally across streamlines in a channel due to inertial forces, they experience a lateral drag force against their direction of movement, that could be estimated using the Stokes drag force [31] when the Reynolds number is $Re < 1$.

$$Re = \rho U D_h / \mu \tag{1}$$

In Eq. (1), the fluid density and dynamic viscosity are denoted with ρ and μ, respectively; U represents the fluid velocity either in the axial (U_x) or lateral (U_L) directions, and D_h shows the channel hydraulic diameter. Despite many advantages, particle separation and washing in straight microchannels is limited by low throughputs and multiple particle focusing points. Passive methods using curved microchannels have been introduced to address these challenges [28,32–36].

In a pressure driven flow in curvilinear microchannels like the one used in this study, fluid elements close to the channel center are pushed outwards due to their larger inertia. This would result in a radial pressure gradient [29], which recirculates the relatively motionless fluid elements near the wall, and create the secondary Dean vortices [37]. These symmetric counter-rotating Dean vortices can be characterized by the dimensionless Dean number, which is often used to specify the strength of the secondary flows [38].

$$De = Re\sqrt{\frac{D_h}{2R}} \tag{2}$$

where R represents the radius of curvature of the curved microchannel.

The net inertial lift force on a particle in a curved microchannel can be calculated based on Eq. (3).

$$F_L = \rho \dot{\gamma}^2 C_L a^4 \tag{3}$$

Here, $\dot{\gamma}$ is the shear rate, C_L is the average lift coefficient, and a represents the particle diameter. The shear rate is defined as the ratio of maximum axial velocity ($U_{\max}$) to the channel hydraulic diameter (D_h) as shown in Eq. (4).

$$\dot{\gamma} = \frac{U_{max}}{D_h} \tag{4}$$

In curved microchannels, the secondary Dean vortices could modify the inertial equilibrium positions of particles from two in straight rectangular channels to one position at the inner wall of the curved channel. The Dean drag force (F_D) acting on the particles in a curvilinear microchannel and against their lateral direction of motion can be calculated based on Eq. (5).

$$F_D = 3\pi\mu a V_{De} \tag{5}$$

where V_{De} stands for the average Dean velocity, which shows the average velocity of the secondary Dean vortices in the channel.

The ratio between the Dean drag force and the net inertial lift force, R_f in Eq. (6), specifies the new equilibrium streams as a function of particle size. This has enabled a complete size-based particle separation with a reduced channel footprint while decreasing the required power in spiral microchannels [32,37,39].

$$R_f = \frac{F_L}{F_D} \tag{6}$$

When $R_f \gg 1$, the net inertial force has a dominant effect on particle focusing, while $R_f \ll 1$ results in the dominance of the Dean drag force [28]. Under the dominant effect of inertial forces, particles are focused closer to the inner wall of the channel, while particles are entrained with the Dean vortices along the channel cross section when Dean drag force is larger.

Considering the common range of De in microfluidic applications ($0 < De < 30$), experimental and numerical studies were carried out in our group to fully investigate the effect of channel aspect ratio, radius of curvature, and hydraulic diameter on the Dean velocity (V_{De}) [27,40]. We reported a semi-empirical correlation which could provide an estimation of the average V_{De} of water in a curved microchannel (Eq. (7)) [27].

$$V_{De} = 0.031\, \vartheta/_S De^{1.63} \tag{7}$$

Here, $\vartheta = \mu/_\rho$ is the kinematic viscosity of the fluid and $s = \max(w,h)$ is the largest channel cross-sectional dimension, where the channel width and height are denoted with w and h, respectively.

In order to transfer a target microparticle from a sample fluid into a clean buffer in a curved microchannel with two inlets (one for sample and one for buffer), two criteria should be satisfied simultaneously. First, the R_f value in Eq. (6) must be larger than one to ensure particle focusing at the inner wall of the channel. Second, fluid displacement should be controlled to exactly 0.5 recirculation using the lateral fluid migration (L_R) that can be calculated from Eq. (8) [27,28].

$$L_R = L_s \frac{V_{De}}{V_x} \tag{8}$$

In Eq. (8), V_x *is* the fluid axial velocity and the switching length, L_s, represents the required channel length to reach the first fluid exchange point (i.e. 0.5 recirculation) [27]. The correlations above were used in this paper for designing the curved microchannel for fluid and particle manipulation.

3. Materials and methods

3.1. Sample preparation

A simulated eDNA solution was prepared using 50 mg of Atlantic salmon (*Salmo salar*, L. 1758) tissue spiked into 250 mL of distilled water (DI) and incubated at room temperature for 30 min. This master solution was diluted 100x, which resulted into a detectable range of DNA in a qPCR process (with maximum Cq of 35) [22–24]. One liter of the prepared sample was withdrawn at a flow rate of 1.0 L min^{-1} using a peristaltic pump (MasterFlex, Canada) and passed through a 1.2 μm nitrocellulose membrane filter (Sterlitech Corp., USA). Each filter membrane was rolled up loosely and placed into a 3 mL lysis buffer tube (Biomeme's Sample Homogenization Kit, Biomeme Inc., USA) with the surface area of the filter fully exposed to the buffer. The container was then capped and shaken vigorously for 30 s to release the adsorbed DNA into the buffer. The 3 mL buffer solution was then diluted using 17 mL of DI water. This resulted in final DNA concentration of [DNA] = 10 ng mL^{-1}. In addition, to evaluate the performance of the device at lower

concentrations of DNA, samples with 5 ng mL^{-1} and 2.5 ng mL^{-1} DNA were prepared.

Humic acid (HA) has been reported as an abundant environmental inhibitor alongside tannic acid and gallic acid [8]. To simulate the presence of PCR inhibitors, HA powder (Sigma Aldrich, USA) was added to the prepared buffers at two different concentrations of [HA] = 50 μg mL^{-1} and 100 μg mL^{-1}. These concentrations are mimicking the real environmental sample concentrations, which are highly variable across various environmental samples in different geographical locations, and are in the range that inhibits the PCR reactions as reported by others [41–43].

Microparticles with different surface affinities to DNA or HA were then spiked into the 20 mL samples for further processing in the microfluidic device, as described below. DNA- and HA-free DI water containing non-functionalized microparticles was used as the control sample.

3.2. Microparticle suspension preparation

In order to capture the DNA and PCR-inhibiting HA molecules on separate carriers within the media, 10 μm hydroxyl-terminated and 1 μm amine-terminated silica microspheres (Alpha Nanotech Inc., Canada) were used, respectively. The amine groups on the 1 μm particles' surface bind to the carboxyl group on HA. Other surface chemistries more specific towards targets and inhibitors of interest may also be used with our method. For both particles, equivalent-size non-functionalized microparticles (Spherotech Inc., USA) were used during singleplex and duplex particle-based characterization steps in the microfluidic device. The 1 μm particles with and without affinity to HA molecules are denoted in this paper by *1Aff* and *1Reg*, respectively. Similarly, 10 μm particles with and without affinity to DNA are shown by *10Aff* and *10Reg*, correspondingly.

The effect of particle surface affinities on the DNA-HA separation was investigated by preparing four different particle solutions of (i) 10Reg-1Reg, (ii) 10Reg-1Aff, (iii) 10Aff-1Reg, and (iv) 10Aff-1Aff at constant concentrations of [DNA] = 10 ng mL^{-1}, and [HA] = 50 μg mL^{-1}. These particles were added to the DNA-HA solutions with an approximate concentration of 5×10^5 particles per mL in both singleplex and duplex experiments. The prepared samples were then stirred on a vortex mixer and incubated for 15 min at room temperature. In order to avoid particle aggregation, 1% w v^{-1} Tween 20 (Sigma Aldrich, USA) was added to all solutions [44]. Trypan blue solution (0.4%, sterile-filtered from Sigma-Aldrich) was used to dye the sample solutions (10% v v^{-1}) for enhanced visualization in the fluid investigation steps.

3.3. Microfluidic device

Our curved microchannel, as shown in Fig. 1, was fabricated in polydimethylsiloxane (PDMS, Sylgard 184 silicone elastomer kit, Dow Corning) with 320 μm × 85 μm rectangular cross section, and a curvature radius of $R = 12$ mm. The design consisted of two inlets (inlet-I, and inlet-O) for co-flowing the sample solution and the clean buffer, respectively, a 180° curvature channel for particle and fluid manipulation, and a 30x expanded outlet zone to visualize the particles at a damped velocity under a microscope. Three bifurcated outlets were implemented to enable sample collection and analysis outside of the microfluidic device when particles were too small to be visualized under the microscope. An inverted microscope (Bio-imager, Canada) and a high-speed camera (FASTEC IL3, Canada) were used to capture images across the A-A cross section as shown in Fig. 1.

The Dean flow of liquids 1 (from inlet-I) and 2 (from inlet-O) in our curve channel leads to the generation of three regions at the outlet after 0.5 Dean recirculation, i.e., an inner-wall liquid 2 region (outlet-I), an outer-wall liquid 1 region (outlet-O), and an in-between region with a mixture of liquids 1 and 2 (outlet-M). Our first intention with having three outlets was to capture these fluids separately, especially at outlet-I with a higher purity of liquid 2.

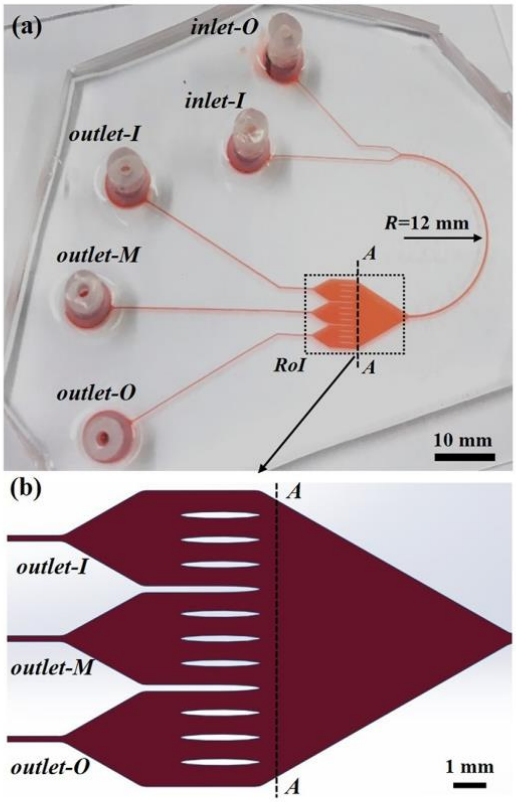

Fig. 1. Microfluidic device for DNA separation from HA in water and simultaneous solution exchange. (**a**) Curved-channel microfluidic device which consisted of two inlets and three bifurcated outlets (I; Inner, M: Middle, O: Outer). The rectangular cross section of the 180-degree curved channel had a w = 320 μm width and an h = 85 μm height with a R = 12 mm radius of curvature. Particles were supplied through inlet-I, alongside a clean DI water buffer at inlet-O. The target 10 μm microparticles were focused and collected at the outlet-I, while smaller 1 μm particles were pushed towards the outer wall. (**b**) Enlarged representation of the expanded outlet shown by Region of Interest (RoI) in (a). Oval micropillars were used to ensure the structural stability of the outlet.

Photolithography and soft lithography were used to fabricate the replication mold and the microfluidic device, respectively. The master mold was prepared using SU-8 2075 photoresist (Micro-Chem Corp., USA) patterned on a silicon wafer (Wafer World Inc., USA). Initially, photoresist was spin coated on a 4-inch diameter wafer at 2500 rpm. Pre-baking was performed at 65 °C and 95 °C, followed by UV light exposure with a dose of 215 mJ cm^{-2} using a photomask and an Ultraviolet Exposure System (UV-KUB 2, KLOE, France). The master mold was then developed in SU8 developer after post-baking at 65 °C and 95 °C. Finally, the silicon master mold was hard-baked at 200 °C. Microfluidic devices were fabricated from casting 10-to-1 ratio base-to-reagent PDMS prepolymer on the mold using the standard soft lithography technique [45] and

bonding the layers onto glass slides using pre-exposure to oxygen plasma.

3.4. Data analysis

3.4.1. Dean flow induced fluid recirculation in the curved channel

A co-flow of DI water dyed with 10% v v^{-1} trypan blue and undyed DI water in inlet-O and inlet-I of the microfluidic device was used to investigate the fluid exchange behavior at three flow rates of Q_t = 1, 1.5, and 2 mL min^{-1} (Q = 0.5, 0.75, and 1 mL min^{-1} for each co-flow stream). Co-flows were video recorded with the inverted microscope at 5x magnification. Using the open source software ImageJ [46,47], color intensities, c_i, were measured across the channel width at 10° intervals. The standard deviation of intensities along the channel width (σ in Eq. (9)) were used to calculate the switching index, *SI*, in Eq. (10).

$$\sigma = \sqrt{(1/N)\sum_{i=1}^{N}(c_i - \bar{c})^2} \tag{9}$$

, where $\bar{c}$ shows the average intensity value and N is the number of points (pixels) across the channel width.

The switching index *SI* in Eq. (10) was defined as the normalized standard deviation of color intensities at different intervals along the channel, with respect to the maximum standard deviation observed at the channel entrance (σ_{max}).

$$SI = \sigma/\sigma_{max} \tag{10}$$

3.4.2. Particle sorting efficiency and purity

Microparticles were introduced from the inner wall inlet-I into the device, while DI water was supplied through the inlet-O. Using the high-speed camera, images were captured across the cross-section A-A at a frame rate of 1400 fps (see Supplementary Video 1). The images were then transferred to ImageJ, where the particles were counted using the WrMTrck plugin [48]. At each stage, approximately 1 s of flow was recorded and used to count the number of collected particles at each outlet. Where particles were difficult to be seen in the device due to small size or high velocity, image analysis was not used and the collected solutions from all outlets were analyzed using a hemocytometer (Marienfeld, Germany).

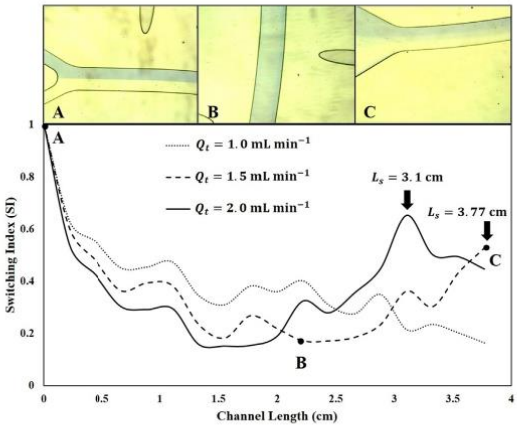

Fig. 2. Swtiching index, SI, values alongside the channel length for co-flow of DI water in the curvilinear microchannel (w = 320 μm, h = 85 μm, and R = 12 mm) at various flow rates. Co-flow images at the entrance (A), mid-section (B), and outlet (C) of the channel are also shown on top row at Q_t = 1.5 mL min^{-1}. Peak values of SI = 0.53 and SI = 0.65 were obtained for co-flows at Q_t = 1.5 and 2 mL min^{-1}, respectively. Full fluid exchange did not occur at Q_t = 1 mL min^{-1} so a peak SI was not obtained. L_s indicates the channel length at which the first switch or 0.5 recirculation occurred.

The separation efficiency of particles was calculated by the ratio of particles collected at each outlet divided by the total number of particles in all outlets as shown in Eq. (11) [49]:

$$\text{Efficiency} = \frac{\text{Number of Target Particles in Selected Outlet}}{\text{Total Number of Target Particles in All Outlets}} \times 100 \tag{11}$$

Duplex experiments using the 1 μm and 10 μm particles were performed in order to achieve the optimum condition for separation of the target particles (i.e. 10 μm). An ideal separation in a multiplex case requires the maximum collection efficiency (Eq. (11)) and purity for the target particles in a selected outlet. Sample purity was calculated as the ratio between the number of target particles and the total number of particles collected in each specific outlet as shown in Eq. (12) [49].

$$\text{Purity} = \frac{\text{Number of Target Particles in the Selected Outlet}}{\text{Total Number of All Particles in the Selected Outlet}} \times 100 \tag{12}$$

3.4.3. DNA purification, extraction and qPCR detection

After optimizing the flow rate in our preliminary studies, DNA-HA solutions at different concentrations, spiked with various microparticle combinations, were supplied through the inner inlet-I of the microfluidic device. DI water was infused as the clean buffer through inlet-O. For each test, 10 mL of fluid from the inner outlet-I (Fig. 1) was collected and centrifuged (5 min at 4000 rpm) to separate the target particle-DNA conjugates. Then, the conjugates were washed with 500 μL of protein wash and 500 μL of salt wash buffers, successively. Finally, to release the DNA from particles, purified DNA was eluted in 500 μL of the elution buffer. All the buffers above were procured from Biomeme Inc., USA.

The eluted DNA solution was quantified using a Franklin™ Real-Time qPCR Thermocycler (Biomeme Inc). Three different samples were run in triplicate PCR using lyophilized Atlantic salmon assay test strips containing a duplexed synthetic internal positive control (IPC) assay that indicates the presence of PCR inhibitors. For each sample, wells 1 and 2 were run with 5 μL of elution buffer and 15 μL of deionized ultrapure water for a total reaction volume of 20 μL. Well 3 was run with a double concentration of elution buffer (10 μL of elution buffer and 10 μL of deionized ultrapure water) to compare with the lower concentrations of wells 1 and 2. The quantification cycle (*Cq*), which is inversely proportional to the amount of target DNA in the sample, was used as an index for the approximate amount of the targets. The mean *Cq* values with the standard deviation of three independent experiments were reported. A lower *Cq* correlates with a higher target concentration in a sample. For example, a 10-fold change in the DNA concentration will result in a *Cq* change of 3.3 [50].

3.5. Statistical analysis

Each experiment was done three times and particle counts or *Cq*

values were determined for particle sorting efficiency and purity measurements and PCR detection, respectively. Results are presented as the average value ± the standard deviation. The difference between the *Cq* values were compared using a one-way ANOVA test, where a p-value of less than 0.05 indicates a significant difference. Different significance levels were identified by * for $p < 0.05$ and ** for $p < 0.01$.

4. Results and discussion

Our proposed solution to the problem of co-extracting PCR inhibitors alongside DNA from environmental samples consisted of a microfluidic device (Fig. 1), for separating DNA from inhibitor molecules in a source buffer, while simultaneously washing the DNA molecules into a clean buffer for subsequent PCR detection. Large 10 μm particles were used to immunologically capture DNA and focus them at the inner wall of the channel (outlet-I). Meanwhile, small 1 μm particles were used to capture the inhibitor molecules and transfer them away to the outer wall of the channel (outlet-M and outlet-O). Simultaneous particle separation and solution exchange were achieved by proper design of the microfluidic device to obtain desired forces for focusing of larger particles and a single Dean flow-based solution exchange (0.5 fluid recirculation) as described in the section below.

4.1. Design of the microfluidic device

The optimum design should simultaneously enable focusing, separation and washing of 10 μm microparticles. To achieve this design, channel width, height, and the radius of curvature were considered as optimization variables. As reported by Martel et al. [51], the maximum channel hydraulic diameter should satisfy the $a/D_h > 0.07$ condition for the larger 10 μm particles to inertially focus in the channel. Therefore, the approximate minimums and maximums for the width (w = 250–320 μm) and height (h = 50–120 μm) of the channel were selected while practical limitations of microfabrication were also taken into consideration. A range of radii of curvature, R, between 10 mm and 25 mm was also used to investigate the proper channel dimensions for separation of 10 μm from 1 μm particles.

The R_f ratio between the net inertial lift and the Dean drag forces in Eq. (6) determines the focusing position of microparticles in the curved microchannel. In order to capture the DNA-conjugated 10 μm particles close to the inner wall (outlet-I) under the dominant influence of inertial lift force (Eq. (3)), the R_f ratio should be significantly larger than one. At the same time, the inhibitor-carrying 1 μm microparticles should have a low R_f with the dominance of the Dean drag force (Eq. (5)). Considering the available channel length in the 180° curvature ($L_c = \pi R$), a range of the acceptable switching length (L_s) between $0.95L_c$ to $1.05L_c$ was investigated.

Among a total of 3600 cases investigated, the designs were first filtered (see Supplementary File Section S1) based on the condition above to obtain a half fluid recirculation at the curved channel exit. A total of 513 cases satisfied this condition. Out of these, only 105 cases satisfied the condition for the dominant effect of the net inertial lift force on the 10 μm particles ($R_{f,10} > 1$). These 105 designs were sorted based on their R_f value and the switching lengths, L_s; and the cases with the highest R_f, and closest L_s to $L_c = \pi R$ were considered. As shown in Fig. 1, the optimum case for our microchannel design was a curvilinear microchannel with a 320 μm × 85 μm rectangular cross section, and a curvature radius of R = 12 mm. These specific dimensions resulted in $R_{f,10} = 1.71$ at maximum total flow rate of $Q_t = 2$ mL min^{-1}, which should theoretically keep the 10 μm particles focused close to the inner wall. Based on the average Dean velocity in Eq. (7), at the maximum flow rate, we can also expect a complete fluid exchange at the channel outlet (i.e. 0.5 fluid recirculation).

4.2. Fluid behavior and solution exchange

In order to investigate the fluid exchange behavior in the designed microchannel with 320 μm × 85 μm cross section and R = 12 mm, co-flows of DI water were supplied through the inlets. The switching indices, *SI* in Eq. (10), at three flow rates of $Q_t = 1, 1.5,$ and 2 mL min^{-1} were experimentally obtained. These flow rates corresponded to axial velocities of $V_x = 0.61$, 0.92, and 1.23 m s^{-1}, respectively. The effect of flow rate on *SI* alongside the channel, which represented fluid switching, is illustrated in Fig. 2. At the channel entrance (point A), the switching index is equal to unity. Moving alongside the channel, the *SI*-value decreases gradually due to the lateral Dean vortices. The minimum *SI*-value indicates the cross section at which the inlet-I fluid is sandwiched between top and bottom layers of inlet-O fluid (point B). After this point, the *SI* increases due to continuous fluid recirculation to a peak-value representing the fluids switching location, L_s, at 0.5 recirculation (point C).

At $Q_t = 1$ mL min^{-1}, the secondary Dean flow was weak and *SI* did not reach a peak value at the channel outlet showing that a full fluid exchange did not happen at the channel exit. However, at 1.5 mL min^{-1} the *SI* reached a peak value of 0.53 right at the end of the channel, which indicates a half fluid recirculation at the outlet (L_s = 3.77 cm). Moreover, at $Q_t = 2$ mL min^{-1}, the maximum *SI* value of 0.65 appeared at $L_s = 3.1$ cm. This indicates that the fluid switch occurred slightly before the channel outlet, which is not desirable for solution exchange of target microparticles in later experiments. The results of this investigation suggested that a flow rate of 1.5 mL min^{-1} is the best option to achieve a full solution exchange in our microfluidic device.

4.3. Singleplex particle focusing

In parallel with fluid exchange investigations in the previous section, we examined the particle transport behavior and size-selective focusing of microparticles in the curved channel at flow rates of Q_t = 1, 1.5, and 2 mL min^{-1}. The particle solutions were prepared with a concentration of 5×10^5 particles mL^{-1} and supplied through the inner inlet (inlet-I in Fig. 1). DI water was supplied through inlet-O as the clean buffer. The collection efficiencies were calculated at the three outlets for each particle size based on Eq. (11) as shown in Fig. 3.

When solutions were supplied at $Q_t = 1$ mL min^{-1}, the 1 μm particles with $R_{f,1} = 0.001$ were entrained with Dean vortices and scattered alongside the channel width. Here, since fluid recirculation was not complete, around 32.5 ± 2.0% of smaller particles remained close to the inner wall (Fig. 3a). Meanwhile, the 10 μm particles with $R_{f,10} = 1.33$ were under the dominant effect of inertial forces and collected at 96.0 ± 1.5% efficiency at the inner outlet as shown in Fig. 3b. This can be attributed to both inertial focusing and lack of significant fluid recirculation.

As the flow rate was increased to Q_t = 1.5 mL min^{-1}, we observed a half fluid recirculation (Fig. 2) and 1 μm particles were pushed towards the outer wall by the Dean drag ($R_{f,1} = 0.0015$) and only 28.4 ± 2.0% of them were collected at outlet-I, as illustrated in Fig. 3a. Larger 10 μm particles ($R_{f,10} = 1.54$), on the other hand, still remained close to the inner wall due to the dominance of inertial forces, and were collected with an efficiency of 94.5 ± 2.0% at outlet-I.

When the co-flows were supplied at $Q_t = 2$ mL min^{-1}, fluids had completed a half recirculation before the end of the curvature

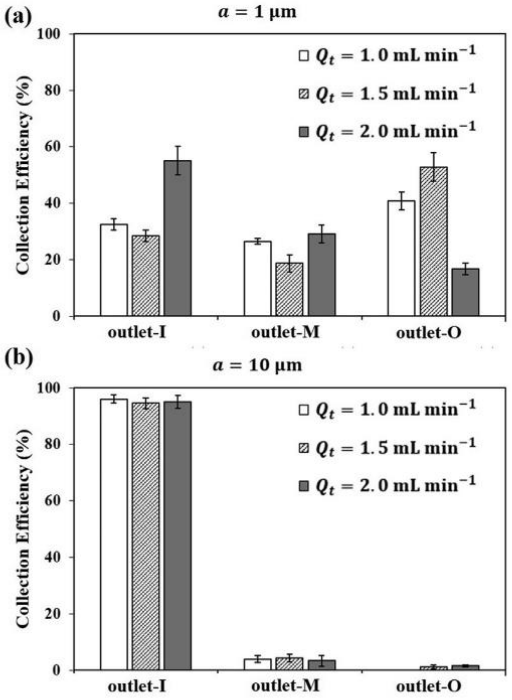

Fig. 3. Collection efficiency of particles at the three outlets of the microfluidic device at flow rates of Q_t = 1, 1.5, and 2 mL min^{-1} for (**a**) 1 μm and (**b**) 10 μm particles. Numbers on the y-axis represent the average efficiency of three samples and error bars indicate the related standard deviations.

(L_s = 3.1 cm), as previously illustrated in Fig. 2. Therefore, the continuous Dean vortices entrained the 1 μm particles ($R_{f,1}$ = 0.0017) back to the inner wall, where 55.1 ± 5.1% of them were collected close to the inner wall at outlet-I (Fig. 3a). At this flow rate, the dominant inertial forces kept the 10 μm particles ($R_{f,10}$ = 1.71) close to the inner wall with around 95.1 ± 2.3% of larger particles collected at outlet-I as shown in Fig. 3b. The results of singleplex experiments suggested that a flow rate of 1.5 mL min^{-1} might be the best option to achieve separation of the two microparticles.

4.4. Duplex particle separation

The focusing and separation of 1 μm and 10 μm microparticles in coexistence (duplex condition) were investigated at three flow rates of Q_t = 1, 1.5, and 2 mL min^{-1}. Microparticle solutions were prepared at the total concentration of 10^6 particles mL^{-1} and supplied through the inner inlet (inlet-I in Fig. 1). DI water was supplied through the inlet-O as the clean buffer. The collection efficiencies from each outlet were calculated for both particles, as shown in Fig. 4a–c.

For all flow rates, 1 μm particles were entrained with the Dean vortices since $R_{f,1}$ «1. As illustrated in Fig. 4a and b, at low and moderate flow rates of 1 and 1.5 mL min^{-1}, 1 μm particles were pushed towards the outer outlet with efficiencies of 69.4 ± 2.5%, and 56.2 ± 5.5%, respectively. At the high flow rate of 2 mL min^{-1}, the small microparticles were entrained with the Dean vortices towards the inner outlet with an efficiency of 64.2 ± 4.2% as shown in Fig. 4c. Slight differences between the singleplex and duplex distribution of 1 μm particles in Figs. 3 and 4 may be due to the duplex nature of the experiments, higher concentration of particles, or the two different counting methods used in these studies (see Materials and Methods section) which requires further investigation in the future.

The larger 10 μm particles were mainly concentrated at the inner outlet for all three flow rates under the dominant effect of net inertial lift forces ($R_{f,10}$ >1). As illustrated in Fig. 4a, at 1 mL min^{-1}, larger particles were collected with an efficiency of 92.6 ± 1.4% close to the inner wall at outlet-I. The collection efficiencies in outlet-I at 1.5 mL min^{-1} (Figs. 4b) and 2.0 mL min^{-1} (Fig. 4c) were 92.1 ± 1.6%, and 92.7 ± 1.5%, respectively. Compared to the singleplex experiments in Fig. 3, the collection efficiencies of 10 μm particles at outlet-I dropped negligibly by 2–3% at the respective flow rates.

The optimum separation condition could be selected based on the collection efficiencies of the duplex experiments and the purity of the target 10 μm particles. As presented in Fig. 4a–c, the collection efficiencies at outlet-I for the target particles stayed relatively constant and high at ~92% at all flow rates. Microparticle purities for duplex separation are presented in Fig. 4d, where target 10 μm particles could be collected with a purity of 88 ± 1% through outlet-I at the low flow rate of 1 mL min^{-1}. However, as illustrated in Fig. 2, this flow rate could not provide a complete fluid exchange at the outlet. As the flow rate increased to 1.5 mL min^{-1}, collection purity dropped to 79 ± 2% at outlet-I, since a higher number of 1 μm particles ended up close to the inner wall. However, as previously shown in Fig. 2, this flow rate resulted in 0.5 fluid recirculation at the channel outlet and could transfer the target particles into the clean DI water. Further increase in the flow rate up to 2 mL min^{-1} resulted in a significant drop of the sample purity at outlet-I down to 59 ± 5%. In order to achieve the highest possible separation efficiency, purity and solution exchange at the same time, Q_t = 1.5 mL min^{-1} was selected as the optimum condition to perform the DNA extraction experiments. This design resulted in the collection of 10 μm particles in the outlet-I with a purer liquid to enhance particle separation purity and DNA solution exchange. Moreover, the design allowed reducing the liquid volume collection to 1/3rd in each outlet, which directly translated into a higher concentration of collected particles.

4.5. DNA separation, washing, and PCR detection

Rare DNA molecules are at most risk of being overlooked by the interference of inhibitors in the PCR detection process crucial to eDNA studies. Various methods have been suggested for the enrichment of microbial samples before PCR [52–56]. Therefore, we aimed to investigate the application of our optimized microfluidic device for (i) separating DNA from PCR-inhibiting HA molecules in a source buffer, (ii) simultaneously washing the DNA molecules into a clean buffer, and (iii) investigating the effect of this microfluidic-based sample preparation step on a subsequent qPCR detection using a commercially available and portable thermocycler. HA has been reported as an abundant environmental inhibitor alongside tannic acid and gallic acid [8,41–43], so it was used in our studies as a PCR inhibitor at environmentally-relevant concentrations and also as a surrogate for other molecules that may be separated from target DNA with our device.

As described in the Materials and Methods section, surface functionalized 10 μm and 1 μm particles were used to capture the DNA and HA molecules, respectively, while sample processing was done in the optimized device (w = 320 μm, h = 85 μm, and R = 12 mm) at the optimum flow rate of Q_t = 1.5 mL min^{-1} to sort

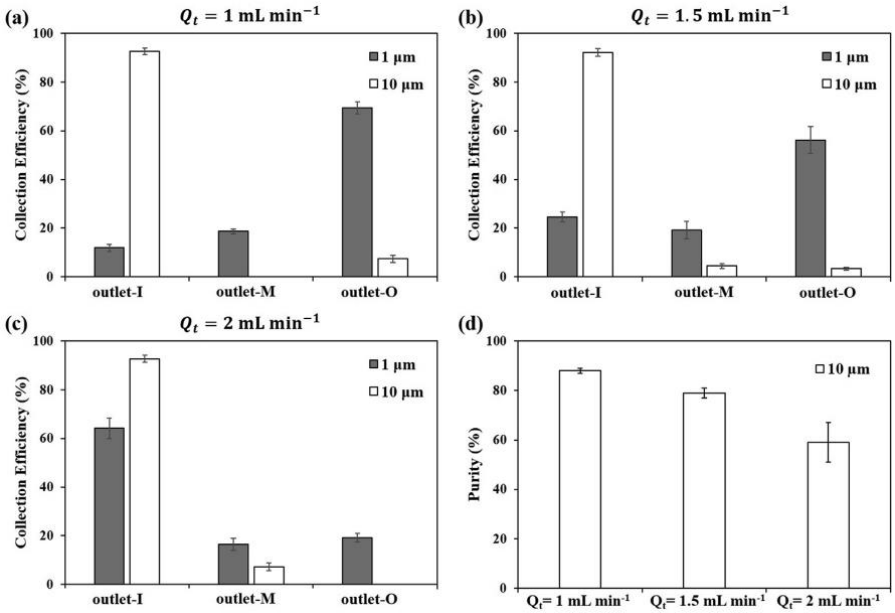

Fig. 4. Duplex particle separation at each outlet for 1 µm and 10 µm particles at three different flow rates of **(a)** Q_t = 1 mL min^{-1}, **(b)** Q_t = 1.5 mL min^{-1}, **(c)** Q_t = 2 mL min^{-1}, and **(d)** Purities of target 10 µm particles at different flow rates. Numbers on the y-axis represent the average efficiencies and purities of three samples with standard deviations shown as error bars.

the conjugates, and to wash the DNA-particle complexes into a detection-ready water sample.

Our first study involved investigating the effect of functional groups of the microparticles on qPCR-based detection of DNA. The DNA and HA concentrations used in this study were 10 ng mL^{-1} and 50 µg mL^{-1}, respectively, except for the control sample which contained non-functionalized particles and no added DNA and HA. After collecting the fluids from outlet-I of the microdevice, DNA contents were eluted and quantified using qPCR with the Franklin™ Thermocycler from Biomeme Inc. The quantification cycles (*Cq*) were recorded for each sample as shown in Fig. 5. The IPC *Cq* values from 500 copies of synthetic DNA are also reported alongside the *Cq* results. Any major variation in IPC *Cq* values out of the range 27–29 would indicate a likely presence of PCR inhibitors [57]. In addition to functionalized particles shown by the "Aff" in Fig. 5, we also spiked the samples with various mixtures of particles without immunological affinity to DNA and HA molecules, symbolled with "Reg" in Fig. 5.

As shown in Fig. 5, no DNA was detected in the control sample. For the DNA-spiked water sample and in the absence of affinity functions on 10 µm (10Reg) and 1 µm (1Reg) particles, no DNA was detected by qPCR within 38 cycles of operation, indicating a very low concentration of target DNA recovered from outlet-I of the device. Since we have a 0.5 Dean flow recirculation in the channel (Fig. 2), the DNA molecules that entered the device from inlet-I were potentially exited from the outlets M and O of the device, given the additional fact that they could not be captured by the blank 10 µm particles. Moreover, the disruptive presence of inhibitor molecules may have further degraded the detection results which was further confirmed in the following experiments.

In the next step, 1 µm functionalized particles (1Aff) were used alongside the regular 10 µm (10Reg) particles. This led to a *Cq* value of 36.65 ± 0.4, which still indicated a low concentration of detectable DNA. However, compared to the previous case (10Reg-1Reg), the use of functionalized 1 µm particles could decrease the inhibitor content in the final sample resulting in a detectable quantification cycle range. However, due to the same reason in the previous experiment, DNA was probably lost to other outlets in the device.

Upon introduction of functionalized 10 µm particles (10Aff), while regular 1 µm particles were used, a significant decrease in *Cq* value to 31.39 ± 0.4 was observed (p-value<0.01 compared to 10Reg-1Aff). This is because the DNA molecules were immunologically captured by the larger microparticles focused at the inner wall of the channel, and washed into the clean buffer before qPCR detection.

Finally, simultaneous use of the functionalized 10 µm and 1 µm particles (10Aff-1Aff) caused a further decrease in the target *Cq* to 30.35 ± 0.1, which indicated a higher copy number of target DNA extracted by the microdevice (~6–7 fold increase compared to 10Aff-1Reg). This result was statistically different (p-value<0.05) from the case with regular 1 µm particles, indicating the importance of HA separation on the outcome of the qPCR process. According to Fig. 4b, at a flow rate of 1.5 mL min^{-1}, the small particles are further pushed towards the outlet-O of the device, and in this case carrying a higher percentage of HA attached to them away from the DNA molecules. This removal of inhibitors by the device, also verified by a small drop in the IPC *Cq* values, may have contributed to the slight enhancement of qPCR detection in Fig. 5.

Next, the device performance was studied at different DNA and HA concentrations, using microparticles with surface affinities to these molecules. Initially, the effect of DNA concentration was

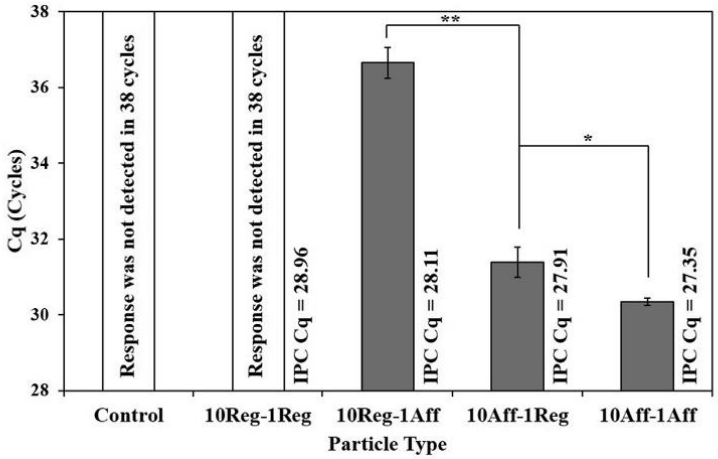

Fig. 5. The effect of particle surface affinity on the qPCR quantification cycle (Cq) of separated DNA streams in outlet-I of the microfluidic device with [DNA] = 10 ng mL^{-1} and [HA] = 50 μg mL^{-1}. The control sample contained non-functionalized (Reg) particles but no added DNA and HA (*: $p < 0.05$, **: $p < 0.01$). Numbers on the x-axis show the microparticle diameters in μm. "Reg" and "Aff" refer to blank and functionalized microparticles, respectively. Cq values on the y-axis represent the average quantification cycle of a triplicate PCR analysis and error bars indicate the related standard deviations. IPC Cq values are reported alongside their respective columns.

explored at a constant HA concentration of 50 μg mL^{-1}. Here, solutions were spiked at three different DNA concentrations of 2.5, 5, and 10 ng mL^{-1} and processed with our device at 1.5 mL min^{-1}. As before, outlet-I samples were tested with qPCR. As illustrated in Fig. 6a, decreasing the DNA concentration from 10 to 5 ng mL^{-1} increased the *Cq* value from 30.35 ± 0.1 to 36.11 ± 0.2 with p-value<0.01. Although this represents a significant change, but target DNA was still detectable by qPCR after processing with our device. A further decrease of the DNA concentration to 2.5 ng mL^{-1} resulted in an undetectable *Cq* value in the qPCR. Accordingly, the limit of DNA processing by our device was 5 ng mL^{-1}. This may be improved in the future with using a higher concentration of microparticles to enhance the chances of capturing the DNA molecules.

Furthermore, the effect of inhibitor content was studied at a constant DNA concentration of 10 ng mL^{-1}. At this point, the solutions were spiked with two different concentrations of HA at 50 and 100 μg mL^{-1}. As shown in Fig. 6b, in the absence of the inhibitor, target DNA was detected with a $Cq = 30.9 \pm 0.2$. Increasing the HA content up to 50 μg mL^{-1} led to a *Cq* of 30.35 ± 0.5, which was not significantly different (p-value>0.05) compared to the control sample with no inhibitor molecules. This result indicated the effective removal of inhibitor molecules using the functionalized microparticles in the microdevice. A further increase in the inhibitor content up to 100 μg mL^{-1} resulted in no DNA detection. This clearly showed the disruptive effect of inhibitor presence in the final sample despite using the small microparticles for their removal, which may be due to a low concentration of these particles and a saturation in binding of HA molecules to them. We concluded that the limit of inhibitor processing with our device was 50 μg mL^{-1}. Removing the inhibitor molecules at higher concentrations might be achievable in the future via the use of higher concentrations of microparticles and/or multiple passing of the sample through the device.

Our results indicated the efficient separation of DNA and inhibitor molecules using functionalized microparticles inside the microfluidic device. This would facilitate the preparation of an

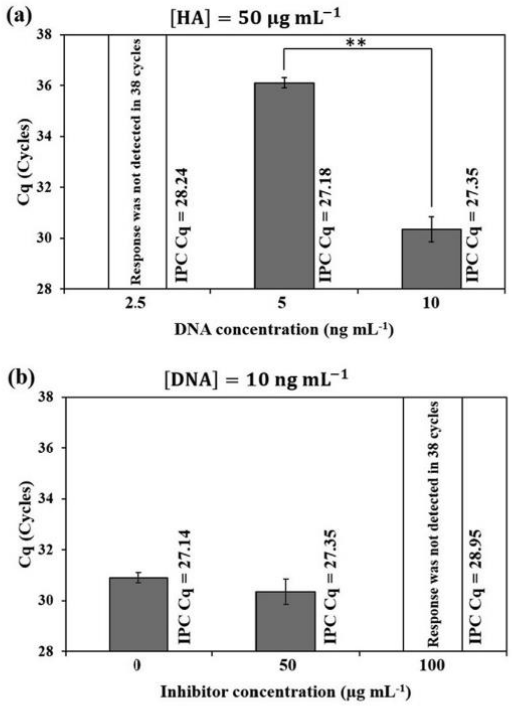

Fig. 6. The effects of (**a**) DNA and (**b**) HA concentrations on the qPCR quantification cycle (Cq) at a constant dose of (**a**) HA (50 μg mL^{-1}) and (**b**) DNA (10 ng mL^{-1}). **: $p < 0.01$. Cq values on the y-axis represent the average quantification cycle of a triplicate PCR analysis and error bars indicate the related standard deviations. IPC Cq values are reported alongside their respective columns.

enriched PCR sample leading to an enhanced DNA detectability. Here, the qPCR detection range was extended by selectively removing the inhibitor molecules at a high throughput. Previous microfluidic separation methods have mostly focused on DNA purification at high concentrations, in the order of ng μL^{-1}, in samples such as whole blood [22,24,58]. Here, we have successfully achieved separation of DNA from inhibitors at lower DNA concentrations of ng mL^{-1}, which fits the need for environmental applications. Our method enables high throughput processing of samples with multi-milliliter volumes at a flow rate of $Q_t = 1.5$ mL min^{-1}, while it removes moderate concentrations of inhibitors and washes low concentrations of DNA from the original sample into a clean detection-ready buffer. This separation and washing throughput offers a significant improvement compared to previous reports, where DNA purifications were performed on microliter-scale sample volumes at flow rates in the order of μL min^{-1} [22,25].

HA is one of the reported inhibitors found in the environmental investigations. However, our method is not exclusive to this inhibitor. In terms of affinity of particles, the 1 μm particles were amine-terminated. The amine group on these particles binds to carboxyl groups on HA so it makes the chemistry non-specific. Applying alternative particles and chemistries would be possible with proper modifications in the microchannel design and use of other functional groups. The design principle would remain the same since it is based on inertial separation. Therefore, dependent on the particle sizes selected, the curve channel can be designed in a way to separate one size of the particles from the others, and perhaps perform multiplex separation of particles in the future. In terms of the functional groups, more specific chemistries can be applied to particle surfaces so that they gain affinity towards specific targets. Additionally, DNA sample enrichment can be further improved in the future by multiple passing of the solution through the microfluidic centrifuge. To our knowledge, this is the first study describing the application of a microfluidic curved-channel centrifuge to enhance the sensitivity of PCR-based DNA detection. This method could potentially be applied to the development of portable point-of-care and point-of-need sample preparation devices such as commercially available methods to detect the rare environmental DNA samples [50].

5. Conclusion

In this study, a microparticle-based sample preparation method was proposed for separation of DNA from inhibitor molecules and simultaneous DNA washing into a clean buffer using a Dean flow-based curved microchannel. Functionalized 1 μm and 10 μm particles with surface affinities to inhibitor and DNA molecules were used to effectively remove the disruptive inhibition effect in qPCR samples. Our designed microdevice with a 320 μm × 85 μm cross section and 12 mm radius of curvature enabled DNA enrichment and enhanced the DNA detectability using a commercial and portable qPCR machine. Through a precise control over the Dean flow-based recirculation of sample and buffer co-flows, Dean drag-based lateral transport of small particles, and inertial force-based focusing of large particles, we achieved simultaneous DNA-inhibitor separation and solution exchange at a flow rate of $Q_t = 1.5$ mL min^{-1} and particle concentration of 10^6 particles mL^{-1}.

The performance of our microfluidic method was investigated in various particle configurations and at different DNA and inhibitor concentrations. It was demonstrated that the use of affinity function groups on the microparticles is necessary in our method. Including both functionalized microparticles at the same time enhanced the performance of the qPCR detection significantly more than the use of only one functionalized particle. Concentration studies demonstrated the limits of processing with our device to be 5 ng mL^{-1} of DNA and 50 μg mL^{-1} of HA. Further investigations on particle concentration could enhance the efficiency of our method at lower DNA concentrations or higher inhibitor content. Moreover, the bifurcated outlet design could be potentially used for a triplex separation and washing process in the future. Our method can also be a vital step towards a portable field-deployable detection device in POU applications.

CRediT authorship contribution statement

Arsalan Nikdoost: Methodology, Formal analysis, Investigation, Data curation, Writing – original draft, preparation. **Ali Doostmohammadi:** Methodology, Formal analysis, Investigation, Data curation, Writing – original draft, preparation. **Kevin Romanick:** Data curation, Formal analysis. **Mario Thomas:** Conceptualization, Resources, Supervision, Funding acquisition, Writing – review & editing. **Pouya Rezai:** Conceptualization, Methodology, Validation, Resources, Writing – review & editing, Supervision, Funding acquisition.

Declaration of competing interest

The authors declare that they have no known competing financial interests or personal relationships that could have appeared to influence the work reported in this paper.

Acknowledgement

This project was funded by the Ontario Ministry of Agriculture, Food and Rural Affairs (OMAFRA) to PR, through the Ontario Agri-Food Innovation Alliance. The authors would like to thank Dr. Steve Crookes for the detailed assessment of the manuscript and constructive recommendations to improve it.

Appendix A. Supplementary data

Supplementary data to this article can be found online at https://doi.org/10.1016/j.aca.2021.338449.

References

[1] K. Bohmann, A. Evans, M.T.P. Gilbert, G.R. Carvalho, S. Creer, M. Knapp, D.W. Yu, M. de Bruyn, Environmental DNA for wildlife biology and biodiversity monitoring, Trends Ecol. Evol. 29 (2014) 358–367, https://doi.org/10.1016/j.tree.2014.04.003.

[2] K.M. Ruppert, R.J. Kline, M.S. Rahman, Past, present, and future perspectives of environmental DNA (eDNA) metabarcoding: a systematic review in methods, monitoring, and applications of global eDNA, Glob. Ecol. Conserv. 17 (2019), https://doi.org/10.1016/j.gecco.2019.e00547 e00547.

[3] K. Deiner, H.M. Bik, E. Mächler, M. Seymour, A. Lacoursière-Roussel, F. Altermatt, S. Creer, I. Bista, D.M. Lodge, N. de Vere, M.E. Pfrender, L. Bernatchez, Environmental DNA metabarcoding: transforming how we survey animal and plant communities, Mol. Ecol. 26 (2017) 5872–5895, https://doi.org/10.1111/mec.14350.

[4] K.D. Balasingham, R.P. Walter, D.D. Heath, Residual eDNA detection sensitivity assessed by quantitative real-time PCR in a river ecosystem, Mol. Ecol. Resour. 17 (2017) 523–532, https://doi.org/10.1111/1755-0998.12598.

[5] A.C. Thomas, S. Tank, P.L. Nguyen, J. Ponce, M. Sinnesael, C.S. Goldberg, A system for rapid eDNA detection of aquatic invasive species, Environ. DNA. (2019) 1–10, https://doi.org/10.1002/edn3.25.

[6] H.C. Rees, B.C. Maddison, D.J. Middleditch, J.R.M. Patmore, K.C. Gough, The detection of aquatic animal species using environmental DNA - a review of eDNA as a survey tool in ecology, J. Appl. Ecol. 51 (2014) 1450–1459, https://doi.org/10.1111/1365-2664.12306.

[7] T.M. Wilcox, K.S. McKelvey, M.K. Young, A.J. Sepulveda, B.B. Shepard, S.F. Jane, A.R. Whiteley, W.H. Lowe, M.K. Schwartz, Understanding environmental DNA detection probabilities: a case study using a stream-dwelling char Salvelinus fontinalis, Biol. Conserv. 194 (2016) 209–216, https://doi.org/10.1016/j.biocon.2015.12.023.

[8] R. Alaeddini, Forensic implications of PCR inhibition - a review, Forensic Sci. Int. Genet. 6 (2012) 297–305, https://doi.org/10.1016/j.fsigen.2011.08.006.

Appendix B.

Curved microchannel dimensions:

Appendix Table B-1: Curved microchannel geometries.

No.	$\boldsymbol{R}$ (cm)	**Curvature** $\boldsymbol{\Theta}$ (degree)	$\boldsymbol{W}$ (μm)	$\boldsymbol{H}$ (μm)	$\boldsymbol{AR}$ = H/W	$\boldsymbol{L_R}$
1	0.5	330	150	150	1.0	$0.62\times D_h$
2	1.0	330	150	75	0.5	$0.8\times D_h$
3	1.0	330	150	150	1.0	$0.62\times D_h$
4	1.0	330	150	225	1.5	$0.59\times D_h$
5	1.5	330	150	150	1.0	$0.62\times D_h$
6	2.0	330	150	150	1.0	$0.62\times D_h$
7	1.0	300	150	75	0.5	$0.8\times D_h$
8	1.0	300	150	150	1.0	$0.62\times D_h$
9	1.0	300	150	225	1.5	$0.59\times D_h$
10	1.0	300	225	150	0.67	$0.67\times D_h$
11	1.0	300	300	150	0.5	D_h
12	1.5	225	150	150	1.0	$0.62\times D_h$
13	1.5	300	150	150	1.0	$0.62\times D_h$
14	2.0	150	150	150	1.0	$0.62\times D_h$
15	2.0	300	150	150	1.0	$0.62\times D_h$

Detailed results of the rheological characterization of PEO solutions:

Appendix Table B-2: Viscosity of PEO solutions at different shear rates.

Shear rate (1/s)	**Viscosity** (mPa.s)			
	125 ppm	***500 ppm***	***1000 ppm***	***2000 ppm***
99.3	1.94	1.93	2.73	5.79
125.0	1.85	1.82	2.58	5.34
157.5	1.73	1.77	2.46	4.79
198.2	1.64	1.72	2.34	4.36
249.5	1.57	1.67	2.26	4.02
314.3	1.48	1.64	2.18	3.66
395.1	1.41	1.62	2.09	3.40
622.0	1.27	1.50	1.89	3.02
783.8	1.24	1.47	1.84	2.91
1240.7	1.20	1.46	1.77	2.75
1563.7	1.18	1.40	1.73	2.68
2469.0	1.16	1.39	1.66	2.53
3121.6	1.15	1.37	1.64	2.46
4945.6	1.15	1.33	1.59	2.36
7850.4	1.21	1.38	1.64	2.31
9880.0	1.21	1.35	1.60	2.24

Appendix C.

Effects of Weissenberg, Dean, and Elasticity numbers on the Dean velocity-based Reynolds number

In order to investigate the effect of fluid relaxation time (λ) and viscosity (μ) on the average Dean velocity, the Reynold number based on the average Dean velocity ($Re_{V_{De}}$) was drawn as a function of Weissenberg (*Wi*), Dean (*De*), and Elasticity (*El*) numbers in Figures C-1 and C-2.

Appendix Figure C-1 represents the $Re_{V_{De}}$ with respect to *Wi* and *De* numbers for co-flows of PEO solutions at various concentrations in square cross-section curved microchannel (150 × 150 μm^2) with various radii of curvatures, *R*.

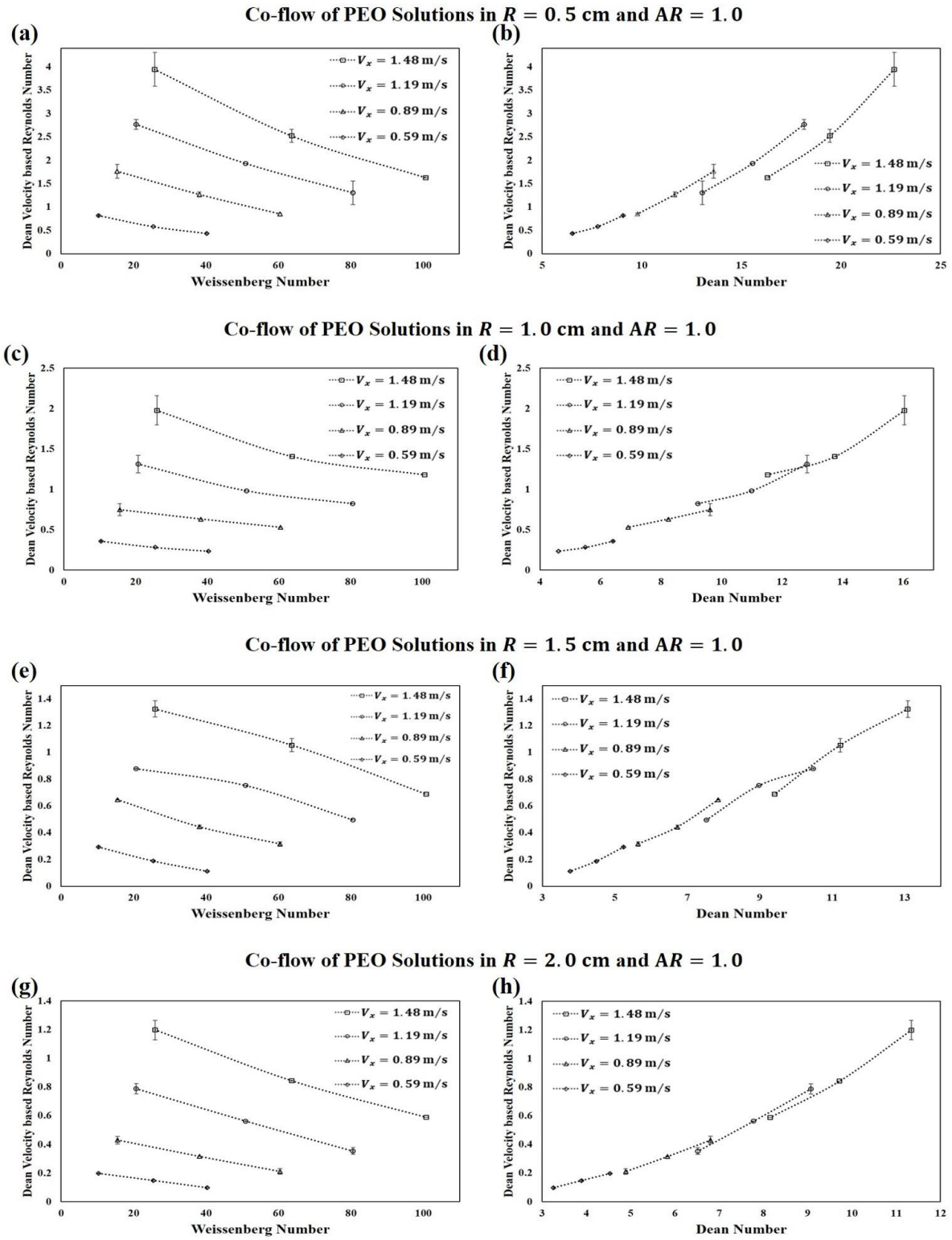

Appendix Figure C-1: Dean velocity-based Reynolds number plotted against Weissenberg and Dean numbers for the co-flows of PEO solutions in a square microchannel with (a-b) R= 0.5 cm, (c-d) R= 1.0 cm, (e-f) R= 1.5 cm, and (g-h) R= 2.0 cm.

Appendix Figure C-2 represents the $Re_{V_{De}}$ with respect to *Wi* and *De* numbers for co-flows of PEO solutions at various concentrations in curved microchannel with aspect ratios *AR* = 0.5 and 1.5 (*h* = 75 and 225 μm respectively).

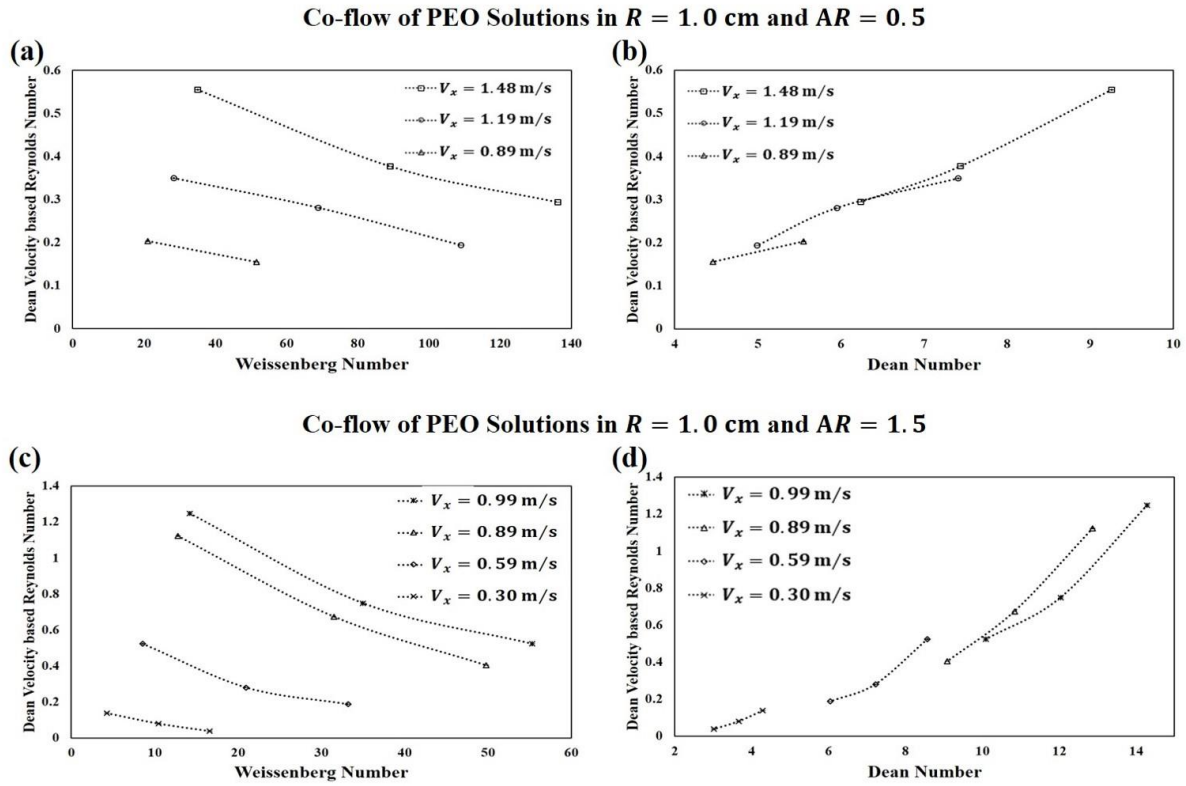

Appendix Figure C-2: Dean velocity-based Reynolds number plotted against Weissenberg and Dean numbers for the co-flows of PEO solutions in curved microchannels with R = 1.0 cm and (a-b) AR = 0.5 and (c-d) AR = 1.5.

To further investigate the effect of relaxation time, the Dean velocity-based Reynolds number could be drawn against the elasticity number (*El*), where *El* represents the ratio of the axial *Re* to *Wi*, as shown in Eq. (1-25).

Appendix Figure C-3, illustrates the effect of *El* number on the $Re_{V_{De}}$ for co-flows of PEO solutions in a square microchannel with different radii of curvatures.

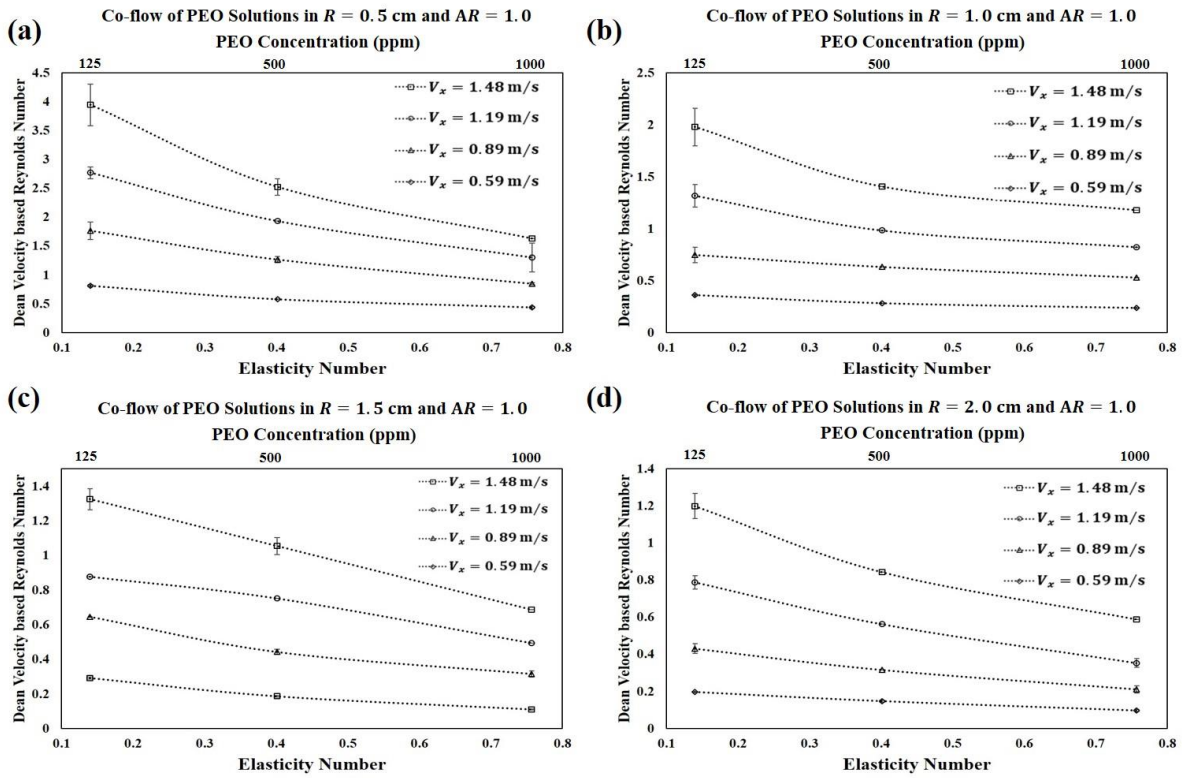

Appendix Figure C-3: Dean velocity-based Reynolds number plotted against Elasticity number for the co-flow of PEO solutions in a square microchannel with (a) R = 0.5 cm, (b) R = 1.0 cm, (c) R = 1.5 cm, and (d) R = 2.0 cm.

Appendix Figure C-4 represents the effect of *El* number on the $Re_{V_{De}}$ for the co-flow of PEO solutions in a rectangular microchannel with *R* = 1.0 cm and *AR* = 0.5 and 1.5.

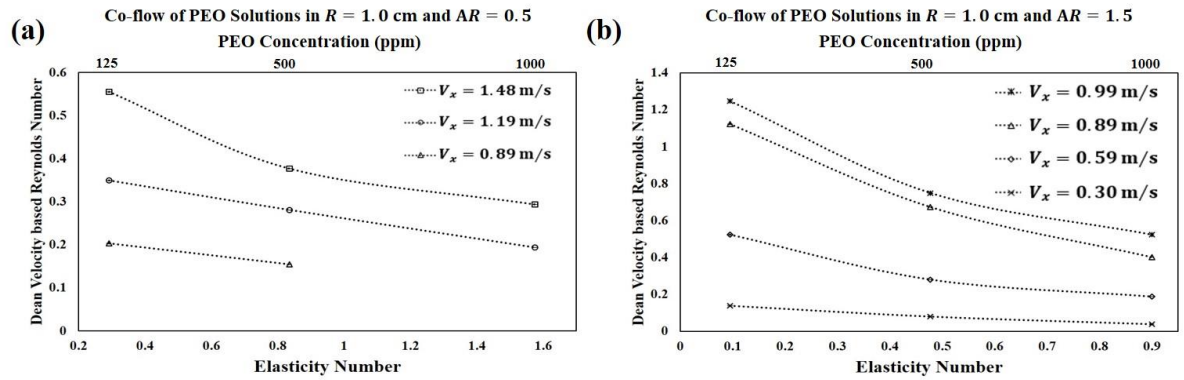

Appendix Figure C-4: Dean velocity-based Reynolds number plotted against Elasticity number for the co-flow of PEO solutions in a R = 1.0 cm rectangular microchannel with (a) AR= 0.5 and (b) AR= 1.5.

Appendix D.

Effect of axial velocity, channel radius of curvature and channel width on the average Dean velocity of SiO_2 nanofluids:

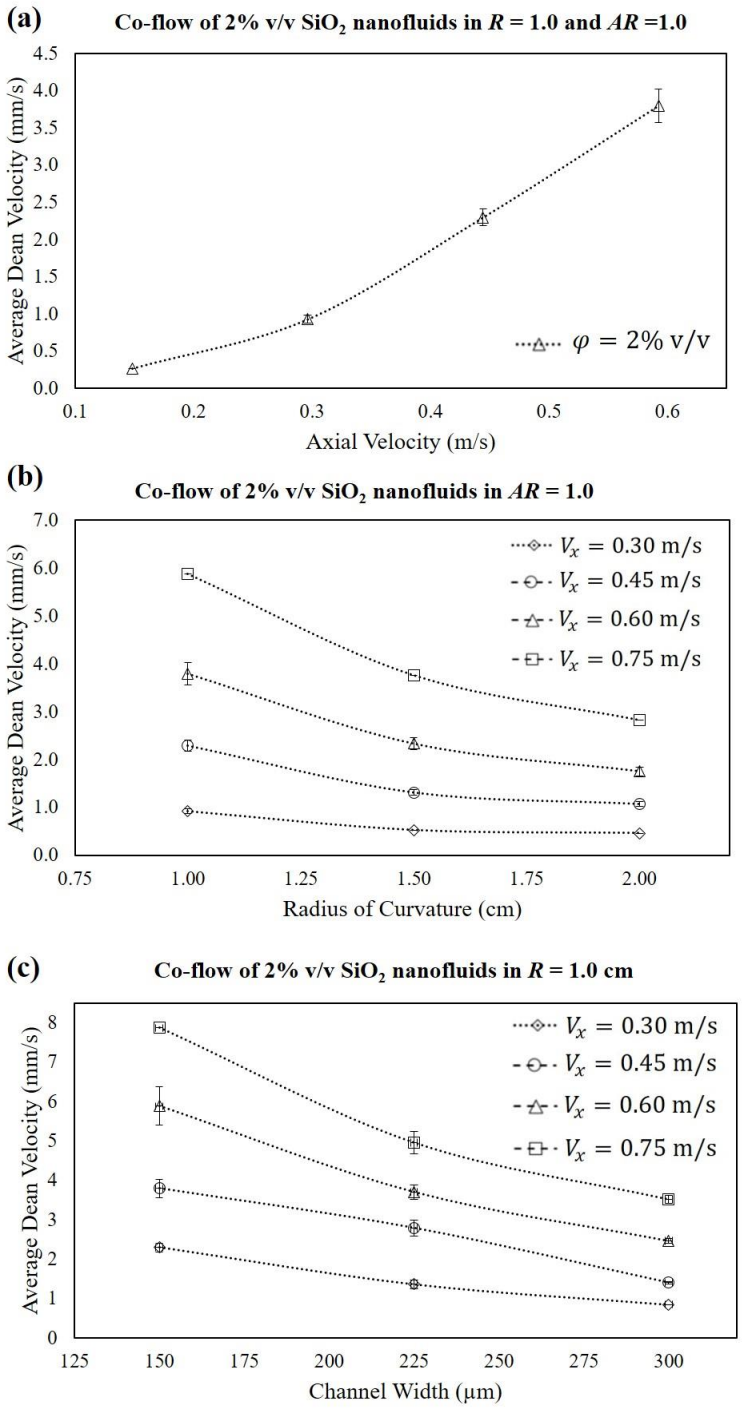

Appendix Figure D-1: Representative experiments illustrating the effect of (a) axial velocity ($V_{x,}$), (b) channel radius of curvature (R), and (c) channel width (w) on V_{De} for the co-flows of 2% v/v SiO_2 nanofluids in curvilinear microchannels. A channel cross section of 150 × 150 μm^2 in (a) and (b), and a channel height of h = 150 μm in (c).Error bars are included for all data points but are not visible in cases of small errors.

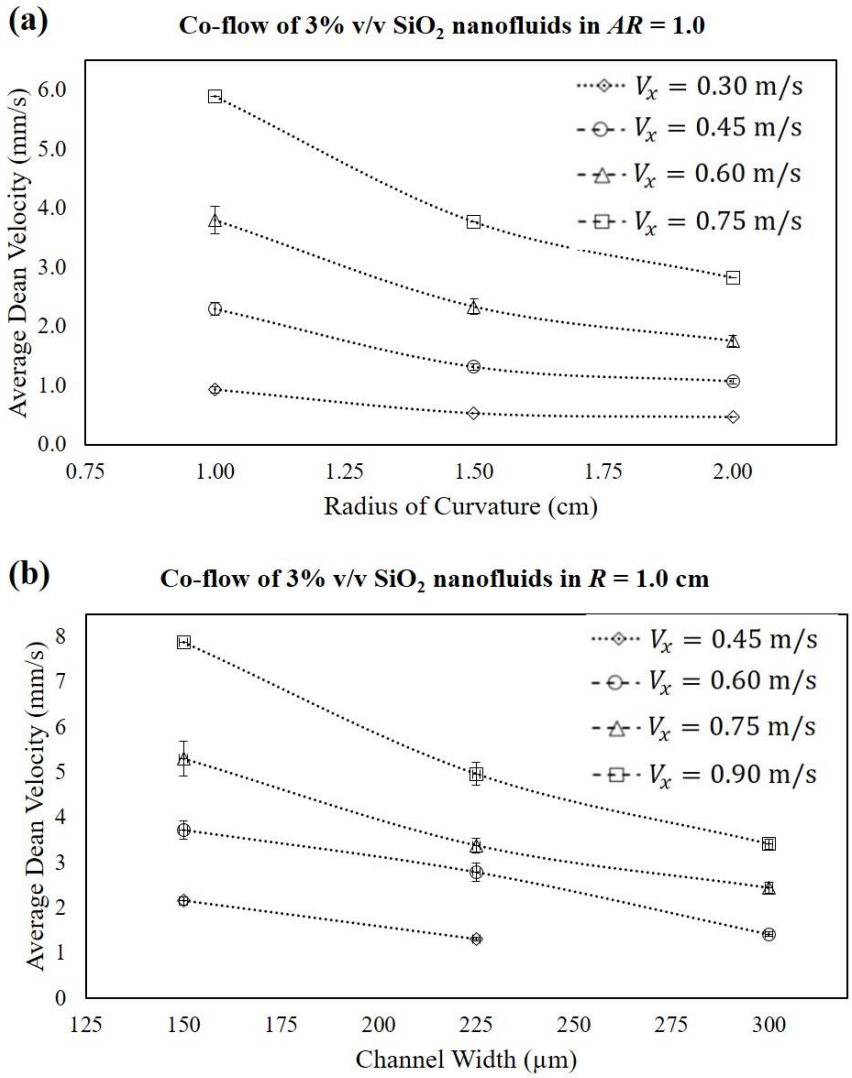

Appendix Figure D-2: Representative experiments illustrating the effect of (a) channel radius of curvature (R), and (b) channel width (w) on V_{De} for the co-flows of 3% v/v SiO_2 nanofluids in curvilinear microchannels. A channel cross section of 150 × 150 µm^2 in (a) and a channel height of h = 150 µm in (b).Error bars are included for all data points but are not visible in cases of small errors.

Appendix E.

Effects of fluid axial velocity on normalized number of particles alongside the channel outlet.

For all experiments, the particles were supplied through inlet-I alongside a clean buffer in inlet-O. Figures represent the particle distribution for different PEO concentrations at various axial velocities.

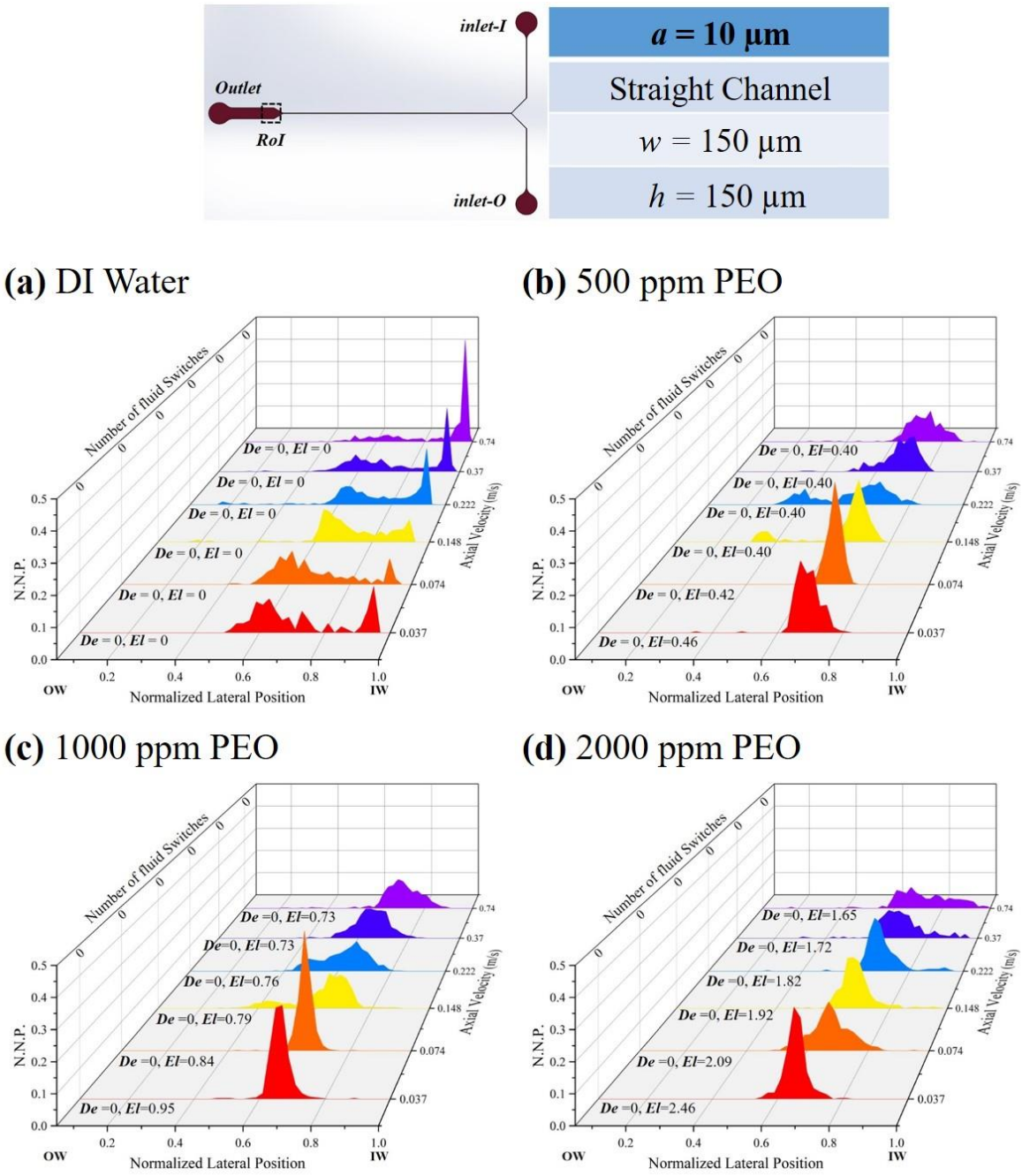

Appendix Figure E-1: Normalized number of particles alongside their normalized lateral position for 10 µm particles inside a square straight microchannel (150 ×150 µm^2 at various axial velocities.

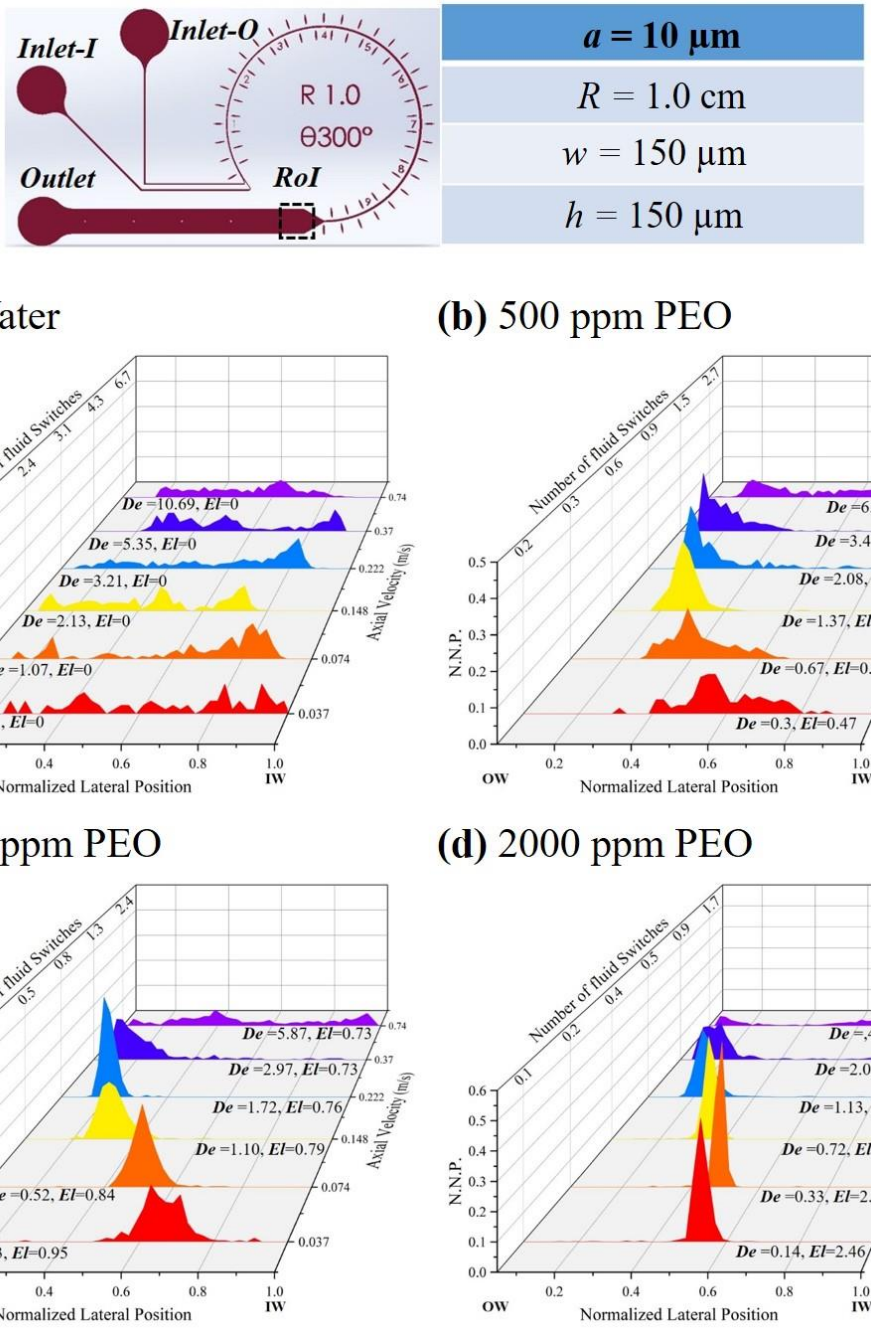

Appendix Figure E-2: Normalized number of particles alongside their normalized lateral position for 10 µm particles inside a square microchannel (150 × 150 µm^2) with R = 1.0 cm at various axial velocities.

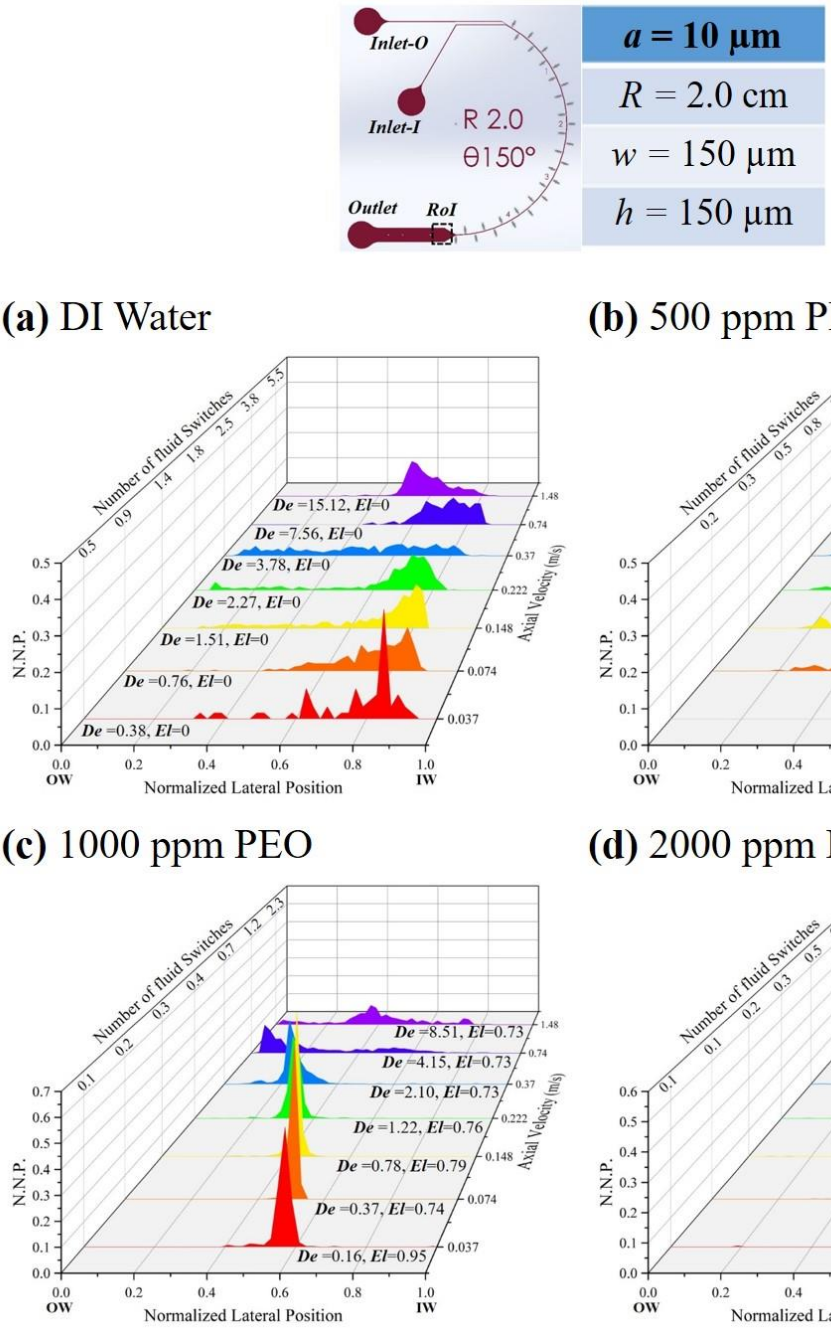

Appendix Figure E-3: Normalized number of particles alongside their normalized lateral position for 10 µm particles inside a square microchannel (150 × 150 µm^2) with R = 2.0 cm (θ = 150 °) at various axial velocities.

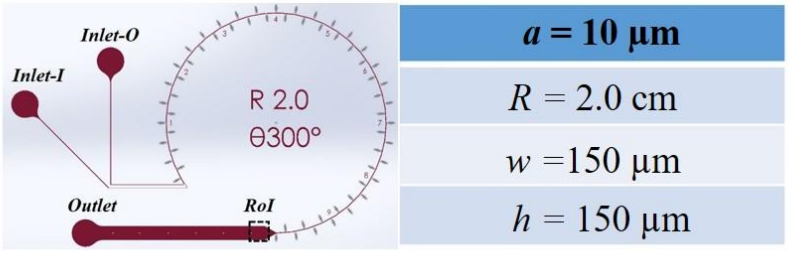

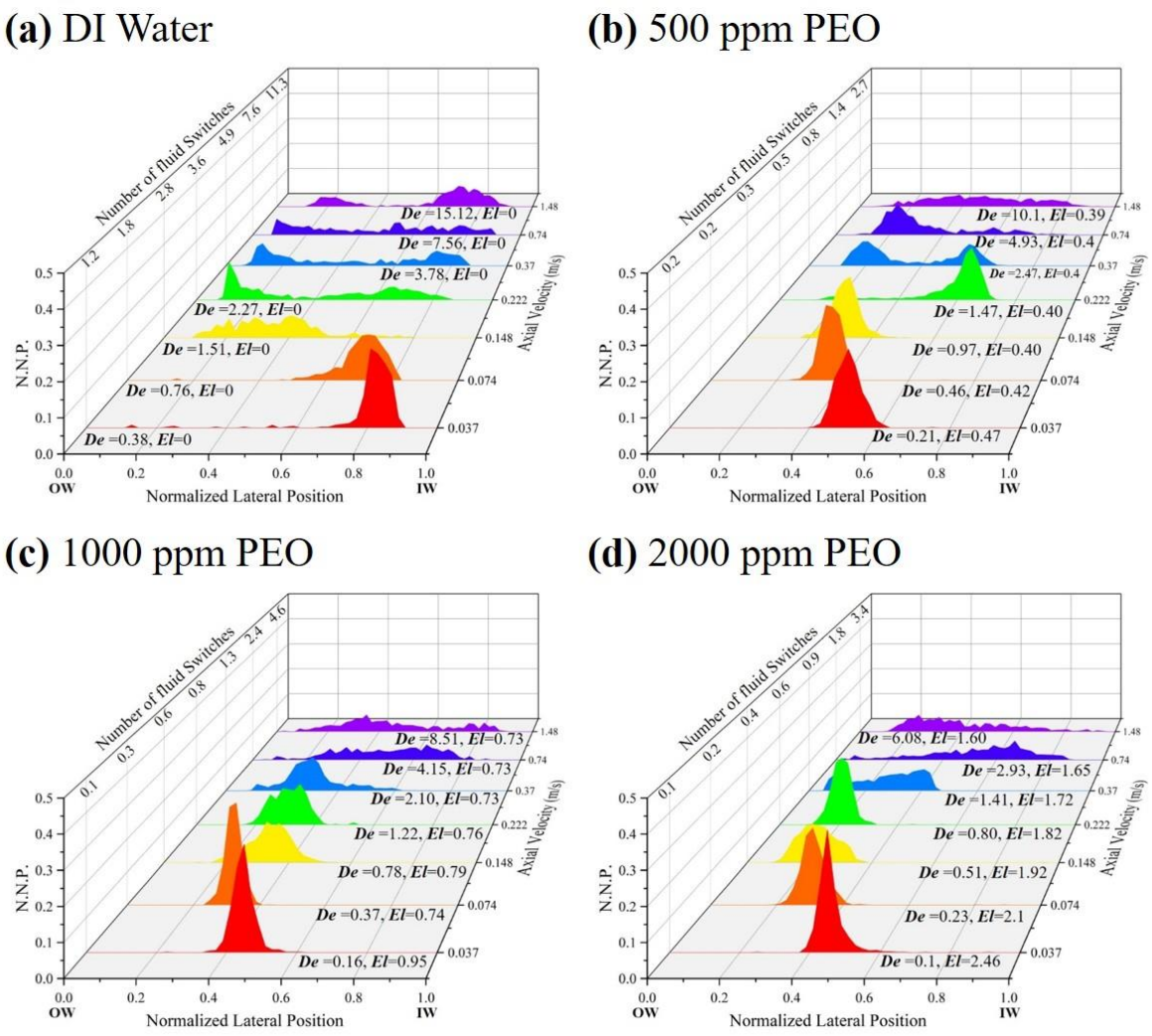

Appendix Figure E-4: Normalized number of particles alongside their normalized lateral position for 10 µm particles inside a square microchannel (150 × 150 µm^2) with R = 2.0 cm (θ = 300°) at various axial velocities.

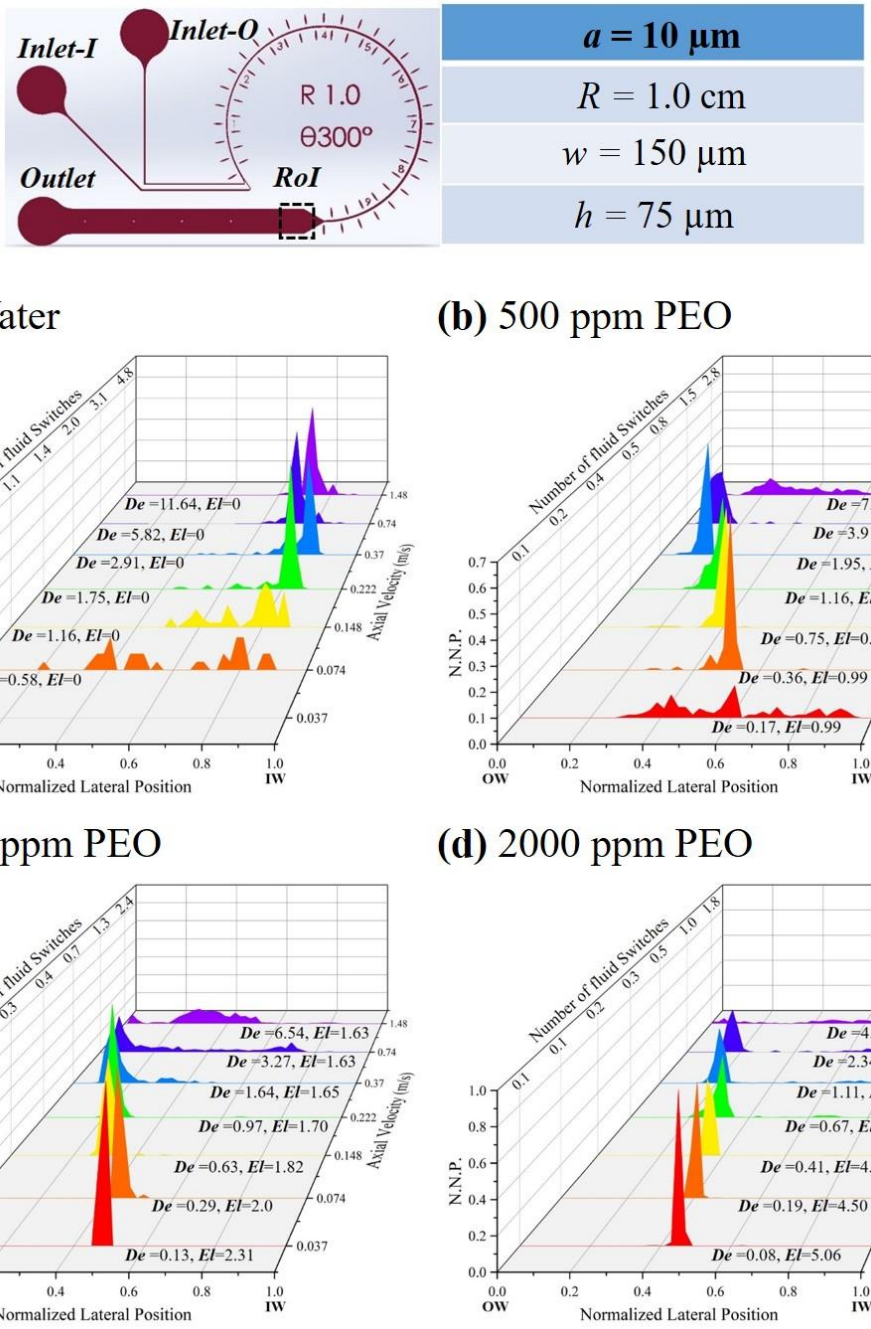

Appendix Figure E-5: Normalized number of particles alongside their normalized lateral position for 10 µm particles inside a rectangular microchannel (150 × 75 µm^2) with R = 1.0 cm at various axial velocities.

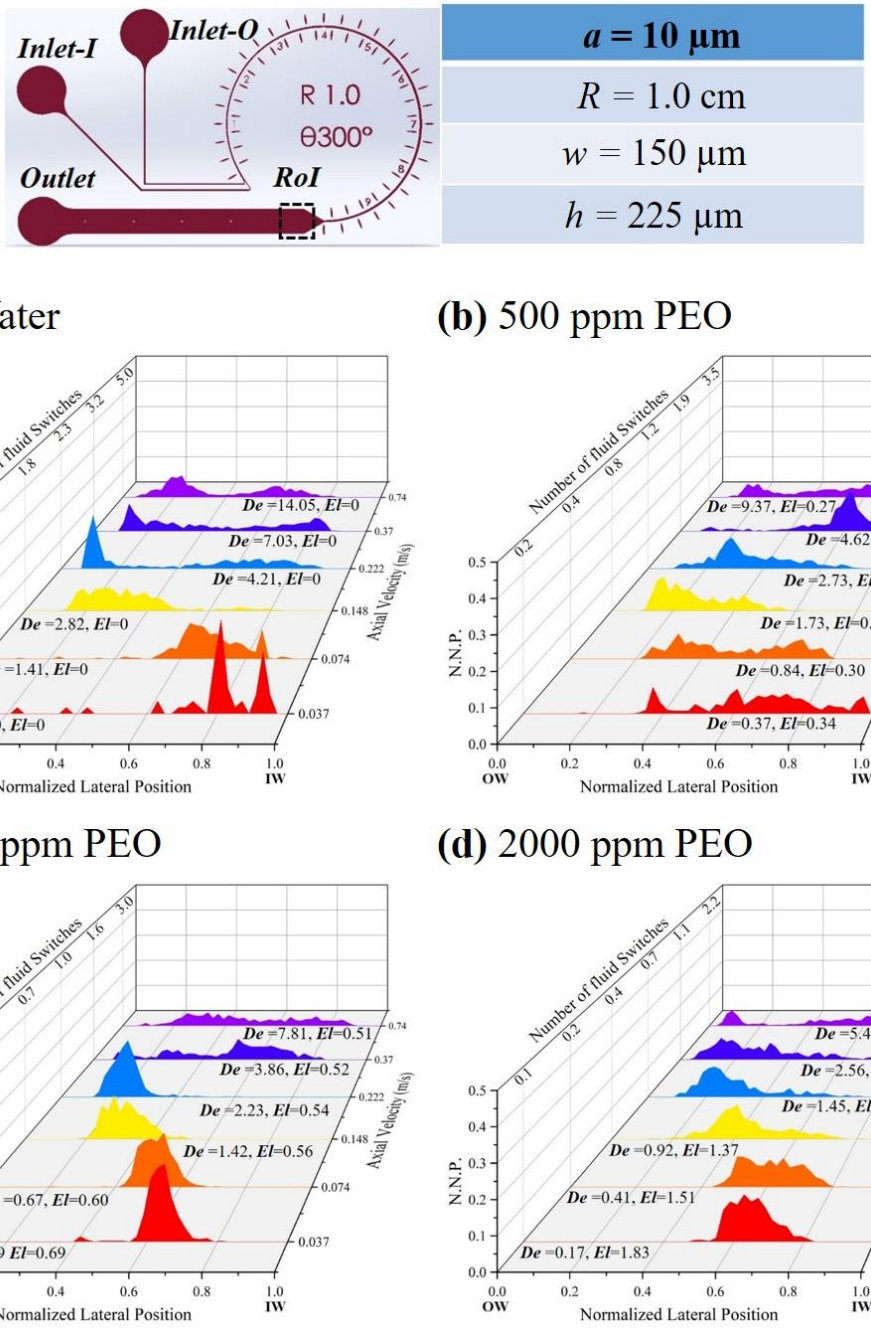

Appendix Figure E-6: Normalized number of particles alongside their normalized lateral position for 10 µm particles inside a rectangular microchannel (150 × 225 µm^2) with R = 1.0 cm at various axial velocities.

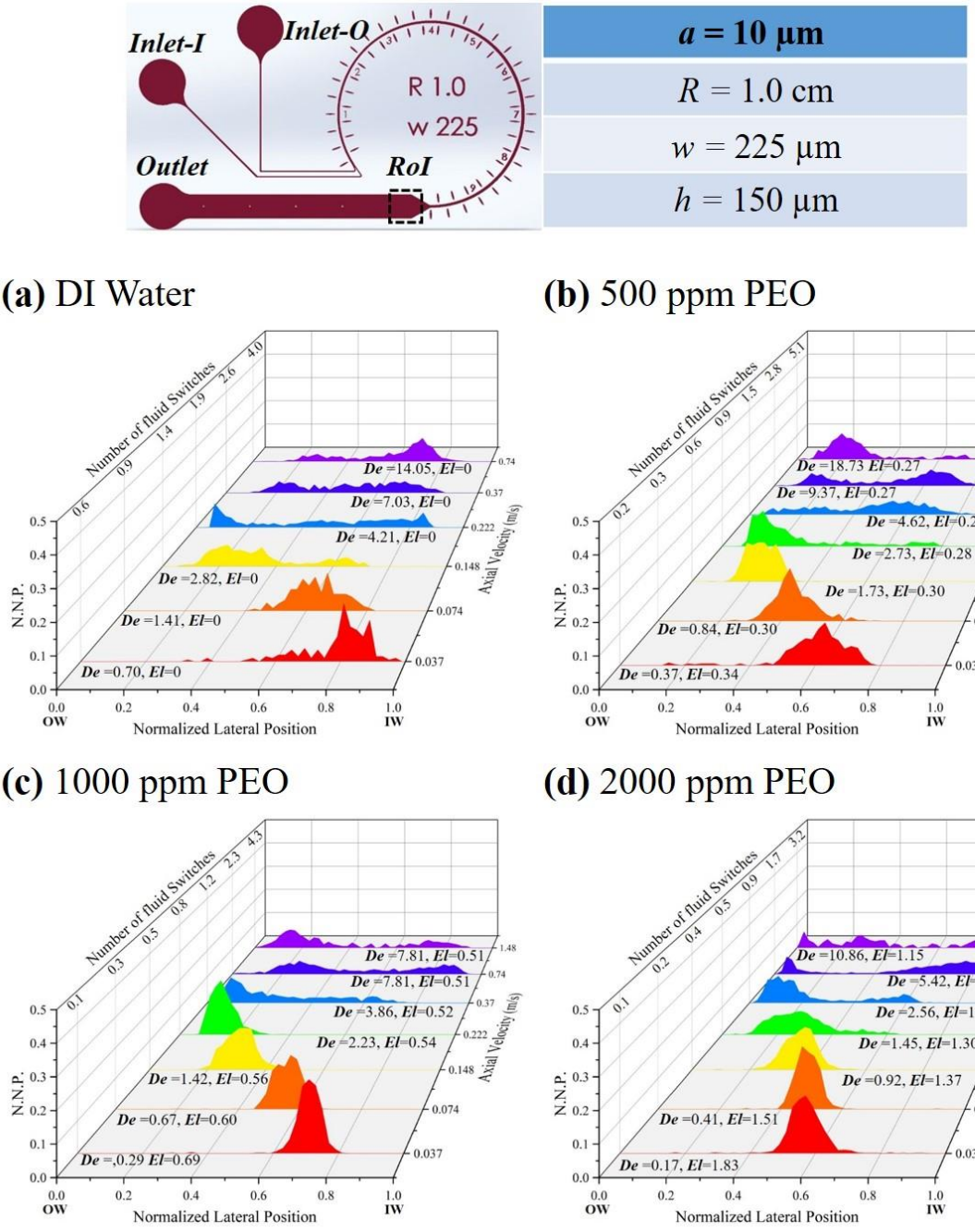

Appendix Figure E-7: Normalized number of particles alongside their normalized lateral position for 10 µm particles inside a rectangular microchannel (225 × 150 µm^2) with R = 1.0 cm at various axial velocities.

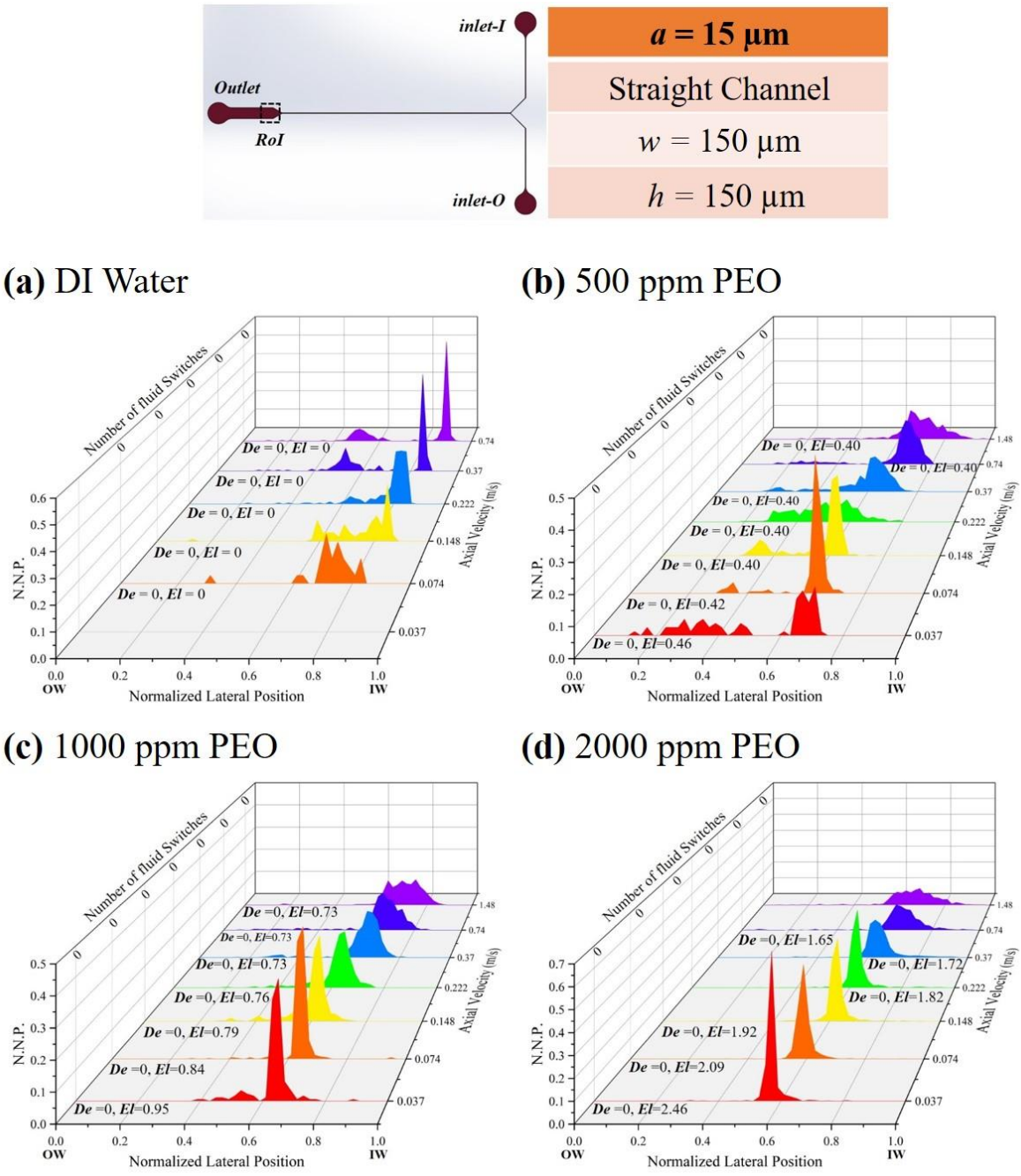

Appendix Figure E-8: Normalized number of particles alongside their normalized lateral position for 15 µm particles inside a straight square microchannel (150 × 150 µm^2) at various axial velocities.

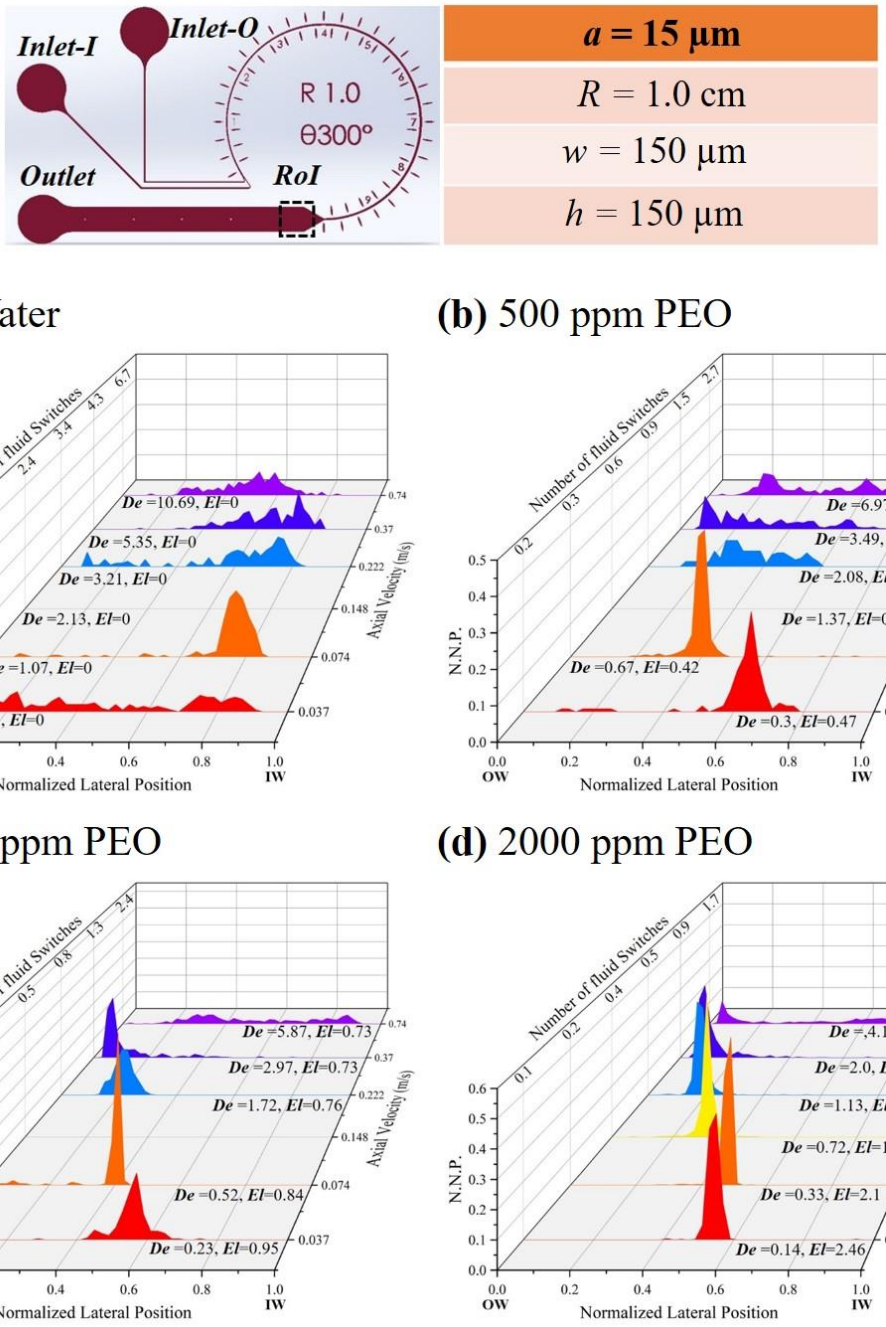

Appendix Figure E-9: Normalized number of particles alongside their normalized lateral position for 15 µm particles inside a square microchannel (150 × 150 µm^2) with R = 1.0 cm at various axial velocities.

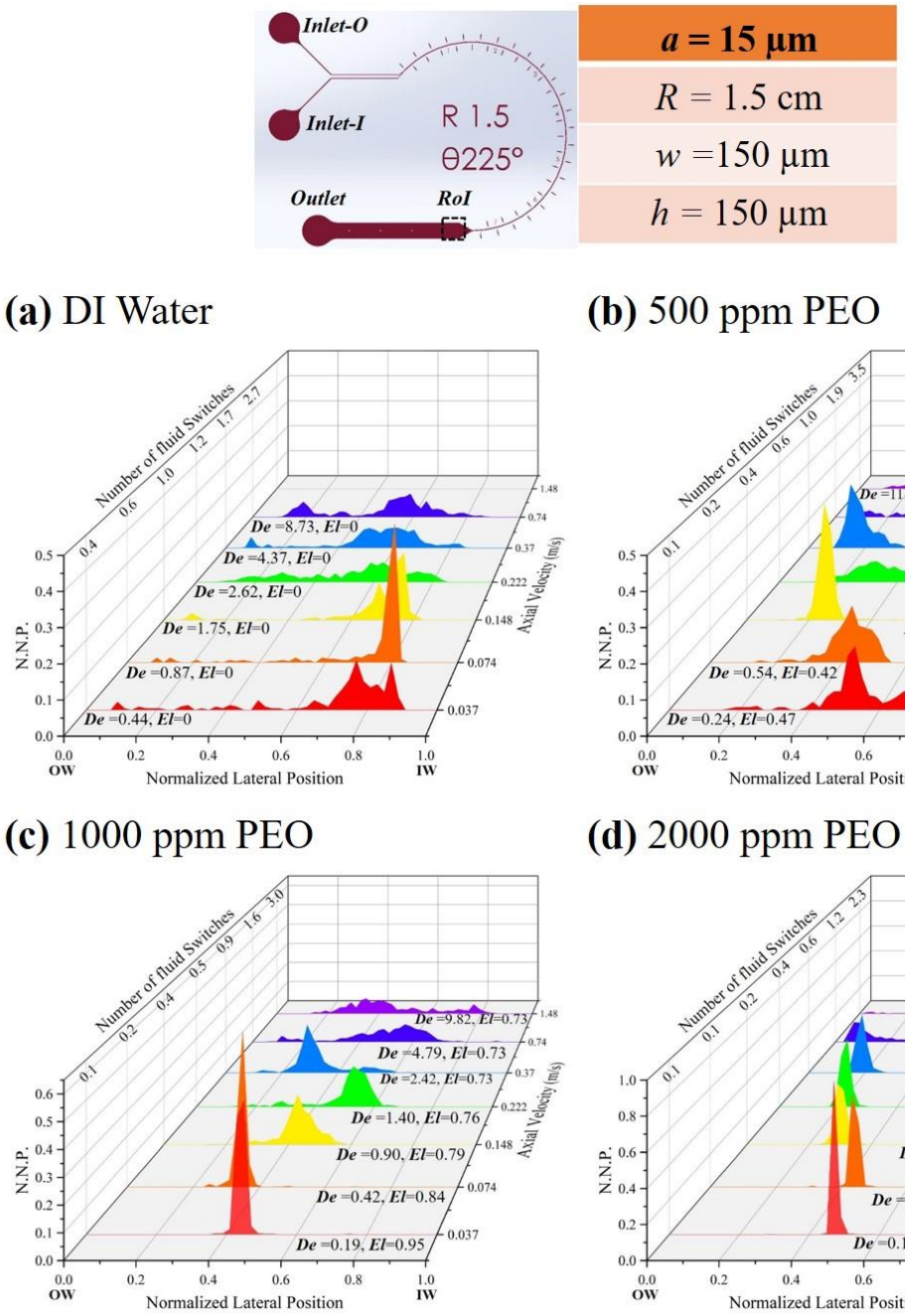

Appendix Figure E-10: Normalized number of particles alongside their normalized lateral position for 15 µm particles inside a square microchannel (150 × 150 µm^2) with R = 1.5 cm (θ = 225 °) at various axial velocities.

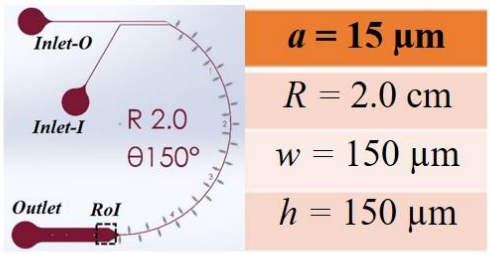

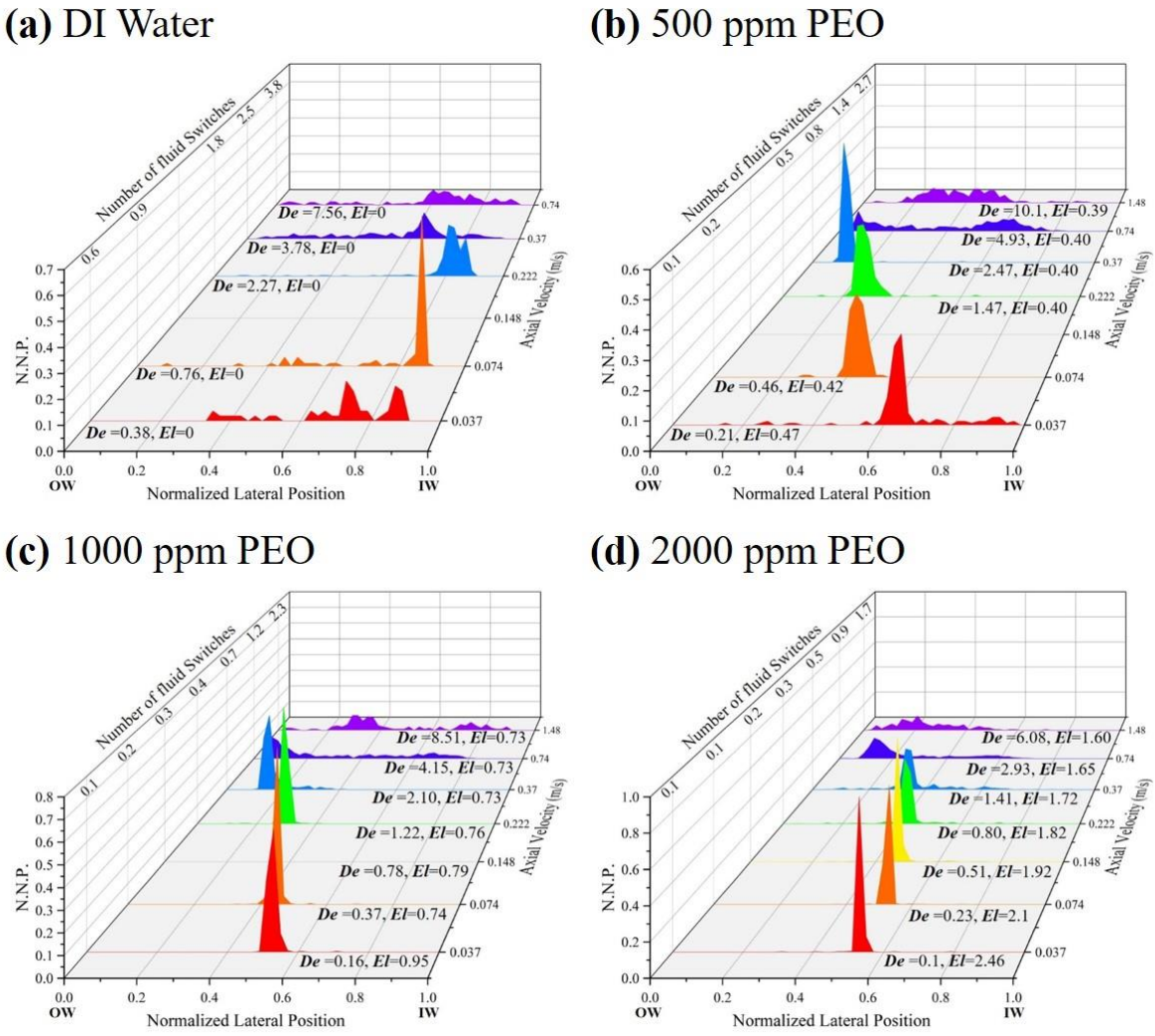

Appendix Figure E-11: Normalized number of particles alongside their normalized lateral position for 15 µm particles inside a square microchannel (150 × 150 µm^2) with R = 2.0 cm (θ = 150°) at various axial velocities.

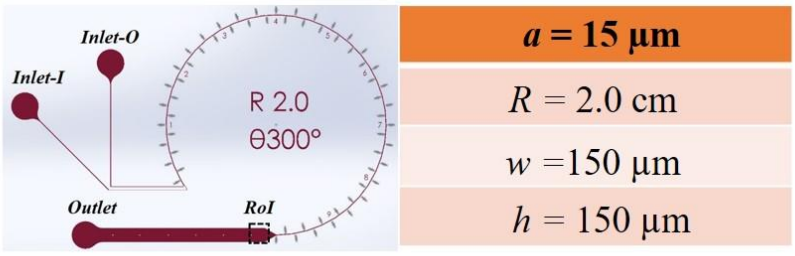

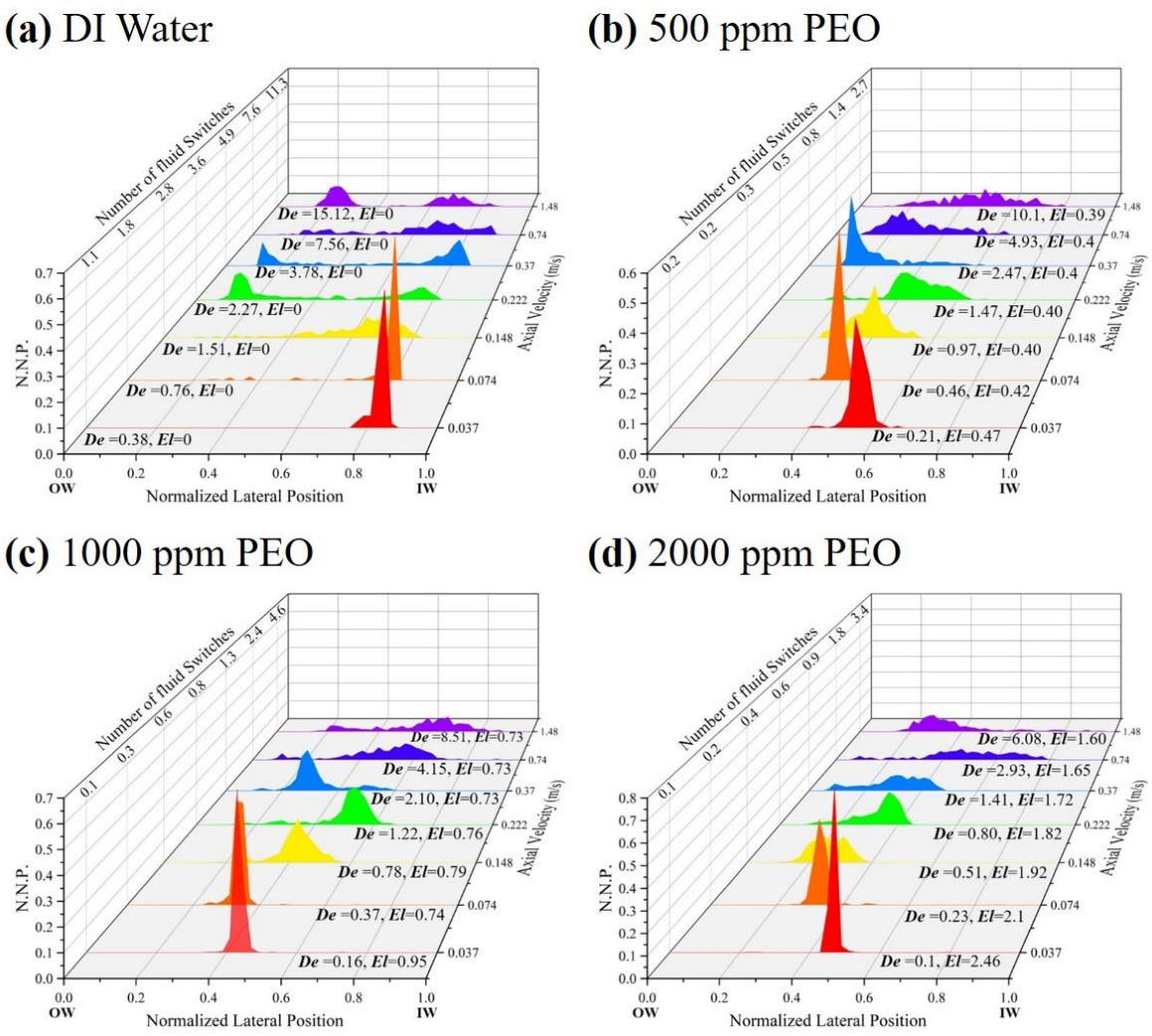

Appendix Figure E-12: Normalized number of particles alongside their normalized lateral position for 15 µm particles inside a square microchannel (150 × 150 µm^2) with R = 2.0 cm (θ = 300°) at various axial velocities.

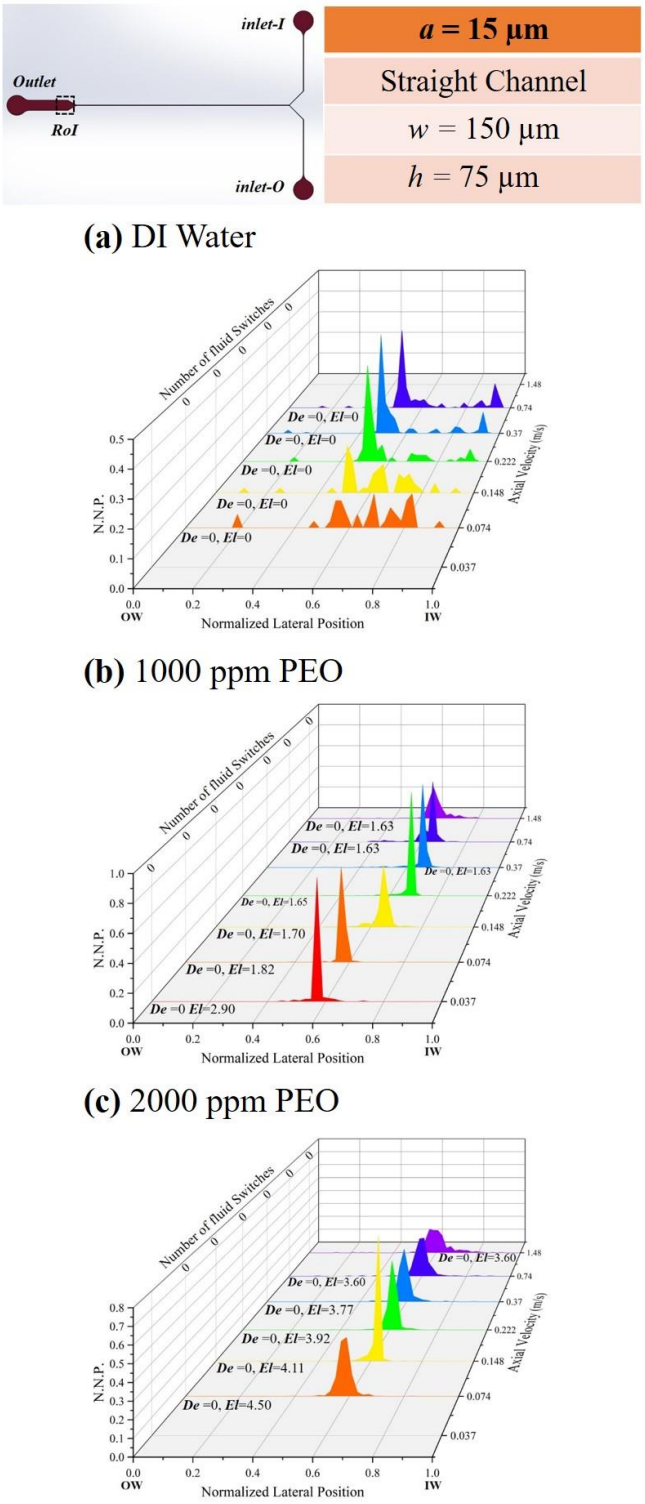

Appendix Figure E-13: Normalized number of particles alongside their normalized lateral position for 15 µm particles inside a straight rectangular microchannel (150 × 75 µm^2) at various axial velocities.

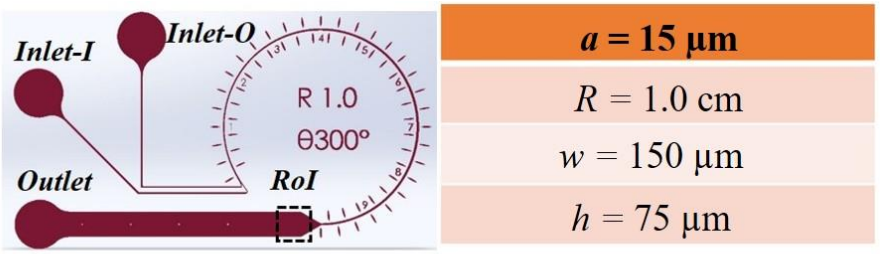

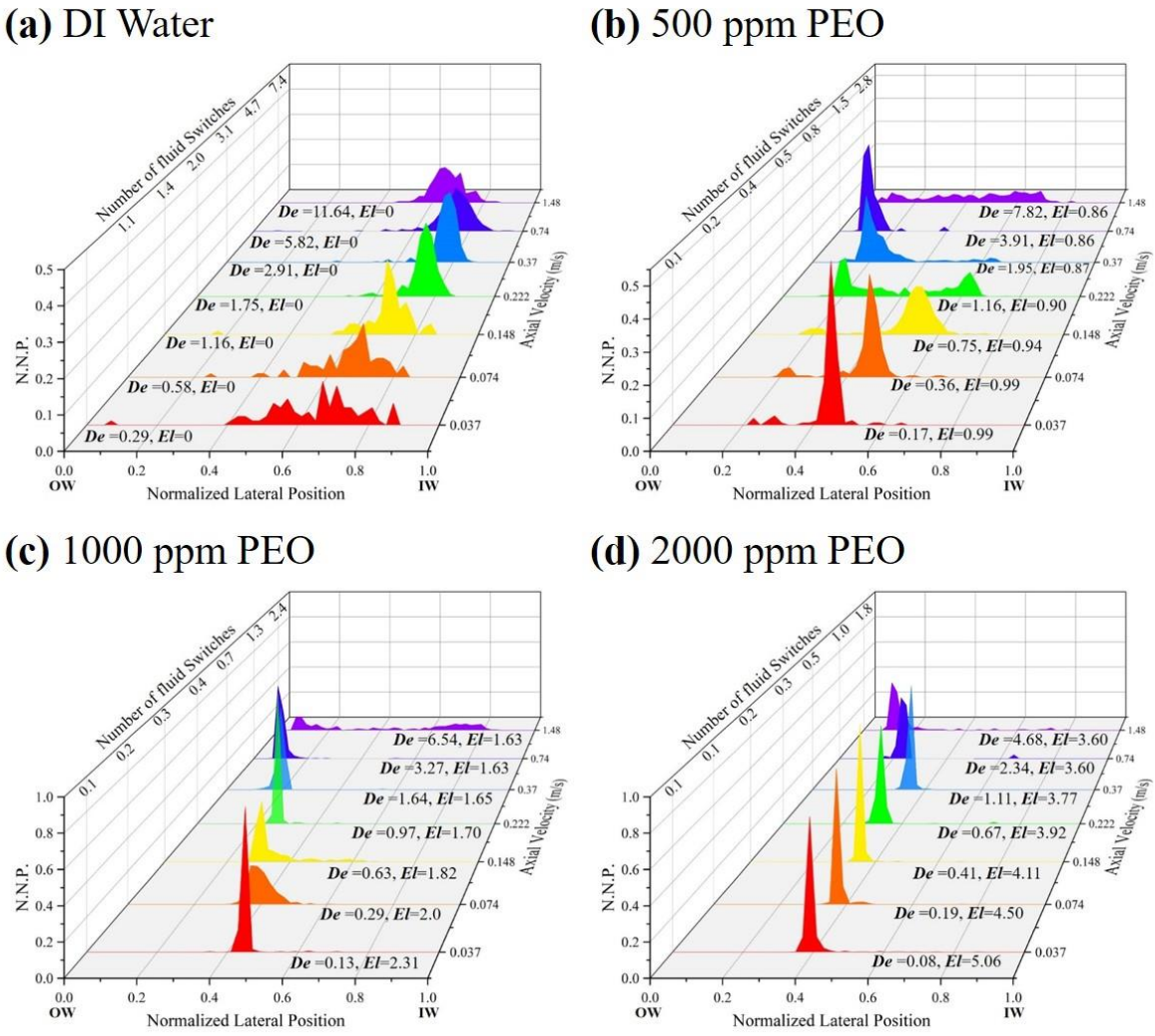

Appendix Figure E-14: Normalized number of particles alongside their normalized lateral position for 15 µm particles inside a rectangular microchannel (150 × 75 µm^2) with R = 1.0 cm at various axial velocities.

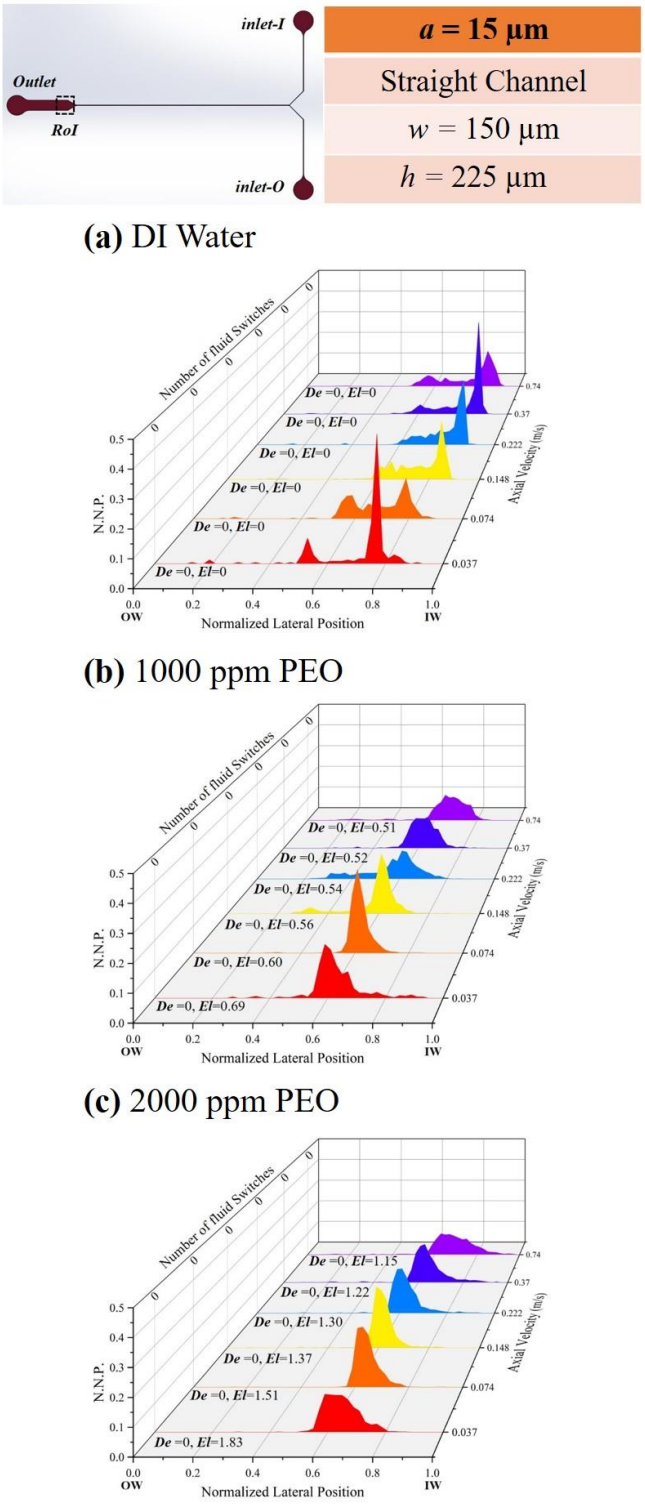

Appendix Figure E-15: Normalized number of particles alongside their normalized lateral position for 15 µm particles inside a straight rectangular microchannel (150 × 225 µm^2) at various axial velocities.

(b) 500 ppm PEO

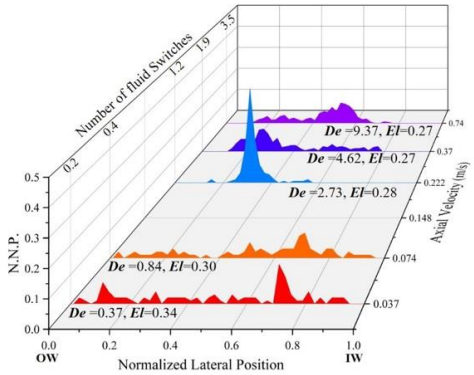

(c) 1000 ppm PEO

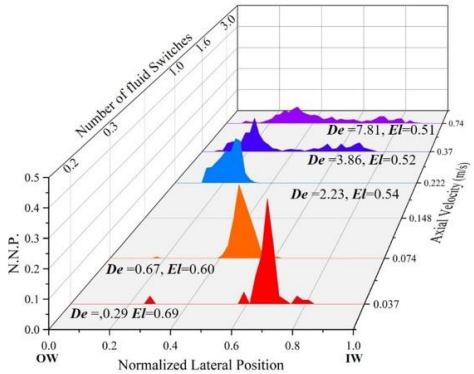

(d) 2000 ppm PEO

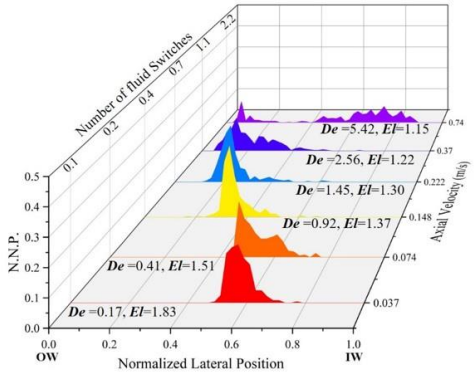

Appendix Figure E-16: Normalized number of particles alongside their normalized lateral position for 15 µm particles inside a rectangular microchannel (150 × 225 µm^2) with R = 1.0 cm at various axial velocities.

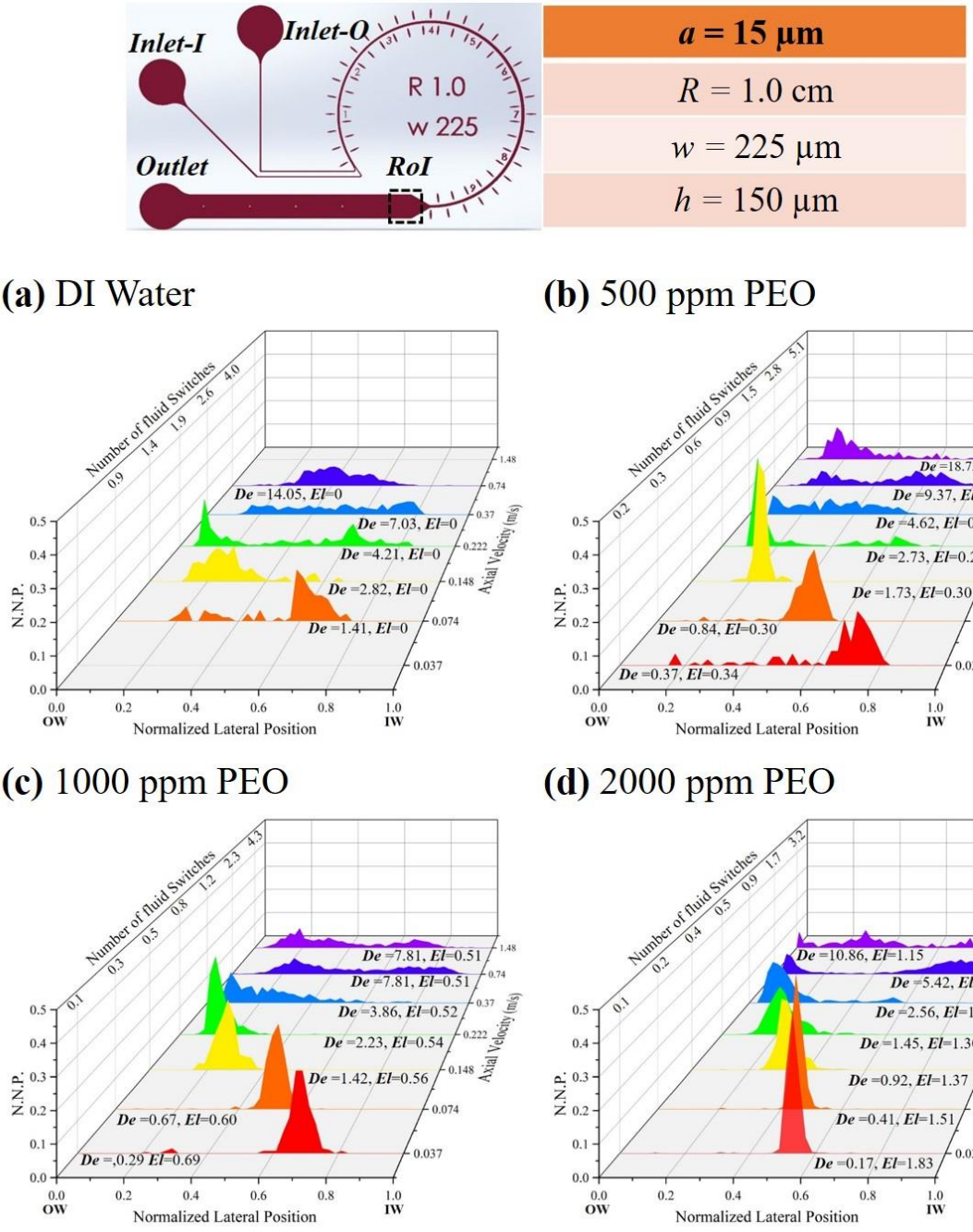

Appendix Figure E-17: Normalized number of particles alongside their normalized lateral position for 15 µm particles inside a rectangular microchannel (225 × 150 µm^2) with R = 1.0 cm at various axial velocities.

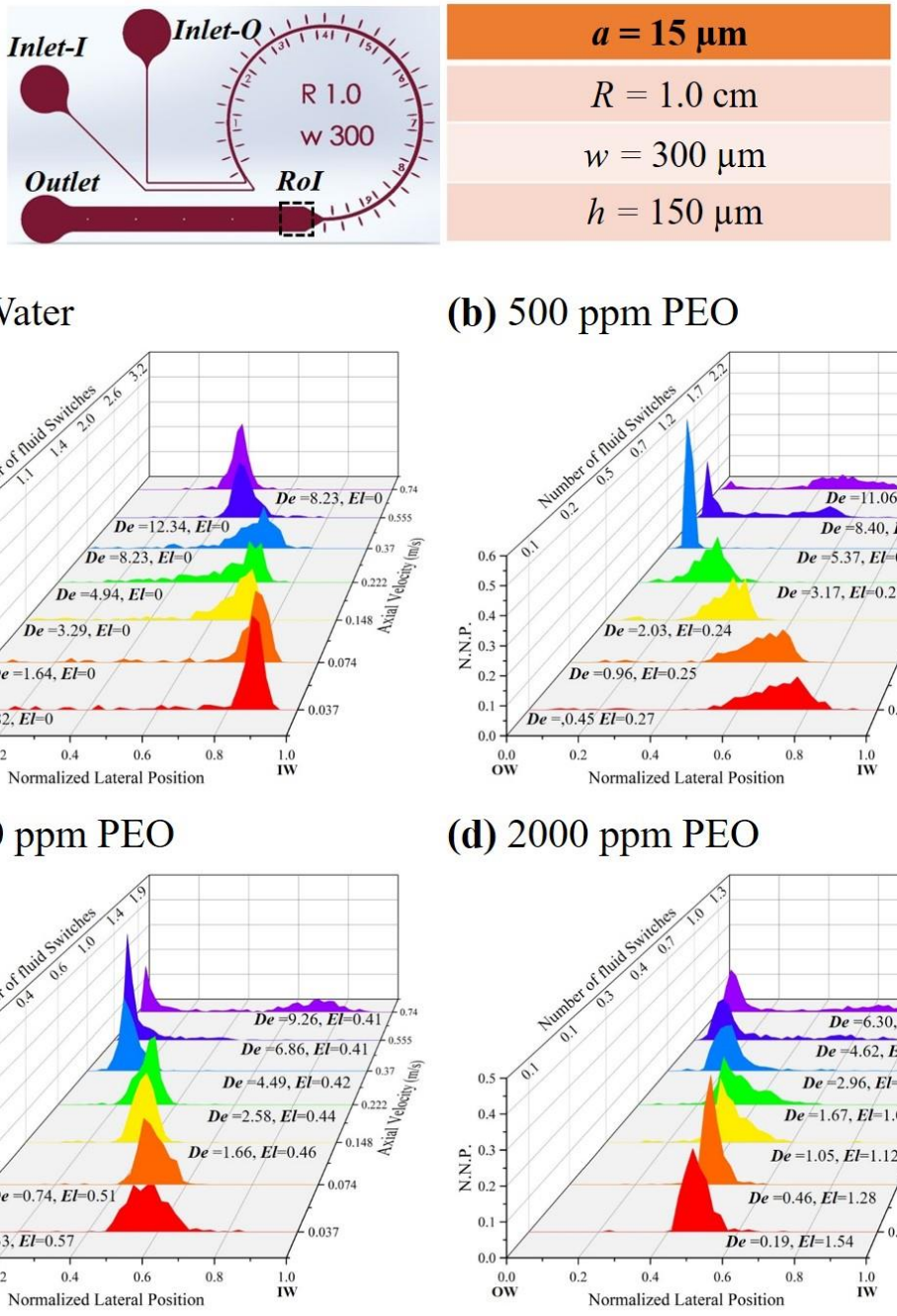

Appendix Figure E-18: Normalized number of particles alongside their normalized lateral position for 15 µm particles inside a rectangular microchannel (300 × 150 µm^2) with R = 1.0 cm at various axial velocities.

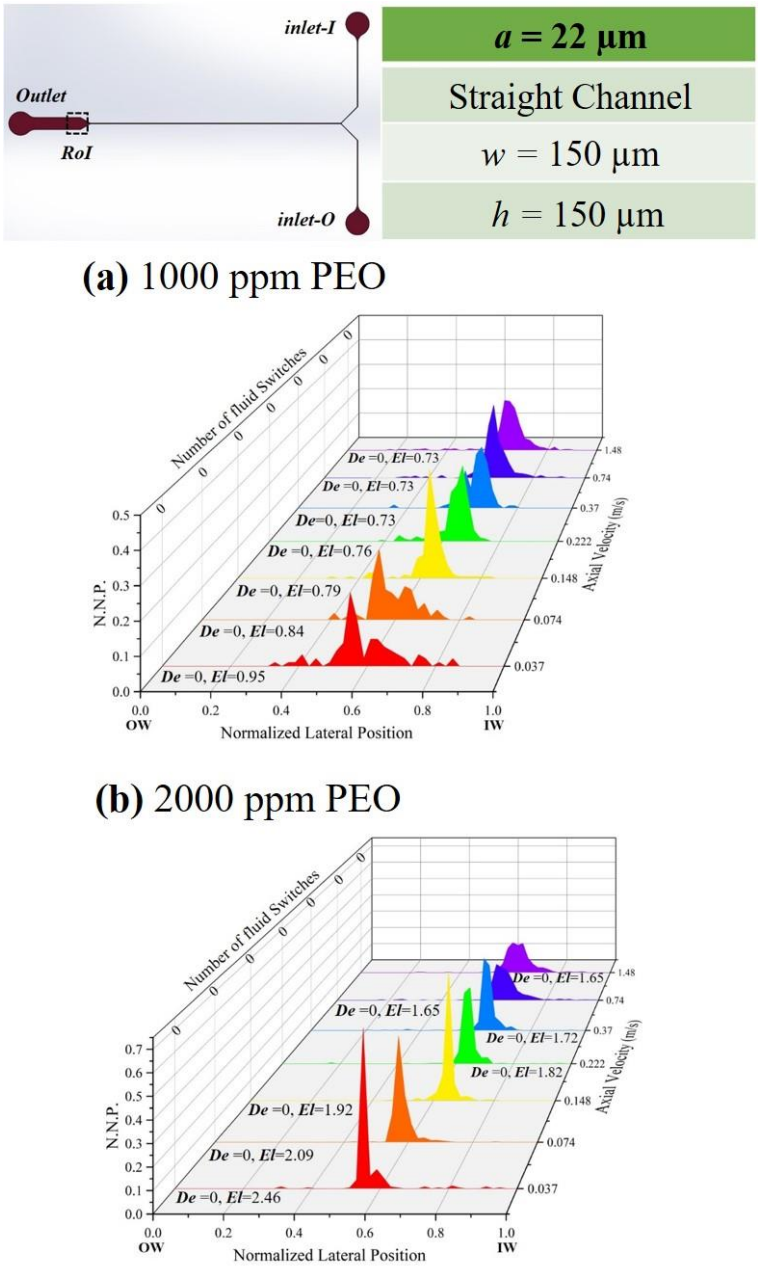

Appendix Figure E-19: Normalized number of particles alongside their normalized lateral position for 22 µm particles inside a straight square microchannel (150 × 150 µm^2) at various axial velocities.

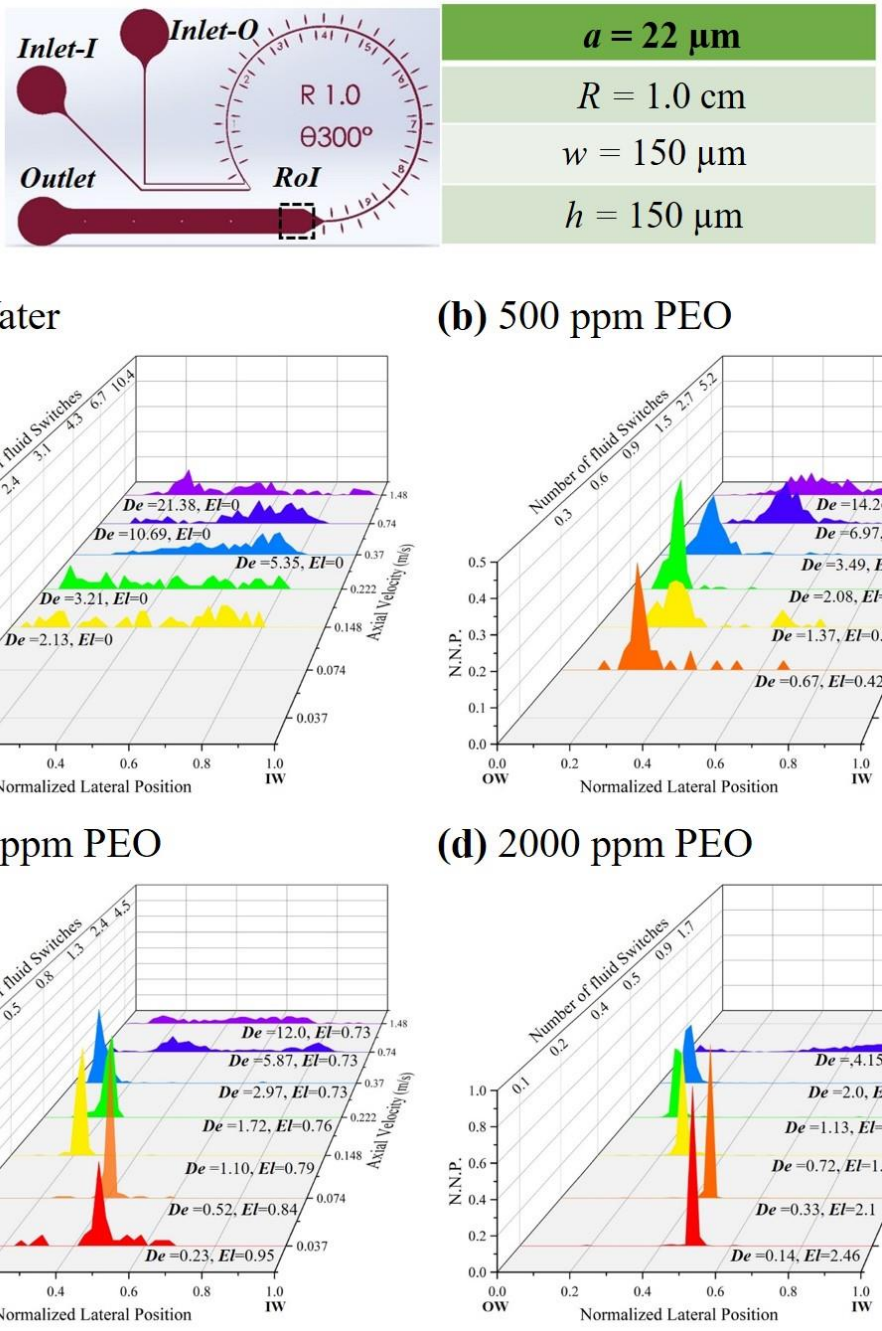

Appendix Figure E-20: Normalized number of particles alongside their normalized lateral position for 22 µm particles inside a square microchannel (150 × 150 µm^2) with R = 1.0 cm at various axial velocities.

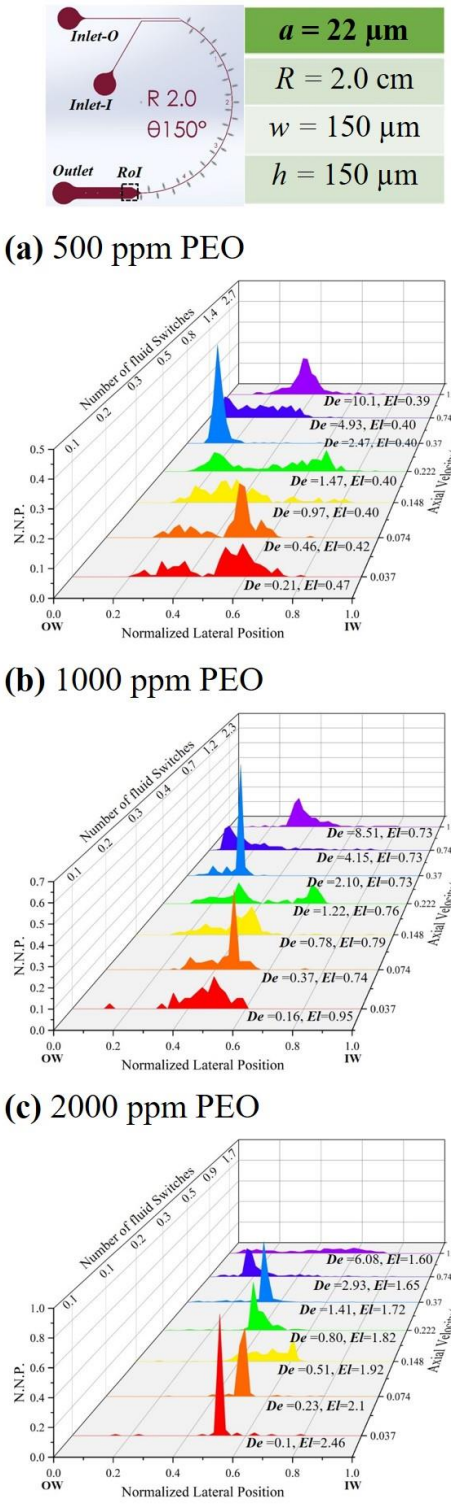

Appendix Figure E-21: Normalized number of particles alongside their normalized lateral position for 22 µm particles inside a square microchannel (150 × 150 µm^2) with R = 2.0 cm (θ = 150°) at various axial velocities.

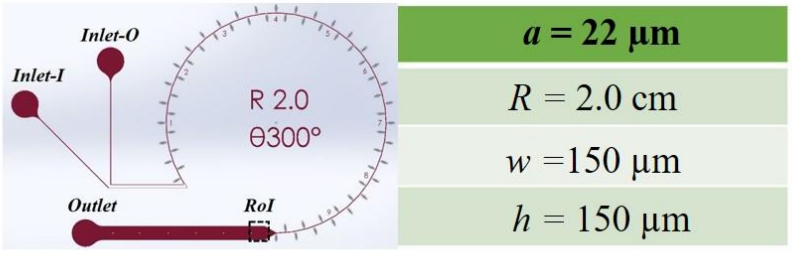

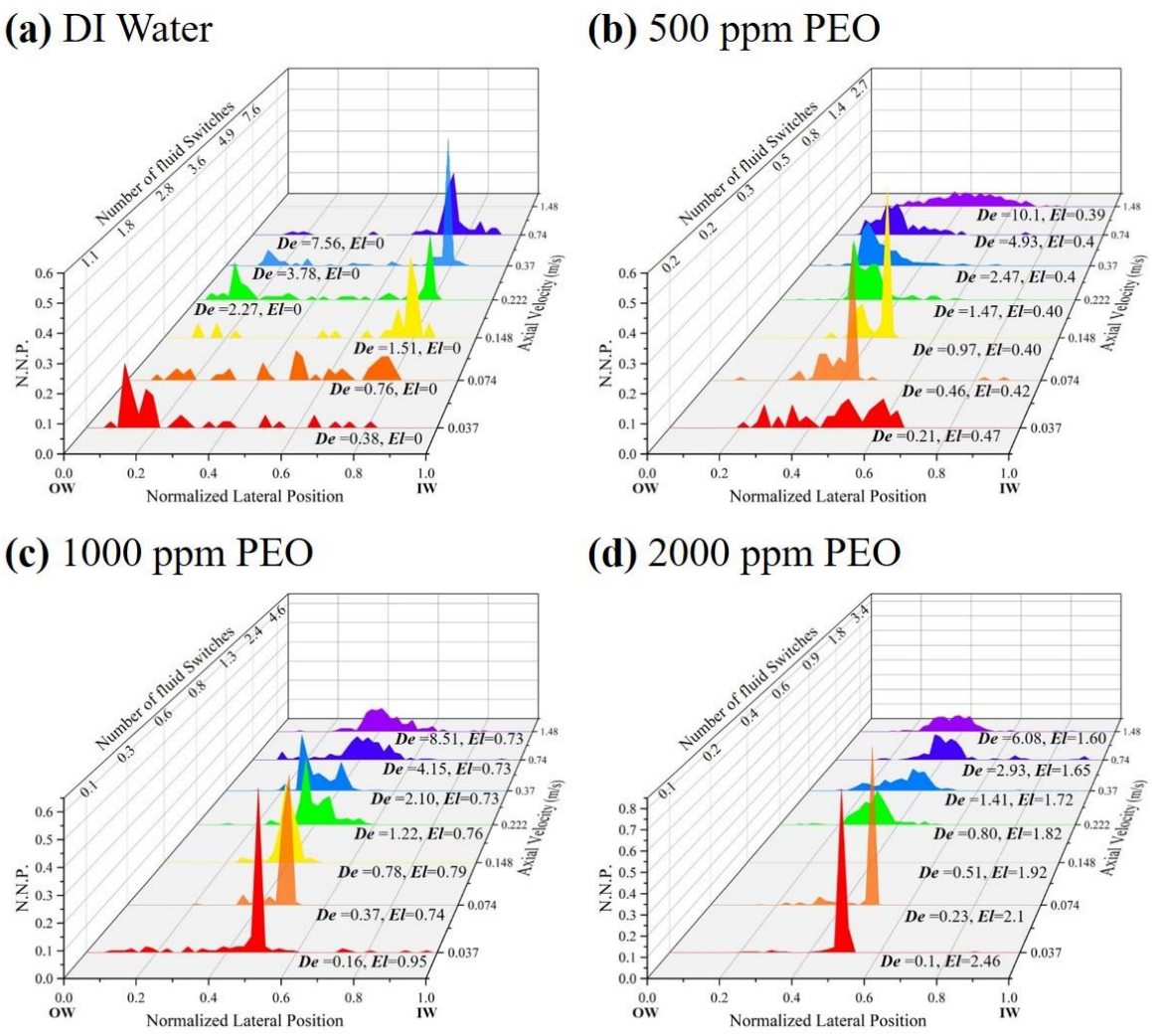

Appendix Figure E-22: Normalized number of particles alongside their normalized lateral position for 22 µm particles inside a square microchannel (150 × 150 µm^2) with R = 2.0 cm (θ = 300 °) at various axial velocities.

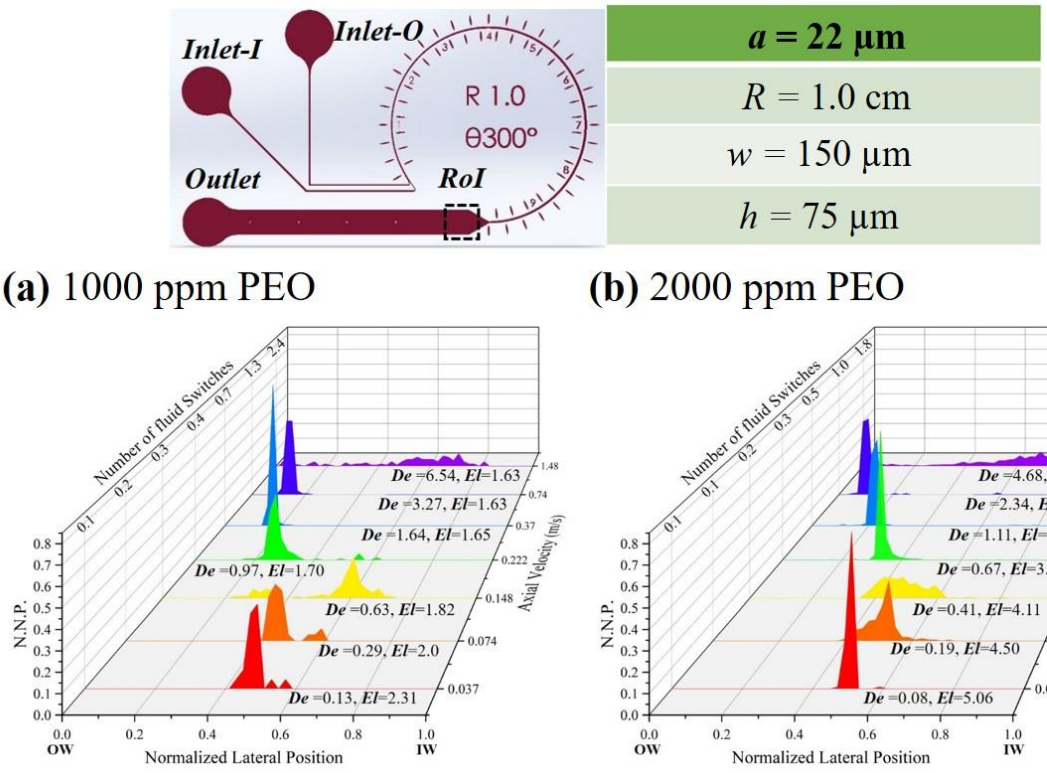

Appendix Figure E-23: Normalized number of particles alongside their normalized lateral position for 22 µm particles inside a rectangular microchannel (150 × 75 µm^2) with R = 1.0 cm at various axial velocities.

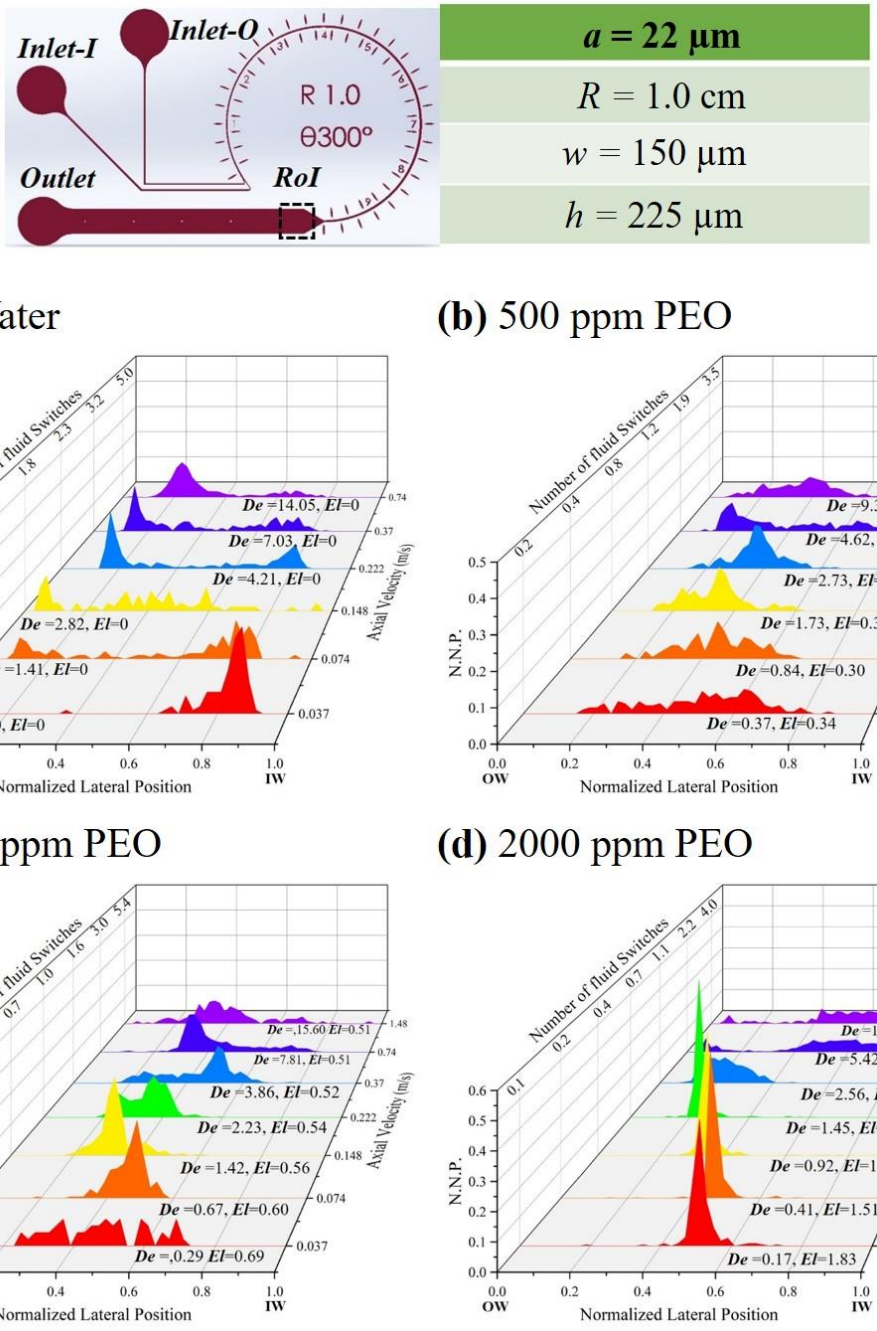

Appendix Figure E-24: Normalized number of particles alongside their normalized lateral position for 22 µm particles inside a rectangular microchannel (150 × 225 µm^2) with R = 1.0 cm at various axial velocities.

(a) 500 ppm PEO

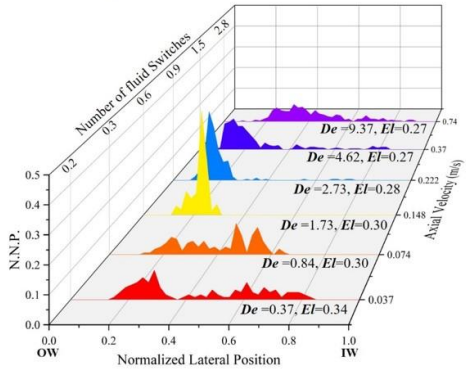

(b) 1000 ppm PEO

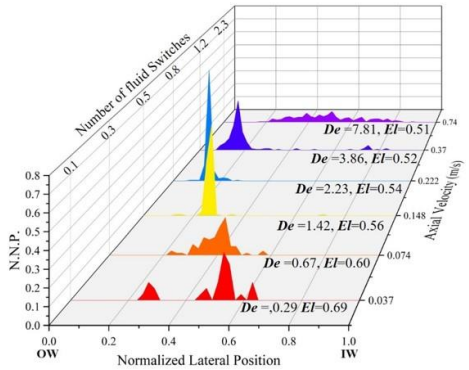

(c) 2000 ppm PEO

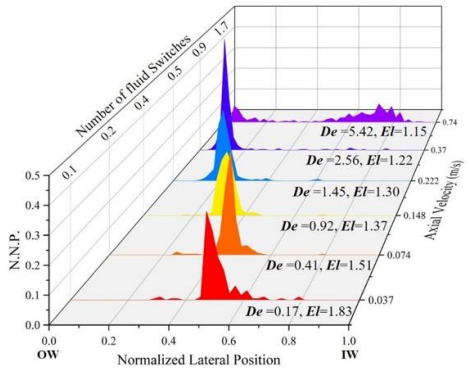

Appendix Figure E-25: Normalized number of particles alongside their normalized lateral position for 22 µm particles inside a rectangular microchannel (225 × 150 µm^2) with R = 1.0 cm at various axial velocities.

Appendix F.

Effects of fluid axial velocity on normalized number of particles alongside the channel outlet.

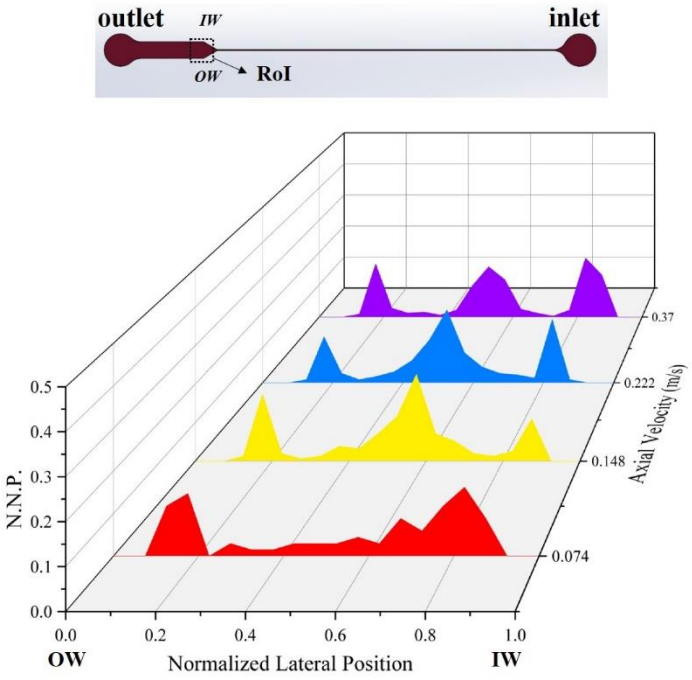

Appendix Figure F-1: Normalized number of particles alongside their normalized lateral position for 15 µm particles in 3% v/v SiO_2 nanofluid inside a square straight microchannel (150 × 150 μm^2) at various axial velocities.

For all experiments below, the particles were supplied through inlet-I alongside a clean buffer in inlet-O. Figures represent the particle distribution for different SiO_2 concentrations at various axial velocities.

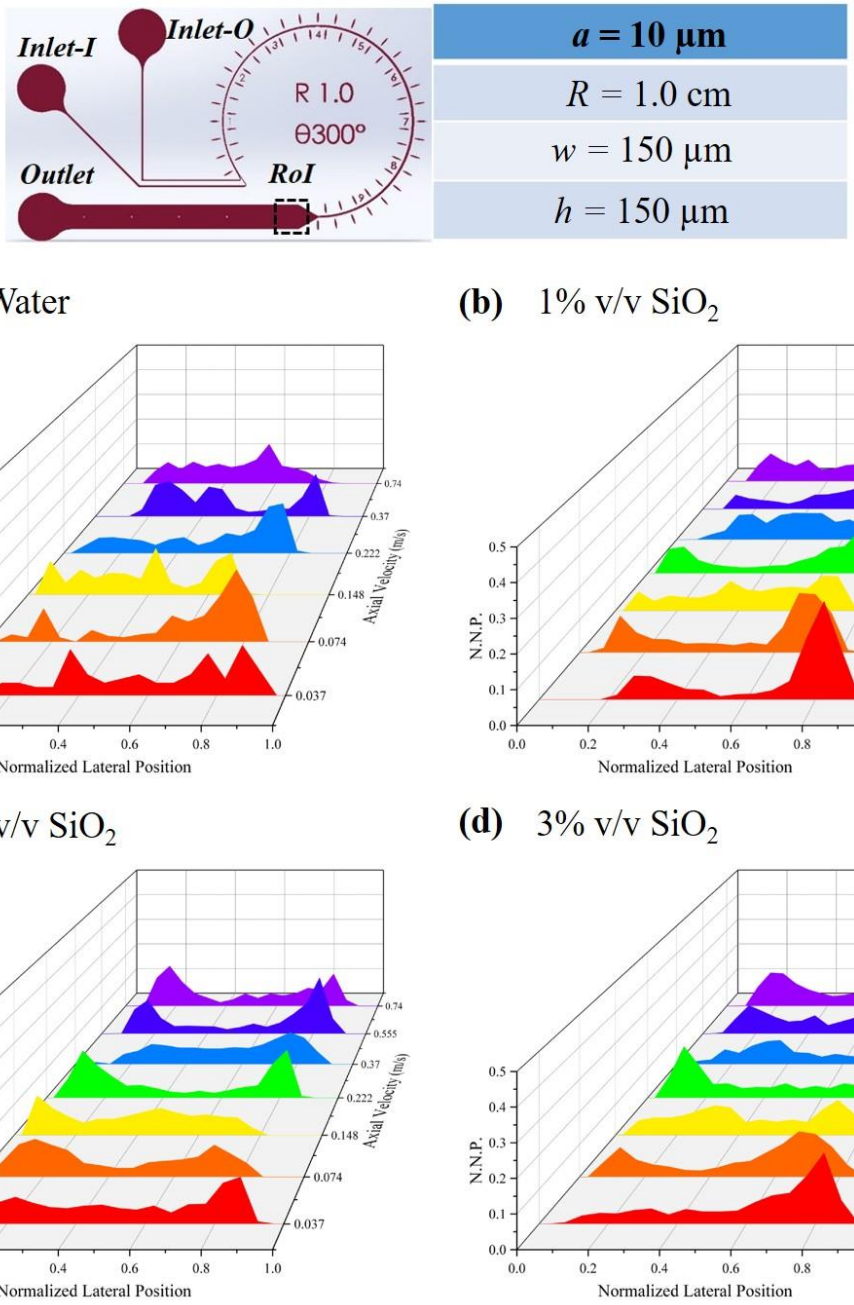

Appendix Figure F-2: Normalized number of particles alongside their normalized lateral position for 10 µm particles inside a square microchannel (150 × 150 µm^2) with R = 1.0 cm at various axial velocities.

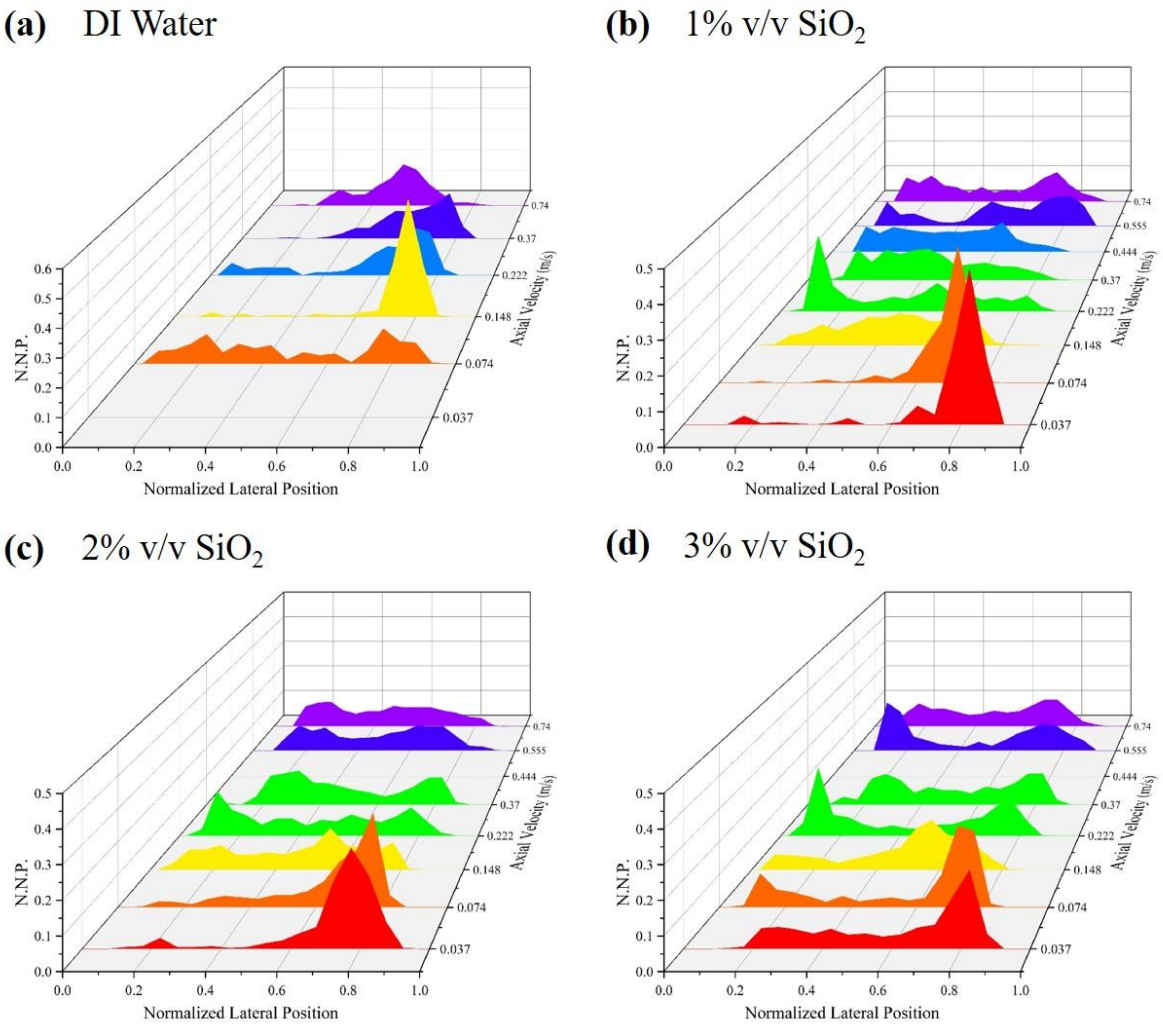

Appendix Figure F-3: Normalized number of particles alongside their normalized lateral position for 15 µm particles inside a square microchannel (150 × 150 µm^2) with R = 1.0 cm at various axial velocities.

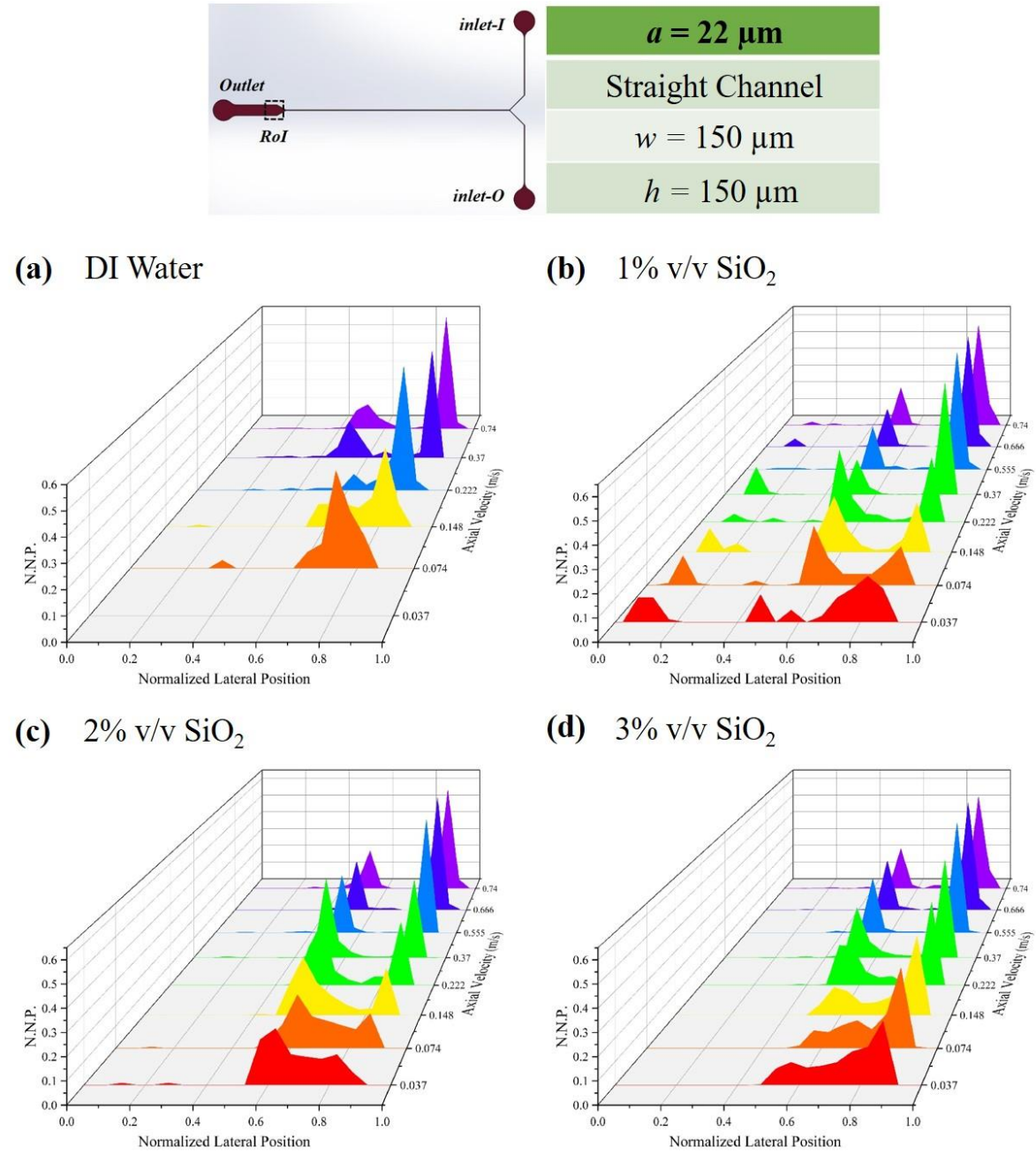

Appendix Figure F-4: Normalized number of particles alongside their normalized lateral position for 10 µm particles inside a square straight microchannel (150 × 150 µm^2) at various axial velocities.

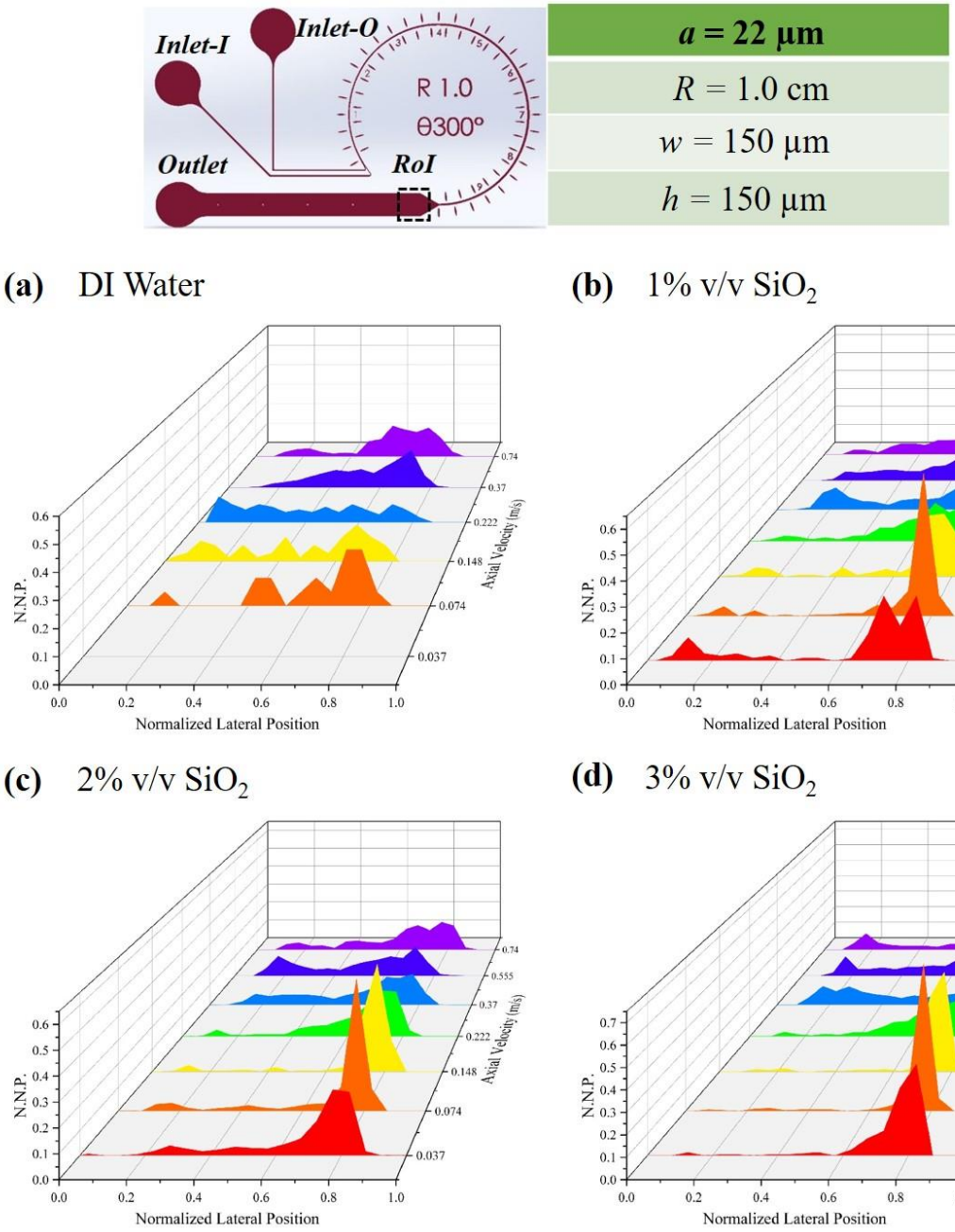

Appendix Figure F-5: Normalized number of particles alongside their normalized lateral position for 10 µm particles inside a square microchannel (150 × 150 µm^2) with R = 1.0 cm at various axial velocities.

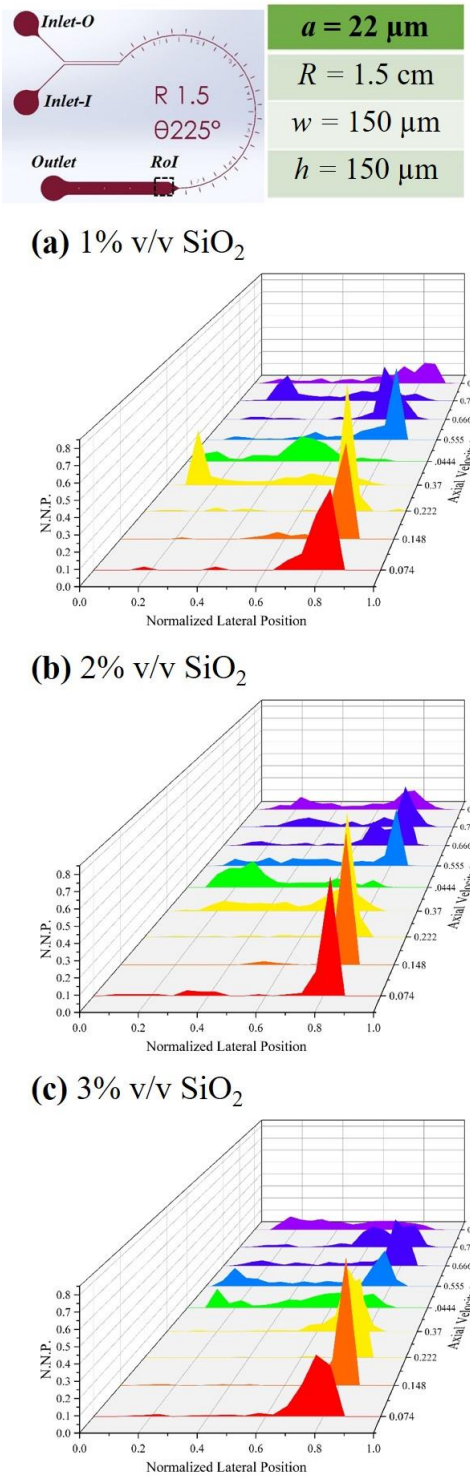

Appendix Figure F-6: Normalized number of particles alongside their normalized lateral position for 10 µm particles inside a square microchannel (150 × 150 µm^2) with R = 1.5 cm at various axial velocities.

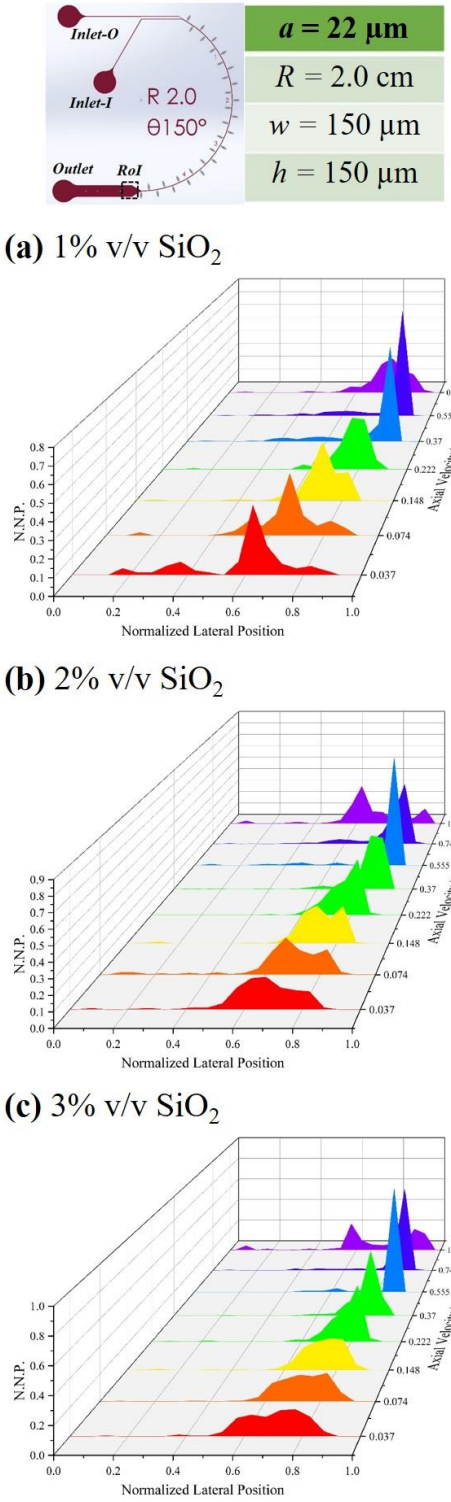

Appendix Figure F-7: Normalized number of particles alongside their normalized lateral position for 10 µm particles inside a square microchannel (150 × 150 µm^2) with R = 2.0 cm at various axial velocities